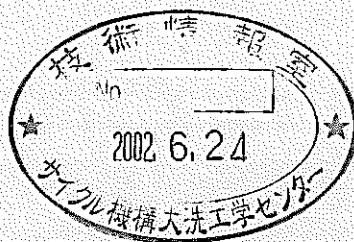


**Research on Fuel-Coolant Interaction by Using a
Multi-phase Multi-component Code**

**多相多成分流体解析コードを用いた高温溶融燃料と
冷却材の相互作用に関する研究**

(博士研究員研究詳細報告書)



March, 2002

**O-ARAI ENGINEERING CENTER
JAPAN NUCLEAR CYCLE DEVELOPMENT INSTITUTE**

本資料の全部または一部を複写・複製・転載する場合は、下記にお問い合わせください。

〒319-1184 茨城県那珂郡東海村大字村松4番地49
核燃料サイクル開発機構
技術展開部 技術協力課

Inquiries about copyright and reproduction should be addressed to :
Technical Cooperation Section,
Technology Management Division,
Japan Nuclear Cycle Development Institute
4-49 Muramatsu, Tokai-mura Naka-gun, Ibaraki, 319-1184
Japan

© 核燃料サイクル開発機構 (Japan Nuclear Cycle Development Institute)
2002

Research on Fuel-Coolant Interaction by Using a Multi-phase Multi-component Code

Xuewu CAO*

Abstract

Fuel Coolant Interactions (FCIs) are the important phenomena during the Core Disruptive Accidents (CDAs) in Liquid Metal Cooled Fast Breeder Reactors (LMFBRs) or Core Melt Accidents (CMAs) in Light Water Reactors (LWRs) and have been numerically investigated in recent years. The development and verification of models for the fundamental processes in FCIs are required for the application of a multi-phase, multi-component, fluid-dynamics computer code. In this study the drag coefficient model and the thermal fragmentation models for melt droplets are developed and verified through the application of SIMMER-III code, which is being developed at JNC, to the experiments, QUEOS, MIXA and KROTOS.

The FCI phenomena are characterized by a configuration that hot particles/droplets surrounded with vapor film moves in coolant liquid. The correlation of drag coefficient has not been developed for such a configuration. In this study, based on the basic conservative equations and the mixture viscosity concept, the drag coefficients between melt droplets with vapor film and the surrounding coolant liquid under laminar and turbulent flow conditions are developed, which are expressed as functions of Reynolds number, vapor/liquid viscosity and density ratios and the other two dimensionless numbers newly introduced in this study. The proposed correlations are coupled into the SIMMER-III code and applied to simulate the QUEOS experiment. The results show that the proposed correlations reasonably improve the agreement of the calculated results with the experimental data.

Thermal fragmentation mechanisms have been studied for many years, but the fragmentation models, triggered by boiling effect and surface solidification effect, are not available for numerical simulation tools. In this study, based on the Taylor instability, the fragmentation models, triggered by surface solidification and vapor film collapse are developed and simplified non-dimensional correlations are proposed for convenient application to simulation tools. The proposed thermal fragmentation correlations are verified both by comparing the model's predictions of fragments' size with experimental data and by simulating the MIXA experiment and KROTOS experiments, respectively.

* Nuclear system Safety Research Group, Advanced Technology Division, O-arai Engineering Center, JNC

多相多成分流体解析コードを用いた高温溶融燃料と冷却材の相互作用に関する研究 (博士研究員研究詳細報告書)

曹 学武*

要 旨

燃料—冷却材相互作用 (Fuel Coolant Interaction : FCI) は高速炉の炉心損傷事故および軽水炉のシビアアクシデントにおける重要な現象であり、近年、主に、数値計算的手法を用いて研究されている。この燃料—冷却材相互作用の研究には多相多成分流体解析コードが利用されるため、要素物理モデルの開発と検証が不可欠である。本研究では、核燃料サイクル開発機構で開発中の SIMMER-III コードを用いて QUEOS, MIXA, KROTOS などの実験を解析することにより、高温粒子・液滴の抵抗係数と溶融燃料の熱的細粒化モデルの開発・検証を行っている。

燃料—冷却材相互作用では、冷却材中を運動している高温粒子・液滴が蒸気膜で覆われていることが特徴である。この高温粒子・液滴の抵抗係数を適切に評価できるモデルは、まだ開発されていない。本研究では、基礎保存式と混合粘性モデルに基づいて、層流および乱流条件下で高温粒子・液滴に対する抵抗係数を評価する無次元抵抗関係式を開発した。この抵抗係数はレイノルズ 数、蒸気と冷却材との密度比および粘度比、そして本研究で新たに導入した 2 つの無次元数の関数として記述される。この関係式を SIMMER-III コードに組み込み、QUEOS 実験の解析に適用した結果、実験結果と解析結果との一致は適切に改善された。

溶融粒子熱細粒化メカニズムについては、これまでも多くの研究がなされているが、シミュレーションコードに使用できるような沸騰効果と表面固化を trigger とする微粒化モデルは開発されていなかった。本研究では、FCI 現象の数値シミュレーション技術の高度化を図るために、溶融燃料の熱的細粒化モデルを新たに提案した。このモデルは、圧力変化、沸騰効果および表面固化に基づく熱的細粒化メカニズムを Taylor 不安定性のメカニズムと組み合わせたものである。本モデルを粗混合過程と propagation の模擬実験解析に適用し、熱的細粒化モデルの有効性を確認した。

* 大洗工学センター 要素技術開発部 リスク評価研究グループ

Contents

ABSTRACT.....	I
要 旨	II
CONTENTS.....	III
LIST OF FIGURES	VII
LIST OF TABLES	XIV
1. INTRODUCTION	1
1.1 BACKGROUND	1
1.2 OBJECTIVE	1
1.3 OUTLINE OF THIS STUDY	1
1.4 OUTLINE OF THIS REPORT	2
REFERENCES	3
2. SIMULATION OF PREMIXING EXPERIMENT QUEOS BY SIMMER-III	4
2.1 INTRODUCTION	4
2.2 DESCRIPTION OF EXPERIMENT	5
2.3 SIMMER-III REPRESENTATION	7
2.3.1 Geometry, Initial Conditions and Calculation System.....	7
2.3.2 Code Version and Computer Used.....	8
2.4 RESULTS AND DISCUSSION	8
2.4.1 QUEOS Q-08 Test Base Case.....	9
2.4.2 Investigation of the Influence of the Drag Coefficient on Mixing Region in Q-08 Test.....	11
2.4.3 Investigation of the Influence of Gas Composition on Pressure in Q-08 Test...	12
2.4.4 QUEOS Q-12 Test Base Case.....	12
2.4.5 Investigation of the Influence of the Drag Coefficient on Mixing Region in Q-12 Test.....	14

2.5 CONCLUSIONS	15
2.6 RECOMMENDATIONS FOR MODEL IMPROVEMENTS	15
REFERENCES	16
3. STUDY ON DRAG COEFFICIENT FOR THE PARTICLE/DROPLET WITH VAPOR FILM.....	44
3.1 INTRODUCTION	44
3.2 THE DRAG COEFFICIENT FOR A SINGLE HOT PARTICLE.....	47
3.2.1 The Drag Coefficient Expression.....	47
3.2.2 The Drag Correlation under Laminar Flow Condition	48
3.2.3 The Drag Correlation under Turbulent Flow Condition	52
3.3 DRAG COEFFICIENT FOR MULTI-PARTICLE SYSTEM.....	55
3.3.1 Drag Correlation under Laminar Flow Condition	56
3.3.2 Drag Correlation under Turbulent Flow Condition	57
3.4 APPLICATION OF THE PROPOSED DRAG CORRELATIONS	58
3.5 CONCLUSION.....	59
REFERENCES	60
4. SIMULATION OF THE MIXA-06 EXPERIMENT BY SIMMER-III	75
4.1 INTRODUCTION	75
4.2 DESCRIPTION OF EXPERIMENT	76
4.3 SIMMER-III REPRESENTATION	76
4.3.1 Geometry, Initial Conditions and Calculation System.....	77
4.3.2 Code Version and Computer Used.....	78
4.3.3 Parametric Cases	78
4.4 RESULTS AND DISCUSSION	79
4.4.1 Base Case	79
4.4.2 Sensitivity Calculations	81
4.4.3 Fragmentation Mechanism in High Melting Point FCI	83
4.5 CONCLUSIONS	85
4.6 RECOMMENDATIONS FOR MODEL IMPROVEMENTS	85
REFERENCES	85
5. PROPOSAL OF THERMAL FRAGMENTATION MODELS FOR NUMERICAL STUDY OF FUEL-COOLANT INTERACTION.....	108

5.1 INTRODUCTION	108
5.2 THERMAL FRAGMENTATION MECHANISM	111
5.2.1 Review of Fragmentation Mechanism	111
5.2.2 Acceleration Mechanisms	114
5.2.2.1 External Pressure Pulse	114
5.2.2.2 Boiling Effect	114
5.2.2.3 Surface Solidification	115
5.3 DEVELOPMENT OF THERMAL FRAGMENTATION MODELS	116
5.3.1 Growth Rate of the Spikes on the Surface of a Melt Droplet	116
5.3.2 Fragmentation Rate of a Melt Droplet	117
5.3.3 Proposal of Thermal Fragmentation Models	118
5.3.3.1 Thermal Fragmentation Model Induced by Surface Solidification	118
5.3.3.2 Thermal Fragmentation Model Induced by External Pressure Pulse	120
5.3.3.3 Fragmentation Model Induced by Boiling Effect	122
5.4 VERIFICATION OF THE PROPOSED THERMAL FRAGMENTATION MODELS	124
5.4.1 Thermal Fragmentation Model Induced by Surface Solidification	125
5.4.2 Thermal Fragmentation Model Induced by External Pressure Pulse	126
5.4.3 Thermal Fragmentation Model Induced by Boiling Effect	127
5.4 CONCLUSIONS	127
REFERENCES	129
6. CONCLUSIONS	150
6.1 CONCLUDED REMARKS	150
6.2 FUTURE STUDY	151
NOMENCLATURE	153
LIST OF PUBLICATIONS	156
ACKNOWLEDGMENTS	158
APPENDIX A: DRAG COEFFICIENT FOR A SINGLE PARTICLE UNDER LAMINAR FLOW CONDITION	159
APPENDIX B: DRAG COEFFICIENT FOR A SINGLE PARTICLE UNDER TURBULENT FLOW CONDITION	162

APPENDIX C: INSTABILITY ANALYSIS ON THE SURFACE OF A DROPLET...	165
REFERENCES	169
APPENDIX D: VAPOR FILM COLLAPSE MODEL.....	170
REFERENCES	173
APPENDIX E: ESTIMATION OF THE PRESSURIZATION IN A MELT DROPLET IMMERSED INTO COOLANT.....	178
REFERENCES	183

List of Figures

Fig. 2- 1	Scheme of the QUEOS facility	17
Fig. 2- 2	Simulation Model of QUEOS test.....	18
Fig. 2- 3	Pressure in the vessel at position of P2 and P6 in Q-08.....	19
Fig. 2- 4	Water level transient in the vessel in Q-08.....	19
Fig. 2- 5	Evolution of the leading edges of the sphere cloud and water in Q-08.	20
Fig. 2- 6	Contour graphs of the volume fraction of the sphere cloud in Q-08, plotted at time of 0.53, 0.59, 0.65, 0.71, 0.77 and 0.83 second from (a) through (f).	22
Fig. 2- 7	Contour graphs of the volume fraction of water in Q-08, plotted at time of 0.53, 0.59, 0.65, 0.71, 0.77 and 0.83 second from (a) through (f).	24
Fig. 2- 8	Images of molybdenum sphere cloud falling in water in Q-08 experiment...25	
Fig. 2- 9	Evolution of the leading edge of the sphere cloud in cases with different drag coefficient multipliers CDD and CCD of 0.125, 0.25, 1.0 and 2.0 in Q-08.	26
Fig. 2- 10	Evolution of the leading edge of water in cases with different drag coefficient multipliers CDD and CCD of 0.125, 0.25, 1.0 and 2.0 in Q-08.	26
Fig. 2- 11	Contour graphs of the volume fraction of the sphere cloud in Q-08, plotted at time of 0.77 second for the cases with drag coefficient multiplier of 0.125, 0.25, 1.0 and 2.0 from (a) through (d).	27
Fig. 2- 12	Contour graphs of the volume fraction of water in Q-08, plotted at time of 0.77 second for the cases with drag coefficient multiplier of 0.125, 0.25, 1.0 and 2.0 from (a) through (d).	28
Fig. 2- 13	Pressure transients in the vessel at position of P6 in the cases of Q-08 with different multiplier of drag coefficient	29
Fig. 2- 14	Evolution of the leading edge of the sphere cloud in cases with different drag coefficient multipliers CDD and CCD in Q-08.	29
Fig. 2- 15	Pressure transients in vessel at position of P6 in the cases of Q-08 with different ratio of air to vapor in air space.	30
Fig. 2- 16	Pressure in the vessel at position of P2 and P6 in Q-12.....	30

Fig. 2- 17	Influence of pressure drop coefficient on pressure in flow exit in Q-12.....	31
Fig. 2- 18	Evolution of the leading edge of the sphere cloud and water in Q-12, the half of the volume fraction contour line is defined as the boundary of the cloud.....	31
Fig. 2- 19	Water level transient in the vessel in Q-12.....	32
Fig. 2- 20	Contour graphs of the volume fraction of the sphere cloud in Q-12, plotted at time of 0.53, 0.586, 0.642, 0.698, 0.754 and 0.81 second from (a) through (f).....	34
Fig. 2- 21	Contour graphs of the volume fraction of water in Q-12, plotted at time of 0.53, 0.586, 0.642, 0.698, 0.754 and 0.81 second from (a) through (f)...	36
Fig. 2- 22	Images of molybdenum sphere cloud falling in water in Q-12.....	37
Fig. 2- 23	Volume flow rate through venting pipe in Q-12	38
Fig. 2- 24	Evolution of the leading edge of the sphere cloud in cases with different drag coefficient multiplier CDD and CCD of 0.05, 0.25 and 1.0 in Q-12...	38
Fig. 2- 25	Evolution of the leading edge of water in cases with different drag coefficient multiplier CDD and CCD of 0.05, 0.25 and 1.0 in Q-12.....	39
Fig. 2- 26	Contour graphs of the volume fraction of the sphere cloud in Q-12, plotted at time of 0.698 second for the cases with drag coefficient multiplier of 0.025, 0.05, 0.25 and 1.0 from (a) through (d).	40
Fig. 2- 27	Contour graphs of the volume fraction of water in Q-12, plotted at time of 0.698 second for the cases with drag coefficient multiplier of 0.025, 0.05, 0.25 and 1.0 from (a) through (d).	41
Fig. 2- 28	Pressure transient in the vessel at position of P6 in the cases of Q-12 with different multiplier of drag coefficient.....	42
Fig. 2- 29	Gas flow rate through venting pipe in the cases of Q-12 with different multiplier of drag coefficient.	42
Fig. 2- 30	Evolution of the leading edge of the sphere cloud in cases with different combination of drag coefficient multipliers in Q-12.	43
Fig. 3- 1	Configuration of a single droplet moving in coolant in Nelson experiment (NUREG/CR-2718)	62
Fig. 3- 2	Scheme of a hot particle moving in coolant liquid	63
Fig. 3- 3	The drag coefficients obtained from the experimental data and those	

	predicted by the fitted correlation under turbulent condition arranged in Reynolds number	64
Fig. 3- 4	The drag coefficients obtained from the experimental data and those predicted by the fitted correlation under turbulent condition arranged in Ev number	65
Fig. 3- 5	The relativity of the drag coefficient predicted by equation (3-29) and their experimental data	66
Fig. 3- 6	The variation of the drag coefficient of the particles with vapor film under laminar condition with Reynolds number. (Ev number is 200, μ_0 is 0.12, ρ_0 is 0.00056 and g_0 is 8×10^6 . The alpha is the volume fraction of the particles)	67
Fig. 3- 7	The variation of the drag coefficient of the particles with vapor film under laminar condition with Ev number. (Reynolds number is 1000, μ_0 is 0.12, ρ_0 is 0.00056 and g_0 is 8×10^6 . The alpha is the volume fraction of the particles)	68
Fig. 3- 8	The variation of the drag coefficient of the particles with vapor film under laminar condition with the volume fraction of the particles. (Ev number is 200, μ_0 is 0.12, ρ_0 is 0.00056 and g_0 is 8×10^6 . The alpha is the volume fraction of the particles)	69
Fig. 3- 9	The variation of the drag coefficient of the particles with vapor film under turbulent condition with Reynolds number. (Ev number is 200, μ_0 is 0.12, ρ_0 is 0.00056 and g_0 is 8×10^6 . The alpha is the volume fraction of the particles)	70
Fig. 3- 10	The variation of the drag coefficient of the particles with vapor film under turbulent condition with Ev number. (Reynolds number is 10000, μ_0 is 0.12, ρ_0 is 0.00056 and g_0 is 8×10^6 . The alpha is the volume fraction of the particles)	71
Fig. 3- 11	The variation of the drag coefficient of the particles with vapor film under turbulent condition with the volume fraction of the particles. (Ev number is 200, μ_0 is 0.12, ρ_0 is 0.00056 and g_0 is 8×10^6 . The alpha is the volume fraction of the particles)	72

Fig. 3- 12	The advancements of the particle cloud in QUEOS-12, calculated by different drag coefficient correlations.....	73
Fig. 3- 13	The advancements of the particle cloud in QUEOS-35, calculated by different drag coefficient correlations.....	74
Fig. 4- 1	Scheme of the MIXA facility.....	88
Fig. 4- 2	The computational domain used in the MIXA-06 simulation	89
Fig. 4- 3	Front advancement of the droplet stream in water in the experiment and the simulation (base case) of MIXA-06.....	92
Fig. 4- 4	The pressure transient in the free gas space in the experiment and the simulation (base case) of MIXA-06.....	93
Fig. 4- 5	Steam flow rate in the experiment and the simulation (base case) of MIXA-06.	94
Fig. 4- 6	Cumulative steam volume in the experiment and the simulation (base case) of MIXA-06.	95
Fig. 4- 7	Water level swell in the experiment and the simulation (base case) of MIXA-06.	96
Fig. 4- 8	Front advancement of the droplet stream in water in the experiment and the simulation (case1) of MIXA-06.....	97
Fig. 4- 9	The pressure transient in the free gas space in the experiment and the simulation (case1) of MIXA-06.....	98
Fig. 4- 10	Steam flow rate in the experiment and the simulation (case1) of MIXA-06.	99
Fig. 4- 11	Cumulative steam volume in the experiment and the simulation (case1) of MIXA-06.	100
Fig. 4- 12	Front advancement of the droplet stream in the simulation of MIXA-06 with different fragment size in Taylor fragmentation model.	101
Fig. 4- 13	Front advancement of the droplet stream in the simulation of MIXA-06 with different fragmentation time interval in Taylor correlation. Case3: fragmentation time is divided by 1000.	102
Fig. 4- 14	Front advancement of the droplet stream in the simulation of MIXA-06 with different fragmentation models (1). Base case: Taylor correlation. Case4: no fragmentation.	103

Fig. 4- 15	Front advancement of the droplet stream in the simulation of MIXA-06 with different fragmentation models (2). Base case: Taylor correlation. Case5: Pilch_Erdman correlation.	104
Fig. 4- 16	Front advancement of the droplet stream in the simulation MIXA-06 with different fragmentation rate. Base case: CFSB, CFSD=1.0, We _{cr} =12. Base6: CFSB, CFSD=1.0, We _{cr} =0.12. Case7: CFSB, CFSD=0.001, We _{cr} =0.12.	105
Fig. 4- 17	Front advancement in the simulation of MIXA-06 with different fragment size. Case1: the radius of fragmented droplets is set to 0.001. Case8: the radius of fragmented droplets is set to 0.0015. Case9: the radius of fragmented droplets is set to 0.0007.	106
Fig. 4- 18	Front advancement of the droplet stream in water in the experiment and the simulation (base case) of MIXA-01.	107
Fig. 5- 1	Typical boiling curve for saturated pool boiling of water at atmospheric pressure	132
Fig. 5- 2	The Fragmentation mechanism map considering the thermal condition of the melt droplet and coolant.	133
Fig. 5- 3	Aluminum bubble showing what appears to be interior aluminum that was forced through the outer shell.	134
Fig. 5- 4	Interior of completely mossy lead after fragmentation.	134
Fig. 5- 5	Pressurization on the solid-liquid interface induced by the surface solidification of the melt droplet.	135
Fig. 5- 6	Thickness of the shell during the solidification process	135
Fig. 5- 7	Total surface tension including the effect of the solid shell	136
Fig. 5- 8	The instability index during the solidification process	136
Fig. 5- 9	Fragmented mass induced by the surface solidification of the melt droplet.	137
Fig. 5- 10	The parameter C_B in equation (20) for the case that the fragmentation is induced by surface solidification	137
Fig. 5- 11	Fragmented mass induced by external pressure pulse applying on the melt droplet	138
Fig. 5- 12	Pressure in vapor film induced by external pressure pulse applying on the melt droplet	138

Fig. 5- 13	The parameter C_b in equation (20) for the case that the triggering event is external pressure pulse	139
Fig. 5- 14	Fragmented mass induced by external pressure pulse applying on the melt droplet	139
Fig. 5- 15	Pressure in vapor film induced by boiling effect	140
Fig. 5- 16	The parameter C_b in equation (20) for the case that the fragmentation is triggered by boiling effect.....	140
Fig. 5- 17	The comparison of fragment size with experimental data	141
Fig. 5- 18	Front Advancement of the melt droplets in water in MIXA-06.....	142
Fig. 5- 19	Front Advancement of the melt droplets in water in MIXA-01.....	143
Fig. 5- 20	The comparison of fragment size with experimental data	144
Fig. 5- 21	KROTOS test facility simulation model	145
Fig. 5- 22	Advancement of shock wave in the test tube in KROTOS 28.....	146
Fig. 5- 23	Pressure profile in test tube in KROTOS 44.....	148
Fig. C- 1	The instability analysis model.....	169
Fig. D- 1	The analytical model for vapor film collapse.....	174
Fig. D- 2	The generated pressure in the vapor film during the collapse induced by external pressure pulse.....	174
Fig. D- 3	The thickness of the vapor film during the collapse induced by external pressure pulse.....	175
Fig. D- 4	The initial pressure pulse effect on the generated pressure in the vapor film during the collapse induced by external pressure pulse.....	175
Fig. D- 5	The droplet temperature effect on the generated pressure in the vapor film during the collapse induced by external pressure pulse.....	176
Fig. D- 6	The ambient pressure effect on the generated pressure in the vapor film during the collapse induced by external pressure pulse.....	176
Fig. D- 7	The generated pressure in the vapor film due to heat transfer model change	177
Fig. E- 1	Analytical model of solidification	185
Fig. E- 2	Schematic of solid layer stability model.....	185

Fig. E- 3	The variation of the C_B in equation (20) with the Young's module.....	186
Fig. E- 4	The variation of the C_B in equation (20) with the radius of the droplet.....	186
Fig. E- 5	The variation of the C_B in equation (20) with the melting temperature of the droplet	187
Fig. E- 6	Stress in the solid shell induced by the surface solidification of the melt droplet	187

List of Tables

Table 4- 1	Data of the experiment MIXA-06.....	90
Table 4- 2	Data used for the simulation of MIXA-06.....	91

1. Introduction

1.1 Background

Fuel Coolant Interactions (FCIs) are the important phenomena during the Core Disruptive Accidents (CDAs) in Liquid Metal Cooled Fast Breeder Reactors (LMFBRs) or Core Melt Accidents (CMAs) in Light Water Reactors (LWRs). When the molten metals are released from the reactor vessel to contact with coolant liquid, FCIs occur, which include the processes of jet breakup, premixing, fragmentation, propagation and expansion. Several mathematical models of multi-phase multi-component flow, based on a multi-field description, have been developed with the aim of describing these events. The SIMMER-III code, a two-dimensional, three-velocity-field, multi-phase, multi-component, Eulerian, fluid-dynamics computer code developed at JNC [1,2], is one of them. Although the multi-phase multi-component numerical simulation tool is an effective mean to study the interaction of high temperature molten materials with coolant, to some extent, the current models are not enough to analyze the phenomena. Due to the complexity of the physical phenomena in the process, detailed models of them, especially the jet breakup, fragmentation and propagation, are required to analyze the FCI processes and the consequences.

1.2 Objective

The objective of this study is to develop and validate these models and introduce them into SIMMER-III code. This study will improve the capability of SIMMER-III model to analyze FCI process and provides the better understanding of the mechanism of mechanical energy generation in FCI process.

1.3 Outline of This Study

The physical phenomena of premixing, fragmentation escalation, propagation and jet breakup in FCIs will be modeled, included and validated in the SIMMER-III code through the simulation of experiments performed for the FCI's processes as stated in the

following.

(1) The models related to the premixing process will be verified through the simulation of experiments, selected from QUEOS and MIXA, the out-of-pile experiment series. The small particles or droplets of molten material surrounded by a vapor film in quasi-steady state are mainly featured in this process. The drag coefficient models of hot particles/droplets with vapor film will be developed and validated.

(2) The models related to the fragmentation, and propagation process will be verified through the simulation of experiments selected from MIXA and KROTOS experiment series. This process features the rapid fragmentation of small molten material droplets. The models of fragmentation of melt droplets, based on thermal mechanism, will be developed, included in the code and validated.

(3) The jet breakup model will be developed and validated through the simulation of the experiments selected from a series of JET and FARO experiments. During the reactor severe accidents, the molten material may flow into coolant as a jet and it is broken up into small droplets in-vessel or ex-vessel. Based on the observation and analysis of experiments, the model to describe the jet breakup process will be developed and included in the code. Then it will be validated through the simulation of the selected experiments.

1.4 Outline of This Report

This report is the summary of my current research in JNC. Chapter 2 is the summary of the simulation of premixing experiment QUEOS by SIMMER-III, which show that a drag coefficient model of a particle/droplet with vapor film moving in coolant liquid is required to be developed [3]. Then the drag correlations for a hot particle/droplet with vapor film are developed based on the basic conservative equations and the mixture viscosity concept and verified through the simulation of QUEOS, summarized in chapter 3 [4]. In chapter 4 the MIXA experiments are simulated by SIMMER-III to show the requirement of the development of fragmentation model based on freezing-provoked droplet fragmentation mechanism for simulation code [5]. Chapter 5 is the summary of the development of thermal fragmentation model, induced by surface

solidification and collapse of vapor film, based on Taylor instability and verification through the simulation of MIXA and KROTOS experiments [6]. The final chapter is the conclusion of current research results.

References

- (1) Kondo, Sa., *et al.*: Status and Achievement of Assessment Program for SIMMER-III, a Multiphase, Multicomponent Code for LMFR Safety Analysis, *Proc. of Eighth International Topical Meeting on Nuclear Reactor Thermal-Hydraulics*, Vol. 3, P. 1340, Kyoto, Japan, Sept. 30-Oct. 4 1997.
- (2) Morita, K., *et al.*: SIMMER-III Application to Fuel-Coolant Interactions, *Proc. of the OECD/CSNI Specialists Meeting on Fuel- Coolant Interactions*. P. 785, May 19-21, 1997, JAERI, Tokai-mura, Japan.
- (3) Xuewu Cao and Yoshiharu Tobita, Simulation of Premixing Experiment QUEOS by SIMMER-III, JNC TN9400 2001-100.
- (4) Xuewu Cao and Yoshiharu Tobita, Study on Drag Coefficient For the Particle/Drop Under FCI Condition, JNC TN9400 2001-055.
- (5) Xuewu Cao and Yoshiharu Tobita, Simulation of MIXA-06 Experiment by SIMMER-III, JNC report, JNC TN9400 2001-122.
- (6) Xuewu Cao and Yoshiharu Tobita, "Proposal of the Thermal Fragmentation Models for Numerical Study of FCI, JNC report", JNC TN9400 2001-123.

2. Simulation of Premixing Experiment QUEOS by SIMMER-III

2.1 Introduction

That the high temperature materials (fuel) interact with the low temperature material (coolant) is the important phenomena in nuclear reactor severe accident, which has been numerically studied in recent years. The SIMMER-III code, a two-dimensional, three-velocity-field, multi-phase, multi-component, Eulerian, fluid dynamics computer code coupled with a space and energy dependent neutron kinetics model, developed in JNC [1, 2], is being applied to study the fuel coolant interaction (FCI), which needs to extrapolate the constitutive correlations used in the simulation code to describe the FCI processes. The prediction of the premixing region in FCI is important to estimate the consequences of the FCI, which is dominated by the momentum exchange between the fuel and the coolant liquid. In the premixing phase, that the droplets of the fuel moving in the coolant liquid are surrounded by vapor film is featured. Currently employed drag coefficient correlations in SIMMER-III code are those developed by Ishii [3] for two-phase flow. The applicability of those correlations on the premixing phase of FCI, in which droplets are surrounded by vapor film will be estimated through the simulation of the premixing experiment QUEOS [4, 5].

The QUEOS experiment has been simulated by other mathematical models, for example, PM-ALPHA [6], IVA-KA [7] as the verification of their models. Due to the advantages of the fixed particle size and long range of temperature from room temperature to 2300 K, the experiment Q-08 and Q-12 are selected to estimate the influence of the drag correlations between the fuel and the coolant on the mixing region. The influence of the fuel temperature on the momentum exchange between the fuel and the coolant liquid will be estimated through the simulation of these two experiments. In this study the pressure transient, the shapes of the particle cloud and the penetration behavior of the particle cloud in water are calculated to estimate the influence of the drag correlations between the fuel and the coolant on the mixing region.

2.2 Description of Experiment

As shown in Fig. 2-1, the QUEOS facility, as described in [4, 5] consists of the test vessel, the furnace and the valve system separating the vessel and the furnace. The solid molybdenum spheres are heated in an electric radiation furnace in an argon atmosphere. After the pneumatically activated release of the spheres, they fall onto a heat-resistant sliding door valve and stay there for less than one second. During this time, the top valve is closed gas tight and the lower one is opened. Then the middle valve opens symmetrically to two sides within 40 ms and the spheres are discharged into the water with a drop height of 130 cm. The diameter of the sphere stream is 100 mm after the discharge from the middle valve and the spheres fall freely without touching any walls.

The water vessel is made of stainless steel frames and glasses and has a square cross section of 0.7 meter side length and is 1.38 meter high. Three walls have glass windows, with a field of view of 50 by 113.5 cm. A reference grid of 10x10 cm is mounted close to the inside of each of the windows, consisting of steel wire with 2 mm diameter. The fourth wall is instrumentation wall made of steel. At its upper end, there is an opening of 100 mm diameter, connected to the steam venting pipe. The pipe is guard-heated and insulated to prevent condensation. The venting pipe restricts the outflow of the steam from the vessel and therefore the pressure increase in the vessel is both a function of the vaporization rate and flow resistance of the steam pipe. The total pressure loss coefficient, defined as $\zeta = \Delta p / (\rho v^2 / 2)$, was measured with steady state air flow being $\zeta = 4.54$, with the density ρ of steam and the average velocity v in the pipe. The test vessel is filled with water (0.5 m^3) to a level of 1 m. The water is heated externally. All sides of the vessel are heated from outside by radiators, to obtain a uniform temperature of the water. The bottom of the vessel is covered with 49 (a matrix of 7x7) square boxes (10x10x5 cm) for determining the final distribution of the spheres.

The temperature of water and steam are measured by Ni-CrNi-thermocouples. Six piezoresistive pressure transducers measure the vessel pressure. They are installed at

various positions below and above the water level within a shielding tube, which extends 20 mm into the water. In the steam venting pipe, the pressure is measured by miniature piezoresistive transducers 160 cm before the vortex flow meter. The steaming rate is measured by a vortex flowmeter, which works on the principle of vortex shedding. The water level is measured by two impedance level meters positioned in opposite corners of the test vessel.

Experiment Q-08 was performed with the molybdenum spheres with an initial temperature of 300K. 10 kg molybdenum spheres, rested for almost a minute on the middle valve, were released into water pool. The first spheres start to fall at 0 second from the height of 1.3 m above the water surface. The last spheres start to fall at 0.04 second from the height of 1.38 meter above the water surface. The time of free fall of the first spheres in air 0.015 second. The spheres reach the water surface at 0.515 s and the last spheres reach the water surface at 0.57 s. The corresponding impact velocities are 5.05 m/s and 5.2 m/s for the first spheres and last spheres respectively. When the sphere cloud contacts the water surface, the shape of the cloud was almost a cylinder with a height of 28 cm and a radius of 9 cm. The mean sphere volume fraction was estimated as 0.17 by Meyer [5], although the volume fraction is not uniform, especially at the front and the top of the sphere cloud. There is a large gas volume being dragged deep down into water, when the sphere cloud penetrates into water. The water in the vessel was heated to near the saturated temperature.

Experiment Q-12 was performed with the same molybdenum spheres as Q-08 but with an initial temperature of about 2300K. Because of the high temperature, some of the spheres stuck together within the furnace so that only 6.9 kg were released. The cylinder of the sphere cloud was elongated compared with the theoretical value when it contacts the water surface. The other conditions are the same as the Q-08 experiment.

2.3 SIMMER-III Representation

2.3.1 Geometry, Initial Conditions and Calculation System

The QUEOS experimental vessel, shown in Fig. 2-1, is modeled as an axis-symmetric cylindrical volume with the same cross sectional area as the real vessel in a diameter of 0.8 m and the height of 1.4 m. The computational domain employed is shown in Fig. 2-2, which is a cylindrical vessel and open to outside from the hole with a radius of 0.06 m at the center of the top of the vessel. The simulation starts from the impact of the sphere cloud on the water by a sphere cylinder located at the place 0.056 m above water surface with an initial velocity, slightly less than the value, as described in the report of the experiment by Meyer [4]. The cylinder of spheres with an initial volume fraction of 0.17 has a height of 0.28 m and a radius of 0.09 m, which are estimated by Meyer [5] from the pictures of the images. The front (bottom) of the cylinder of the cloud of the spheres falls to the water level with the initial velocity of 5 m/s. The shape of the cylinder of the spheres has a little difference in two cases in order to match the initial mass of the spheres, which is 10 kg and 6.9 kg in experiments Q-08 and Q-12, respectively. Due to some not yet fully understood mechanisms (possibly some sticking above the sliding doors), the sphere cloud was much longer when contacting the water pool. Although the height of the sphere cloud cylinder in Q-12 is larger than that in Q-08, the same height of the sphere cloud cylinder is assumed in two cases. The top and bottom radius of the cylinder in Q-12 case is smaller than those in Q-08 case. The volume fraction of the sphere cloud is not uniform along the radial direction. In the center, the value is much higher than that at the boundary. Since the shape and volume fraction distribution could not be clearly determined from the experimental data, in order to avoid too much speculation, uniform sphere volume fraction of 0.17, the same as that in Q08 case, is assumed. In the experiment, 49 square boxes are placed on the bottom of the vessel to determine the distribution of the spheres. This is not simulated in the study, since it does not have much influence on the penetration of the sphere cloud.

In this study, the spheres are molybdenum ball with diameter of 4.2 mm which is the same value with the experiments. The total mass of the molybdenum spheres is 10 kg

and 6.9 kg in Q-08 and Q-12 respectively. The initial temperature is 300K and 2300K for Q-08 and Q-12 respectively. The gas space is initially filled with air with initial pressure 1 bar and temperature 370.5 K. The temperature of water in the vessel is assumed as 370.5K.

The geometric model, shown in Fig. 2-2, is discretized radially by 27 nodes with $\Delta r = 0.015$ m and axially by 50 nodes with $\Delta z = 0.03$ (in the water region). The calculations are carried out with a time step of $\Delta t = 4 \times 10^{-5}$ and $\Delta t = 8 \times 10^{-5}$ for Q08 and Q-12 respectively. The initial, minimum and maximum radii of spheres are set to 0.0021 in accordance with the value used in these experiments. 0.001, 0.000001 and 0.0001 are set for the initial, minimum and maximum radii of water respectively. The modified ILUBCG method is selected for fluid dynamics algorithm. The orifices plates are set in the flow-out cells near the center of the top in the calculation domain in order to simulate the venting system in QUEOS experiments. The orifice plate coefficient is 2.27, which is the half of the value measured in the experiments in venting system. The multipliers of the drag coefficient among dispersed components and between dispersed and continuous components are set to 1.0 (default value) respectively. The influence of the drag coefficient by changing the multipliers will be investigated for two cases. The continuous inflow/outflow is set to the boundary cell in the open exit on the top of the domain, in which the pressure is set to constant with 1 bar.

The equation of state for molybdenum is important for the success of the simulation. Here the EOS prepared by Dr. Morita is employed, in which constant density of molybdenum is assumed.

2.3.2 Code Version and Computer Used

Calculations are based on SIMMER-III Version 2.F (ALPHA, DBL, URANAS options on). The computer used was an EWS ALPHA.

2.4 Results and Discussion

The principle results including pressure transients at the positions corresponding

to transducers P2 and P6 in water vessel, water level in the vessel, the evolution of the location of the sphere cloud, the contour graphs of the cloud and mixing region are summarized, in conjunction with the experimental results, in the following. These comparisons focus on the time frame from 0.51 s, at which time spheres contact with the water surface, to 0.8 to 0.9 s, at which the leading edge of the spheres contact the bottom of the water vessel.

2.4.1 QUEOS Q-08 Test Base Case

In Q-08 experiment, 10 kg molybdenum sphere with 300K was released into water. The pressure transients at the positions corresponding to transducers P2 and P6 in the water vessel, given by the experiments and calculated by SIMMER-III, are plotted in Fig. 2-3. Generally, the shapes of the calculated pressure transients in P2 and P6 are in agreement with those in the experiment, but the amplitude of the first generated pressure pulse (due to collapse of gas chimney at around 0.75 second) is smaller than those in the experiment. When the cold spheres enter the water at about 0.51 s, the pressure at the position of P6 slightly increases in the water, lasting about 50 ms, then decreases. At 0.72 s it reaches a minimum of 1.05 bar, 20 mbar higher than that in the experiment, then increases and decreases sharply, forms a highest pressure spike of 1.115 bar, 80 mbar less than the value in the experiment. The maximum pressure peak values occurs at the time a little later than that in the experiment, which coincides with the collapse of the gas chimney formed during the falling of the sphere cloud in the water. In the experiment the high pressure peak reverberates several times with a frequency of 18 Hz and declining amplitude, but in the calculation the reverberation is in a much lower frequency (duration is about 150 ms) and the amplitude slightly higher than that in the experiment. The difference may be caused by not simulating the sphere collection cells on the bottom of the vessel or by the system difference between the real vessel and calculated vessel, which have different inherent frequency. In the experiment, the water vessel is quadratic in cross section and it becomes circle in the calculation. Although the shape of the pressure transient is generally in agreement with that in experiment and the differences are given, it is not enough to be used to estimate the momentum transfer between the

spheres and the water during the penetration, which will be further discussed later.

The 0.5 contour line of water volume fraction is defined as the interface of bulk water and the water level swell is plotted as shown in Fig. 2-4. In the experiment, the water level was measured on the corner of the vessel. Here the calculated water level is the water depth at the position of the place near the radial boundary of the cylindrical vessel. The water level transient shows that the maximum calculated water level occurred at around 0.8 second (instead of 0.7 second in the experiment) are larger than that in the experiment. And then it decreases. The difference may be induced by the definition of the interface and the counted position of the water level. Due to the diffusion of the boundary and the change of the counted position of the water level, the output value changes too much. It is more difficult to compare the calculated value with experimental data.

The contour line of the volume fraction of the sphere cloud with the half (0.085 initially) of maximum value (0.17 initially) of the volume fraction is defined as the interface of the sphere cloud. The leading edge of the sphere cloud is counted, as shown in Fig. 2-5. The 0.5 contour line of the volume fraction of water is defined as the boundary of the water region and the leading edge of the water is plotted as shown in Fig. 2-5. Since the leading edge of the sphere cloud is below the leading edge of the water, here the leading edge of the sphere cloud is taken as the leading edge of the mixing region. The spheres penetrated into water and the leading edge of the mixing region moves down at a velocity of about 2.0 m/s in the experiment, as shown in Fig. 2-5, in which the penetration rate of the cloud is almost linear. The calculated penetration rate is also almost linear and it is about 2.5 m/s, which is a little larger than that in the experiment.

The evolution of the leading edge of the sphere cloud suggests that the momentum exchange between the solid spheres and the water is overestimated just after the cylinder of the sphere cloud completely enters the water (at about 0.61 s) in the current calculation model. The impact of the sphere on water with a velocity of 5 m/s implies high accelerations of the relative motion of the two phases. For the spheres

impact on the water the acceleration term for momentum exchange is negative. Since the virtual term for solid spheres is not considered in the current model, the momentum exchange is overestimated.

The momentum exchange is underestimated after the sphere cloud completely enters the water in current calculation model. In this calculation, the multiplier of drag coefficient is 1.0. The influence of the drag coefficients on mixing region will be investigated later through the change of the multipliers of the drag coefficients. The contour graph of the volume fraction of the sphere cloud and the water in the time of 0.53, 0.59, 0.65, 0.71, 0.77 and 0.83 are plotted in Figs. 2-6 and 2-7. The sphere cloud cylinder becomes thinner and wider with evolution. The volume fraction of the sphere cloud becomes larger (larger than the initial value) in the center and smaller in boundary. The figure 2-7 shows the formation and collapse of the gas chimney. A large bubble is formed in the water. The image of mixing region taken from the experiment is shown in Fig. 2-8, plotted at the same time as the calculated results. The diameter of the mixing region in the calculation is about 0.2 m (0.032 contour line) and 0.24 (0.016 contour line) at the time of 0.77 s. This value is about 0.25 m in the experiment.

2.4.2 Investigation of the Influence of the Drag Coefficient on Mixing Region in Q-08 Test

The influence of the drag coefficients on the mixing region in the cold sphere experiment is investigated through the change of the multipliers CDD and CCD of the drag coefficient among dispersed components and between dispersed and continuous components. The cases with the multipliers of 0.125, 0.25, 1.0 and 2.0 are investigated and the evolutions of the location of the leading edge of the sphere cloud and water are plotted as shown in Figs. 2-9 and 2-10. Due to the underestimation of the momentum exchange, the larger the multiplier, the more the evolution approaches to the experimental data. The evolution of the location of the leading edge of the sphere cloud in the case with the drag coefficient multiplier of 2.0 most approaches to the experimental data. The calculated results show the multiplier of 2.0 for cold sphere

release experiment is suggested. The contour graphs of the sphere cloud and water for the cases with different multipliers are plotted at the time of 0.77 second to see the effect of the drag coefficient on the shape of the mixing region, as shown in Figs. 2-11 and 2-12 respectively. For the cases with larger value of the multiplier, the mixing region becomes wider and shorter, and the gas chimney collapses later.

The pressure transients in the vessel at the position of P6 are shown in Fig. 2-13 for the cases with different multiplier of the drag coefficients. The amplitude of the pressure peak due to the collapse of the gas chimney is not much affected by the drag coefficient, but it affects the occurrence time as shown in Fig. 2-13. The more cases with different CDD and CCD are calculated, as shown in Fig. 2-14. The results show that in Q-08 simulation the drag coefficient between dispersed and continuous components (between solid sphere and water) plays an important role.

2.4.3 Investigation of the Influence of Gas Composition on Pressure in Q-08 Test

The exact composition of gas in the upper free space of the vessel is not clear in the experiment. Three cases with different gas and vapor composition filled in the free space are investigated. The partial pressures set for air and vapor are 99 KPa and 1 KPa, 99.99 KPa and 0.01 KPa respectively for case1 and 3. For case 2 the gas is Xe and its partial pressure is 90 KPa. The remaining vapor partial pressure is 10 KPa. The pressures at point P6 in each case are shown in Fig. 2-15, which suggest that the composition of non-condensable gas and vapor in the free space makes the pressure a little change, but no much difference. The initial pressure transient is improved by specifying lower vapor partial pressure.

2.4.4 QUEOS Q-12 Test Base Case

In Q-12 experiment, 6.9 kg molybdenum sphere with the temperature of 2300K was released into water. The pressure transients in positions corresponding to transducers P2 and P6 in the water vessel, given by the experiments and calculated by SIMMER-III, are plotted in Fig. 2-16, which suggests that the heat transfer in the water/evaporation

process is overestimated in the calculation. When the hot spheres enter the water at time 0.51, the pressure at the position corresponding to P6 increases quickly. It reaches a plateau, which continues about 0.15 s, then it decreases sharply (but not as much as that in the experiment) and reaches to a level slightly higher than the experiment. A small peak is seen in the calculation, which appears in the experiment due to the collapse of the gas chimney at 0.72 s. In this case the pressure transient shape is similar to the experiment, but the amplitude is slightly larger than that in the experiment and the pressure plateau extends 100 ms longer than that in the experiment, which is induced by higher heat transfer to water and evaporation of water.

In order to estimate the effect of the venting pipe, three cases with different orifice plate pressure drop coefficients are calculated and the results are plotted in Fig. 2-17. The coefficients of the pressure drop in the orifice are 1.135, 2.27 and 4.54 in three cases respectively. The pressure in the water (P6) is not sensitive to it. It is not the main factor influencing the pressure transient.

With the same definition of the boundaries between the sphere cloud and the water, the evolution of the location of the leading edge of the hot sphere cloud and water and water level swell are plotted as shown in Figs. 2-18 and 2-19 respectively. The leading edge of the sphere cloud suggests that the momentum exchange between the hot spheres and the water are overestimated. In the hot sphere experiment, spheres are surrounded by vapor film. The drag force with this configuration is not considered in the current SIMMER-III model. Comparing with the cold sphere experiment, the overestimation of the drag force suggests that the model for the drag coefficient considering the influence of the vapor film should be employed. The experimental data shows that the penetration rate is larger in the hot sphere case than that in cold sphere case, but the current calculation results show the reversed tendency. This also shows the current drag model overestimate the drag force of the spheres with vapor film in the hot sphere experiment. The contour graphs of sphere cloud and water are shown in Figs. 2-20 and 2-21, plotted at time 0.53, 0.586, 0.642, 0.754 and 0.81s. The mixing region evolution is larger in diameter than that in the experiment, shown in Fig. 2-22, plotted as

the same time as the calculated results, which induce the same conclusion.

The gas flow rates through the venting pipe given by the experiment and by SIMMER-III are plotted in Fig. 2-23, which show that the evolution of gas flow rate calculated by SIMMER-III is qualitatively consistent with that in the experiment, but the maximum value is about two times of that in the experiment and the total vapor generation in calculation is larger than that in the experiment. Although the vapor generation rate, which corresponds to the pressure transient given by SIMMER-III, is affected by several factors, for example, orifice plate pressure drop coefficient, difference of initial gas composition and initial gas space volume, the larger amount of vapor generation suggests that the heat transfer from spheres to water and its evaporation are overestimated during the falling of the hot sphere cloud in the water by SIMMER-III. Since the sphere radius is fixed, the factors influencing the heat/mass transfer process include the heat transfer coefficients from sphere to water/vapor in different flow regime, water/vapor interfacial area and evaporation of water. Through this simulation, the factors could not be distinguished and the more specific experiments are needed to make further investigation.

2.4.5 Investigation of the Influence of the Drag Coefficient on Mixing Region in Q-12 Test

The influence of the drag coefficient on the mixing region in the hot sphere experiment is investigated through the change of the multipliers CDD and CCD of the drag coefficient among dispersed components and between dispersed and continuous components. The cases with the multipliers (CDD and CCD) of 0.05, 0.25 and 1.0 for Q-12 are calculated. The evolution of the leading edge of the sphere cloud and water are shown in Figs. 2-24 and 2-25 respectively. Since the momentum exchange is overestimated by using the default value. The lower the multiplier, the more the evolution of the leading edge approaches to the experimental data. The multiplier of 0.05 is suggested by the calculated results. The contour graphs of the sphere cloud and water are plotted at the time of 0.698 second, as shown in Figs. 2-26 and 2-27 respectively. The

shapes of the sphere cloud and water region are much affected by the drag coefficient. In the cases with the reduction of drag coefficient of 20 times, the shapes of the sphere cloud approach to the image taken from the experiment.

The pressure transients in the vessel at the position of P6 are shown in Fig. 2-28 for the cases with different the drag coefficients through the change of the multipliers. The pressure is higher for the cases with lower multiplier of the drag coefficient, which corresponds to the vapor generation rate as shown in Fig. 2-29. Other cases with different combination of the CDD and CCD are calculated, as shown in Fig. 2-30. These results suggest that both the momentum exchange between sphere and coolant liquid and the momentum exchange between the sphere and liquid particle are overestimated.

2.5 Conclusions

The momentum exchange between the fuel and coolant liquid in FCI is estimated through the simulation of the QUEOS experiments Q-08 and Q-12 (the experiment of a premixing phase of FCIs). The base cases are carried out by using the standard options of the models and the parameters in SIMMER-III code. Then the difference of the advancement of the sphere cloud between experiments and simulations induced by the drag coefficients is discussed through the change of the multipliers of drag coefficients. The calculated results suggest:

In the case of the cold sphere experiment QUEOS Q-08, SIMMER-III can predict the behavior of the advancement of the sphere cloud, pressure and vapor generation transient.

In the case of the hot sphere experiment QUEOS Q-12, the momentum exchange between the spheres and coolant liquid is overestimated by employing the current Ishii's drag correlations. The Influence of the vapor film surrounded on the sphere moving in the coolant liquid on the drag correlations should be considered.

2.6 Recommendations for Model Improvements

Based on the calculated results, the model improvement is recommended for

SIMMER-III. It is better to develop a drag coefficient model based on the configuration that the hot spheres with vapor film move in coolant liquid.

References

- (1) Kondo, Sa., *et al.*: Status and Achievement of Assessment Program for SIMMER-III, a Multiphase, Multicomponent Code for LMFR Safety Analysis, *Proc. of Eighth International Topical Meeting on Nuclear Reactor Thermal-Hydraulics*, Vol. 3, P. 1340, Kyoto, Japan, Sept. 30-Oct. 4 1997.
- (2) Morita, K., *et al.*: SIMMER-III Application to Fuel-Coolant Interactions, *Proc. of the OECD/CSNI Specialists Meeting on Fuel- Coolant Interactions*. P. 785, May 19-21, 1997, JAERI, Tokai-mura, Japan.
- (3) M.Ishii and N.Zuber, Drag Coefficient and Relative Velocity in Bubbly, Droplet or Particulate Flows, *AIChE Journal* Vol. 25, No. 5 September 1979.
- (4) L.Meyer, QUEOS, an Experimental Investigation of the Premixing Phase with Hot Spheres, *Proceedings of Eighth International Topical Meeting on Nuclear Reactor Thermal-Hydraulics*, Vol. 3, Kyoto, Japan, Sept. 30-Oct. 4 1997
- (5) L.Meyer, G.Schumacher, QUEOS, a Simulation-Experiment of the Premixing Phase of a Steam Explosion with Hot Spheres in Water Base Case Experiments, *FZKA Report 5612*, Forschungszentrum Karlsruhe, April 1996.
- (6) T.Theofanous, W.Yuen and S.Angelini, The Verification Basis of The PM-ALPHA Code, *Proceedings of the OECD/CSNI Specialists Meeting on Fuel-Coolant Interactions* May 19-21, 1997, Tokai-mura, Japan.
- (7) H.Jacobs, L.Vath, K.Thurnay, Constitutive Relations for Multiphase Flow Modeling, *Proceedings of the OECD/CSNI Specialists Meeting on Fuel- Coolant Interactions* May 19-21, 1997, Tokai-mura, Japan.

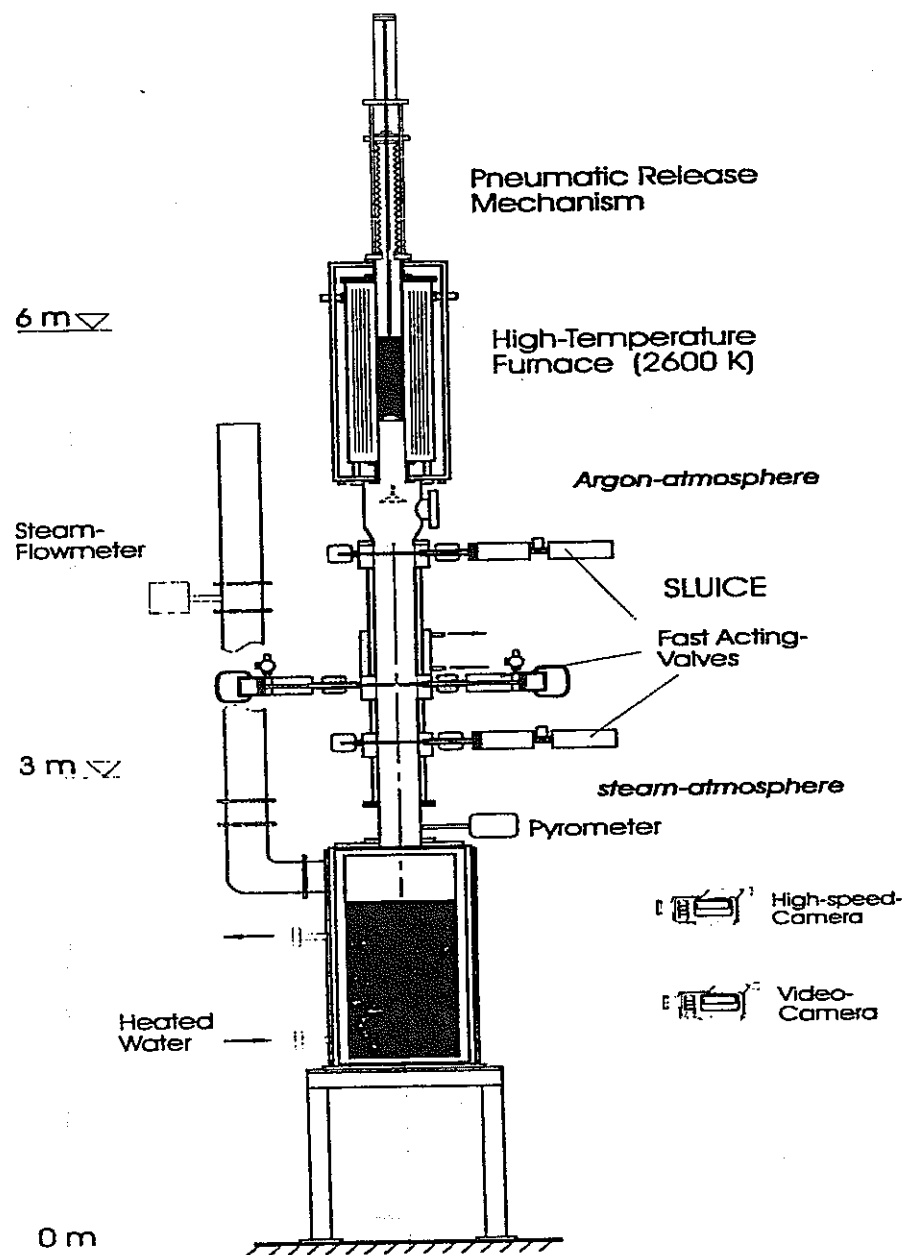


Fig. 2- 1 Scheme of the QUEOS facility

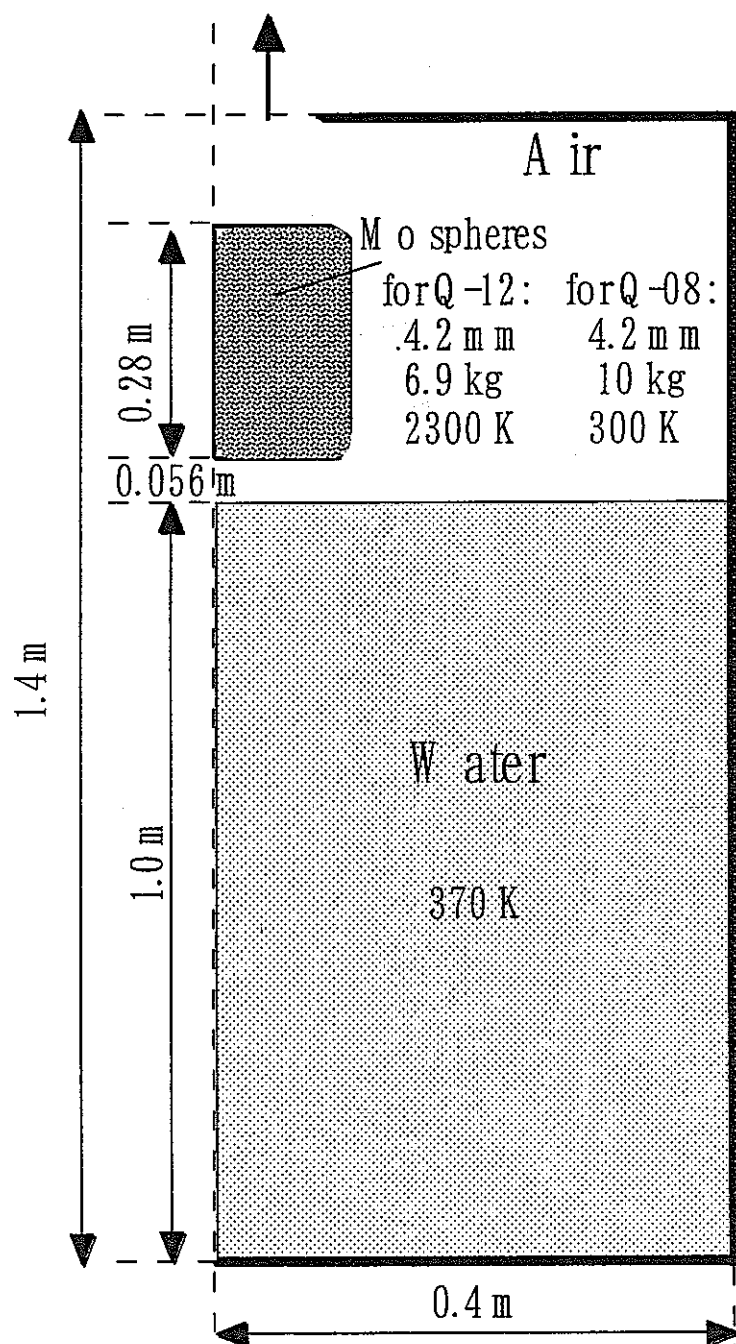


Fig. 2-2 Simulation Model of QUEOS test

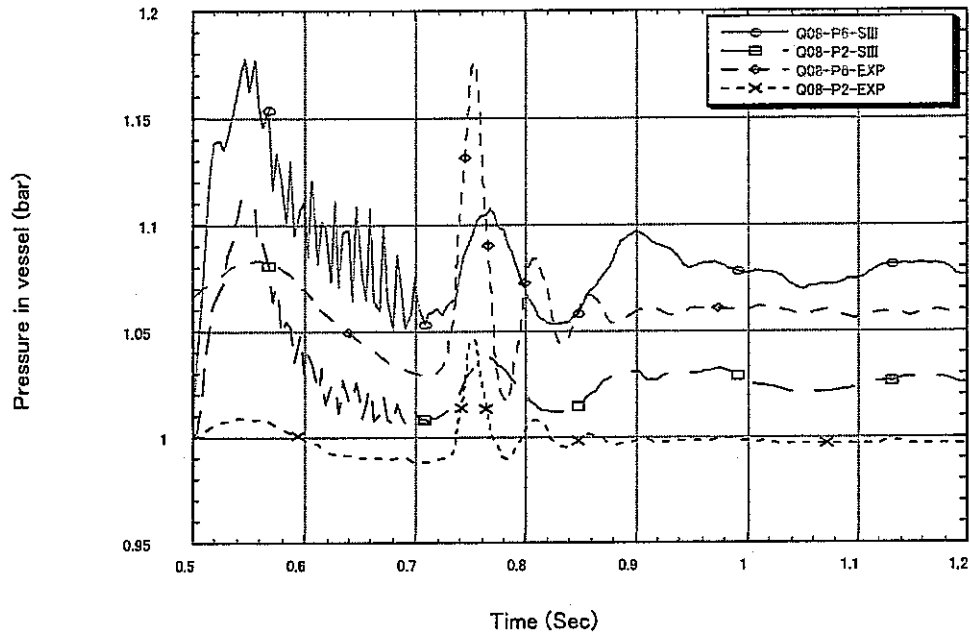


Fig. 2- 3 Pressure in the vessel at position of P2 and P6 in Q-08

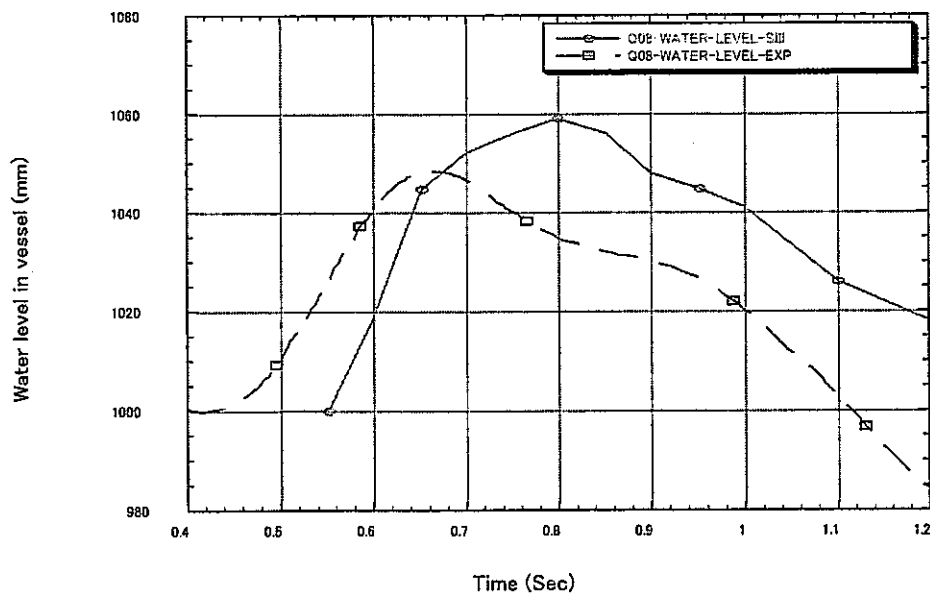


Fig. 2- 4 Water level transient in the vessel in Q-08

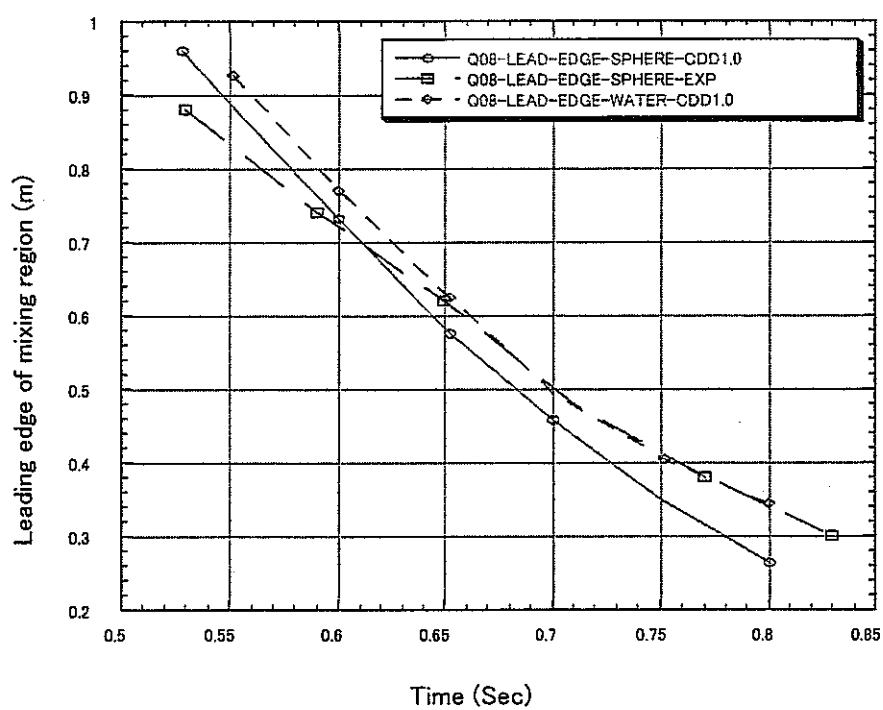
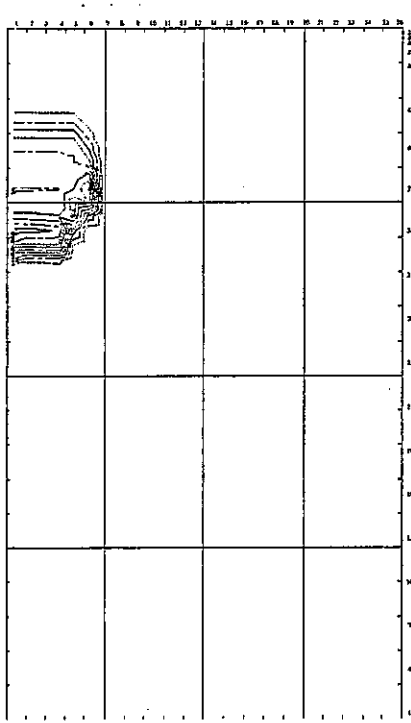
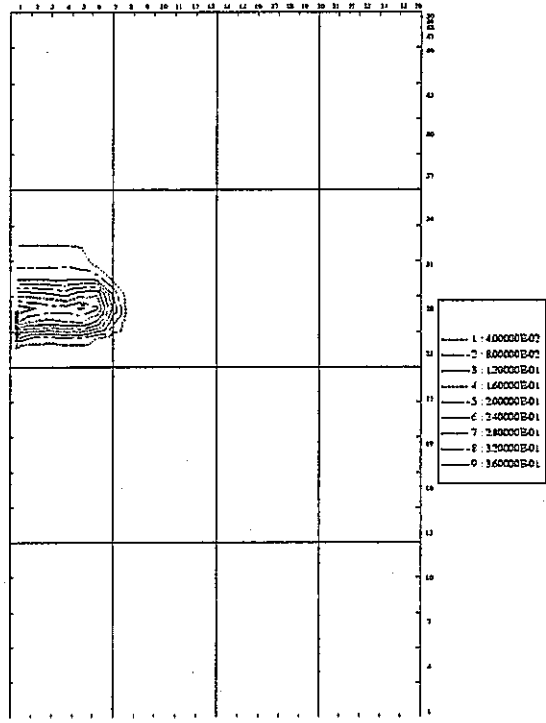


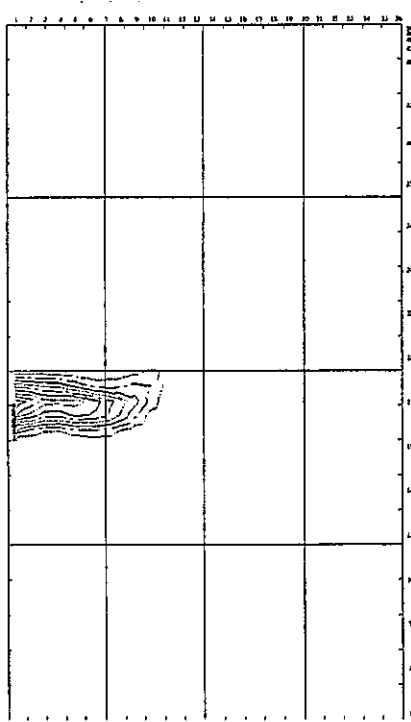
Fig. 2- 5 Evolution of the leading edges of the sphere cloud and water in Q-08.



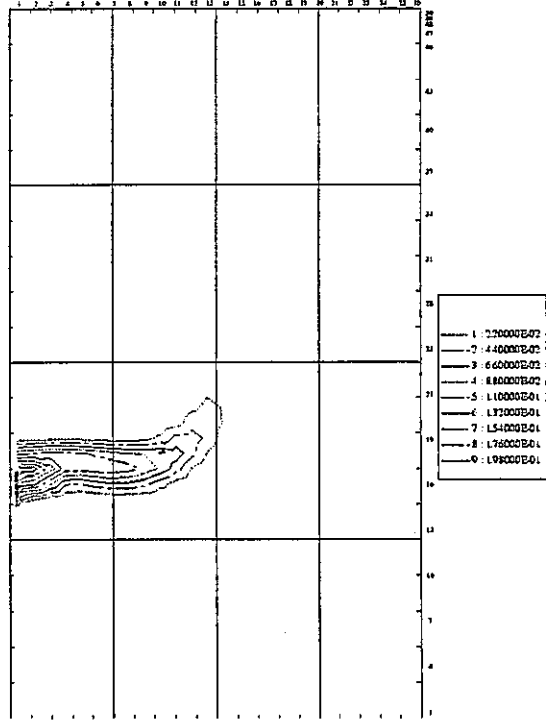
(a)



(b)



(c)



(d)

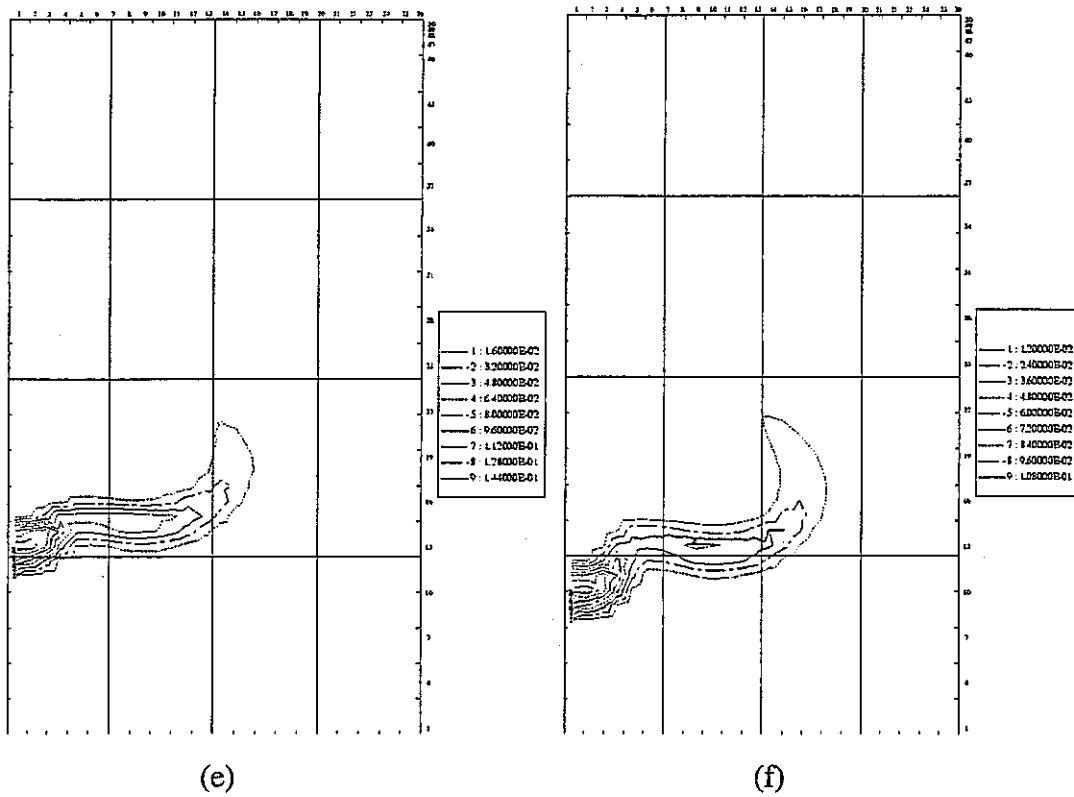
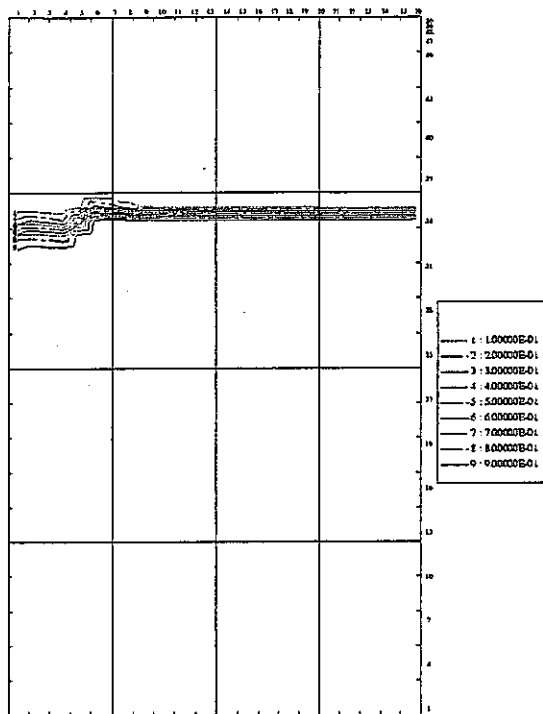
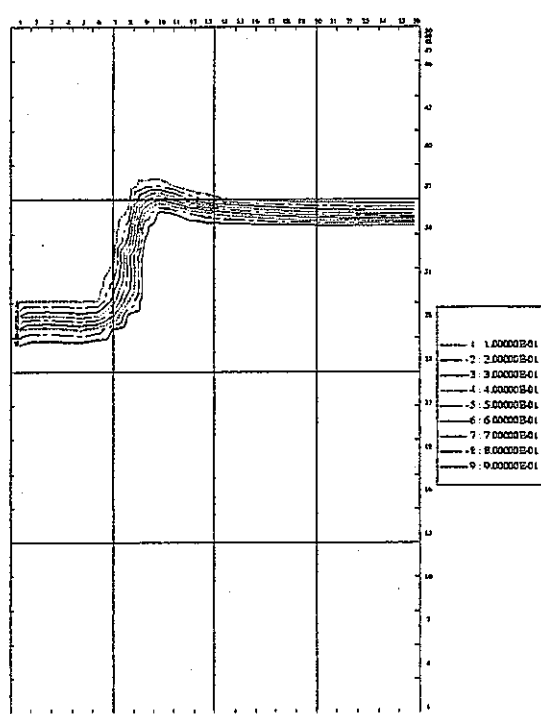


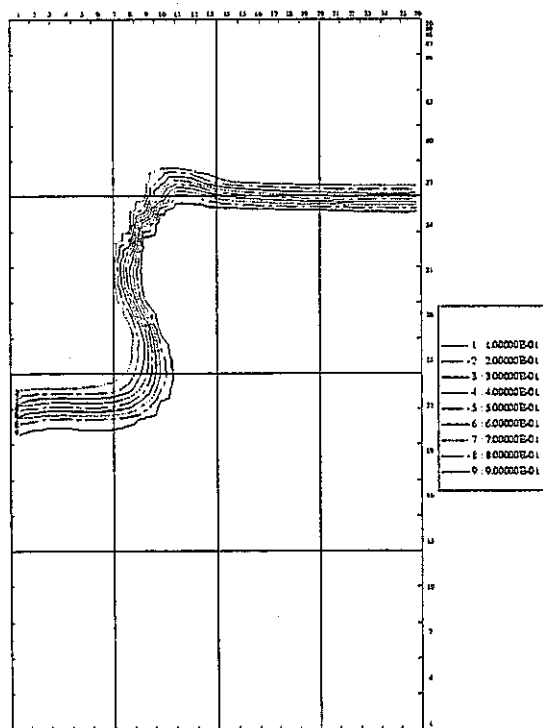
Fig. 2- 6 Contour graphs of the volume fraction of the sphere cloud in Q-08, plotted at time of 0.53, 0.59, 0.65, 0.71, 0.77 and 0.83 second from (a) through (f).



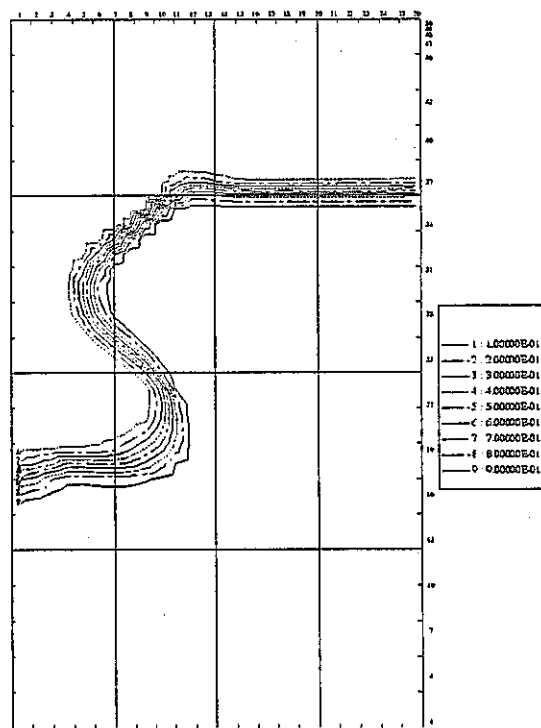
(a)



(b)



(c)



(d)

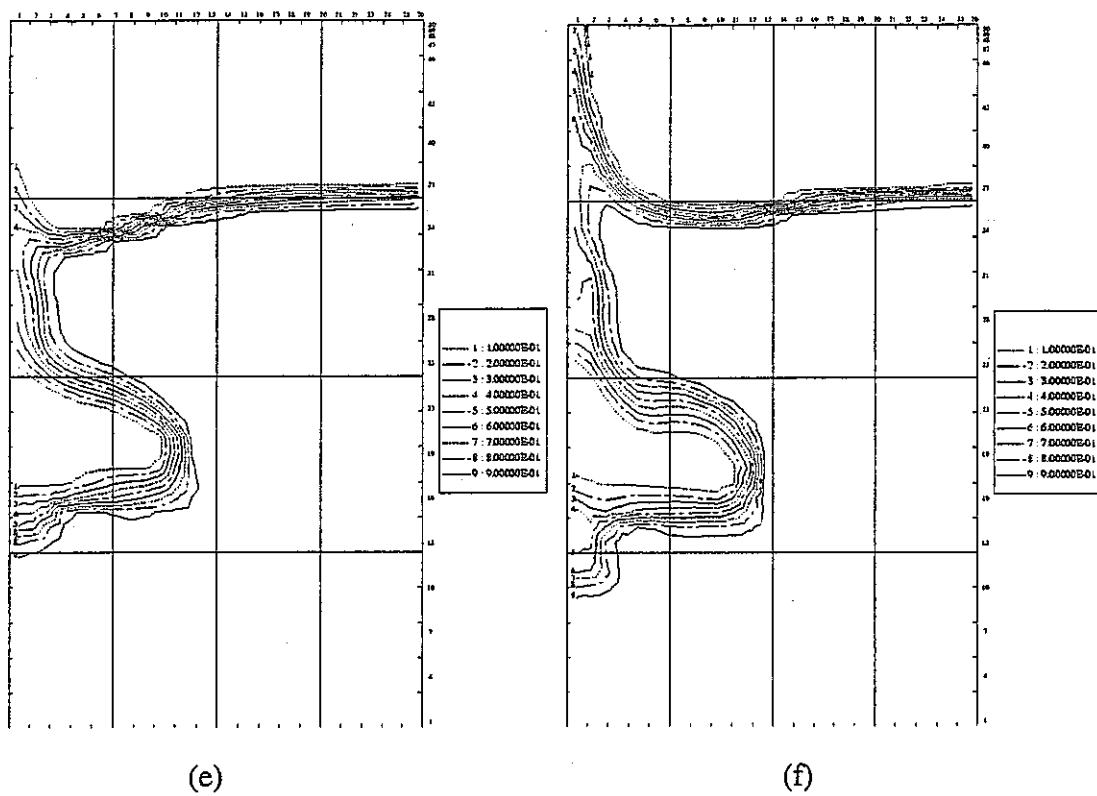


Fig. 2- 7 Contour graphs of the volume fraction of water in Q-08, plotted at time of 0.53, 0.59, 0.65, 0.71, 0.77 and 0.83 second from (a) through (f).

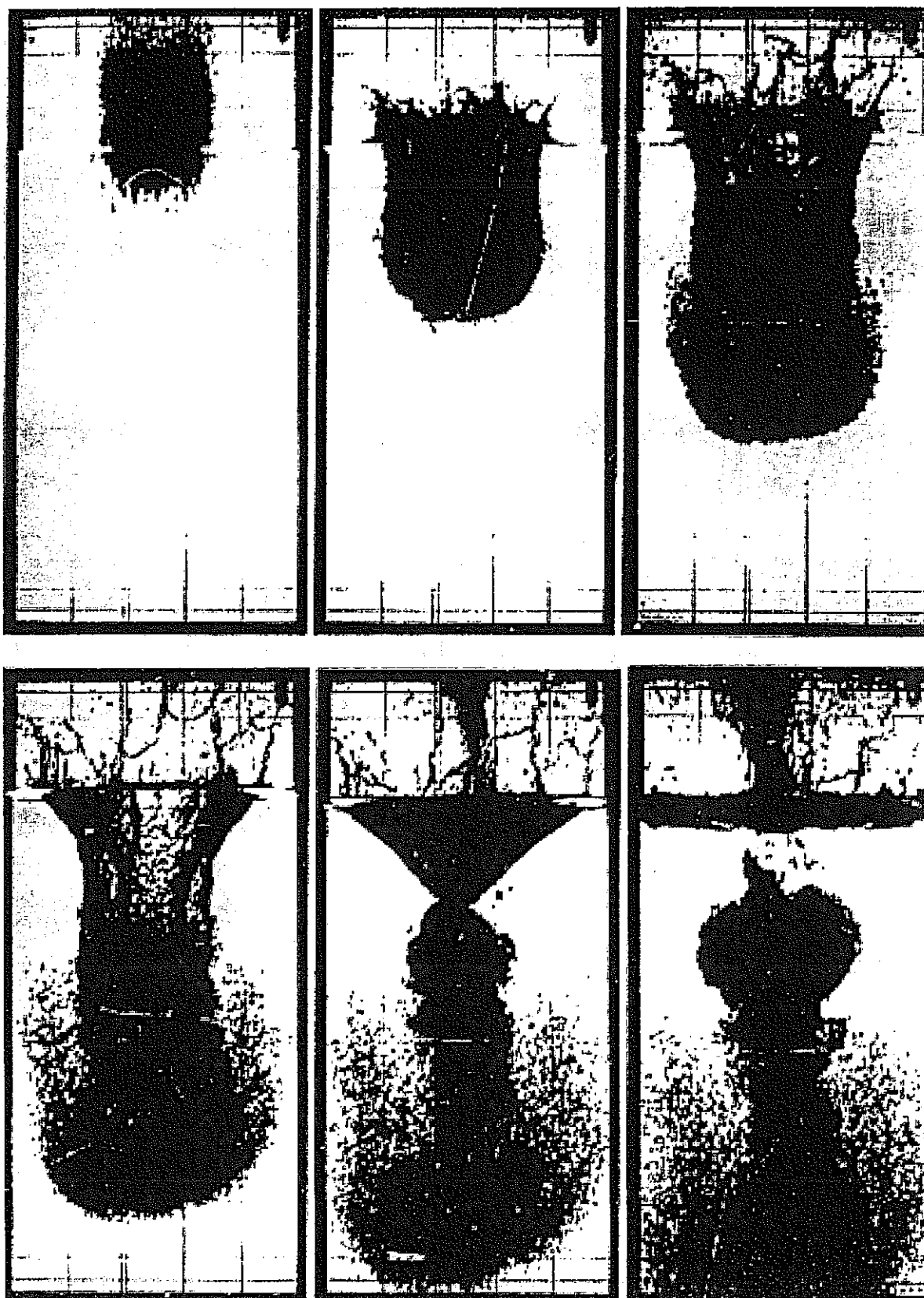


Fig. 2- 8 Images of molybdenum sphere cloud falling in water in Q-08 experiment

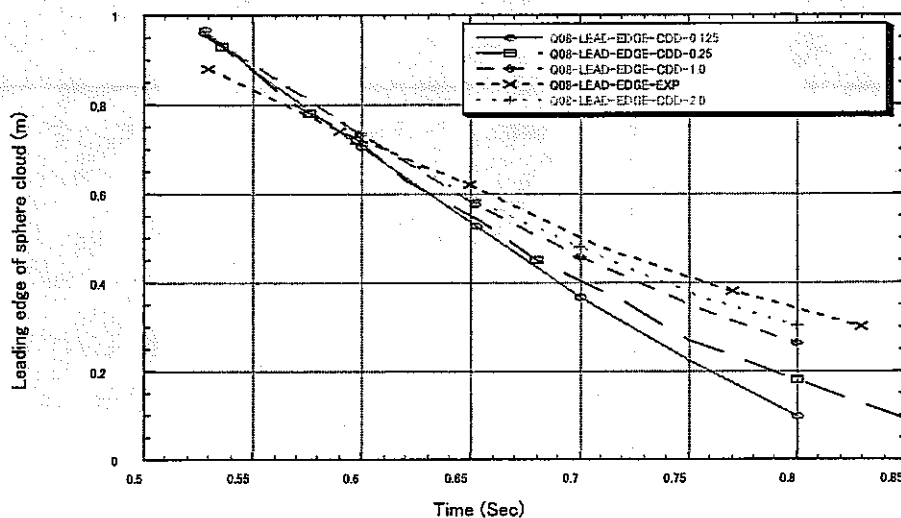


Fig. 2- 9 Evolution of the leading edge of the sphere cloud in cases with different drag coefficient multipliers CDD and CCD of 0.125, 0.25, 1.0 and 2.0 in Q-08.

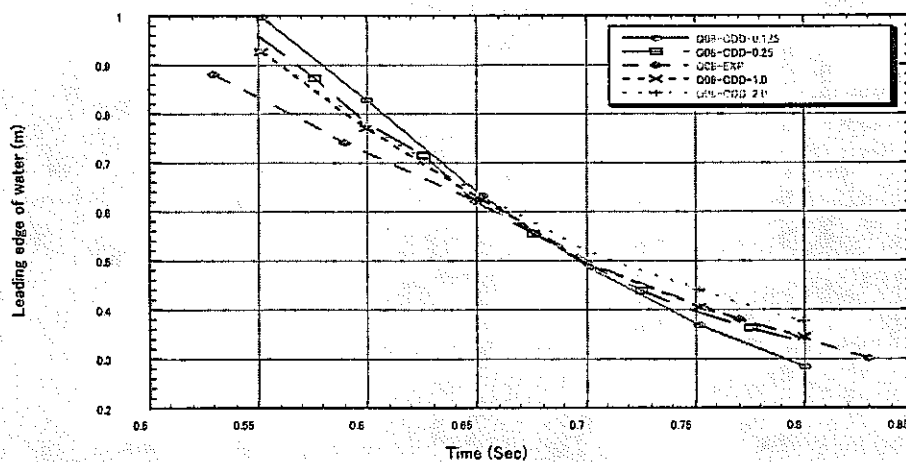


Fig. 2- 10 Evolution of the leading edge of water in cases with different drag coefficient multipliers CDD and CCD of 0.125, 0.25, 1.0 and 2.0 in Q-08.

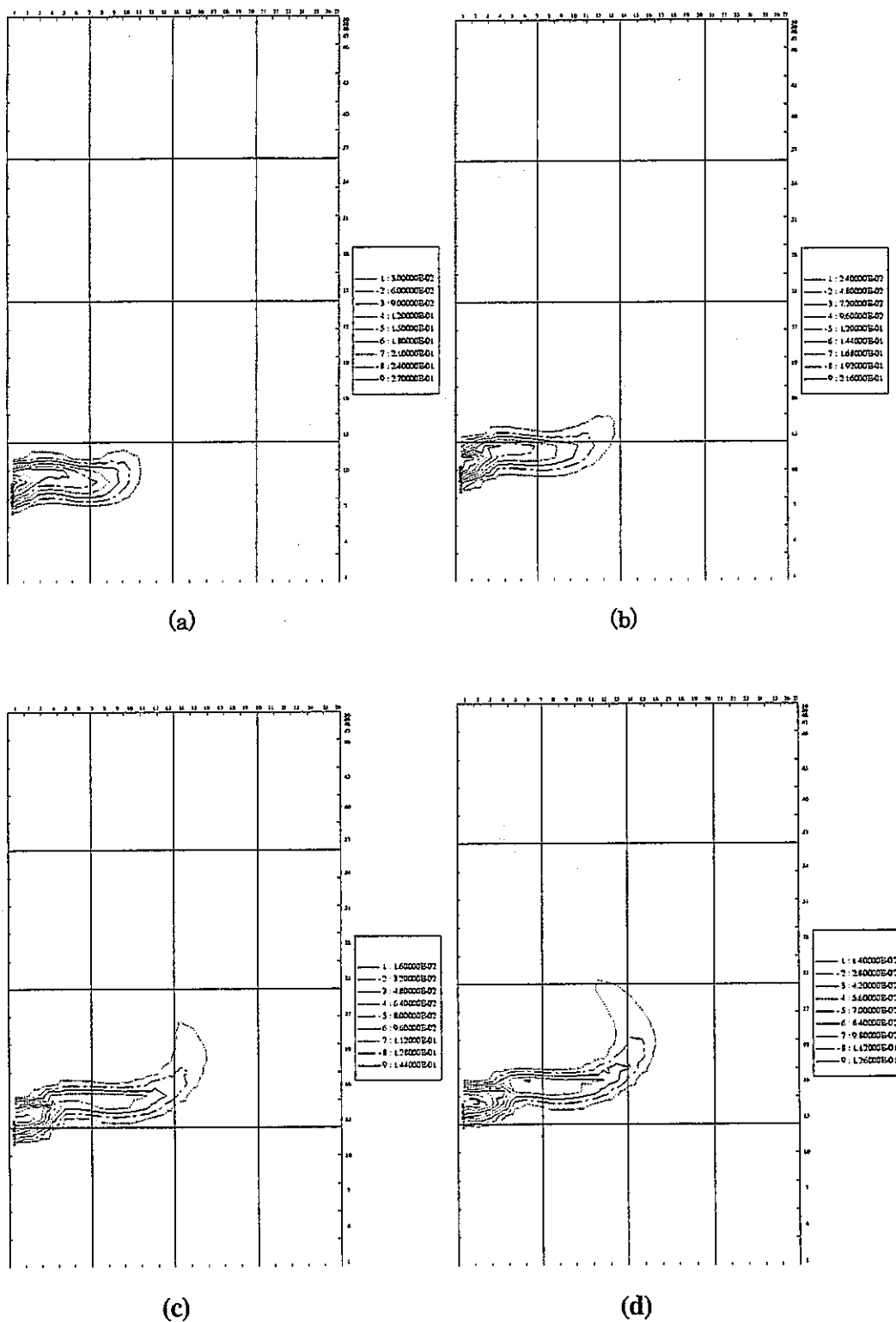


Fig. 2- 11 Contour graphs of the volume fraction of the sphere cloud in Q-08, plotted at time of 0.77 second for the cases with drag coefficient multiplier of 0.125, 0.25, 1.0 and 2.0 from (a) through (d).

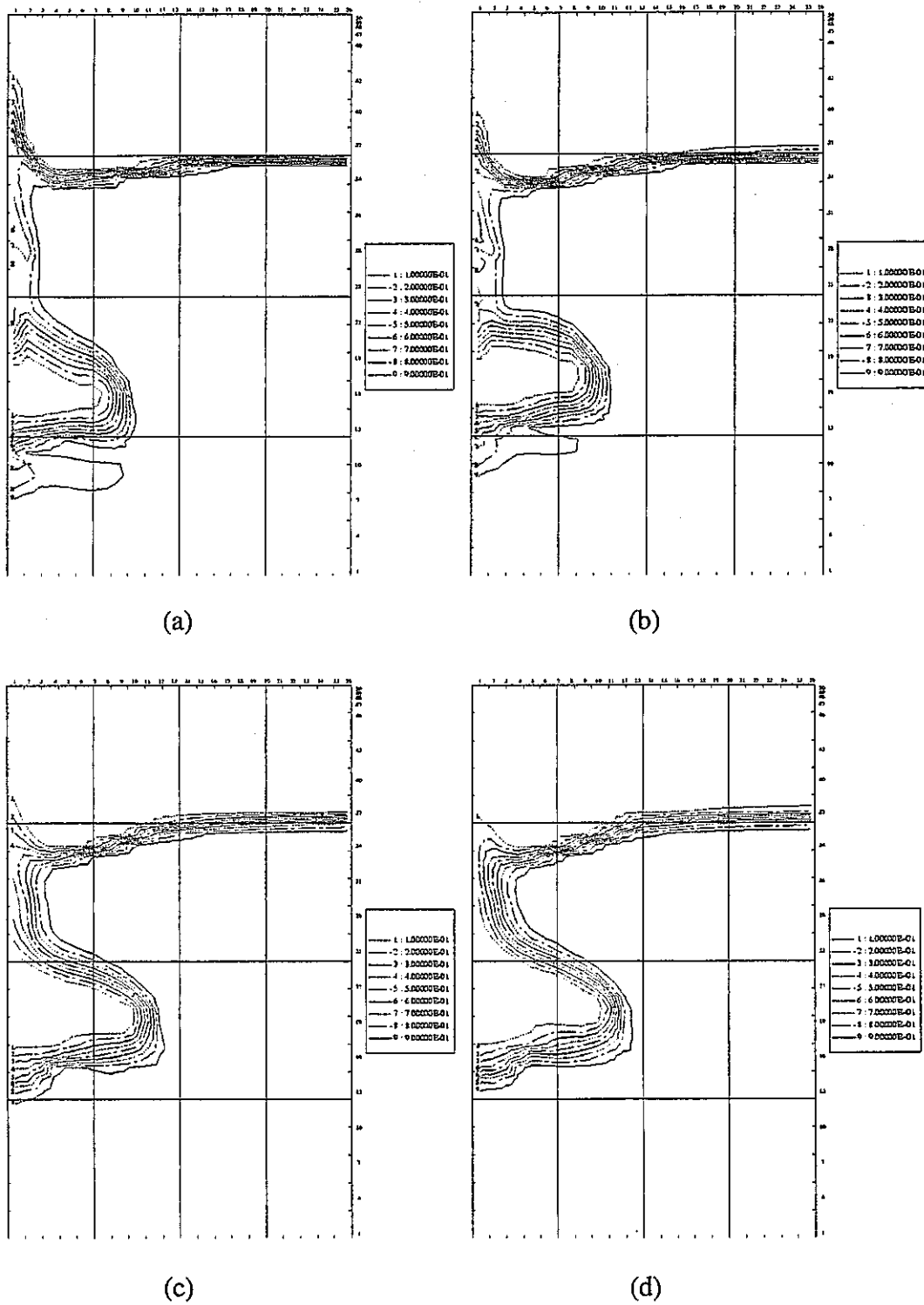


Fig. 2- 12 Contour graphs of the volume fraction of water in Q-08, plotted at time of 0.77 second for the cases with drag coefficient multiplier of 0.125, 0.25, 1.0 and 2.0 from (a) through (d).

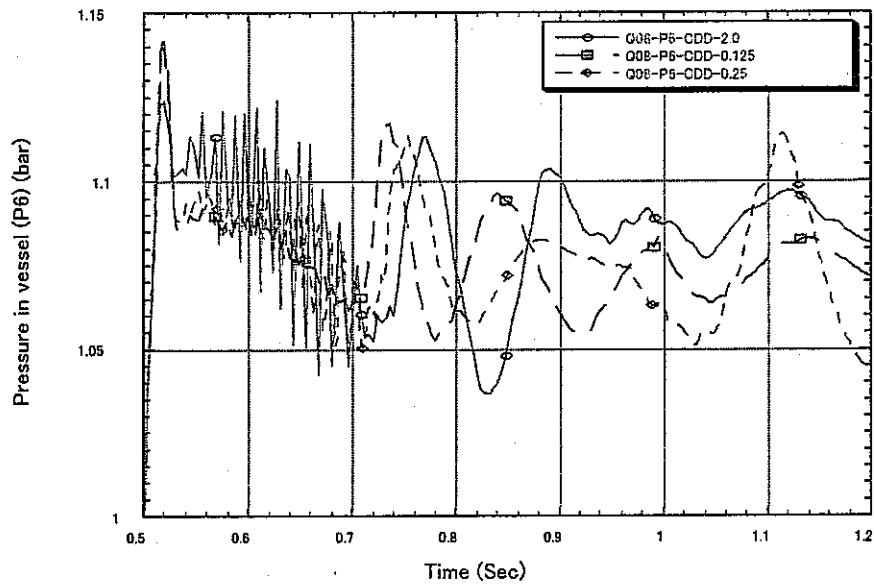


Fig. 2- 13 Pressure transients in the vessel at position of P6 in the cases of Q-08 with different multiplier of drag coefficient

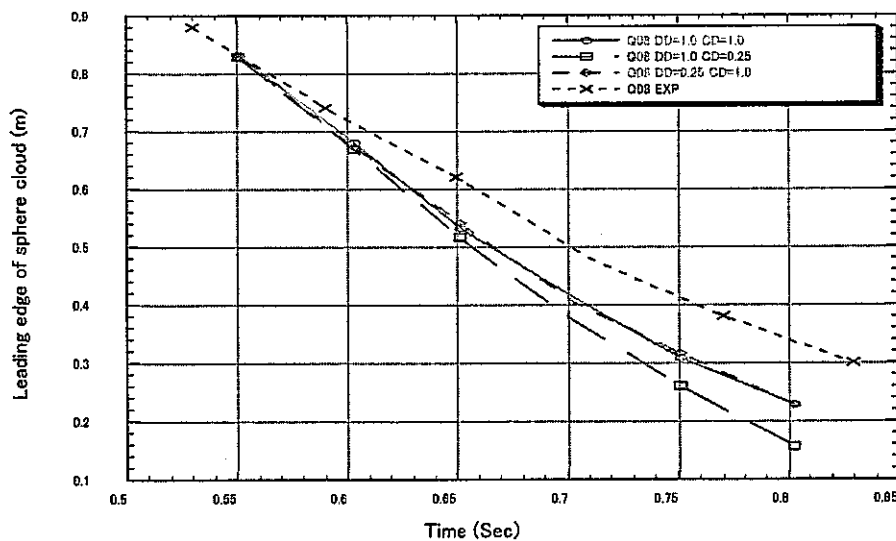


Fig. 2- 14 Evolution of the leading edge of the sphere cloud in cases with different drag coefficient multipliers CDD and CCD in Q-08.

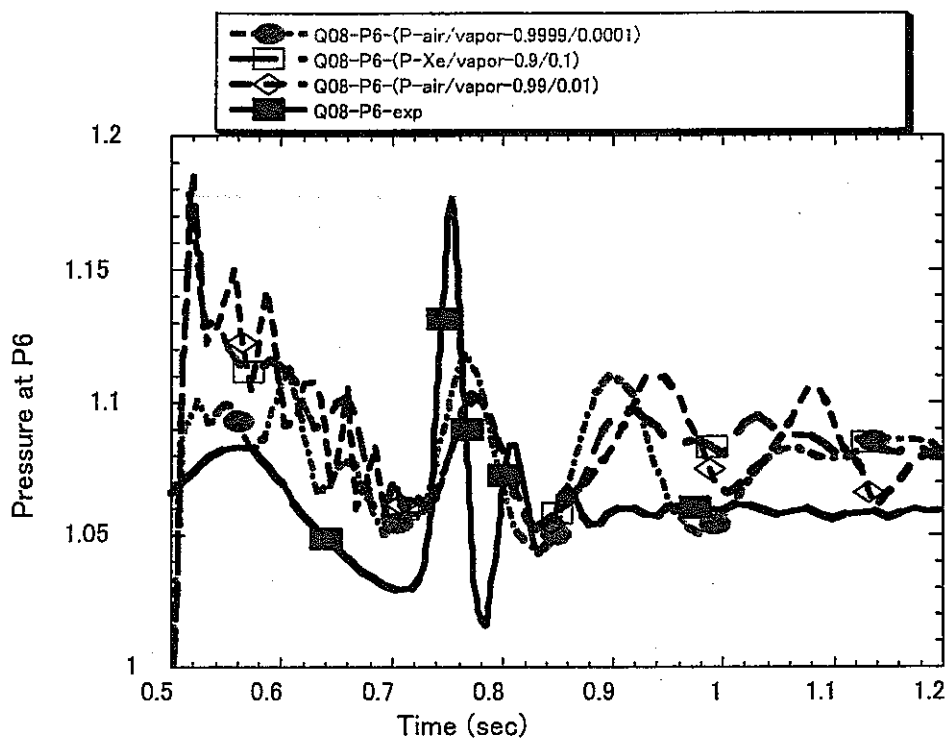


Fig. 2- 15 Pressure transients in vessel at position of P6 in the cases of Q-08 with different ratio of air to vapor in air space.

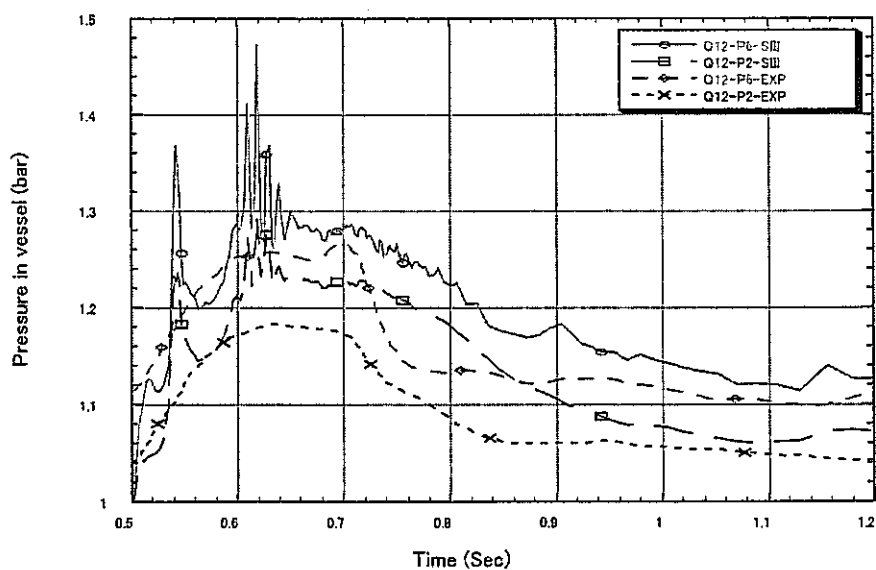


Fig. 2- 16 Pressure in the vessel at position of P2 and P6 in Q-12

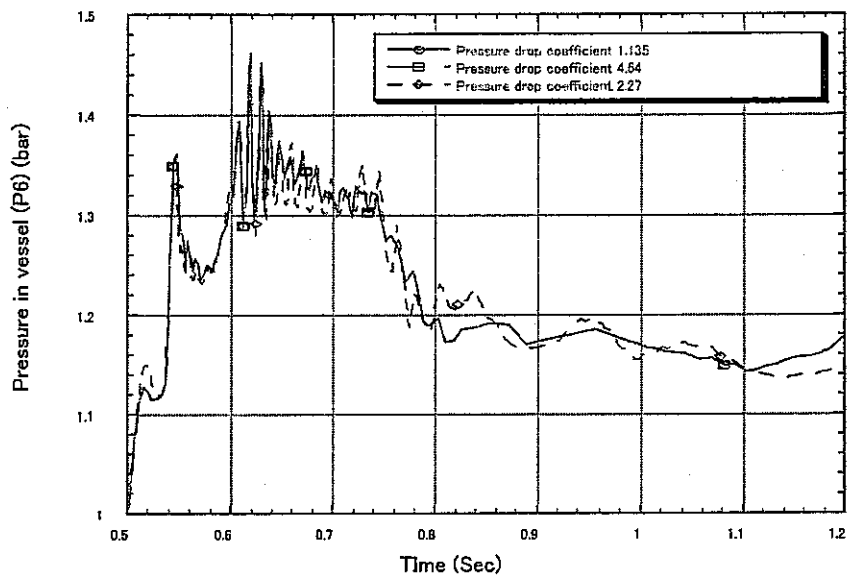


Fig. 2- 17 Influence of pressure drop coefficient on pressure in flow exit in Q-12.

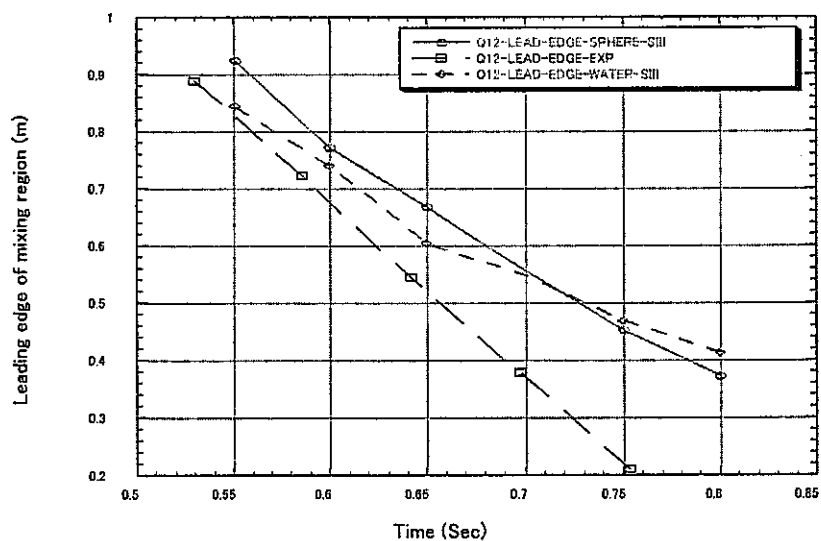


Fig. 2- 18 Evolution of the leading edge of the sphere cloud and water in Q-12, the half of the volume fraction contour line is defined as the boundary of the cloud.

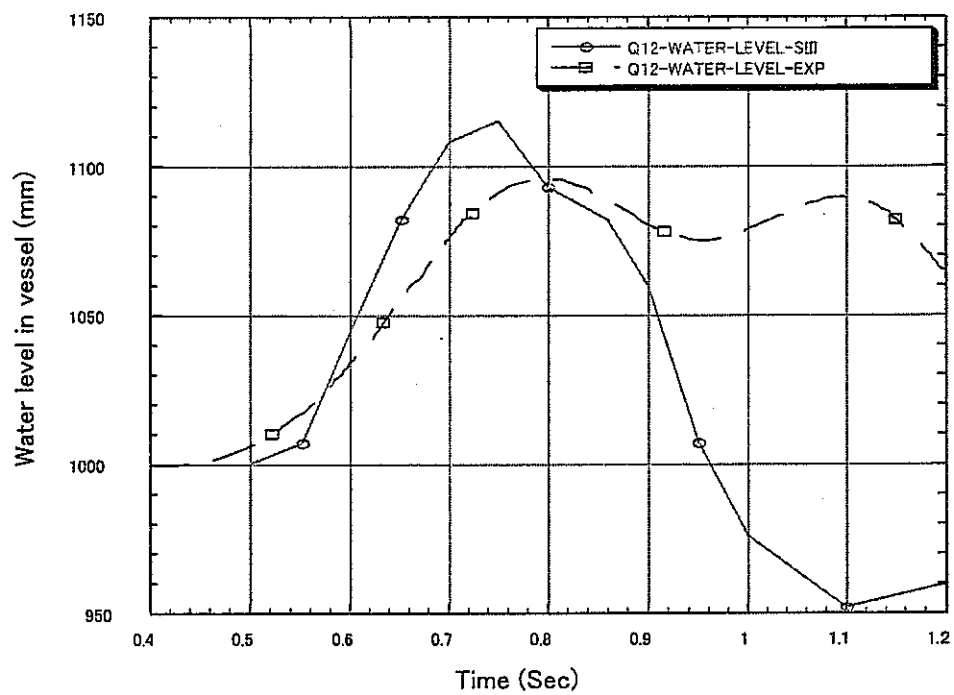
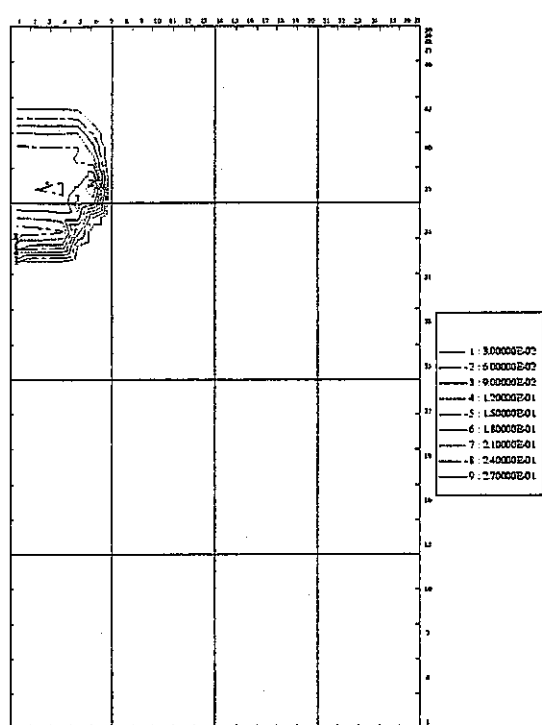
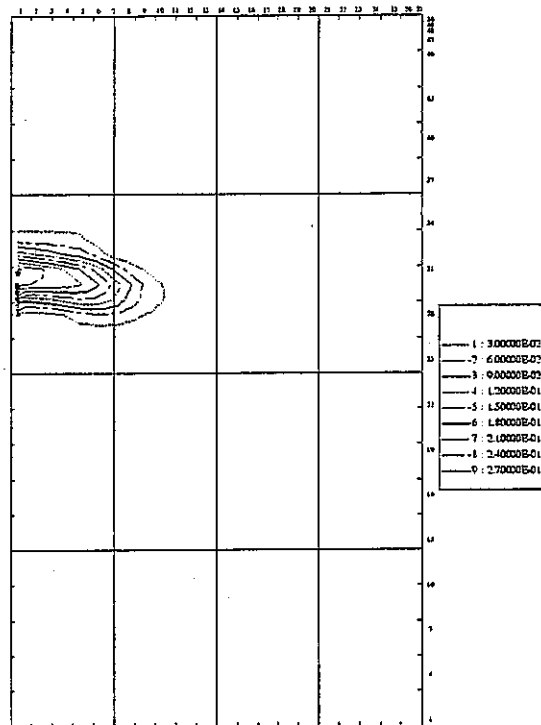


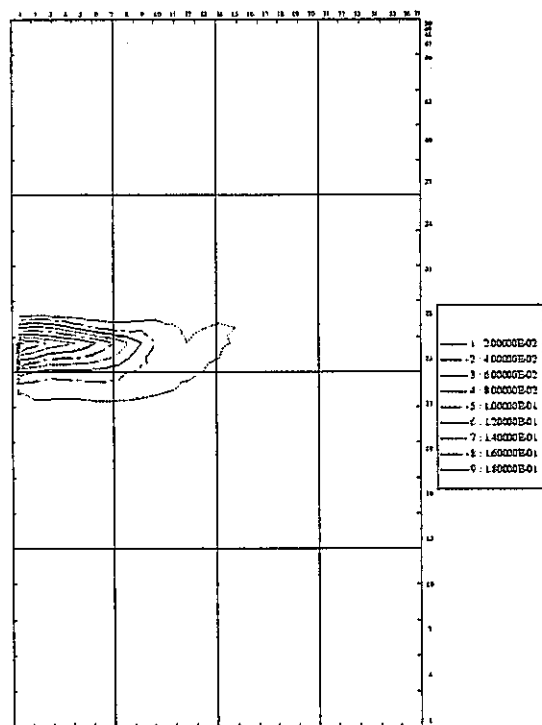
Fig. 2- 19 Water level transient in the vessel in Q-12



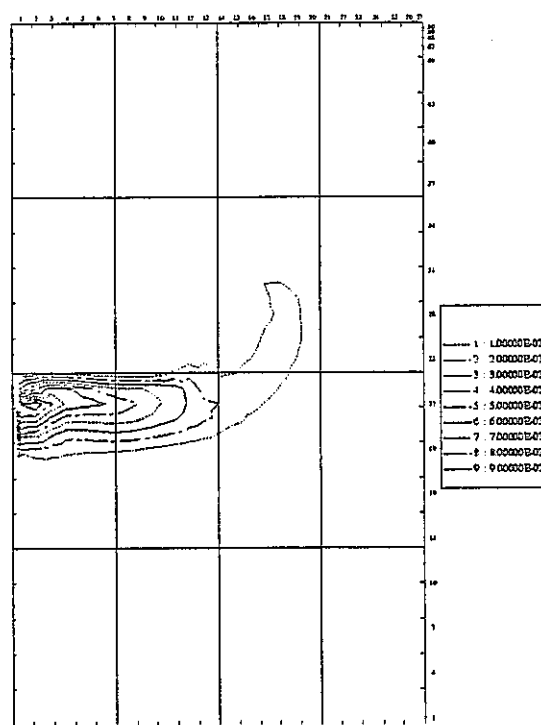
(a)



(b)



(c)



(d)

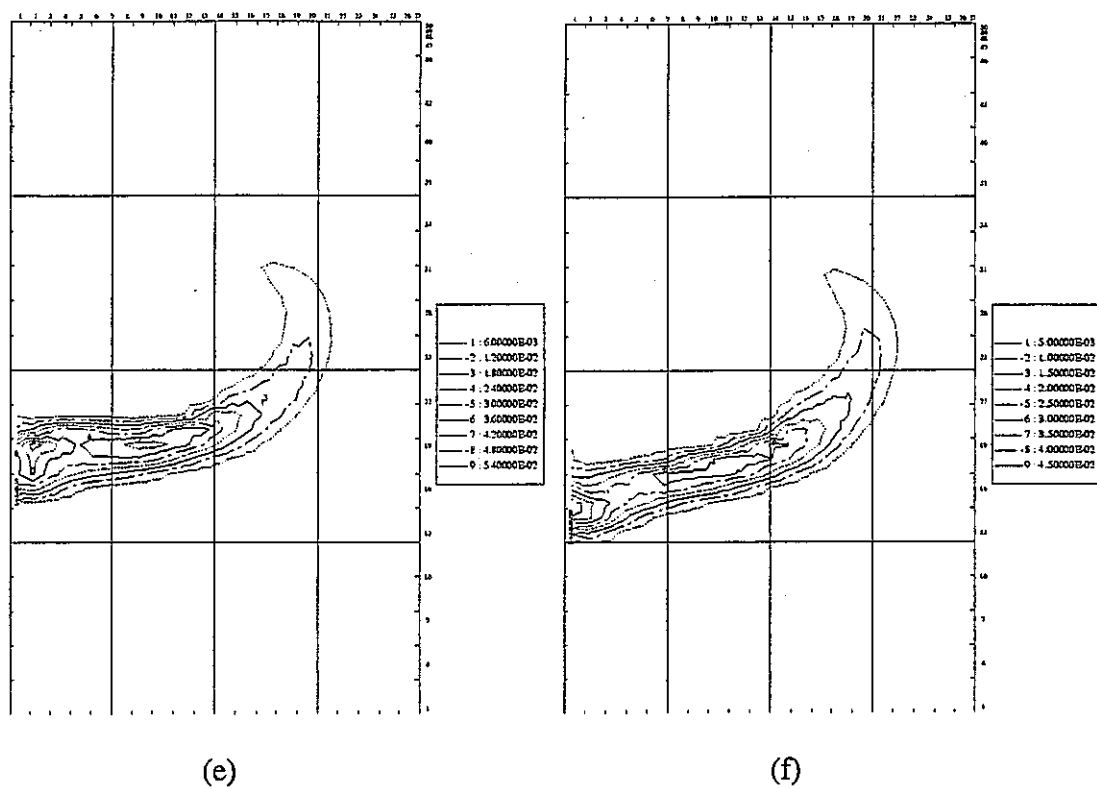
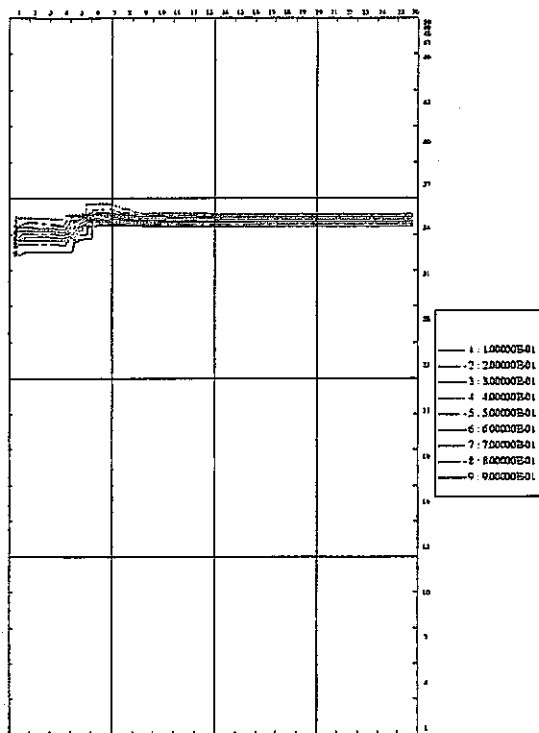
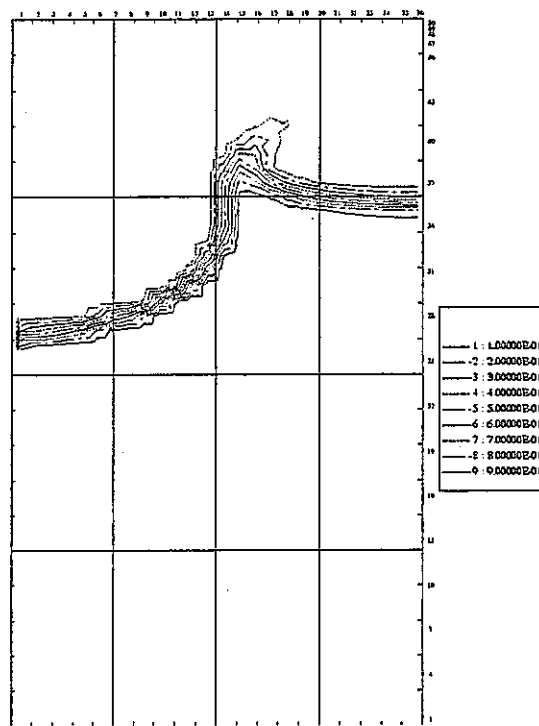


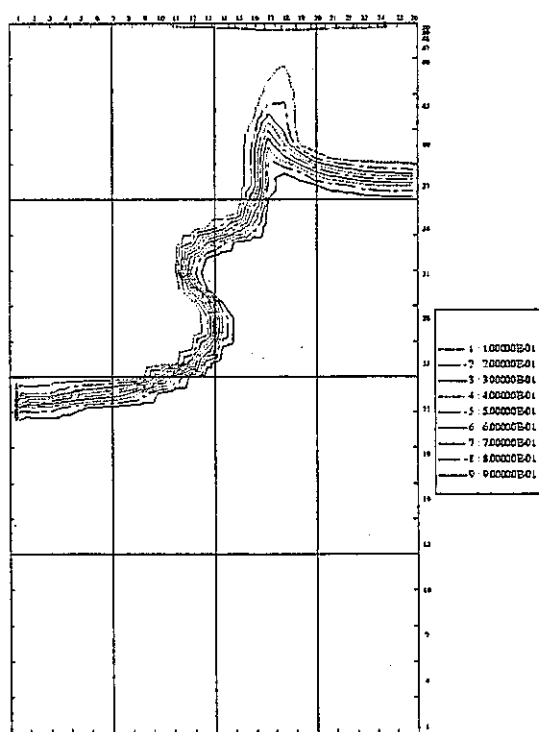
Fig. 2- 20 Contour graphs of the volume fraction of the sphere cloud in Q-12, plotted at time of 0.53, 0.586, 0.642, 0.698, 0.754 and 0.81 second from (a) through (f).



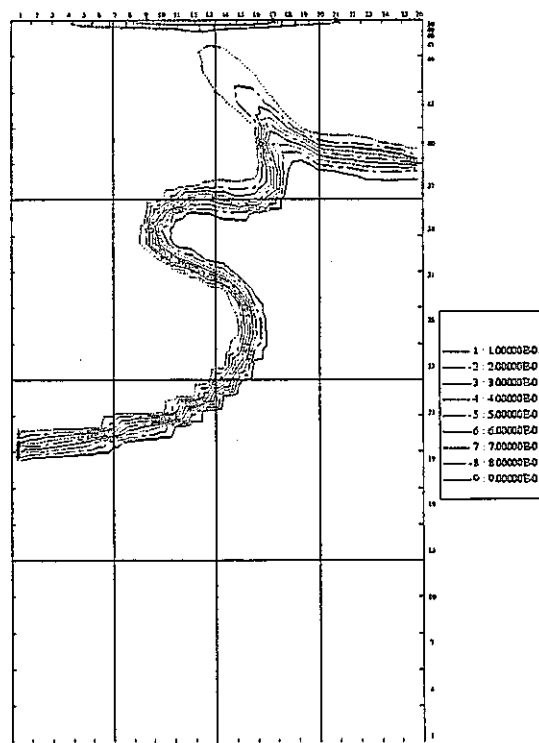
(a)



(b)



(c)



(d)

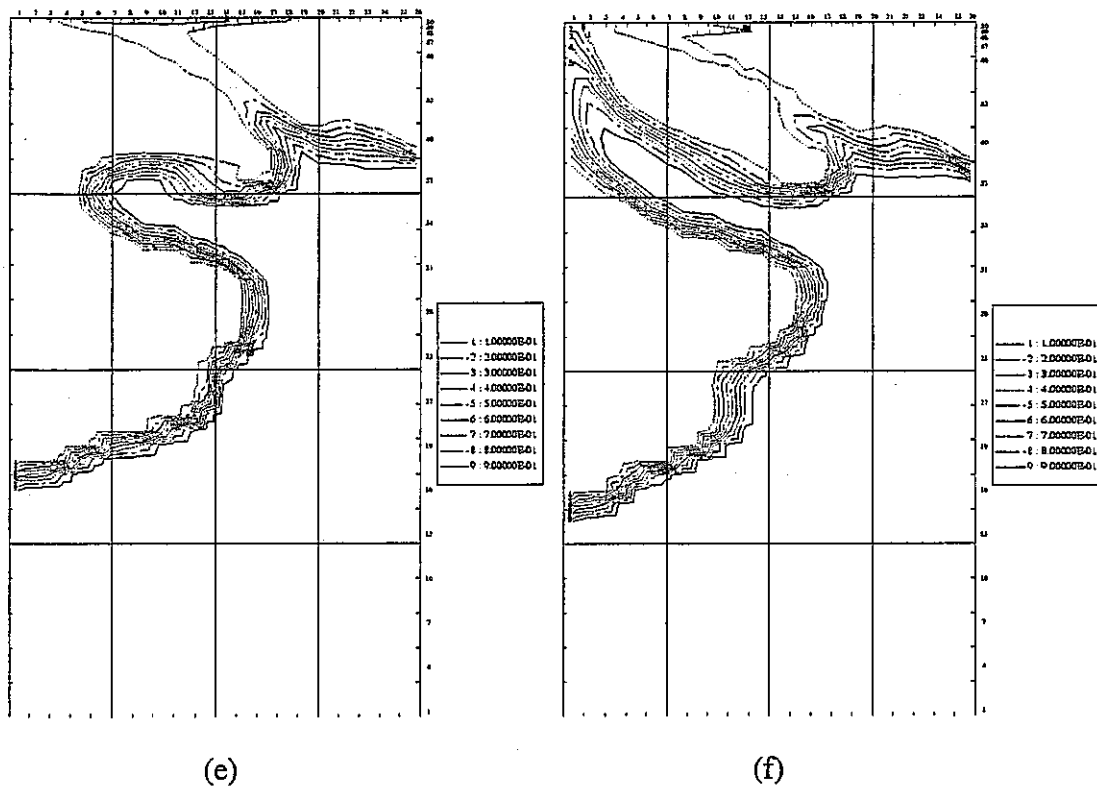


Fig. 2- 21 Contour graphs of the volume fraction of water in Q-12, plotted at time of 0.53, 0.586, 0.642, 0.698, 0.754 and 0.81 second from (a) through (f).

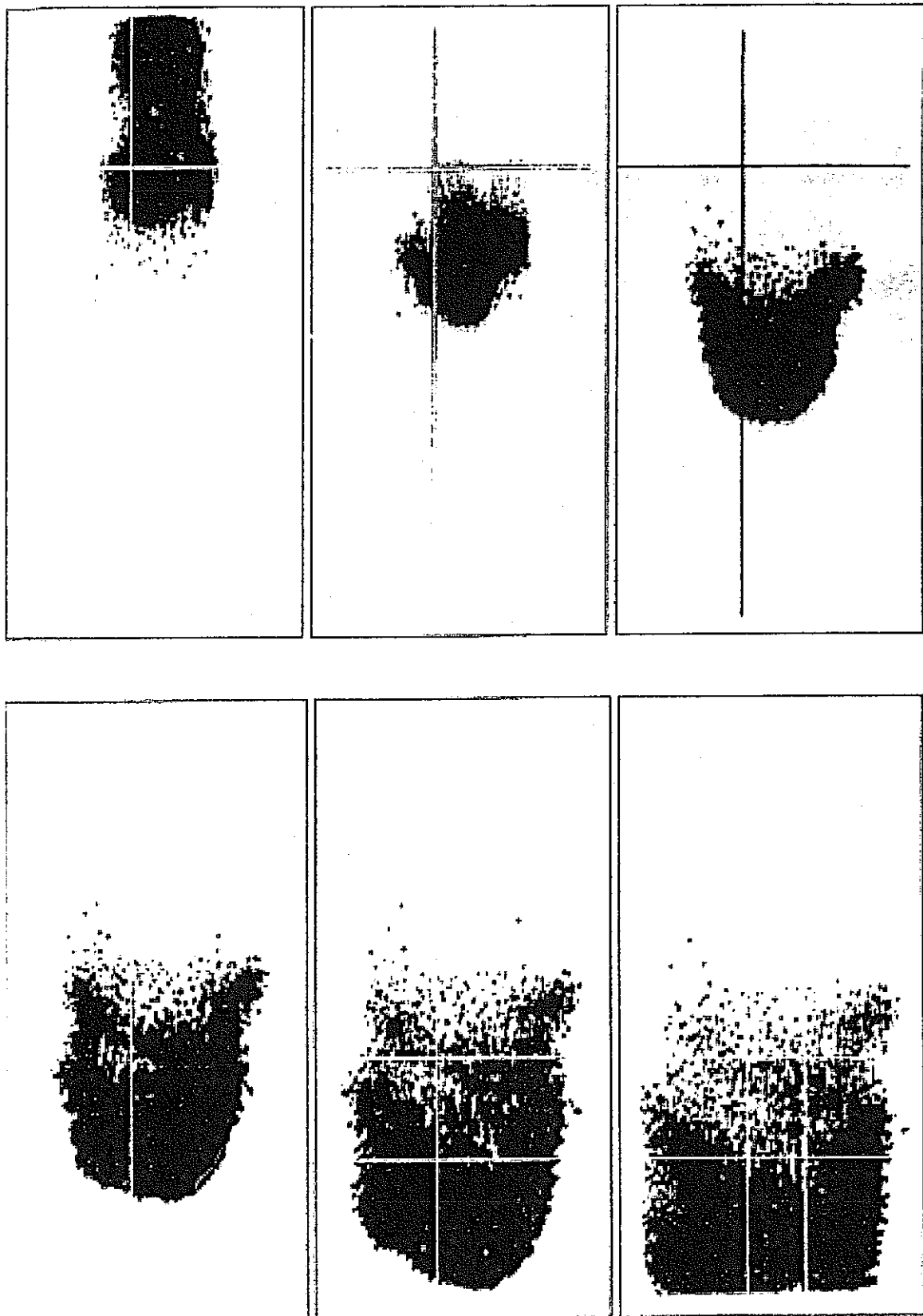


Fig. 2- 22 Images of molybdenum sphere cloud falling in water in Q-12

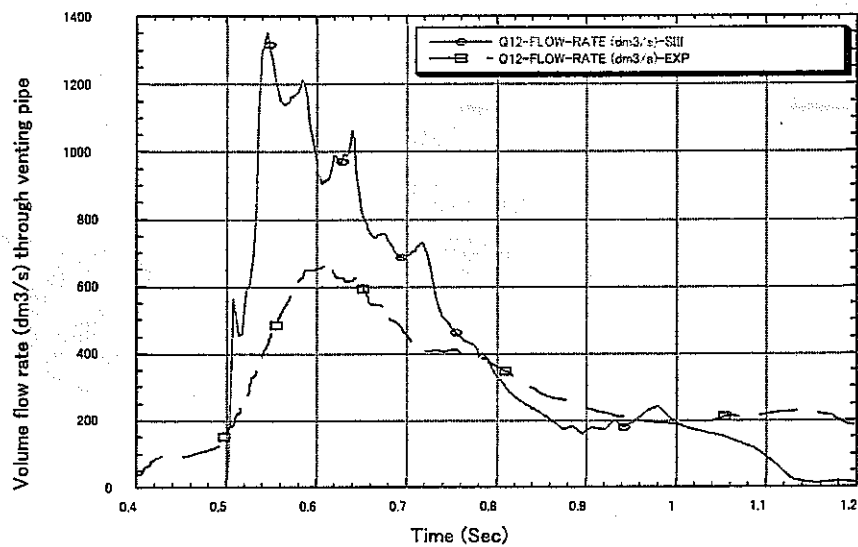


Fig. 2- 23 Volume flow rate through venting pipe in Q-12

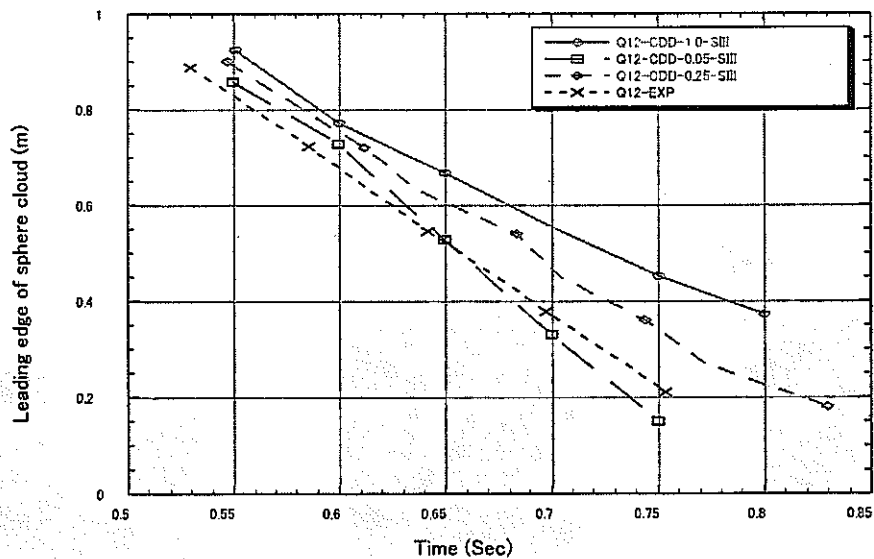


Fig. 2- 24 Evolution of the leading edge of the sphere cloud in cases with different drag coefficient multiplier CDD and CCD of 0.05, 0.25 and 1.0 in Q-12

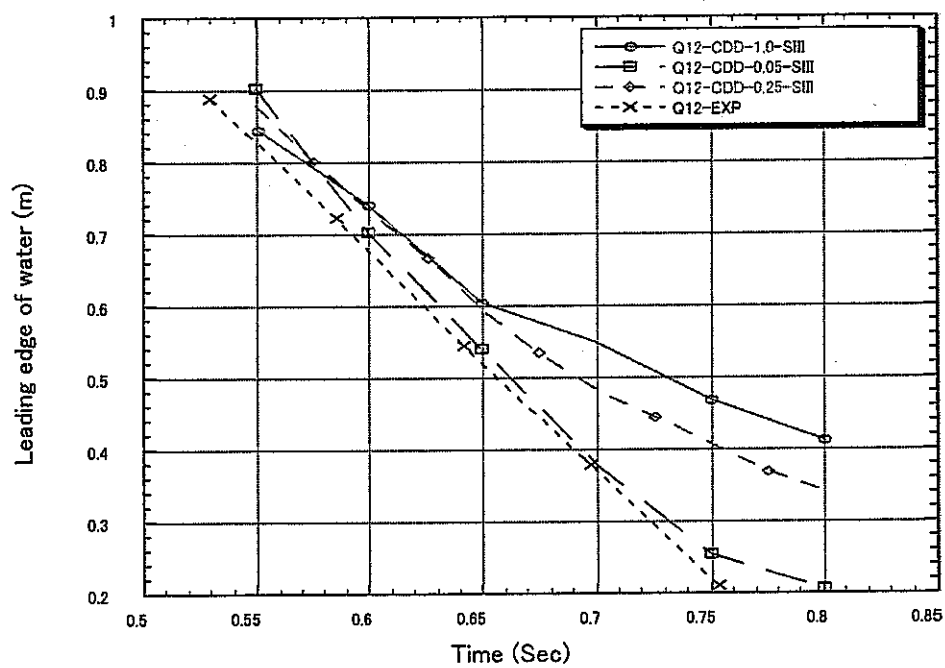


Fig. 2- 25 Evolution of the leading edge of water in cases with different drag coefficient multiplier CDD and CCD of 0.05, 0.25 and 1.0 in Q-12.

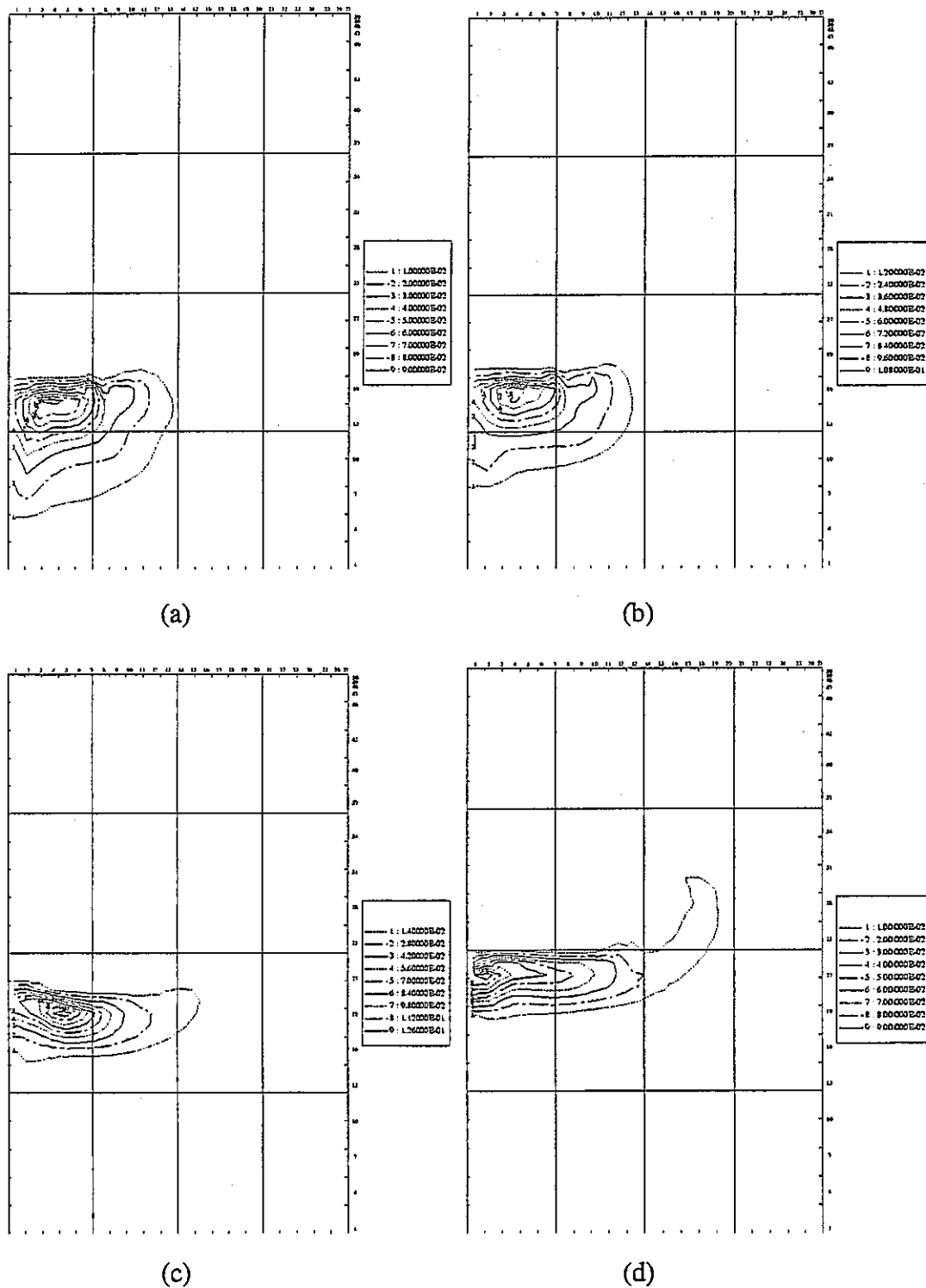


Fig. 2- 26 Contour graphs of the volume fraction of the sphere cloud in Q-12, plotted at time of 0.698 second for the cases with drag coefficient multiplier of 0.025, 0.05, 0.25 and 1.0 from (a) through (d).

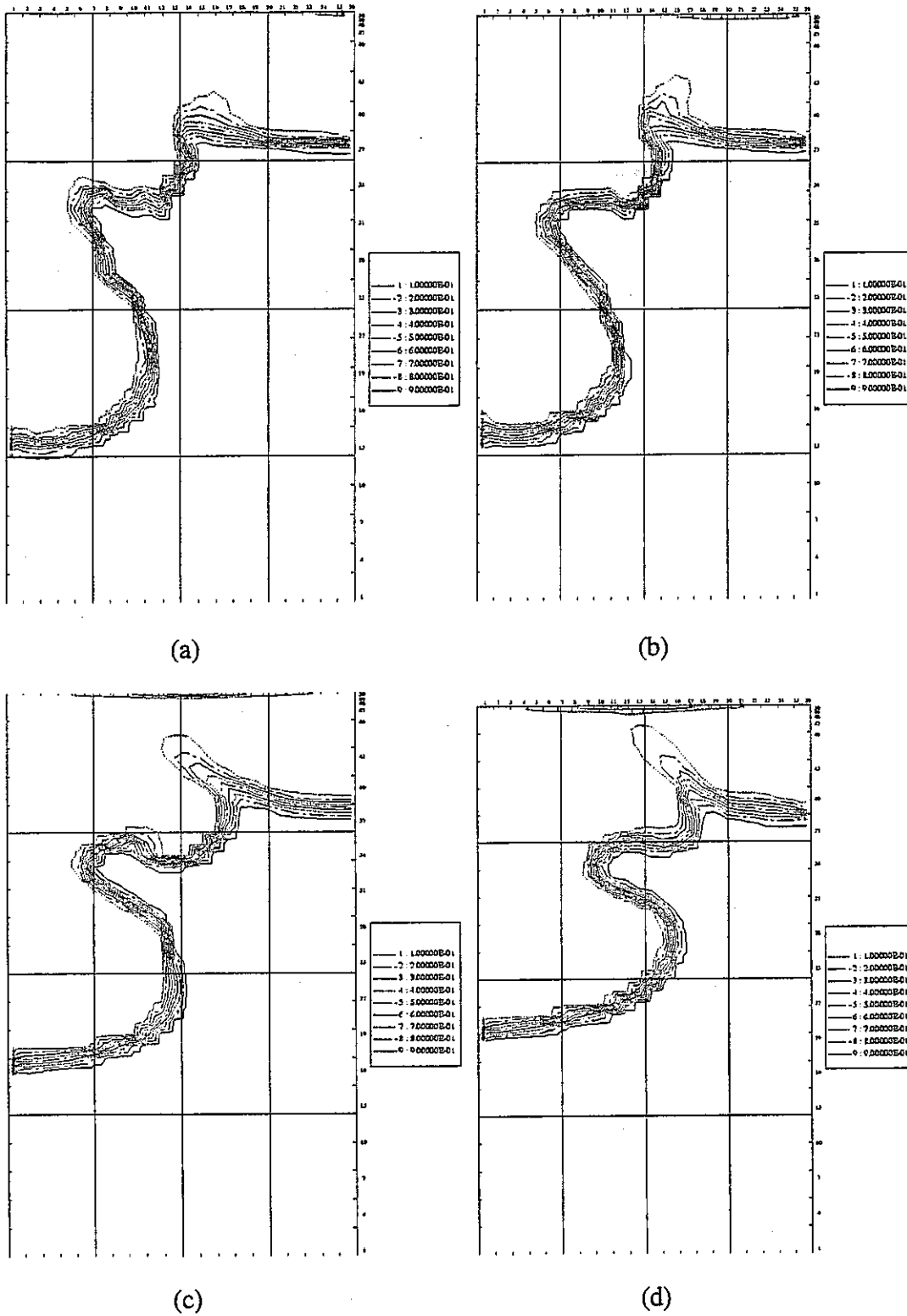


Fig. 2- 27 Contour graphs of the volume fraction of water in Q-12, plotted at time of 0.698 second for the cases with drag coefficient multiplier of 0.025, 0.05, 0.25 and 1.0 from (a) through (d).

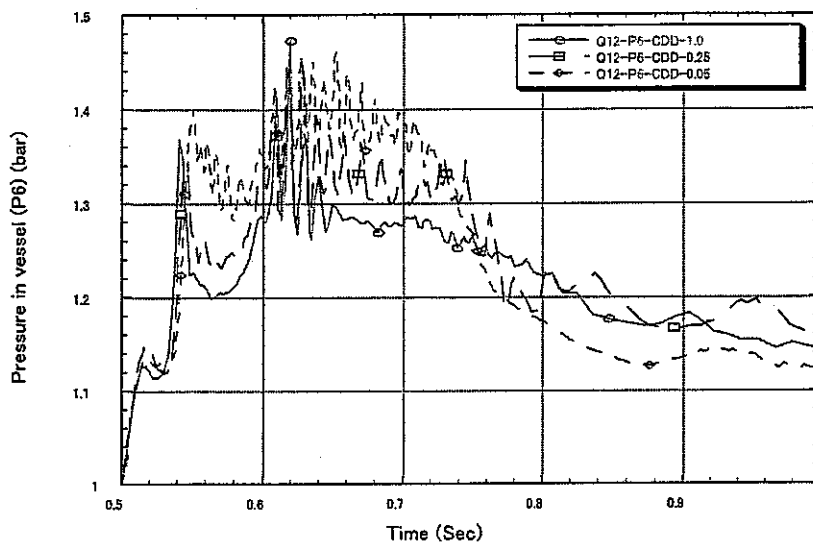


Fig. 2- 28 Pressure transient in the vessel at position of P6 in the cases of Q-12 with different multiplier of drag coefficient.

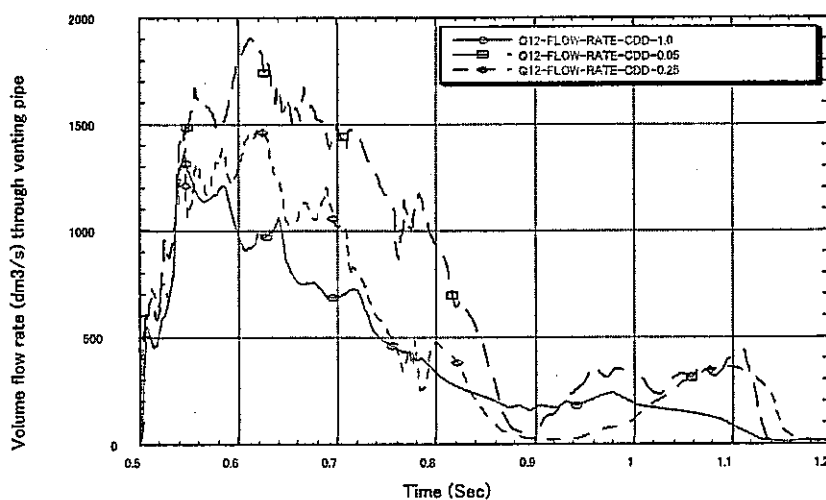


Fig. 2- 29 Gas flow rate through venting pipe in the cases of Q-12 with different multiplier of drag coefficient.

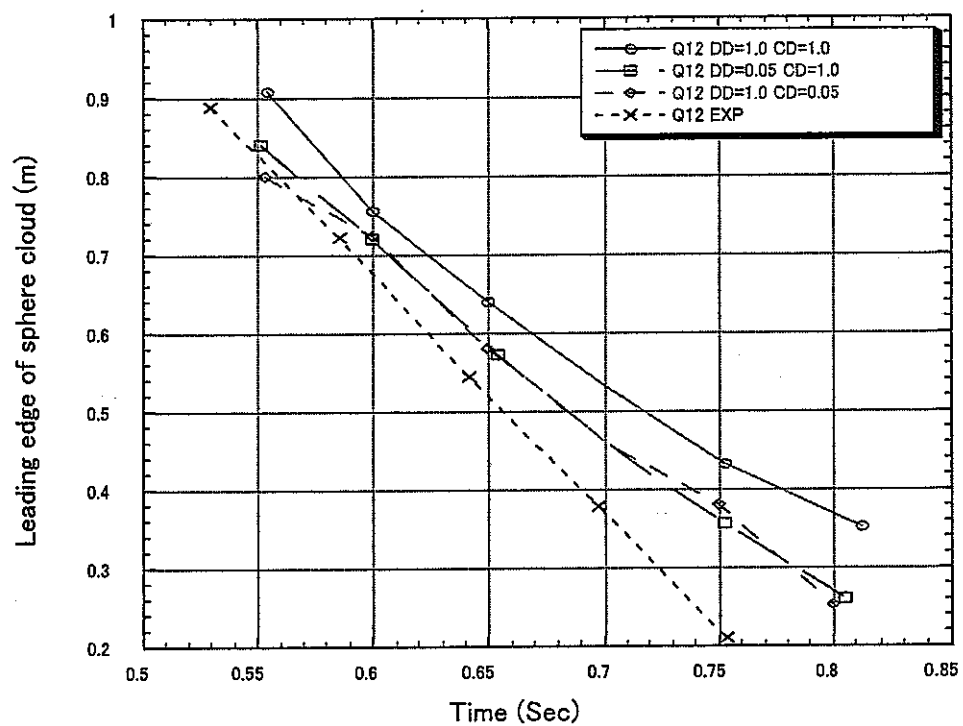


Fig. 2- 30 Evolution of the leading edge of the sphere cloud in cases with different combination of drag coefficient multipliers in Q-12.

3. Study on Drag Coefficient for the Particle/Droplet with Vapor Film

3.1 Introduction

Fuel Coolant Interactions (FCIs) are the important phenomena in nuclear reactor severe accident analysis and have been extensively studied in recent years. Several mathematical models of multi-phase multi-component flow, based on a multi-field description, have been developed with the aim of describing the events during the Core Disruptive Accidents (CDAs) in Liquid Metal Cooled Fast Breeder Reactors (LMFBRs) or Core Melt Accidents (CMAs) in Light Water Reactors (LWRs). The SIMMER-III code, developed at JNC [1,2], is a two-dimensional, three-velocity-field, multi-phase, multi-component, Eulerian, fluid-dynamics computer code coupled with a space-dependent neutron kinetics model. The QUEOS experiment, which studied the premixing phase of a FCI with hot particles released into water [3], was simulated [4,5] by the code to verify the momentum exchange between the fuel and the coolant, in which Ishii's correlations [6] are employed. The simulated results showed disagreement of the front advancement of the particle cloud in the water with the experimental results. The difference was further enhanced with increasing the particle temperature [5]. This means that the capability to predict the drag between the hot particles/droplets and the coolant liquid in multi-particle system should be improved for better analyzing FCIs.

First let us review the drag laws currently employed in the simulation tools. The configuration, based on which these drag laws for a single particle/droplet were developed, is that a fluid particle moves in other continuous fluid and these two fluids directly contact each other. The drag force exerted on the particle/droplet under steady-state condition can be given in terms of the drag coefficient C_D based on the relative velocity between them as

$$F_D = -\frac{1}{2} A_d C_D \rho_c v_{cp} |v_{cp}|, \quad (3-1)$$

where F_D is the drag force exerted on the particle/droplet, A_d is the projected area of the particle/droplet on a plane perpendicular to the velocity direction, C_D is the drag

coefficient between the particle/droplet and the continuous fluid, v_{cp} is the relative velocity given by $v_{cp} = v_c - v_p$ and ρ_c is the density of the continuous fluid.

The drag coefficients of the single particle/droplet in an infinite medium has been studied extensively by many researchers and they are given by the empirical correlations [7, 8, 9]. Based on the single particle/droplet experimental data, Ishii [9] developed the correlations for the multi-particle system. In viscous regime the drag coefficient of the particle/droplet in multi-particle system is given by the correlation:

$$C_D = \frac{24}{Re} (1 + 0.1 Re^{0.75}) \quad (3-2)$$

where Re is the Reynolds number by using the mixture viscosity. In Newton's regime the drag coefficient of the particle/droplet in multi-particle system is given by the correlation:

$$C_D = 0.45 \left(\frac{1 + 17.67[f(\alpha_d)]^{6/7}}{18.67f(\alpha_d)} \right)^2 \quad (3-3)$$

where

$$f(\alpha_d) = (1 - \alpha_d)^{0.5} \left(2 - \frac{\alpha_d}{0.62} \right)^{1.55} \quad (3-4)$$

and α_d is the volume fraction of the particles. It is shown in Eq. (3-1) that the drag force is dominated by the drag coefficient and the surface area of the particles/droplets. If the surface area of the particles/droplets is fixed in the simulation of an experiment, the drag correlation can be estimated. In the previous study, the QUEOS premixing experiment was simulated [4, 5], because in this experiment, the hot solid particles (the surface area of the particles is fixed) were released into water. The front advancement of the particle cloud moving in water (affected by the drag coefficient) was analyzed to estimate the drag correlations. The results show that the front advancement of the particle cloud in the simulation disagreed with that in the experiment and the difference was enhanced with increasing the temperature of the hot particle. These results suggest that the influence of the temperature on the drag coefficient should be considered in the drag correlation in the case of FCI study. This influence is not considered in the currently employed drag

correlations.

Then let us check the configuration of a hot particle/droplet moving in coolant liquid to understand what induced the difference of the front advancement of the particle cloud between the simulation and the experiment. In Nelson's experiment [10], a single droplet FCI, it is showed that when a hot particle/droplet (In this study, hot particle and droplet are the same. In the following the 'particle' is used) moves in coolant liquid, it is surrounded by a thin vapor film, as shown in Fig. 3-1. The hot particle does not contact directly with the coolant liquid. The boundary around the particle is vapor, which is continuously generated from the coolant liquid-vapor interface and flows inside the film from the lower part to the upper part around the particle. It is the vapor flowing inside the film that gives a resistance to the moving particle. The currently employed drag correlations may not be applicable in such a configuration, especially with high particle temperature.

In the multi-particle system, the effect of other particles on the original particle's drag force should be considered. Ishii [6] developed a method to consider the effect of multi-particle (without vapor film) on drag coefficient. In the viscous flow regime, the effect of other particles in the multi-particle system on the original particle's drag is considered by using the mixture viscosity. In his model it is considered that the force exerted on the original particle by other particles is in the form of viscous stress. In the case of the hot particle with vapor film, since the coolant liquid-vapor interfacial velocity is affected by other particles, the force exerted on the original particle can be expressed by viscous stress through the liquid-vapor interface. In this study, the mixture viscosity concept will be employed to develop the drag coefficient for multi-particle system under laminar and turbulent flow conditions.

Since the drag correlation with the effect of the vapor film for a single particle or multi-particle system has not been developed, in this study we will develop the drag correlation of the particle with vapor film moving in coolant liquid. As the first step, the drag coefficients between a single particle with vapor film and the surrounding coolant liquid under laminar and turbulent flow conditions will be developed respectively. Then, based on the single particle model and the mixture viscosity concept, drag coefficients in

multi-particle system under laminar and turbulent flow conditions will be developed respectively. Finally the proposed drag correlations will be employed to again simulate QUEOS experiment.

3.2 The Drag Coefficient for a Single Hot Particle

3.2.1 The Drag Coefficient Expression

From the photograph describing a single hot particle coolant interaction experimented by Nelson [10], as shown in Fig. 3-1, the configuration of the particle moving in coolant liquid can be figured out: when the particle is immersed into coolant, it is surrounded by a thin film of vapor, which is generated continuously from the interface of coolant liquid-vapor, at the front part of the particle. The vapor leaves the particle as a bubble from the top of it, forming a wake region. Based on the observation, the analytical model could be described as shown in Fig. 3-2.

The drag coefficient of the particle with vapor film moving in coolant liquid could be expressed as the following form:

$$C_{D-fb} = \frac{F_y}{\pi r_p^2 \frac{1}{2} \rho_c V_{cp}^2}, \quad (3-5)$$

where C_{D-fb} is the drag coefficient for the particle surrounded with vapor film moving in coolant liquid, V_{cp} is the velocity difference between the particle and coolant liquid, ρ_c is the density of coolant liquid, πr_p^2 is the characteristic area taken to be the area obtained by projecting the particle on a plane perpendicular to the velocity of the coolant flow and F_y is the drag force in y direction exerted on the particle including the pressure and the viscous stress. Although the drag coefficient is defined based on the velocity difference between the particle and coolant liquid, the force exerted on the particle is given directly by the vapor flowing inside the vapor film.

As shown in Fig. 3-2, the vapor flow along the particle surface is divided into two parts, including the laminar (front) region (called region I) and the wake region (called

region II). The forces exerted on the particle surface will be calculated on the two regions separately. The total force exerted on the surface is equal to the sum of the two regions,

$$F_y = F_y^I + F_y^{II} . \quad (3-6)$$

The forces exerted on the region I include pressure and friction. The total force is calculated as

$$F_y^I = \int_0^{\theta_s} (P \cos \theta + \tau_{s1} \sin \theta) 2\pi r_p^2 \sin \theta d\theta , \quad (3-7)$$

where P and τ_{s1} are the pressure and viscosity force exerted on the surface of the particle, r_p is the radius of the particle and θ_s is the separation point of the two regions. In region II wake region, the friction on the surface can be neglected and the pressure in the wake region is the same at the separation point. The force exerted on the region II can be calculated as

$$F_y^{II} = \int_{\theta_s}^{\pi} P_{\theta_s} 2\pi r_p^2 \sin \theta \cos \theta d\theta , \quad (3-8)$$

where P_{θ_s} is the pressure at the separation point. In the following the pressure distribution and viscous stress, which are related to the velocity profile of the vapor in the film, will be calculated according to that the flow condition of the coolant liquid is laminar or turbulent respectively.

3.2.2 The Drag Correlation under Laminar Flow Condition

Since the thickness of the vapor film is thin comparing to the diameter of the particle, the curvilinear orthogonal coordinate (x, y) and the angle θ ($\theta = \frac{x}{R}$) can be

applied to solve this problem, as shown in Fig. 3-2. In this study, the two-dimensional system is employed to model the three-dimensional phenomena, because the main contribution to the force exerted on the particle is induced by the vapor flow in x direction. Comparing with the vapor flow on the x direction, the vapor flow on the circular direction is small, which can be neglected. The following assumptions are made to vapor film and coolant liquid respectively. To the vapor film, the vapor is assumed to form a continuous film layer around the particle, evaporated from the coolant

liquid-vapor interface, which is smooth. The vapor film layer is laminar in region I. (It is reasonable since the calculation shows that local Reynolds number is about several hundreds.) The velocity of the vapor in y direction can be neglected. Evaporation rate is constant along the interface of coolant liquid-vapor. Steady state and steady flow conditions apply. Vapor physical properties are constant. To the coolant liquid, since the laminar flow is assumed in this case, a potential flow field exists in the coolant liquid and the Bernoulli equation is applied to the coolant flow.

Then the governing equations in the vapor film including mass and momentum equations are

$$\frac{\partial \rho u}{\partial x} = 0, \quad (3-9)$$

$$\frac{\partial \rho u^2}{\partial x} = -\frac{\partial P}{\partial x} - \rho g \sin \theta + \mu \frac{\partial^2 u}{\partial y^2}, \quad (3-10)$$

where u is the vapor velocity in the film in x direction, ρ is the vapor density, μ is the vapor viscosity and P is the pressure in the film. The variables without subscript are used to describe the vapor in the film (the same in the following and subscript c refers coolant liquid). The boundary conditions are

$$\begin{aligned} y=0; \quad u=0, \\ y=\delta; \quad u=u_i. \end{aligned}$$

The velocity of the liquid-vapor interface u_i is given by applying potential flow as

$$u_i = \frac{3}{2} V_{cp} \sin \theta. \quad (3-11)$$

The pressure at angle θ , $P(\theta)$ on the liquid-vapor interface can be expressed by applying Bernoulli equation in coolant liquid as

$$P(\theta) = P_0 + \rho_c g r_p \cos \theta + \rho_c \frac{V_{cp}^2}{2} - \frac{\rho_c}{2} \left(\frac{3}{2} V_{cp} \sin \theta \right)^2, \quad (3-12)$$

where P_0 is the pressure at the particle center. If the vapor film is taken as a whole channel, then the following mass equation can be written:

$$\frac{\partial \rho \bar{u} A}{\partial \theta} = \Gamma \frac{\partial S_1}{\partial \theta}, \quad (3-13)$$

where

$$A = \pi \sin \theta (\delta^2 + 2r_p \delta), \quad (3-14)$$

which is the cross area of the vapor film perpendicular to x direction in a control volume (CV) with length scale $rd\theta$ along the channel, δ is the thickness of the vapor film at θ and S_1 is the area on the particle surface,

$$\frac{\partial S_1}{\partial \theta} = 2\pi r_p^2 \sin \theta \quad (3-15)$$

Γ is the evaporation rate on the coolant liquid-vapor interface and

$$\bar{u} = \frac{1}{\delta} \int_0^\delta u dy, \quad (3-16)$$

which is the average velocity of the vapor in the vapor film channel in x direction.

According to the flow pattern of the vapor in the film, separation point between region I and II could be calculated by [12]

$$\left. \frac{\partial u}{\partial y} \right|_{y=0} = 0. \quad (3-17)$$

The velocity profile in the vapor film can be obtained by solving Eqs. (3-9), (3-10), (3-11), (3-12), (3-13), (3-14), (3-15) and (3-16). Then the viscous stress on the surface of the particle is calculated by

$$\tau_{s_1} = -\mu \left. \frac{\partial u}{\partial y} \right|_{y=0}. \quad (3-18)$$

Finally we can calculate the drag coefficient of the single particle with vapor film under laminar condition from Eq. (3-5), (the detailed calculation is presented in the Appendix A,) but the expression is too complicated to be used in simulation codes, which should be simplified. Here we use the following dimensionless numbers,

$$\text{Re} = \frac{V_{cp} D_p \rho_c}{\mu_c}, \quad (3-19)$$

$$\text{Ev} = \frac{\Gamma D_p}{\mu}, \quad (3-20)$$

$$g_0 = \frac{D_p^3 \rho_c^2 g}{\mu_c^2}, \quad (3-21)$$

$$\mu_0 = \frac{\mu}{\mu_c}, \quad (3-22)$$

$$\rho_0 = \frac{\rho}{\rho_c}, \quad (3-23)$$

where Ev and g_0 are newly introduced in this study. The Ev number is defined to describe that the vapor evaporated from the interface flows inside the vapor film. It is a ratio of the evaporation dynamic force to the vapor viscous force,

$$Ev = \frac{\text{dynamic_force}}{\text{viscous_force}}.$$

The dimensionless number g_0 is defined to describe the particle in coolant system with gravity g . It is the ratio of the gravity force to the coolant viscous force,

$$g_0 = \frac{\text{gravity_force}}{\text{viscous_force}}.$$

Then the drag coefficient of the single particle with vapor film under laminar condition can be obtained as

$$\begin{aligned} C'_{D-\text{fb}} = & \frac{9}{8} \left(1 + \left(\frac{2\delta}{D_p} \right) \right) (1 - \cos^2 \theta_s)^2 \\ & + \frac{12\mu_0}{Re} \left(\frac{2\delta}{D_p} \right)^{-1} \left(\frac{1}{3} \cos^3 \theta_s - \cos \theta_s + \frac{2}{3} \right) \\ & - \frac{2g_0}{Re^2} \left(\frac{1}{2} \cos \theta_s - \frac{1}{6} \cos^3 \theta_s + \frac{1}{3} \right) \\ & + \frac{g_0}{Re^2} \left(\frac{2\delta}{D_p} \right) \left(\frac{1}{3} \cos^3 \theta_s - \cos \theta_s + \frac{2}{3} \right) \end{aligned} \quad (3-24)$$

where

$$\left(\frac{\delta}{D_p} \right)^3 + \frac{3Re\mu_0}{2g_0} \left(\frac{\delta}{D_p} \right) = \frac{Ev\mu_0^2}{g_0\rho_0}. \quad (3-25)$$

and

$$\cos \theta_s = -\frac{8\mu_0}{3\text{Re}} \left(\frac{\delta}{D_p} \right)^{-2} - \frac{2g_0}{9\text{Re}^2}. \quad (3-26)$$

By solving Eqs. (3-24), (3-25) and (3-26) the drag coefficient of a particle with a vapor film moving in coolant liquid under laminar flow condition can be calculated. Due to the complexity and inconvenience of the expression (Eq. (3-24)) in applying to a computer code, a simplified drag coefficient correlation is arranged as

$$C_{D-fb}^I = a_0 + \frac{Ev\mu_0}{\text{Re}\rho_0} a_1 + \left(\frac{Ev\mu_0^2}{g_0\rho_0} \right)^{\frac{1}{3}} a_2 + \frac{g_0}{\text{Re}^2} a_3 + \frac{1}{Ev} a_4, \quad (3-27)$$

where $a_0=0.849$, $a_1=0.00205$, $a_2=3.47$, $a_3=0.0424$ and $a_4=-2.18$, which are obtained by fitting the expression (Eq. (3-24)) in the range of Reynolds number from 500 to 3000, Ev number from 60 to 600, g_0 from 10^5 to 10^9 , ρ_0 from 10^{-4} to 10^{-3} and μ_0 from 0.01 to 0.1 respectively. The equation (3-27) shows the drag coefficient of the single particle with vapor film moving in coolant liquid under laminar flow condition is the function of the Reynolds number, Ev number ($\Gamma D_p / \mu$), vapor/liquid viscosity and density ratios and dimensionless number $g_0 (D^3 \rho_c^2 g / \mu_c^2)$. The Ev number is a ratio of the evaporation dynamic force to the vapor viscous force. The dimensionless number g_0 is the ratio of the gravity force to the coolant viscous force. The dimensionless number μ_0 is the ratio of the vapor viscosity to coolant viscosity and the dimensionless number ρ_0 is the ratio of the vapor density to the coolant density. All the five dimensionless number is employed to describe the correlation of the drag coefficient. In this study the definition of these dimensionless numbers is the same. In the next section, based on the same method, the drag coefficient of the single particle with vapor film under turbulent condition will be developed.

3.2.3 The Drag Correlation under Turbulent Flow Condition

In the turbulent flow cases, the assumptions of the potential flow and Bernoulli equation could not be applied in coolant liquid. The energy loss and interfacial velocity change due to turbulence should be considered. Here it is assumed that the interfacial velocity can be written as

$$u_i = AV_{cp} \sin \theta \quad (3-28)$$

and the pressure equation can be written as the same formulation as in laminar flow case by adding one term:

$$P(\theta) = P_0 + \rho_c g R \cos \theta + \rho_c \frac{V_{cp}^2}{2} - B \rho_c \frac{(1 - A \sin \theta)^2 V_{cp}^2}{2} - \frac{\rho_c}{2} (AV_{cp} \sin \theta)^2, \quad (3-29)$$

where A and B are parameters to be used to consider the influence of turbulent flow on interfacial velocity and pressure distribution around the particle. They will be determined by employing experimental data. The assumptions to vapor are the same as in laminar flow case. Then we can use the equations (3-5) through (3-24), replacing (3-11) and (3-12) by (3-28) and (3-29), in turbulent flow case. By solving those equations, the drag coefficient of the particle with vapor film moving in coolant liquid under turbulent flow condition can be obtained from Eq. (3-5) with the undetermined parameters A and B as

$$\begin{aligned} C'_{D-fb} = & \frac{A^2}{2} \left(1 + \frac{2\delta}{D_p} \right) (1 - \cos^2 \theta_s)^2 \\ & - 2B \left(1 + \frac{2\delta}{D_p} \right) \left(\frac{A}{3} \sin^3 \theta_s - \frac{A^2}{4} \sin^4 \theta_s \right) \\ & + \frac{2A\mu_0}{\text{Re}} \left(\frac{2\delta}{D_p} \right)^{-1} \left(\frac{1}{3} \cos^3 \theta_s - \cos \theta_s + \frac{2}{3} \right) \\ & - \frac{2g_0}{\text{Re}^2} \left(\frac{1}{2} \cos \theta_s - \frac{1}{6} \cos^3 \theta_s + \frac{1}{3} \right) \\ & + \frac{g_0}{\text{Re}^2} \left(\frac{2\delta}{D_p} \right) \left(\frac{1}{3} \cos^3 \theta_s - \cos \theta_s + \frac{2}{3} \right), \end{aligned} \quad (3-30)$$

where θ_s satisfies

$$\left(\frac{A^2}{2} + \frac{BA^2}{2} \right) \cos \theta_s - \frac{AB \cos \theta_s}{2 \sin \theta_s} + \left(\frac{\mu_0 A}{2 \text{Re}} \left(\frac{\delta}{D_p} \right)^{-2} + \frac{g_0}{2 \text{Re}^2} \right) = 0. \quad (3-31)$$

and

$$\delta = \left(\frac{\alpha Ev \mu_0}{A \rho_0 \text{Re}} + \beta \left(\frac{Ev \mu_0^2}{g_0 \rho_0} \right)^{\frac{1}{3}} \right) D_p / 2 . \quad (3-32)$$

The detailed calculation is presented in the Appendix B. In turbulent flow case, the separation point of vapor laminar flow is over $\pi/2$, but very near $\pi/2$, which is shown in the Nelson experiment [10] and previous study [12]. Here $\theta_s = \pi/2$ is employed. Then the drag coefficient of the single particle with vapor film under turbulent condition (Eq. (3-30)) can be written into the formula arranged in dimensionless number as the following:

$$C'_{D-fb} = w_0 + \frac{Ev \mu_0}{\text{Re} \rho_0} w_1 + \left(\frac{Ev \mu_0^2}{g_0 \rho_0} \right)^{\frac{1}{3}} w_2 + \frac{g_0}{\text{Re}^2} w_3 , \quad (3-33)$$

where w_i is the constant. By employing the experimental data of Nelson [10] and QUEOS [3] to fit the Eq. (3-33), it is obtained that $w_0 = 0.0065$ $w_1 = 0.0689$ $w_2 = 0.0115$ and $w_3 = 5.11$ (the parameters A and B in Eqs. (3-28) and (3-29) are included in these constants), in the range of Reynolds number from 4000 to 120000, Ev number from 50 to 300, g_0 from 10^5 to 10^9 . In these two experiments, because the coolant water was filled in the tank opening to the outside with the pressure of 1 bar, ρ_0 is about 0.0007 and μ_0 is about 0.05 respectively. The drag coefficients obtained from the experimental data and those predicted by the fitted correlation under turbulent condition arranged in Reynolds number and Ev number are plotted in Figs. 3-3 and 3-4. The relativity of the drag coefficients predicted by Eq. (3-33) and their experimental data is plotted in Fig. 3-5. It is showed that the fitting is acceptable. The equation (3-33) shows the drag coefficient of the particle with vapor film moving in coolant liquid under turbulent flow condition also can be described by the Reynolds number, Ev number ($\Gamma D_p / \mu$), vapor/liquid viscosity and density ratios and dimensionless number $g_0 (D^3 \rho_c^2 g / \mu_c^2)$. In the calculation of Ev number, the film boiling heat transfer is calculated by using the formula in ref. [11]. It should be noted that the QUEOS experiment is a multi-particle premixing experiment, in which hot solid particles are

released into water. The particle velocity at the leading edge of the particle cloud is estimated as the single particle velocity in the experiment, which are employed to fit the parameters in the correlation (Eq. (3-33)). At the leading edge, since the volume fraction of the particles is small, the effect of other particles can be neglected, which will be discussed in the next section.

3.3 Drag Coefficient for Multi-particle System

In the multi-particle system, it is assumed that the configuration of the original particle with vapor film is not deformed by other particles in the system and the force on the original particle by other particles is exerted through the interfacial velocity change, which could be expressed as a factor of viscous force. The drag coefficient of the original particle with vapor film in multi-particle system could be calculated by Eq. (3-5). The governing equations for vapor are the same as those in the single particle case. The effect of other particles on the original particle is considered by the interfacial velocity and pressure distribution equations. It is assumed that the Ishii's model [6], in which the mixture viscosity is used for particles in multi-particle system, can be applied in the case of the particle with vapor film in multi-particle system. The mixture viscosity of the coolant in multi-particle system is given by Ishii [6]

$$\frac{\mu_m}{\mu_c} = (1 - \alpha_p)^n \quad (3-34)$$

where α_p is the volume fraction of the particles in multi-particle system, μ_c is the coolant viscosity, μ_m is the mixture viscosity of the coolant in the multi-particle system and $n=-1.75$ for particles [6]. On the coolant liquid-vapor interface, the viscous force in coolant liquid side can be written as

$$\mu_m \left. \frac{\partial u_c}{\partial y} \right|_{y=\delta^+} = \mu_c \left. \frac{\partial u_c (1 - \alpha_p)^n}{\partial y} \right|_{y=\delta^+}, \quad (3-35)$$

then the interfacial velocity can be written as

$$u_m \Big|_{y=\delta^+} = (1 - \alpha_p)^n u_c \Big|_{y=\delta^+} = (1 - \alpha_p)^n u_i \quad (3-36)$$

where $u_m|_{y=\delta^+}$ is the interfacial velocity on the coolant liquid-vapor interface in multi-particle system considering the effect of other particles and u_i is the interfacial velocity in single particle system. Then the method developed for calculating the drag coefficient of the single particle can be applied to the particle in multi-particle system. The drag correlations under laminar and turbulent flow conditions in multi-particle system will be developed respectively in the following according to the different interfacial velocity as in the single particle cases.

3.3.1 Drag Correlation under Laminar Flow Condition

The velocity of the liquid-vapor interface u_i for the original particle under laminar flow condition can be written as

$$u_i = \frac{3}{2} V_{cp} (1 - \alpha_p)^n \sin \theta. \quad (3-37)$$

The pressure at angle θ on the liquid-vapor interface in the coolant liquid could be expressed as

$$P(\theta) = P_0 + \rho_c g R \cos \theta + \rho_c \frac{V_{cp}^2}{2} - \frac{\rho_c}{2} \left(\frac{3}{2} V_{cp} (1 - \alpha_p)^n \sin \theta \right)^2 \quad (3-38)$$

Then the equations (3-5) through (3-24), replacing (3-11) and (3-12) by (3-37) and (3-38), can be employed to calculate the drag coefficient of the particle with vapor film in multi-particle system under laminar flow condition. By employing the same method in the previous section, the drag coefficient of the particle with vapor film under laminar condition in multi-particle system can be obtained as the formula expressed in dimensionless number:

$$C'_{D-fb} = a_0 (1 - \alpha_p)^{2n} + \frac{Ev \mu_0}{Re \rho_0} (1 - \alpha_p)^{2n} a_1 + \left(\frac{Ev \mu_0^2}{g_0 \rho_0} \right)^{\frac{1}{3}} (1 - \alpha_p)^{2n} a_2 + \frac{g_0}{Re^2} a_3 + \frac{1}{Ev} (1 - \alpha_p)^{2n} \quad (3-39)$$

where the constant a_i and the ranges of Reynolds number, Ev number, g_0 , ρ_0 and μ_0 are the same value as in the single particle case, because, when α_p is 0, Eq. (3-39) is reduced to that for the single particle case expressed in Eq. (3-27).

The drag coefficients of the hot particle, predicted by Eq. (3-39), are plotted in

Figs. 3-6, 3-7 and 3-8, which are arranged according to Reynolds number, Ev number and the volume fraction of the particles. As shown in Fig. 3-6, the drag coefficients decrease with the increase of Reynolds number, but they are not changed too much when Reynolds number becomes larger. It is showed that the drag coefficient of the particle with vapor film is larger than that of the particle without vapor film given by Ishii [6] in laminar case, which can be explained by that in laminar case, the velocity of vapor flowing inside the film is larger than that of the particle moving in coolant liquid. Figure 3-7 shows that the drag coefficients increase slowly with the increase of the Ev number, which can be explained by the increase of the thickness of the vapor film with the increase of the Ev number. Comparing to the drag coefficient of the particle without vapor film, as shown in Fig. 3-8, the drag coefficients of the particle with vapor film increase with the increase of the volume fraction of the particles much faster than that of the particle without vapor film.

3.3.2 Drag Correlation under Turbulent Flow Condition

Based on the same method described in the previous section, the drag coefficient of the original particle with vapor film in multi-particle system under turbulent flow condition can be calculated. The velocity of the liquid-vapor interface u_i for the original particle is assumed as

$$u_i = AV_{cp} (1 - \alpha_p)^n \sin \theta. \quad (3-40)$$

The pressure at angle θ on the liquid-vapor interface in the coolant liquid could be expressed as

$$P(\theta) = P_0 + \rho_c g R \cos \theta + \rho_c \frac{V_{cp}^2}{2} - B \rho_c \frac{(1 - A(1 - \alpha_p)^n \sin \theta)^2 V_{cp}^2}{2} - \frac{\rho_c}{2} (AV_{cp} (1 - \alpha_p)^n \sin \theta)^2 \quad (3-41)$$

where α_p is the volume fraction of the particles. A and B are parameters to be used to consider the influence of turbulent flow on interfacial velocity and pressure distribution around the particle, which is the same as that in the single particle case.

Then the equations (3-5) through (3-24), replacing (3-11) and (3-12) by (3-40) and (3-41), can be employed to calculate the drag coefficient of the particle with vapor film in

multi-particle system under turbulent flow condition. The drag coefficient can be expressed as the formula in dimensionless number:

$$C'_{D-fb} = w_0(1 - \alpha_p)^{p_n} + \frac{Ev\mu_0}{Re\rho_0}w_1(1 - \alpha_p)^r + \left(\frac{Ev\mu_0^2}{g_0\rho_0}\right)^{\frac{1}{3}}w_2(1 - \alpha_p)^{p_n} + \frac{g_0}{Re^2}w_3 \quad (3-42)$$

where the constant w_i and the ranges of Reynolds number, Ev number, g_0 , ρ_0 and μ_0 are the same value as in the single particle case, because, when α_p is 0, Eq. (3-42) is reduced to that for the single particle case expressed in Eq. (3-33).

The drag coefficients of the hot particle, predicted by Eq. (3-42), are plotted in Figs. 3-9, 3-10 and 3-11, which are arranged according to Reynolds number, Ev number and the volume fraction of the particles. As shown in Fig. 3-9, unlike the drag coefficient of the particle without vapor film in turbulent case, the drag coefficients of the particle with vapor film decrease with the increase of Reynolds number. In large Reynolds number cases the drag coefficients are smaller than that of the particle without vapor film, as shown in Fig. 3-9, which can be explained by that in turbulent case, the velocity of vapor flowing inside the film is less than that of the particle moving in coolant liquid. Figure 3-10 shows that the drag coefficients increase with the increase of the Ev number faster than that in laminar case, which can be explained by that in the turbulent flow cases, the thickness of the vapor film is thinner than that in laminar flow cases due to the large interfacial velocity. For the same increase of the evaporation, more increase of the resistance to the particle is given in the turbulent flow cases than in laminar flow cases. Figure 3-11 shows that the drag coefficients increase very fast with the increase of the volume fraction of the particles, which is similar to that of the particle without vapor film.

3.4 Application of the Proposed Drag Correlations

The proposed drag correlations (equations (3-39) and (3-42)) are introduced into the SIMMER-III code and applied to simulate the QUEOS experiments (Q12 and Q35) [3], the experiment for the premixing phase of FCIs, in which 6.9 and 10 kilograms of solid molybdenum spheres with the temperature of 2300K and 1800K are released into water, respectively. The QUEOS facility and the calculation system are described in refs. [3,4,5].

The front advancement of the particle cloud in water is analyzed to validate the proposed drag correlations. In the calculation of Ev number, the film boiling heat transfer is calculated by using the formula in ref. [11]. The front advancement of the particle cloud, moving in coolant water, obtained from the experimental data, predicted by employing the Ishii's correlations and the proposed correlations are plotted in Figs. 3-12 and 3-13, respectively. The results show the proposed correlations improve the agreement of the evolution of the location of the leading edge of the particle cloud with the experimental data. From these figures, the remaining difference is shown between the simulation with the proposed correlation and the experimental data. This is caused by the following reason. During the falling of the particle cloud in the vessel, its front part is mixed with water and the other part is mixed with vapor. The motion of the particle cloud moving in the vapor mixing region is affected by the momentum exchange between the particle and the vapor, including momentum exchange coefficient and vapor velocity. This then affects the contour shape of the particle clouds (as investigated in the previous study [5]). The overestimation of the momentum exchange between the particle and the vapor in vapor mixing region is thought to cause the above remaining difference.

3.5 Conclusion

The drag coefficient for a single particle surrounded by vapor film moving in coolant liquid under laminar and turbulent flow conditions are studied, based on the conservative equations and assumptions. The drag correlations can be described by the Reynolds number, vapor/liquid viscosity and density ratios and the two dimensionless numbers, newly introduced in this study to suitably describe the influence of the vapor film on the drag coefficient. In the turbulent flow regime, the drag coefficient correlation is fitted by experimental data and is smaller than that of the particle without vapor film.

Based on the single particle model and the mixture viscosity concept, the drag correlations of the particle with vapor film in multi-particle system are proposed for the laminar and turbulent flow cases respectively. The proposed drag correlations are used to simulate the QUEOS experiment and the results show that the proposed correlations improve the agreement of the simulated results with the experimental data. Since the

constants in the proposed drag correlations (3-33) and (3-42) under turbulent condition are fitted by experimental data in limited ranges of dimensionless parameters, not necessarily sufficient for covering the reactor conditions, more experimental data are required to verify the proposed correlations.

References

- (1) Kondo, Sa., *et al.*: Status and Achievement of Assessment Program for SIMMER-III, a Multiphase, Multicomponent Code for LMFR Safety Analysis, *Proc. of Eighth International Topical Meeting on Nuclear Reactor Thermal-Hydraulics*, Vol. 3, P. 1340, Kyoto, Japan, Sept. 30-Oct. 4 1997.
- (2) Morita, K., *et al.*: SIMMER-III Application to Fuel-Coolant Interactions, *Proc. of the OECD/CSNI Specialists Meeting on Fuel- Coolant Interactions*. P. 785, May 19-21, 1997, JAERI, Tokai-mura, Japan.
- (3) Meyer, L., Schumacher, G.: QUEOS, a Simulation-Experiment of the Premixing Phase of a Steam Explosion with Hot Spheres in Water Base Case Experiments, *FZKA Report 5612*, Forschungszentrum Karlsruhe, April (1996).
- (4) Cao, X., Tobita, Y.: Verification of SIMMER-III Modeling on FCI Through Simulation of QUEOS experiments, *Proc. of Atomic Energy Society of Japan Spring Meeting*, Section II, N41, Univ. Ehime, Japan (2000).
- (5) Cao, X., Tobita, Y.: Simulation of Premixing Experiment QUEOS by SIMMER-III, JNC TN9400 2000-100.
- (6) Ishii, M., Chawla, T. C.: Local Drag Laws in Dispersed Two-Phase Flow, *NUREG/CR-1230, ANL-79-105* (1979).
- (7) Peebles, F. N. and Garber, H. J., Studies on the Motion of Gas Bubbles in Liquid, *Chem. Eng. Prog.* Vol. 49, 88 (1953)
- (8) Harmathy, T. Z., Velocity of Large Drops and Bubbles in Media of Infinite and Restricted Extent, *AIChE J.* Vol. 6, 281 (1960)
- (9) Wallis, G. B., The terminal speed of Single Drops or Bubbles in an Infinite Medium, *Int. J. Multiphase Flow* 1, 491 (1974)

- (10) Nelson, L. S., Duda, P. M.: Steam Explosion Experiments with Single Drops of Iron Oxide Melted with a CO₂ Laser Part II. Parametric Studies, *NUREG/CR-2718*, *SAND82-1105*, (1985).
- (11) Brear, D. J., A Guide to Heat Transfer Coefficients in SIMMER-III Version 2.D, PNC ZN9410 98-026, (April, 1998).
- (12) Chou, X.S and Witte, L. C., A Theoretical Model for Flow Film Boiling Across Horizontal Cylinders, *Transactions of the ASME, Journal of Heat Transfer*, Vol. 117, p. 167, (Feb., 1995).

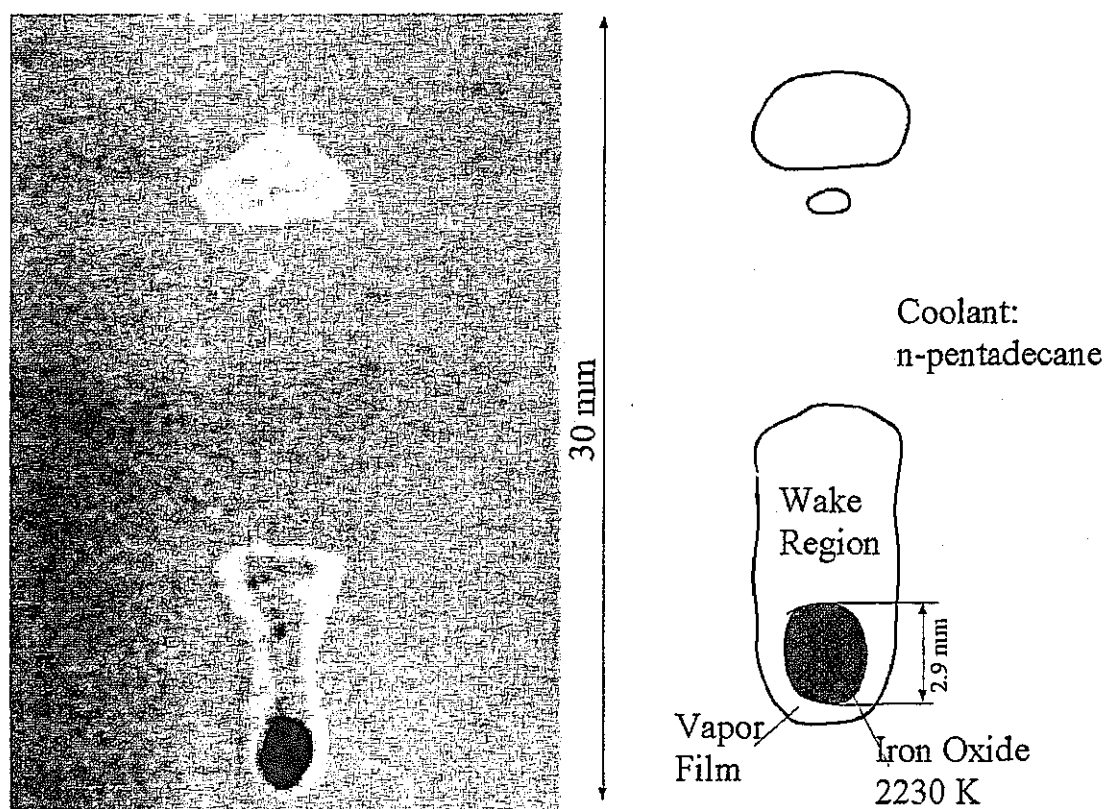


Fig. 3- 1 Configuration of a single droplet moving in coolant in Nelson experiment (NUREG/CR-2718)

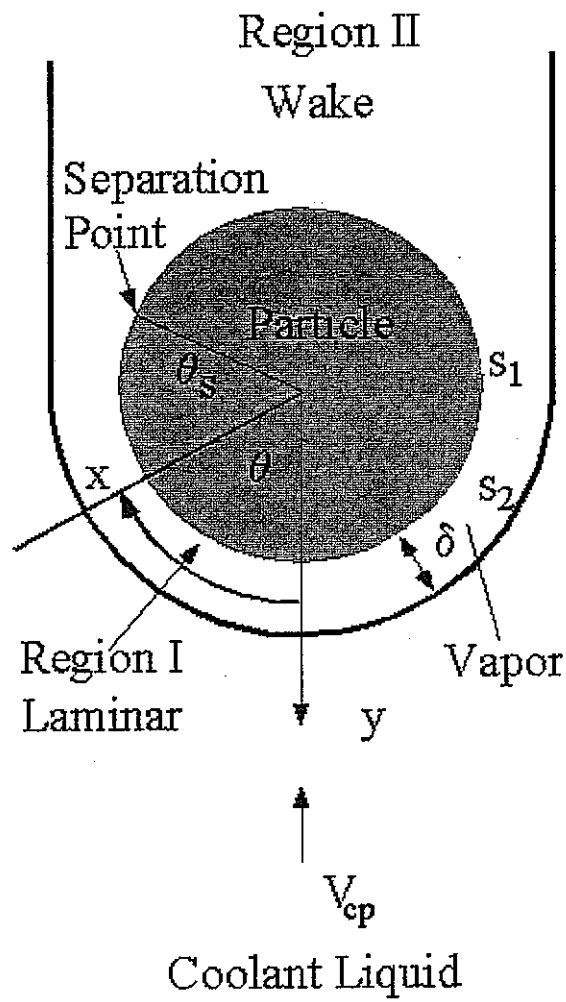


Fig. 3-2 Scheme of a hot particle moving in coolant liquid

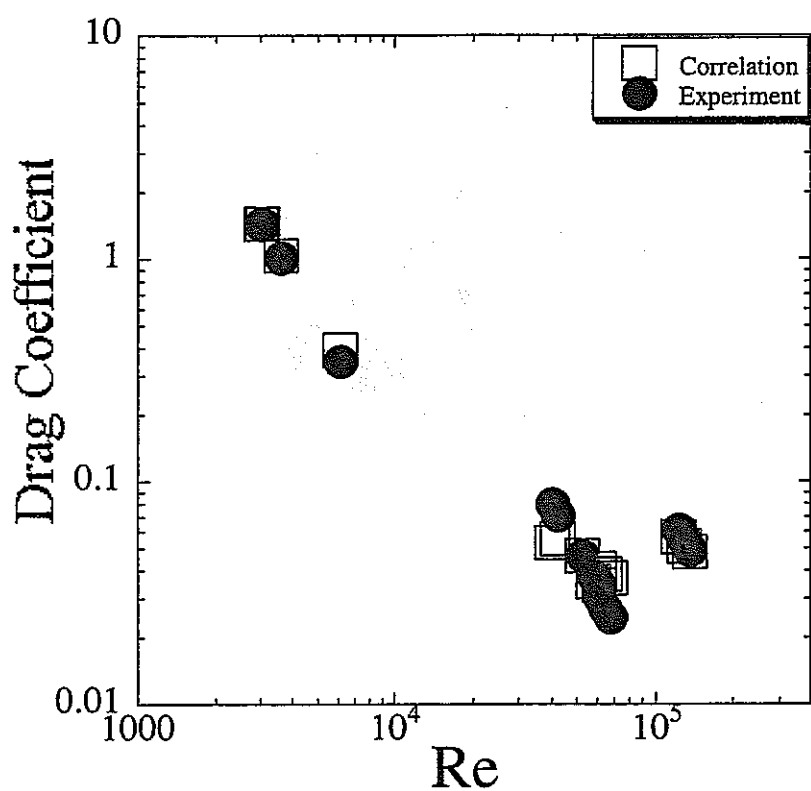


Fig. 3- 3 The drag coefficients obtained from the experimental data and those predicted by the fitted correlation under turbulent condition arranged in Reynolds number

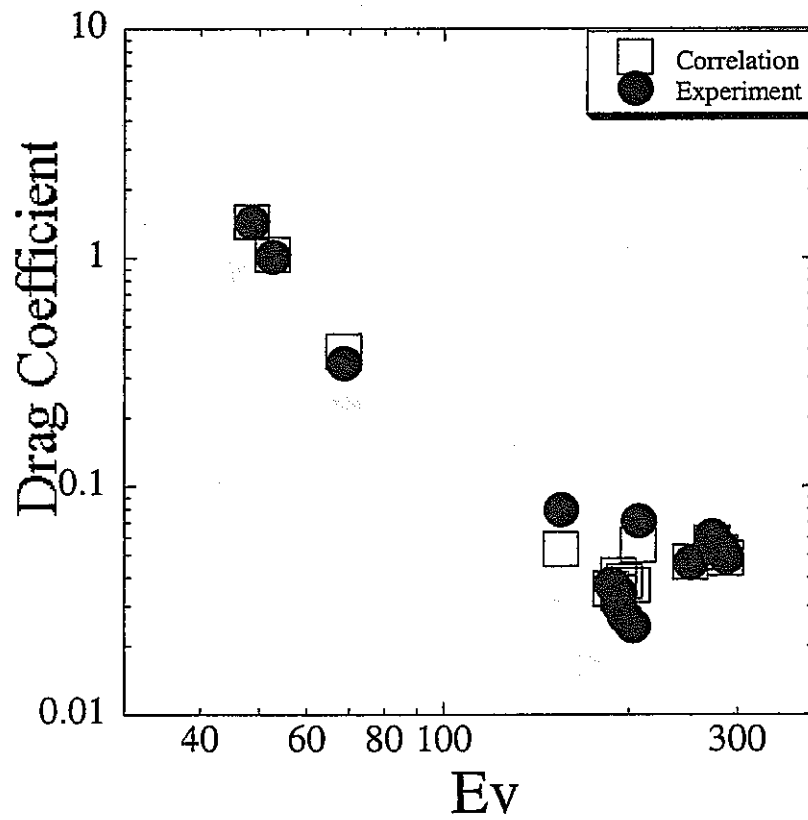


Fig. 3- 4 The drag coefficients obtained from the experimental data and those predicted by the fitted correlation under turbulent condition arranged in Ev number

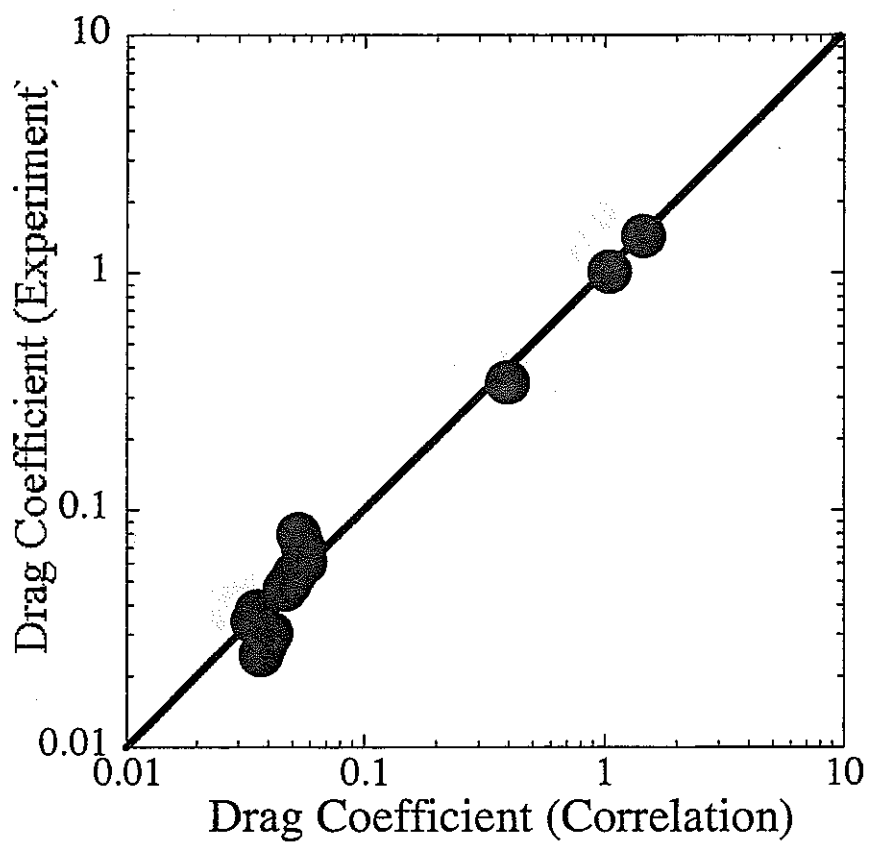


Fig. 3- 5 The relativity of the drag coefficient predicted by equation (3-29) and their experimental data

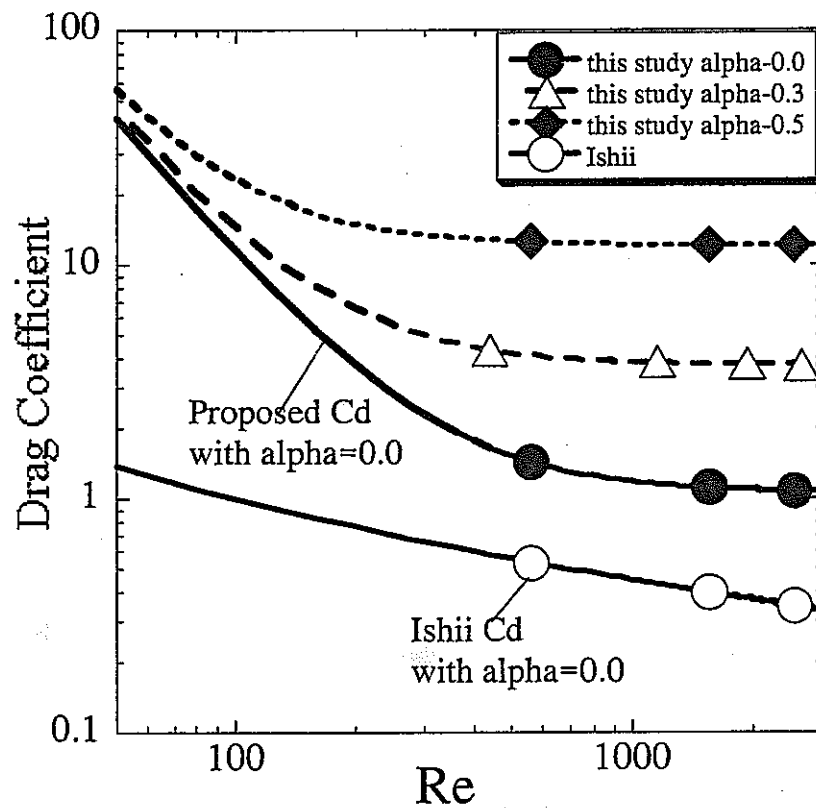


Fig. 3- 6 The variation of the drag coefficient of the particles with vapor film under laminar condition with Reynolds number. (Ev number is 200, μ_0 is 0.12, ρ_0 is 0.00056 and g_0 is 8×10^6 . The alpha is the volume fraction of the particles)

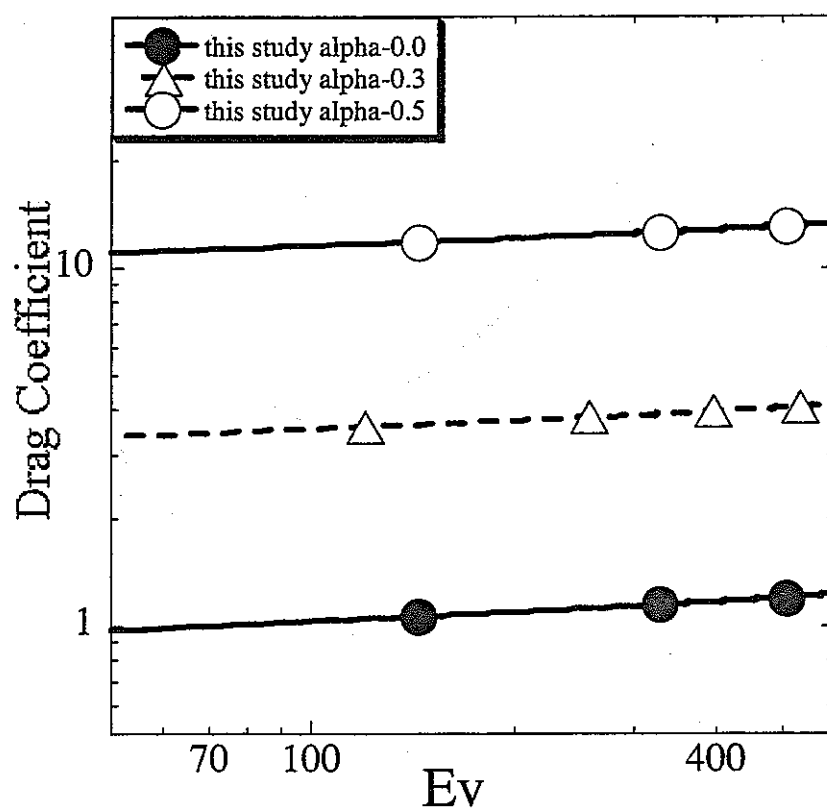


Fig. 3- 7 The variation of the drag coefficient of the particles with vapor film under laminar condition with Ev number. (Reynolds number is 1000, μ_0 is 0.12, ρ_0 is 0.00056 and g_0 is 8×10^6 . The alpha is the volume fraction of the particles)

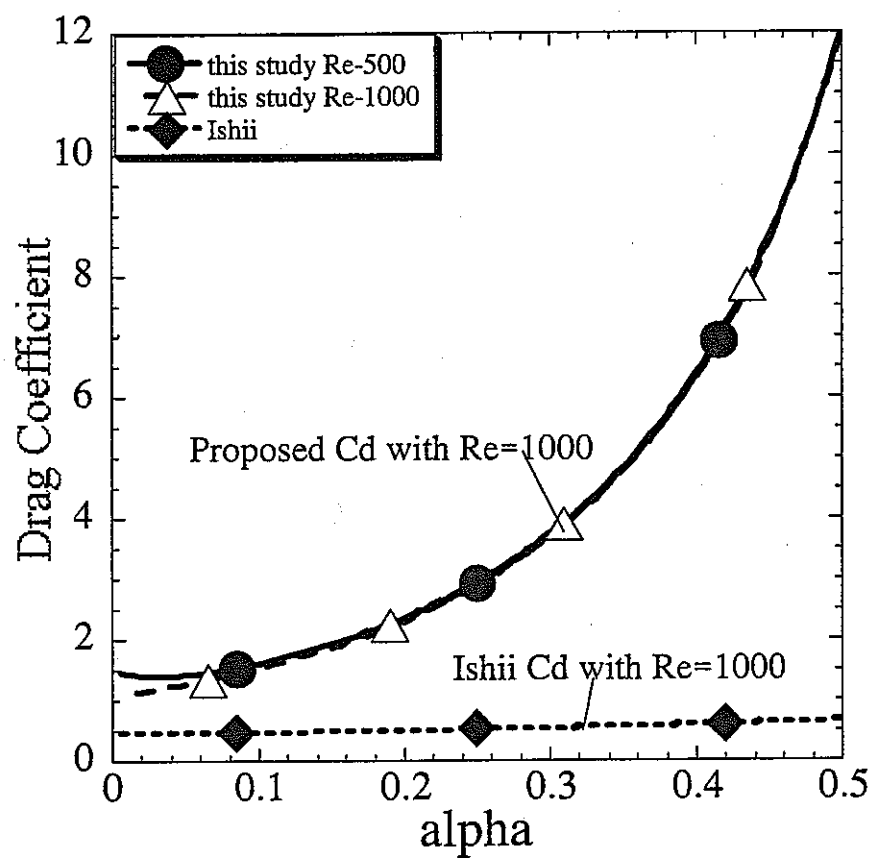


Fig. 3- 8 The variation of the drag coefficient of the particles with vapor film under laminar condition with the volume fraction of the particles. (Ev number is 200, μ_0 is 0.12, ρ_0 is 0.00056 and g_0 is 8×10^6 . The alpha is the volume fraction of the particles)

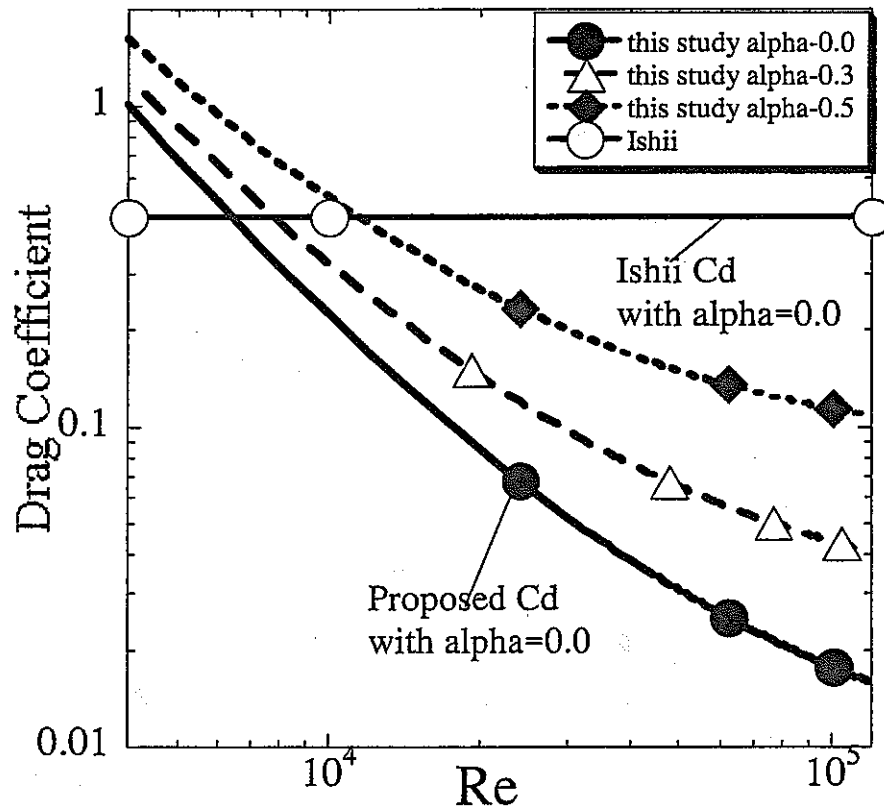


Fig. 3- 9 The variation of the drag coefficient of the particles with vapor film under turbulent condition with Reynolds number. (Ev number is 200, μ_0 is 0.12, ρ_0 is 0.00056 and g_0 is 8×10^6 . The alpha is the volume fraction of the particles)

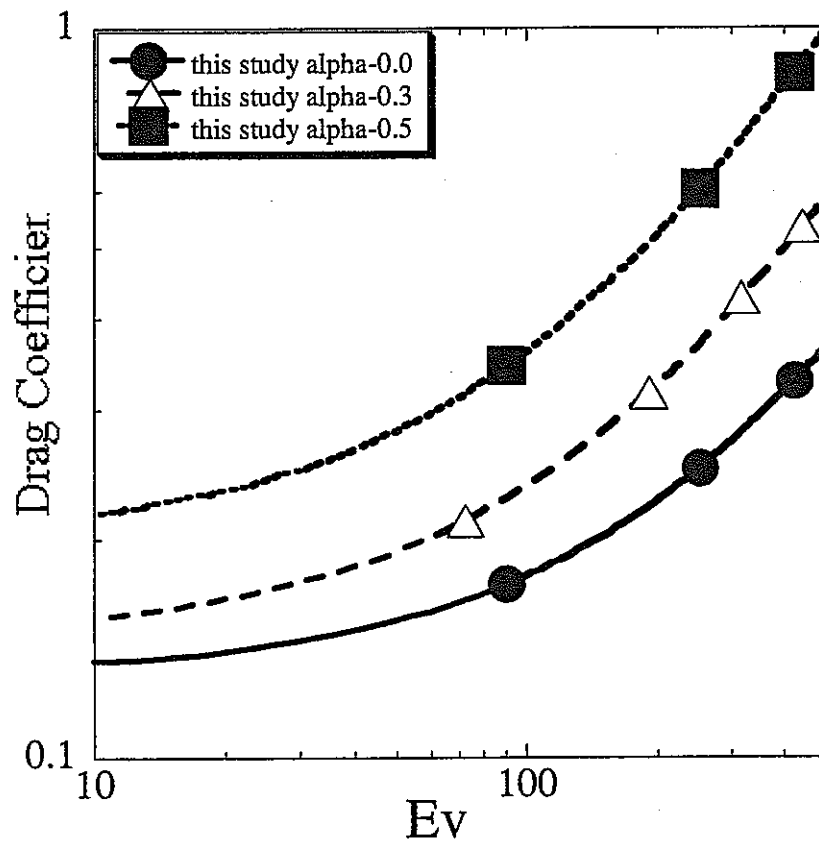


Fig. 3- 10 The variation of the drag coefficient of the particles with vapor film under turbulent condition with Ev number. (Reynolds number is 10000, μ_0 is 0.12, ρ_0 is 0.00056 and g_0 is 8×10^6 . The alpha is the volume fraction of the particles)

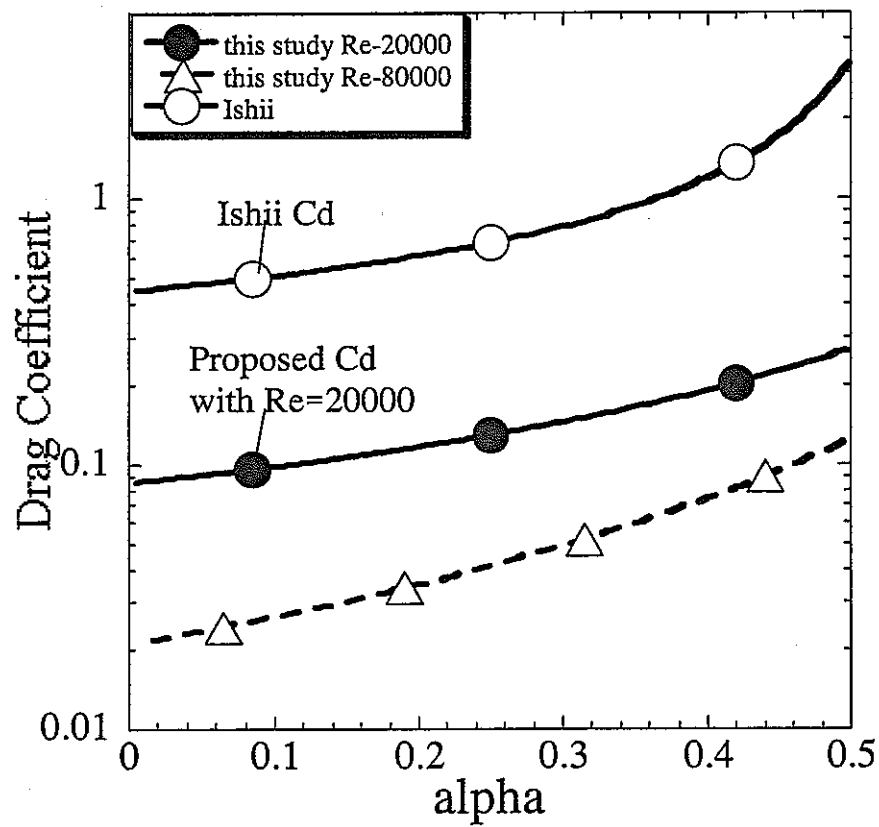


Fig. 3- 11 The variation of the drag coefficient of the particles with vapor film under turbulent condition with the volume fraction of the particles. (Ev number is 200, μ_0 is 0.12, ρ_0 is 0.00056 and g_0 is 8×10^6 . The alpha is the volume fraction of the particles)

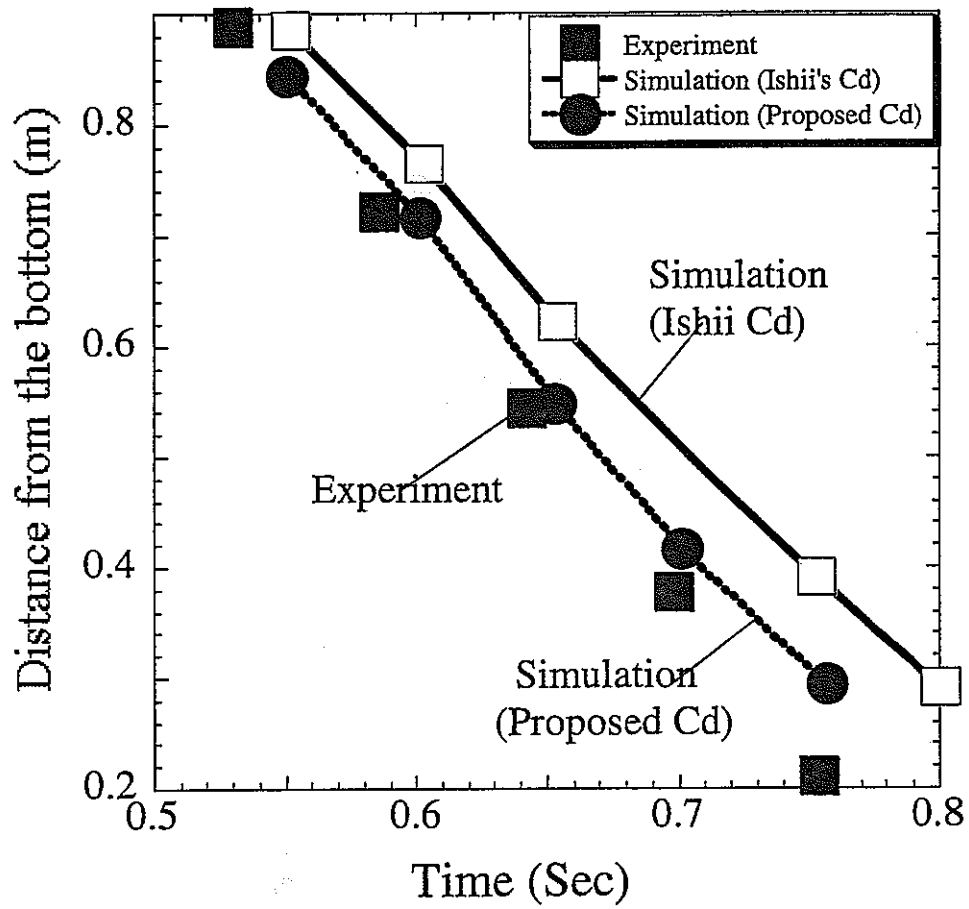


Fig. 3- 12 The advancements of the particle cloud in QUEOS-12, calculated by different drag coefficient correlations

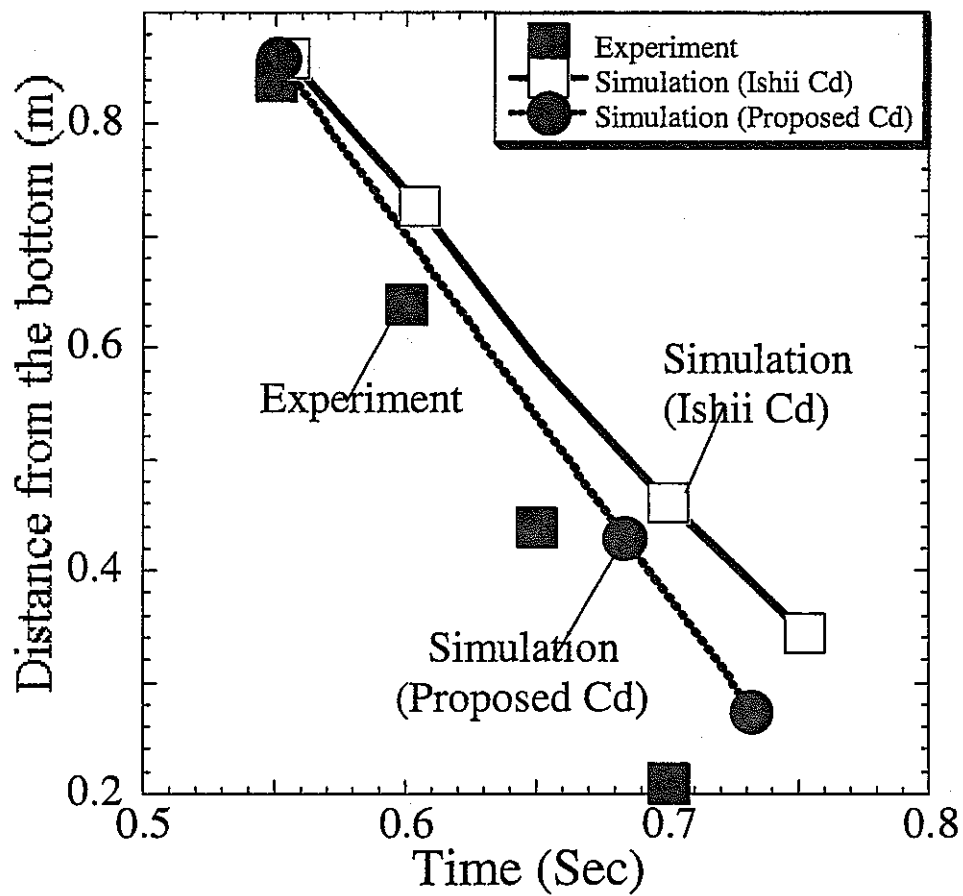


Fig. 3- 13 The advancements of the particle cloud in QUEOS-35, calculated by different drag coefficient correlations

4. Simulation of the MIXA-06 Experiment by SIMMER-III

4.1 Introduction

Fuel Coolant Interactions (FCIs) are the important phenomena in nuclear reactor severe accident analysis, which have been numerically studied in recent years. Several mathematical models have been developed to study the premixing phase of FCIs. The SIMMER-III code is one of them, developed in JNC [1, 2]. The mixing region, which is expressed as the front advancement of the melt droplet stream in this study, is dominated by the drag coefficient (C_d) between the droplets and coolant liquid, the surface area (A_d) of the droplets and the heat transfer from the droplets to the coolant liquid. Since the drag coefficient (C_d) model for the hot droplet with vapor film moving in coolant liquid was estimated through the simulation of the QUEOS experiment [3, 4] by the SIMMER-III code in the previous study [5, 6], and the heat transfer coefficient was estimated in the previous study [7], the difference of the front advancement of the melt droplet stream between the simulated and the experimental results is mainly affected by the surface area (A_d) model, which is related to the fragmentation model of the droplets, suggesting that it is essential to numerically study the FCI process.

Previous studies [8, 9] showed that in high Weber number case, hydrodynamic mechanism dominates the fragmentation process, but under the condition of the low Weber numbers, thermal fragmentation mechanism may dominate the fragmentation process, caused by the vapor film collapse or the surface solidification of the melt droplets. For example, Matsumura [10] experimentally study the self-triggering vapor explosions by using tin-water system. The results show that in a certain range of temperatures of the melt droplet and coolant the thermal fragmentation mechanism dominates the fragmentation of the droplets. Cronenberg [11, 12] and Corradini [9] studied the influence of the surface solidification of the melt droplets and concluded that the influence of the surface solidification should be accounted for the case with a high melting point of the melt droplets. Although the thermal fragmentation mechanism induced by the self-triggering event has been studied many years, the fragmentation rate

model for simulation tools induced by the self-triggering event has not been searched.

In the current SIMMER-III code, the hydrodynamic fragmentation model (Taylor type correlation and Pilch and Erdman's correlation) [1, 2] is employed, which is developed based on the relative velocity between the droplets and coolant liquid. In this study, the validity of the fragmentation model employed in the SIMMER-III code is tested and evaluated through the simulation of the MIXA experiment [13] in the study of the FCI process under the condition of low Weber numbers.

4.2 Description of Experiment

MIXA are the simulant experiments of the mixing study of FCIs, which were performed at Winfrith Technology Centre [13]. The experimental facility is shown in Fig. 4-1, involved the release of several kilograms of molten fuel simulant (81% uranium dioxide and 19% molybdenum metal at a temperature of 3600 K) into the pool of water. A droplet former is employed to ensure that the melt enters the water as a stream of droplets with a diameter of approximately 6 mm. The skirt is attached beneath the droplet former to control the radial spreading of the stream of the droplets. The experimental vessel is of square section with a side of 0.37 m and a pool depth of 0.6 m. The vessel is left open to the atmosphere via a venting line, which contains a flow-meter to measure the steam produced as the melt droplets enter the water. The initial pressure is 0.1 MPa in the experiment and the water is initially heated to near the saturated temperature.

In the MIX-06 experiment a central pour of 3 kg of melt droplets in the form of approximate 6 mm diameter droplets is produced. When the melt droplets are released from the melt generator, the droplet stream of 120 mm in diameter is produced by the cylindrical skirt. The melt droplets pour lasts for a total time of 1.0 s. The main data in the MIXA06 experiment are summarized in table 4-1.

4.3 SIMMER-III Representation

4.3.1 Geometry, Initial Conditions and Calculation System

The MIXA experimental vessel, which is the square-section vessel, as shown in Fig. 4-1, is modeled as an axis-symmetric cylindrical volume with the same cross sectional area as the real vessel in a diameter of 0.42m and a total height of 1.5 m with a depth of 0.6 m region, which consists of a water pool, and 0.9 m region below the melt generator filled with the air, open to outside, as shown in Fig. 4-2. A constant pressure boundary condition is employed at the exit. The melt droplets flow into the vessel through the hole with a diameter of 0.12 m in the center on the vessel top. The stream of the melt droplets with a volume fraction of 0.05 flows into the vessel at a rate of 3 kg/s in a time interval of 1.0 second.

For all calculations, an initial melt droplet size of 6 mm is specified, which is consistent with the value in the experiment. The material of the melt droplets in the experiment is the mixture of 81% uranium dioxide and 19% molybdenum metal at a temperature of 3600 K, which is simulated by 100 % uranium dioxide with the same temperature. The free gas space is initially filled with the air with initial pressure 0.1 MPa and temperature 371 K. Since the vessel is open to the outside, the composite of gas does not have much influence on the calculated results. The temperature of water in the vessel is 371 K. The main data used in the simulations are summarized in table 4-2.

The geometric model, shown in Fig. 4-2, is discretized radially by 10 nodes with $\Delta r = 0.021$ m and axially by 40 nodes with $\Delta z = 0.0375$ m. The calculations are carried out with a time step of $\Delta t = 4 \times 10^{-4}$. The initial radii of the melt droplets are set to 0.003 m. The minimum radius of the melt droplets is set to 0.001 m to correspond average diameter of the droplets of 0.002 m estimated after the experiment. The Taylor correlation (hydrodynamic fragmentation model) is employed to model the fragmentation of the droplets with the fragments of 0.002 m, 0.0001 m, 0.000001 m and 0.0001 m are set for the initial, minimum and maximum radii of water respectively. The modified ILUBCG method is selected for fluid dynamics algorithm. The orifices plate is set in the flow-out cell in the calculation domain in order to simulate the venting system in the experiment. The multipliers of the drag coefficient among dispersed components and

between dispersed and continuous components are set to 1.0 (default value) respectively. The continuous inflow/outflow is set to the boundary cell in the open exit on the top of the domain, in which the pressure is set to constant of 0.1 MPa. The calculation is started from the time of -0.38 second in order to make that the contact time of the melt droplets with water is 0.0 second.

4.3.2 Code Version and Computer Used

Calculations are based on SIMMER-III Version 2.F (ALPHA, DBL, URANAS options on). The computer used was an EWS ALPHA.

4.3.3 Parametric Cases

In order to estimate the influence of the fragmentation model on the mixing region, the following cases are carried out based on the base case described in section 3.1. The differences between these cases and the base case are listed in the following for each case.

Case 1: The fragmentation of the droplets is modeled by setting the same value of the minimum and maximum radii of the melt droplets in the mixing region in this case, which means that when the droplets enter the water region, they are immediately fragmented into small parts with a diameter of 0.002 m.

Case 2: The Taylor correlation is employed to model the fragmentation of the droplets with the fragments of 0.001 m (0.002 m in base case).

Case 3: The difference between this case and the base case is that the time constant multiplier for the Weber breakup of the melt droplets in the bubbly region (CFSB) and the time constant multiplier for the Weber breakup of the melt droplets in the dispersed region (CFSD) is set to 0.001 (1.0 in base case) to investigate the influence of the fragmentation time in Taylor correlation on the mixing region.

Case 4: The maximum and minimum radii of the melt droplets are set to the initial value of 0.003 m in the mixing region, which means no fragmentation of the droplets. This case is designed to understand the influence of the current fragmentation model on

the mixing region by obtaining the difference of the front advancement of the droplet stream induced by the current fragmentation model between two cases.

Case 5: This case is designed to understand the difference between the Pilch and Erdman's correlation [14] for the fragmentation of the droplets and the Taylor correlation in the base case.

Cases 6 and 7: The critical Weber number is set to 0.12. The CFSB and CFSD are set to 1.0 and 0.001 respectively to understand which parameters in the Taylor type correlation for the fragmentation of the droplets affect the fragmentation rate.

Case 8 and 9: The fragmentation model of the melt droplets is specified by setting the same value of the minimum and maximum radii of the melt droplets in mixing region, as in case1. The minimum radius of the droplets is set to 0.0015 and 0.0007 m respectively in the two cases to obtain the influence of the size of the fragmented droplets on the mixing region.

4.4 Results and Discussion

4.4.1 Base Case

The calculated results of the base case include the front advancement of the stream of the melt droplets (the expression of the mixing region), the pressure transient, the steam flow rate, the cumulative steam volume vented and water level swell, summarized in the following.

The front advancements of the stream of the melt droplets in water both in the simulation and the experiment are plotted in Fig. 4-3, which shows that the calculated penetration rate of the stream of the droplets is faster than that measured from the experiment. Since the front advancement of the droplet stream is dominated by the drag coefficient between the droplets and coolant liquid, the heat transfer coefficient and the surface area of the droplets, in which the drag coefficient and the heat transfer coefficient were estimated in the previous studies [5,6,7], the difference of the front advancement of the droplet stream between the simulated and the experimental results is mainly resulted

from the surface area model, which is related to the fragmentation rate of the droplets. The current fragmentation model employed in the base case is the Taylor correlation (hydrodynamic fragmentation model). The calculated results show that the fragmentation rate of the droplets is underestimated. (The underestimation of the surface area of the droplets causes the faster penetration in the water. The simulated result of MIXA01 experiment also suggests this conclusion, as shown in Fig. 4-18.)

The calculated and measured pressure transients in the free gas space in the vessel are plotted in Fig. 4-4, which shows that the predicted pressure transient is larger than that observed in the experiment during the penetration of the droplet stream in the water (from 0 to 0.5 second), although the penetration velocity is much faster than the experiment, which can be explained by the overestimation of the heat transfer coefficient from the droplets to the water.

The transient steam production rate can be compared with the code output, as shown in Fig. 4-5. The experimental data show that the steaming rate increases steadily from zero to a peak of about $1.0 \text{ m}^3/\text{s}$ over a period of 0.7 s. But the calculated results give a high steam production rate at the beginning and lower rate after 0.6 second, which is in accordance with the pressure transient. Integration of the measured steam flow rate shows that in the experiment approximately 0.5 m^3 of steam escaped from the vessel in 1.0 second after the melt droplet stream entered water region. The calculated cumulative steam volume is recorded and plotted in Fig. 4-6, which shows that the calculated steam loss is a little lower than that measured in the experiment. The steam production suggests that the fragmentation rate of the droplets is underestimated by employing the Taylor correlation.

The calculated water level swell is shown in Fig. 4-7, which is much higher than that measured from the experiment. The higher water level is thought to be caused by the measurement method. In the calculation, the highest point in the head of the gas chimney wall is measured as the water level. In the experiment the water level at the corner may be measured as the water level, which is much lower than that in the head of the gas chimney wall. In the base case the 10% water fraction contour is taken to represent the

water level.

The distribution of the droplet size could not be obtained from the calculation. In the base case the radius of the fragments is set to 0.001 m, but it can not be known that during the penetration, whether or not the size of the fragments reaches the value. In the following the cases are calculated to investigate the influence of the parameters on the mixing region, which is related to the fragmentation model.

4.4.2 Sensitivity Calculations

In case 1, the fragmentation of the droplets is modeled by setting the values of the minimum and maximum radii of the melt droplets to 0.001 m in the mixing region, which means that when the droplets enter the water region, they are immediately fragmented into small parts with a diameter of 0.002 m. The front advancements of the stream of the melt droplets in water both in the simulation and the experiment are plotted in Fig. 4-8, which shows that the calculated penetration rate of the stream of the droplets is slower than that measured from the experiment and the base case. The result of this case shows that the fragmentation rate of the droplets is overestimated by using such fragmentation model. The real fragmentation rate of the droplets in the experiment is that between the base case and this case, which is supported by the calculated results of the pressure transient, the steam flow rate, the cumulative steam volume vented in this case (fragmentation rate of the droplets is overestimated), which are shown in Figs. 4-9, 4-10, 4-11 respectively.

In case 2 the Taylor correlation is employed to model the fragmentation of the droplets, but the minimum diameter of the fragments is set to 0.001 m instead of 0.002 m in the base case. The front advancements of the stream of the melt droplets in water both in this case and the base case are plotted in Fig. 4-12, which suggests that the calculated penetration rates of the stream of the droplets are almost the same in both cases. The calculated results suggest that during the penetration, the diameter of most of the fragments does not reach the average value of 0.002 m as estimated from the experiment, which means the Taylor correlation fragmentation model underestimates the

fragmentation rate in the simulation of the experiment.

The case 3 is designed to investigate the influence of the fragmentation time in Taylor correlation on the mixing region. The difference is that CFSB and CFSD are set to 0.001 in this case instead of 1.0 in the base case. The front advancement of the stream of the melt droplets is shown in Fig. 4-13. Although the fragmentation time is set to very small, the front advancement does not changed so much in these two cases, which show this parameter does not work in the calculation of these cases.

Then, the case 4 is designed to understand the influence of the current fragmentation model on the mixing region by obtaining the difference of the front advancement of the droplet stream induced by the current fragmentation model between two cases. The maximum and minimum radii of the melt droplets are set to the initial value, which means no fragmentation in this case. The front advancement of the stream of the melt droplets is plotted in Fig. 4-14, which shows that in this case the front advancement of the melt droplets is faster than those both in the experiment and in the base case. These calculated results suggest that the currently employed fragmentation model works in the simulation of the experiment, but the fragmentation rate is underestimated.

The case 5 is designed to understand the difference between the Pilch and Erdman's correlation [14] for the fragmentation of the droplets (implemented in SIMMER-III) and the Taylor correlation in the base case. The front advancement of the droplet stream is plotted in Fig. 4-15, showing no difference by using these two fragmentation models, which are hydrodynamic fragmentation models.

In the cases 6 and 7, the critical Weber number is set to 0.12. The CFSB and CFSD are set to 1.0 and 0.001 respectively to understand which parameters in the Taylor type correlation for the fragmentation of the droplets affect the fragmentation rate. The front advancement of the droplets are plotted in Fig. 4-16, which shows that when the critical Weber number is set to 12, even though the fragmentation time is set to very small (in case 3), the front advancement of the melt droplets is not changed, but when the critical Weber number is set to 0.12 and fragmentation time is reduced 1000 time, the penetration

rate is much reduced, as shown in the result of case 7. These calculated results suggest that the critical Weber number and the fragmentation time are the factors affecting the fragmentation rate in the simulation of the experiment. The calculation shows that in the experiment, the Weber number of the droplets in the system is around or less than 12, which means part of the fragmentation process of the droplets during the penetration is cut off, inducing low fragmentation rate in the calculation. These results suggest that under the condition of low Weber numbers the hydrodynamic fragmentation model could not describe the fragmentation rate of the melt droplets.

In case 8 and 9 the fragmentation model of the melt droplets is specified by setting the same value of the minimum and maximum radii of the melt droplets in mixing region, as in the case 1. The minimum radius of the droplets is set to 0.0015 and 0.0007 m respectively in the two cases to obtain the influence of the size of the fragmented droplets on the mixing region. The front advancement of the melt plotted in Fig. 4-17, which shows that the front advancement is sensitive to the minimum radius of the melt droplets.

4.4.3 Fragmentation Mechanism in High Melting Point FCI

The investigation suggests that the thermal fragmentation mechanism has contribution to the fragmentation of the melt droplets in the MIXA-06 experiment. Thermal effects include boiling effects, internal pressurization and solidification effects, which are believed to have relation with the collapse of the vapor film. In MIXA-06 what is the correct mechanism for fragmentation of the melt droplets? When the melt droplets are released into water, a vapor film is formed to surround the melt droplet, as shown in Nelson's experiment [17]. Because the temperature of the melt droplets in MIXA-06 is very high (3600 K), the vapor film is stable. Since no strong pressure pulse (triggering event) is applied in the vessel, the stable vapor film collapse induced by pressure pulse is not considered to be the dominant triggering event. Self-triggering vapor film collapse is the possible explanation for fragmentation. Since the volume fraction of the melt droplets is very small, about 0.05 and no pressure peak was recorded in the experiment, quenching is the possible reason for the fragmentation of the droplets.

The quenching process can be explained by the boiling curve. As the temperature of the melt droplets decreases to point D, the heat transfer rate decreases. At point D the vapor film becomes unstable and collapses toward the surface of the melt droplets. The melt droplets are above the boiling point of the coolant and the vapor film is re-established. In this transition region, coolant periodically contacts the heating surface. The transition can be very violent and continuous until the nucleate boiling regime is attained at point C. When the temperature difference between the droplet and water is reduced to about 140 K, the boiling enters transition region, which may induce the breakup of the melt droplets.

In order to check the boiling effect, it should be known that the temperature change during the penetration of the melt droplets into water in MIXA-06. The following equation can be used to describe the temperature change of the melt droplet.

$$mc_p \frac{dT}{dt} = -hA(T - T_s) \quad (4-1)$$

where m is the mass of the melt droplet, T is the temperature of the melt droplet, A is the surface of the melt droplet, h is the heat transfer coefficient from the melt droplet to coolant, T_s is the temperature of the coolant. Then temperature transient of the droplet can be obtained as

$$\frac{T - T_s}{T_m - T_s} = e^{\frac{-3h}{\rho c_p r} t} \quad (4-2)$$

Here the heat transfer coefficient from the melt droplet to water at film boiling is about 10^5 to 10^6 $W/(m^2 K)$. The temperature T_s of water is about 373 K. When the melt droplet with a radius of 0.003 m is cooled from 3600 K to 140 K (freezing is not considered), it takes about 0.005 to 0.05 second, which is less than the time of 0.4 second that the melt droplets take to arrive the vessel bottom. Although the boiling effect can be the triggering event in the experiment, the solidification point of UO₂ is about 3100 K, which is much larger than 400K. This means that the solidification effect is much more possible than the boiling effect. The surface temperature reaches the melting point much

earlier than the estimated value (less than 0.001 to 0.01 second). When the surface temperature becomes lower than the melting point, the outer part of the melt droplet becomes solid. The analysis suggests that the freezing-provoked droplet fragmentation mechanism may be the dominant fragmentation mechanism in the MIXA-06 experiment.

In the experimental analysis, most of the debris was in the form of irregular globules, giving the impression of frozen droplets before they arrived the bottom of the vessel. These droplets, which ranged in size from fine power (<0.1 mm) to 10 mm, had a shiny, polished appearance. The nature of the debris strengthen the analysis that freezing-provoked droplet fragmentation mechanism may be the dominant fragmentation mechanism in the MIXA-06 experiment.

4.5 Conclusions

The hydrodynamic fragmentation model employed in the SIMMER-III code is estimated under the condition of low Weber numbers through the simulation of the MIXA-01 and 06 experiments. The calculated results show that the currently employed hydrodynamic fragmentation model in the SIMMER-III code underestimates the surface area of the droplets in the simulation of the experiment with low Weber numbers. The investigation suggests that the fragmentation model of the melt droplets based on the thermal fragmentation mechanism is required to be developed. The freezing-provoked droplet fragmentation mechanism (thermal fragmentation) is considered to be the dominant mechanism to increase surface area of the droplets in the experiment, which is not taken into account in the current SIMMER-III model.

4.6 Recommendations for Model Improvements

Based on the calculated results, the thermal fragmentation model is recommended to be developed for the SIMMER-III code.

References

- (1) Sa. Kondo, D.J.Brear, Y.Tobita, K.Morita, W.Maschek, P.Coste and D.Wilhelm,

- Status and Achievement of Assessment Program for SIMMER-III, a Multiphase, Multicomponent Code for LMFR Safety Analysis, Proceedings of Eighth International Topical Meeting on Nuclear Reactor Thermal-Hydraulics, Vol. 3, Kyoto, Japan, Sept. 30-Oct. 4 1997
- (2) K.Morita, Sa.Kondo, Y.Tobita and D.J.Brear, SIMMER-III Application to Fuel-Coolant Interactions, Proceedings of the OECD/CSNI Specialists Meeting on Fuel- Coolant Interactions May 19-21, 1997, Tokai-mura, Japan.
 - (3) L.Meyer, QUEOS, an Experimental Investigation of the Premixing Phase with Hot Spheres, Proceedings of Eighth International Topical Meeting on Nuclear Reactor Thermal-Hydraulics, Vol. 3, Kyoto, Japan, Sept. 30-Oct. 4 1997
 - (4) L.Meyer, G.Schumacher, QUEOS, a Simulation-Experiment of the Premixing Phase of a Steam Explosion with Hot Spheres in Water Base Case Experiments, FZKA Report 5612, Forschungszentrum Karlsruhe, April 1996.
 - (5) X. Cao and Y. Tobita, Simulation of Premixing Experiment QUEOS by SIMMER-III, JNC TN9400 2000-100 (2000).
 - (6) X. Cao, and Y. Tobita, A Drag Correlation for a Hot Particle/Droplet with vapor film, (in submission to J. of Nuclear Science and Technology)
 - (7) D.Brear, A Guide to Heat Transfer Coefficients in SIMMER-III Version 2.d, PNC ZN9410 98-026, April 1998
 - (8) G.Berthoud, F.Crecy, R.Meignen, Description of Premixing with the MC3D Code including molten jet behavior modeling. Comparison with FARO Experiment results. Proceedings of the OECD/CSNI Specialists Meeting on Fuel- Coolant Interactions May 19-21, 1997, Tokai-mura, Japan.
 - (9) M. L. Corradini, B. J. Kim and M. D. OH, Vapor explosions in light water reactors: a review of theory and modeling, Progress in Nuclear Energy, Vol. 22, No. 1. pp. 1-117, 1988
 - (10) K. Matsumura, et al, Thermal Interaction Zone and Self-triggering Mechanism of Tin-Water Systems, The international seminar on Intense Multiphase

Interactions, June 9-13,1995, Santa Barbara.

- (11) A.W.Cronenberg,T.C.Chawla and H.K. Fauske, A thermal stress mechanism for the fragmentation of Molten UO₂ upon contact with sodium coolant, Nuclear Eng. Des. 30 (1974) 434-443.
- (12) A.W.Cronenberg,M.A.Grolmest, Fragmentation Modeling Relative to the Breakup of Molten UO₂ in Sodium, Nuclear Safety, Vol, 16, No. 6, 1975.
- (13) M.K.Denham, A.P.Tyler and D.F.Fletcher, Experiments of The Mixing of Molten Uranium Dioxide with Water and Initial Comparision with CHYMES code Calculations, NURETH-5, Salt Lake City, UT, 1992, pp. 1667-1675.
- (14) M.Pilch and C. Erdman, Use of breakup time data and velocity history data to predict the maximum size of stable fragments for acceleration-induced breakup of a liquid drop, Int. J. Multiphase Vol. 13, No. 6, pp.741-757, 1987.
- (15) B. Kim and M. L.Corradini, Modeling of small-scale single droplet fuel/coolant interactions, Nuclear Science and Engineering, Vol. 98, 16-28 (1988)
- (16) W. Zyszkowski, Thermal interaction of molten copper with water, Int. J. Heat Mass Transfer, Vol. 18, No. 2, pp. 271-287, 1975.
- (17) L.S.Nelson, P.M.Duda, Steam Explosion Experiments with Single Drops of Iron Oxide Melted with a CO₂ Laser Part II. Parametric Studies, NUREG/CR-2718, SAND82-1105, 1985.

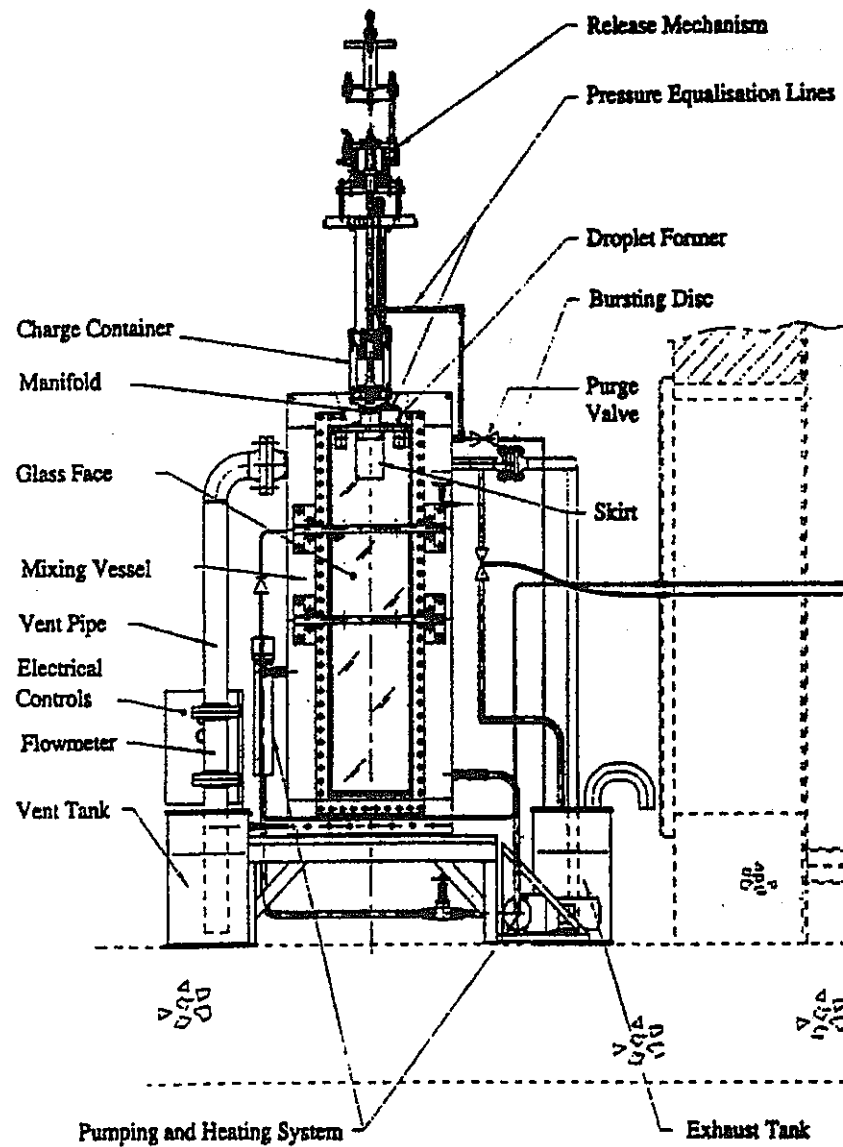


Fig. 4- 1 Scheme of the MIXA facility

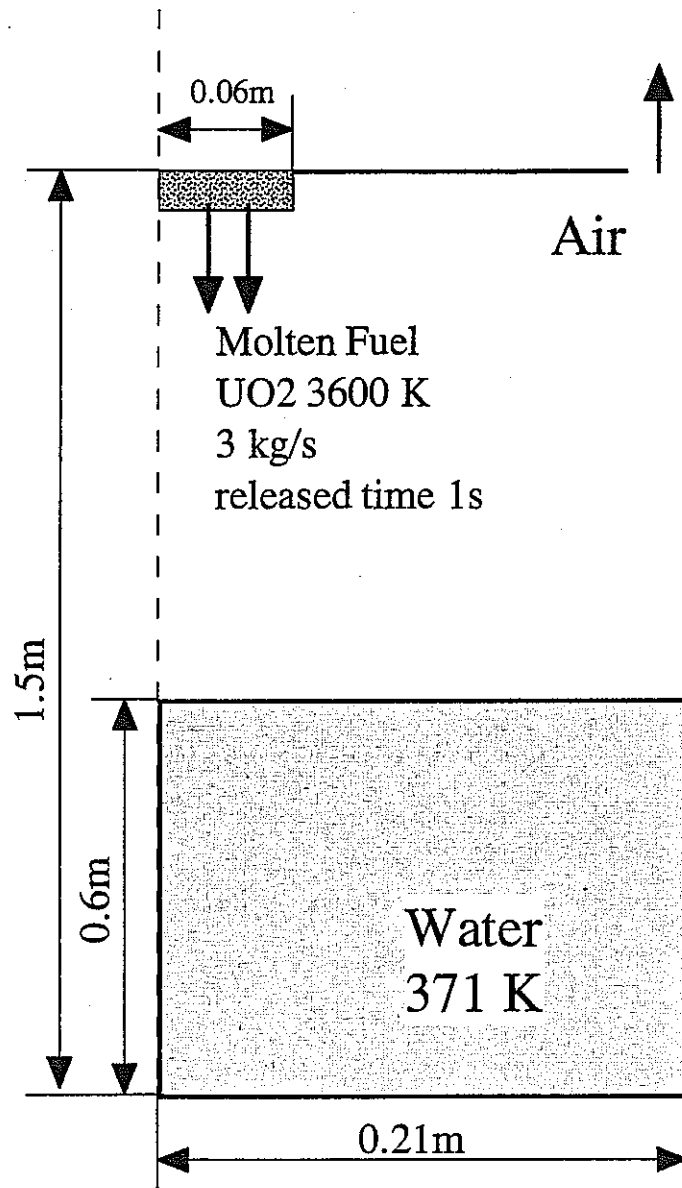


Fig. 4- 2 The computational domain used in the MIXA-06 simulation

Table 4- 1 Data of the experiment MIXA-06

Experimental No.	MIXA-06
Molten Material	UO ₂ 81% + Molybdenum 19%
Initial diameter of drops (mm)	6
Mass of drops released (kg)	3
Initial temperature of drops (K)	3600
Initial radius of melt droplets stream (m)	0.06
Density of spheres (g/cm ³)	8.4
Drops volume fraction at the impact on the water	0.05
Time for first spheres enter water (Sec)	0.0
Water Vessel	
Cross section	37x37 cmxcm
Height (cm)	150
Water level (cm)	60
Water temperature (K)	Near saturated
Pressure loss coefficient of venting pipe	1.0

Table 4- 2 Data used for the simulation of MIXA-06

Simulation No.	MIXA-06
Melt droplet Material	UO ₂
Initial diameter of melt droplets (mm)	6
Mass of melt droplets (kg)	3
Initial temperature of melt droplets (K)	3600
Initial velocity of melt droplets stream (m/s)	0.7
Initial volume fraction of melt droplets	0.05
Initial radius of melt droplets stream (m)	0.06
Water vessel	Cylindrical geometry
Radius (m)	0.21
Height (cm)	1.5
Water level (m)	0.6
Pressure loss coefficient of vent pipe	1.0
Initial pressure in vessel (Pa)	1E5
Temperature of water in vessel (K)	371.0
Temperature of air in gas space (K)	371.0
Time	
Calculation start time (Sec)	-0.38
Real time at cal. Start time (Sec)	-0.38

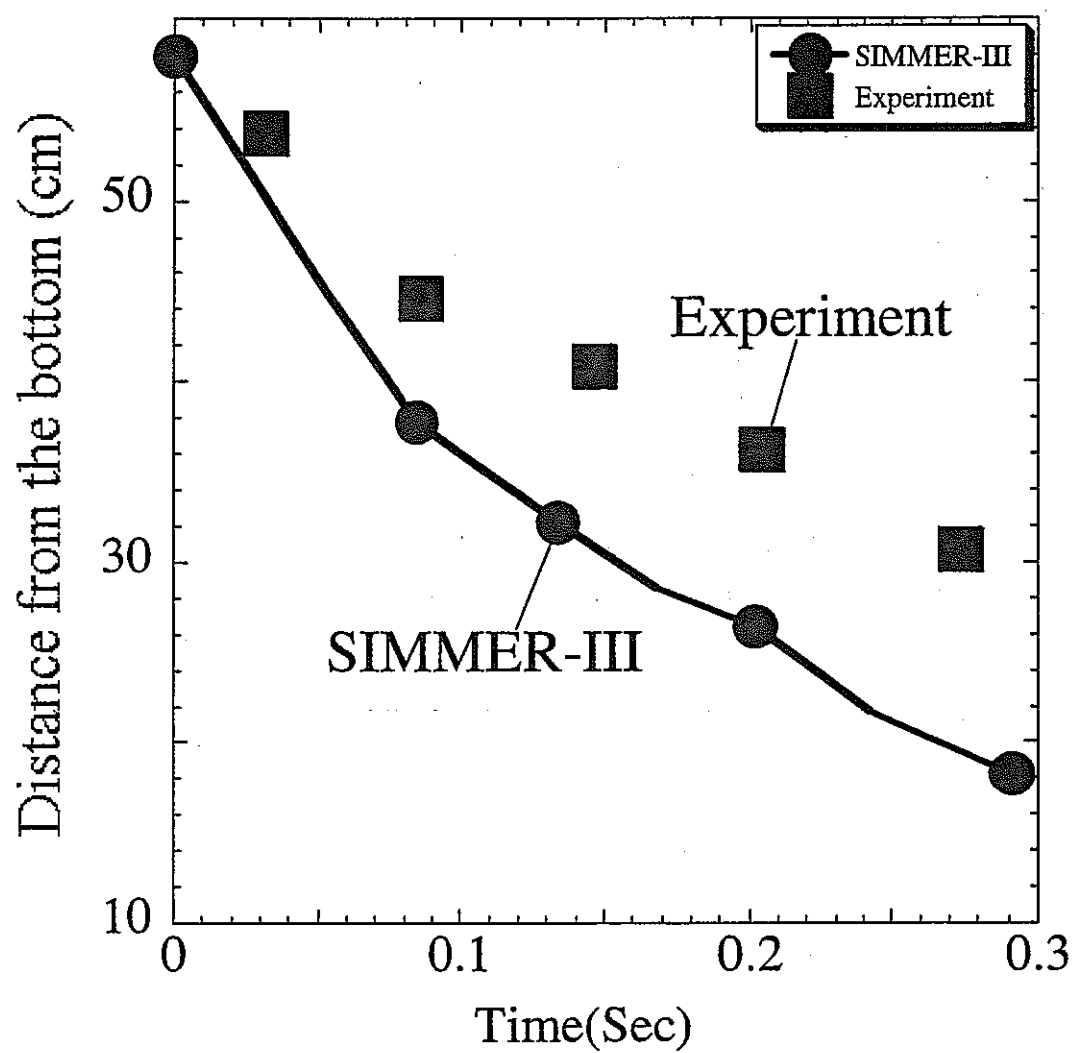


Fig. 4- 3 Front advancement of the droplet stream in water in the experiment and the simulation (base case) of MIXA-06.

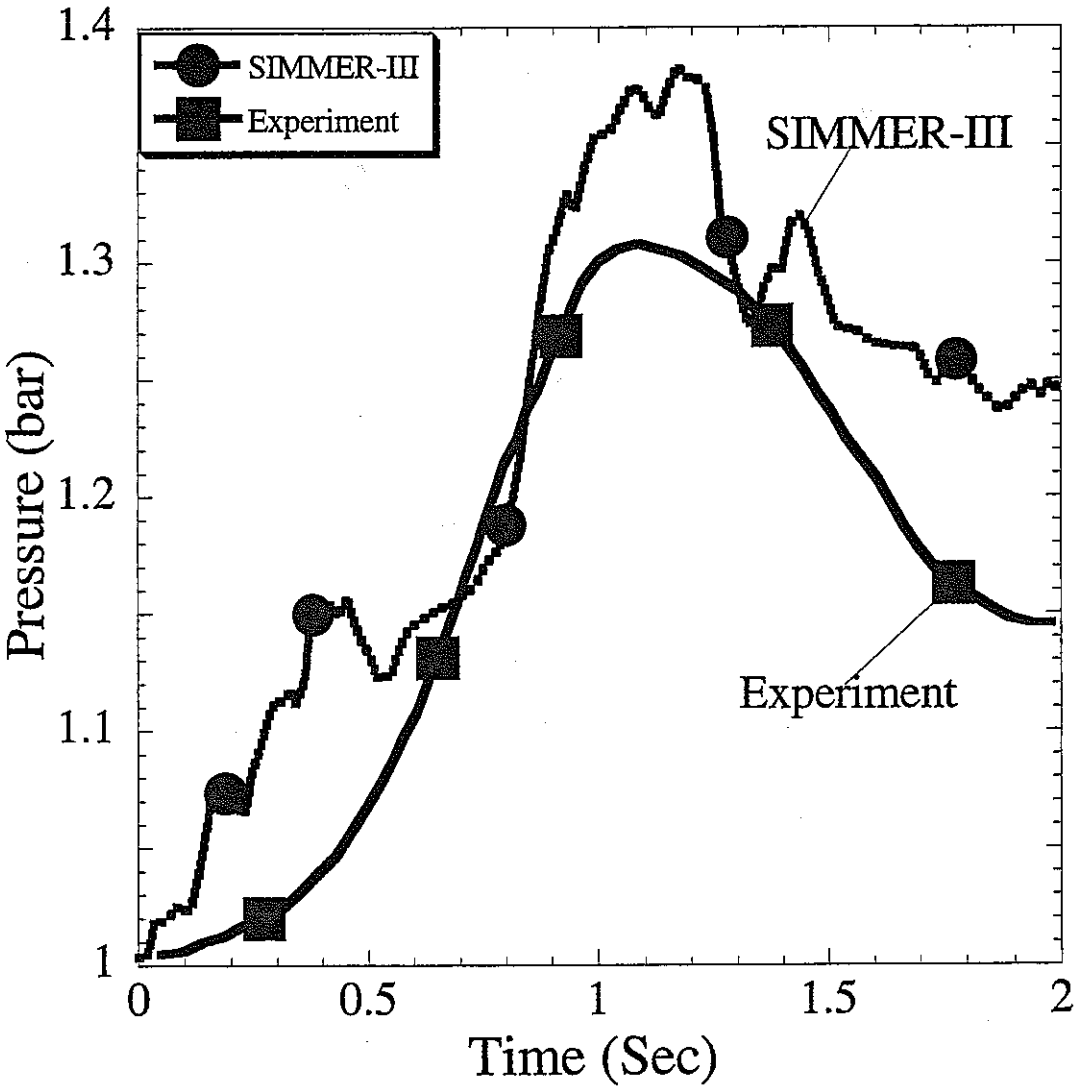


Fig. 4- 4 The pressure transient in the free gas space in the experiment and the simulation (base case) of MIXA-06.

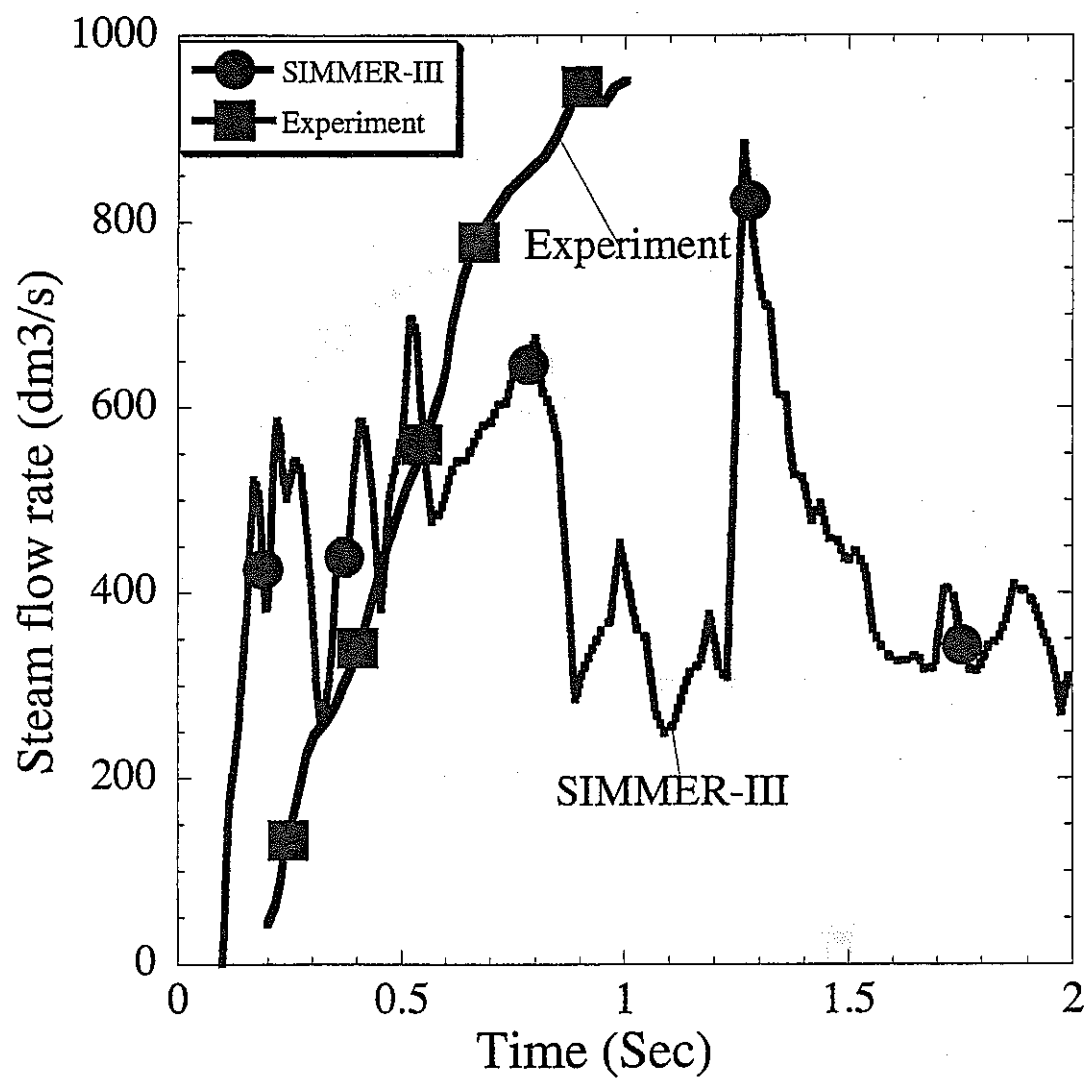


Fig. 4- 5 Steam flow rate in the experiment and the simulation (base case) of MIXA-06.

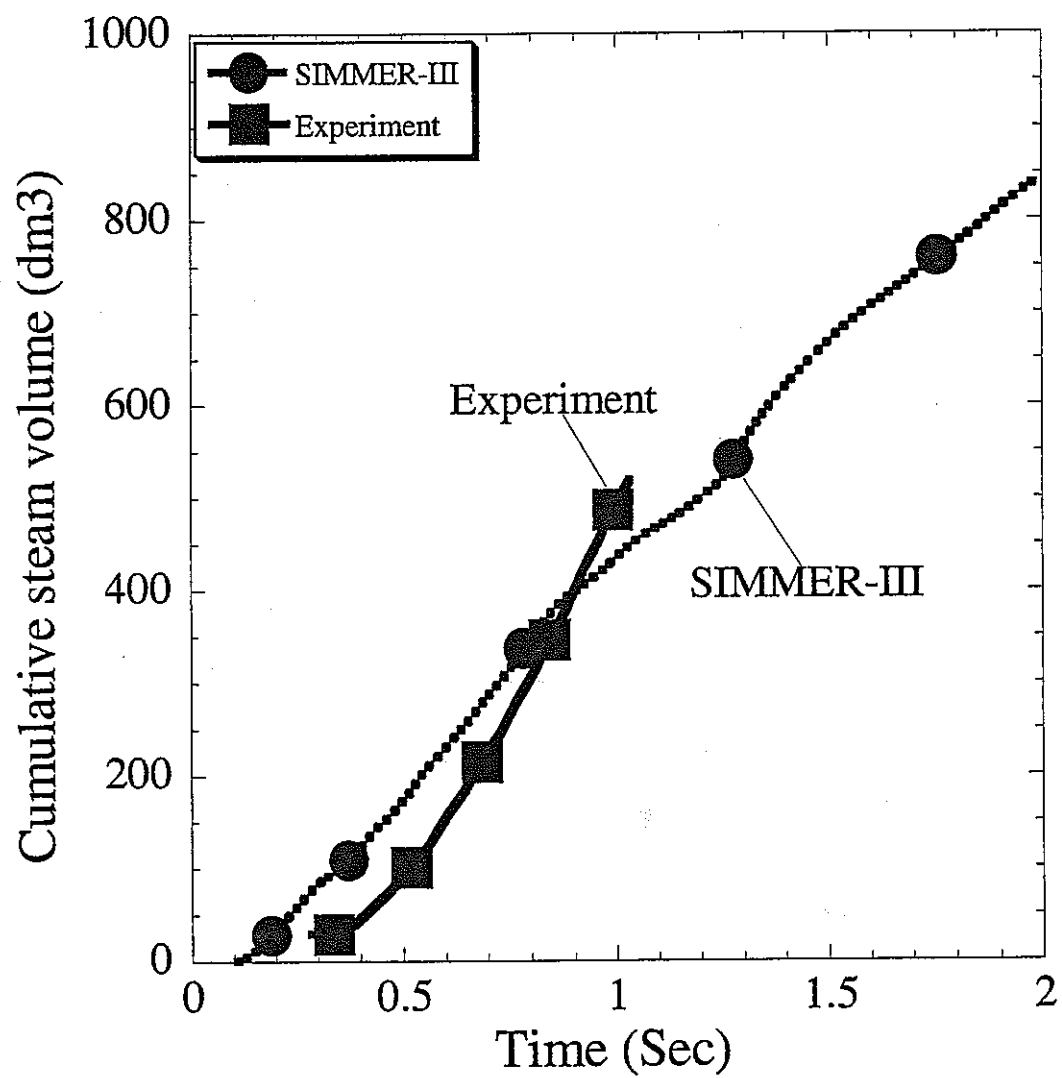


Fig. 4- 6 Cumulative steam volume in the experiment and the simulation (base case) of MIXA-06.

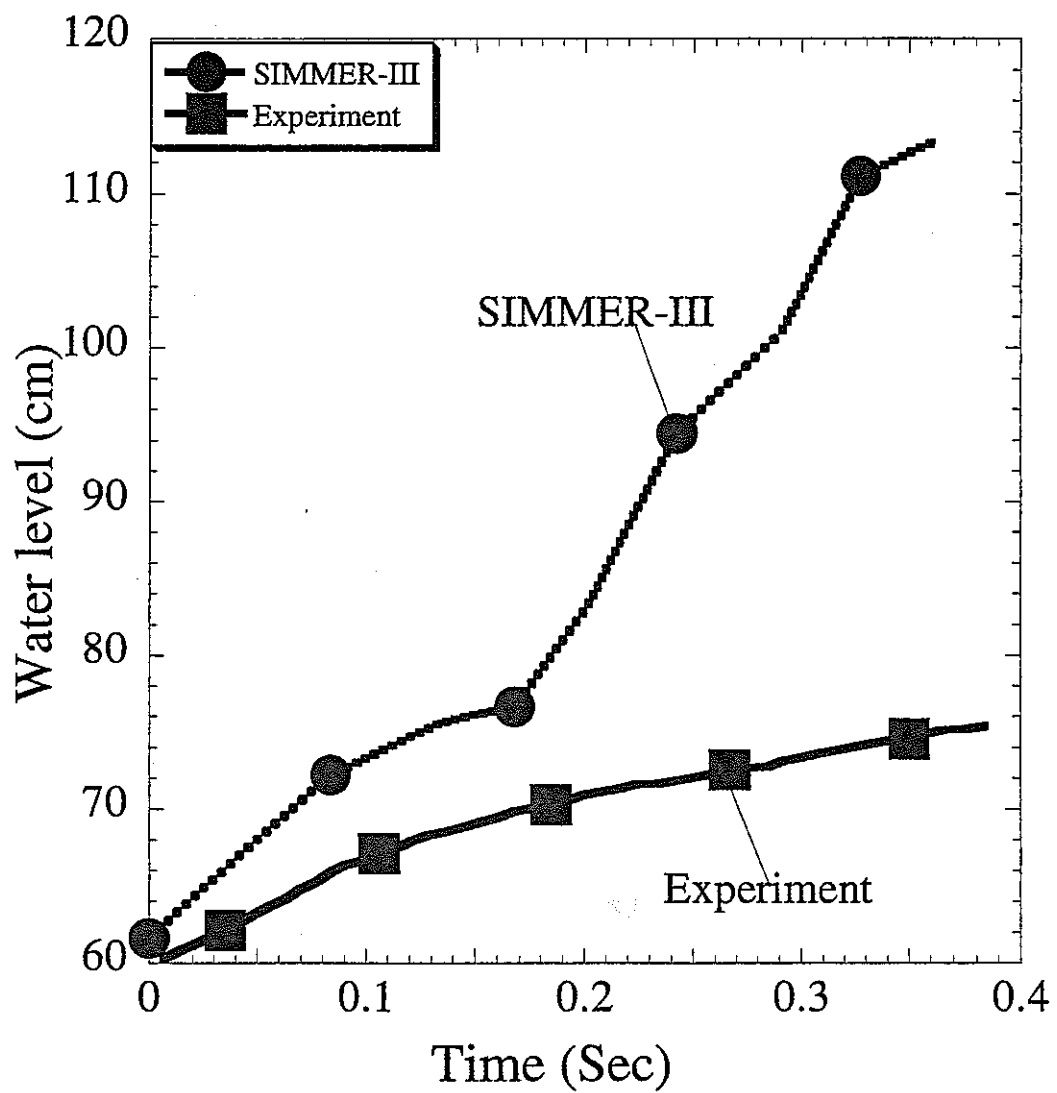


Fig. 4- 7 Water level swell in the experiment and the simulation (base case) of MIXA-06.

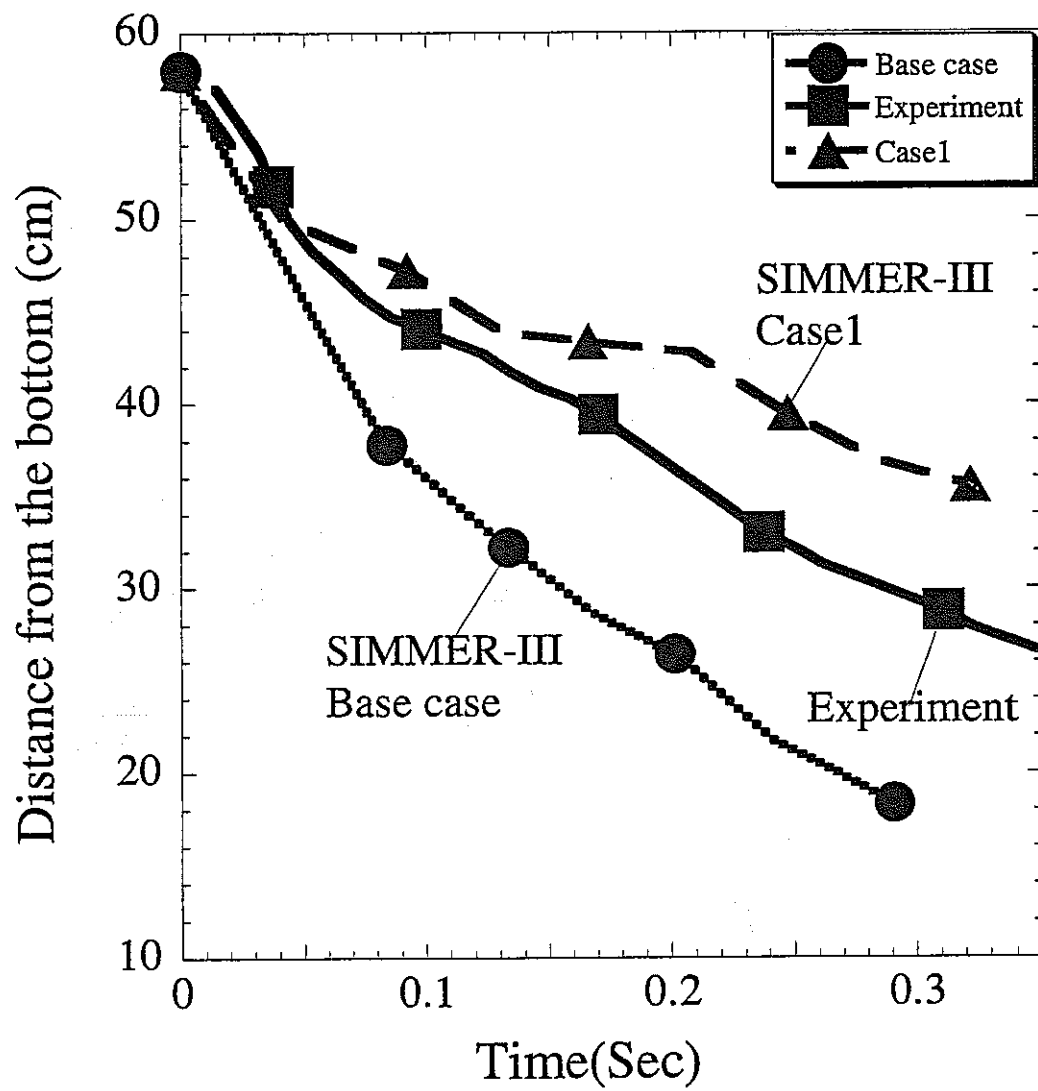


Fig. 4- 8 Front advancement of the droplet stream in water in the experiment and the simulation (case1) of MIXA-06.

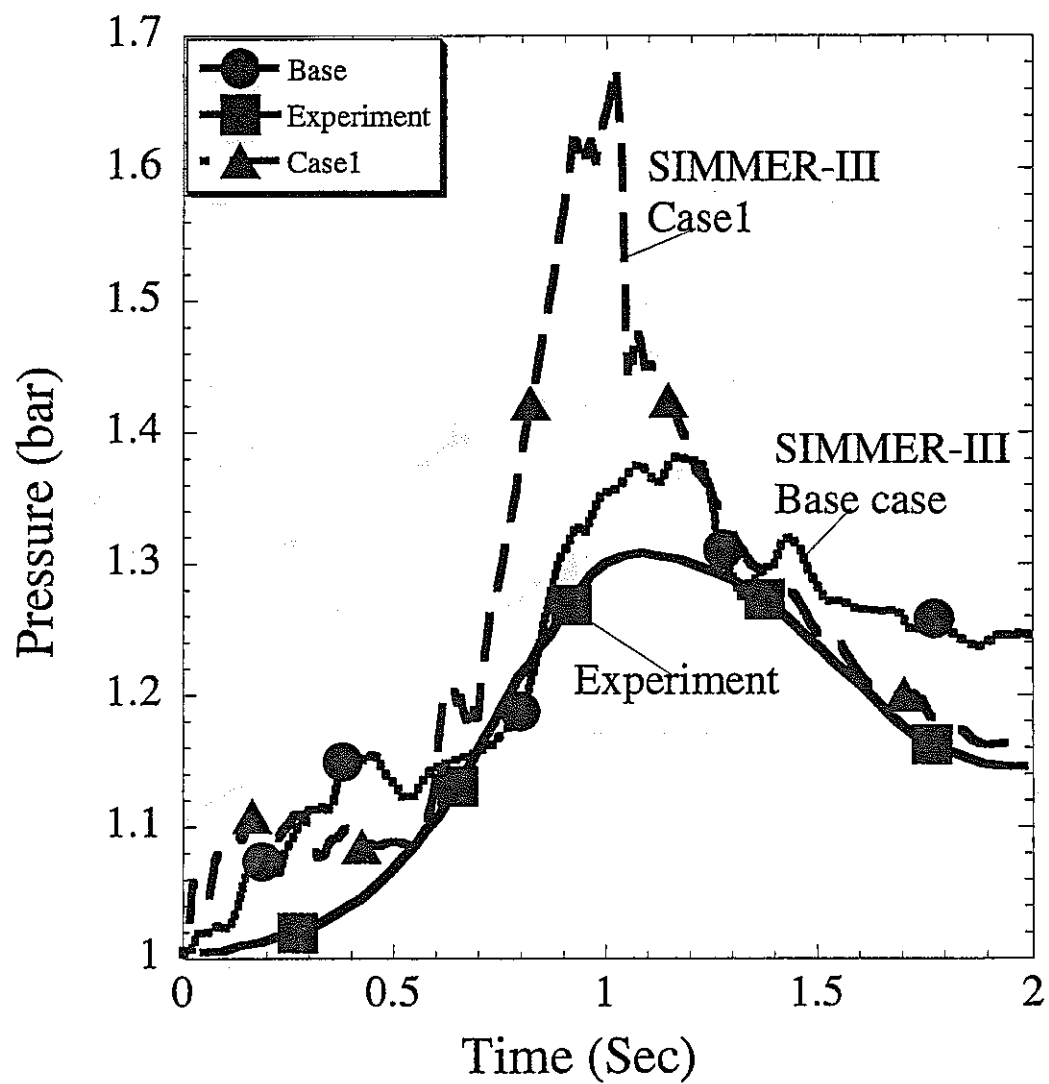


Fig. 4- 9 The pressure transient in the free gas space in the experiment and the simulation (case1) of MIXA-06.

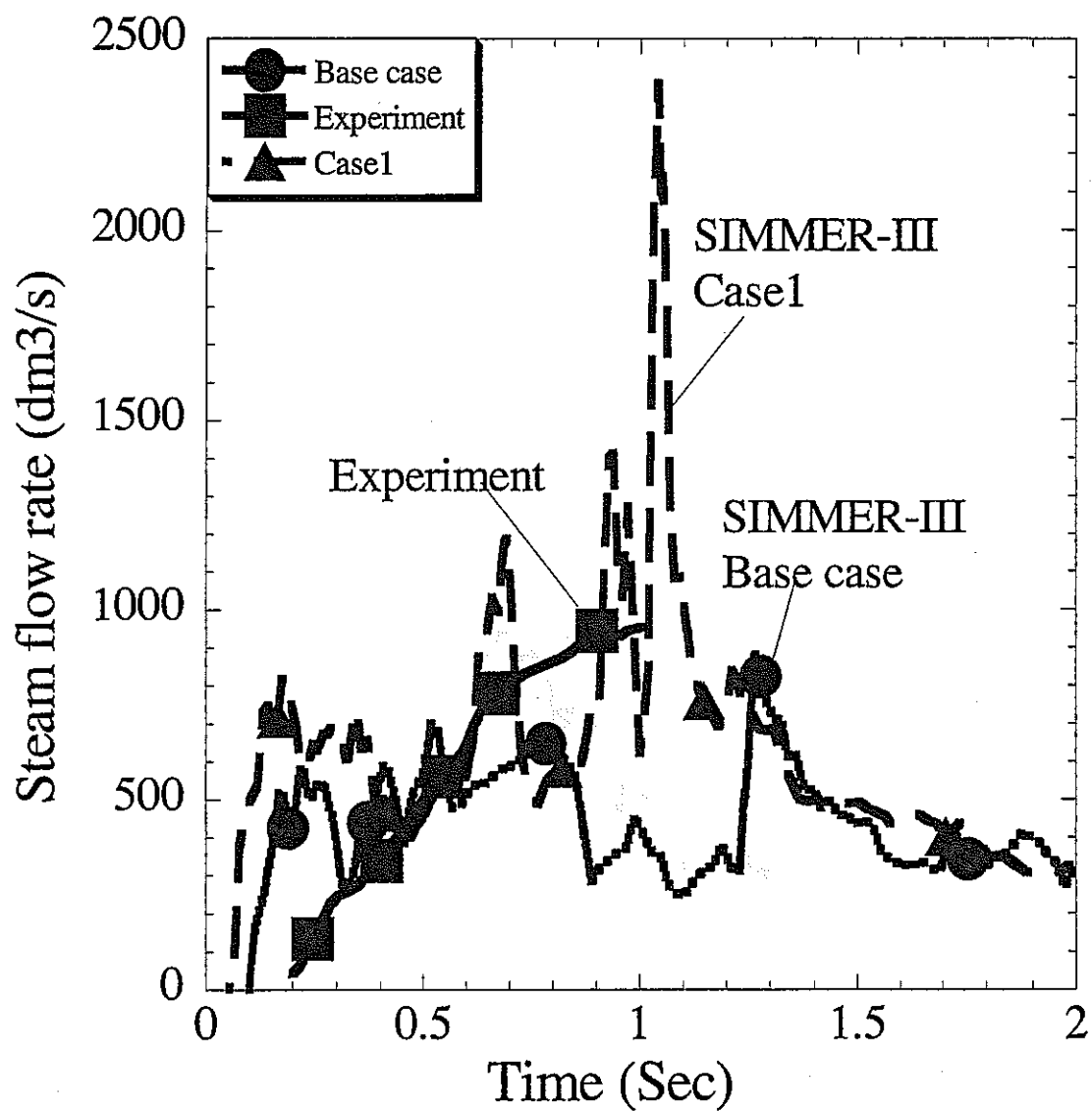


Fig. 4- 10 Steam flow rate in the experiment and the simulation (case1) of MIXA-06.

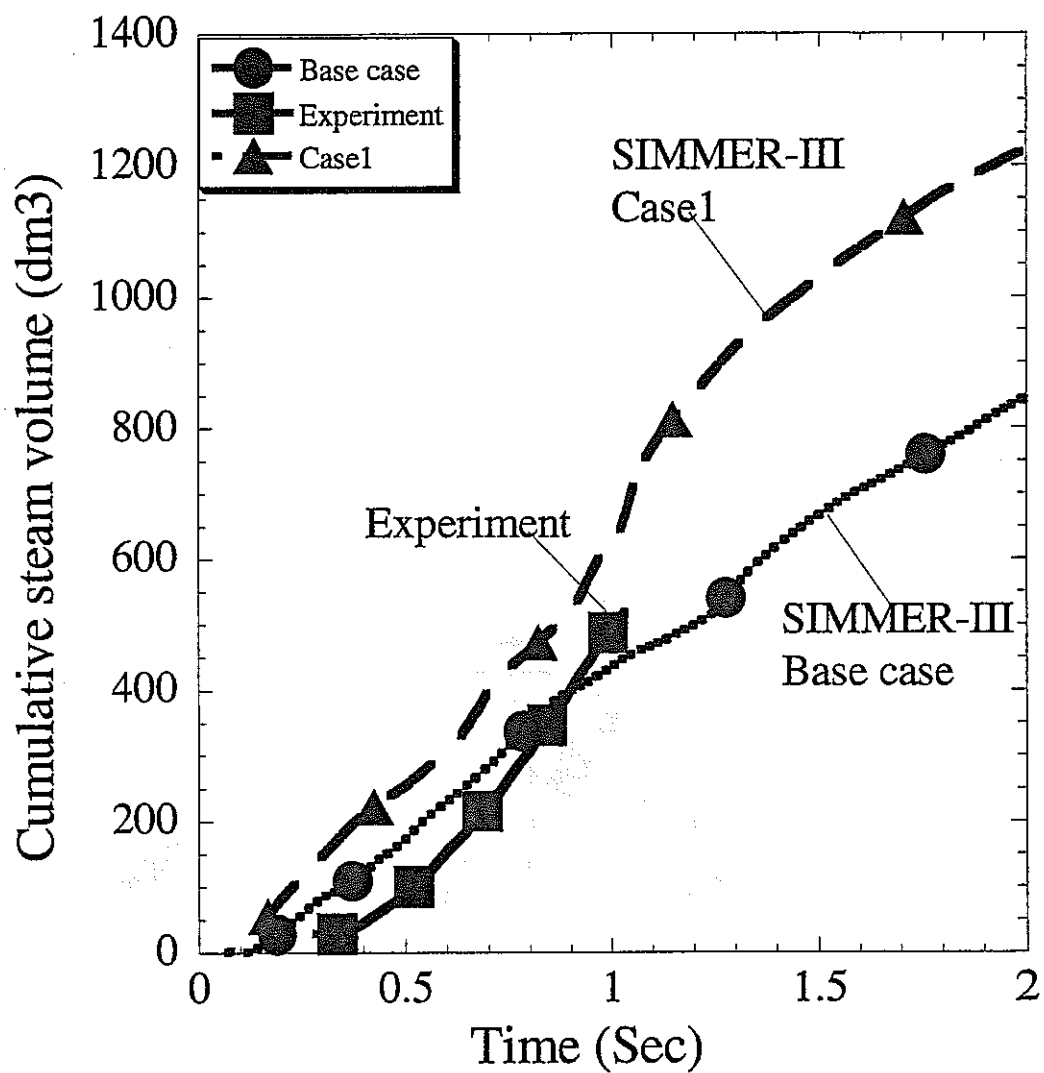


Fig. 4- 11 Cumulative steam volume in the experiment and the simulation (case1) of MIXA-06.

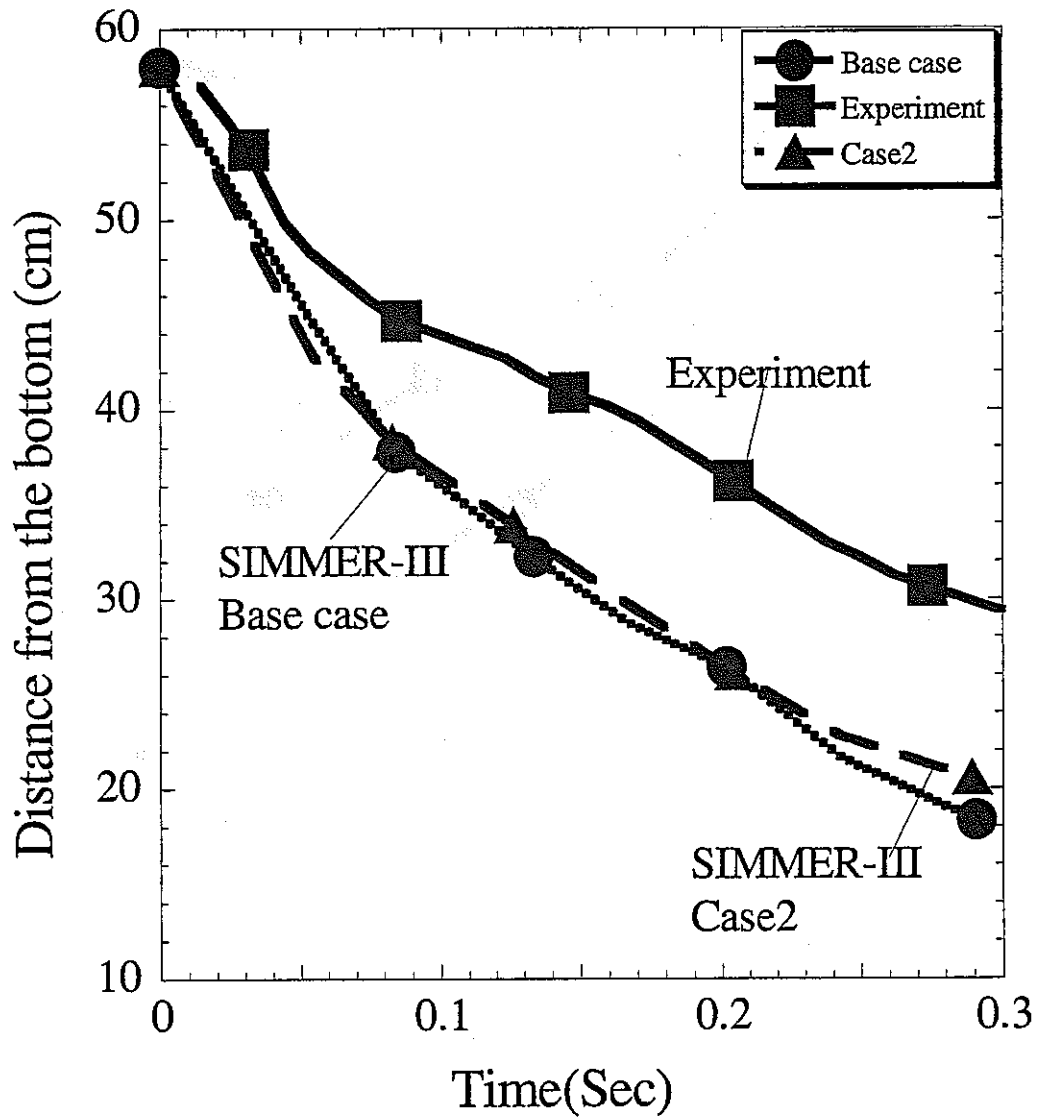


Fig. 4- 12 Front advancement of the droplet stream in the simulation of MIXA-06 with different fragment size in Taylor fragmentation model.

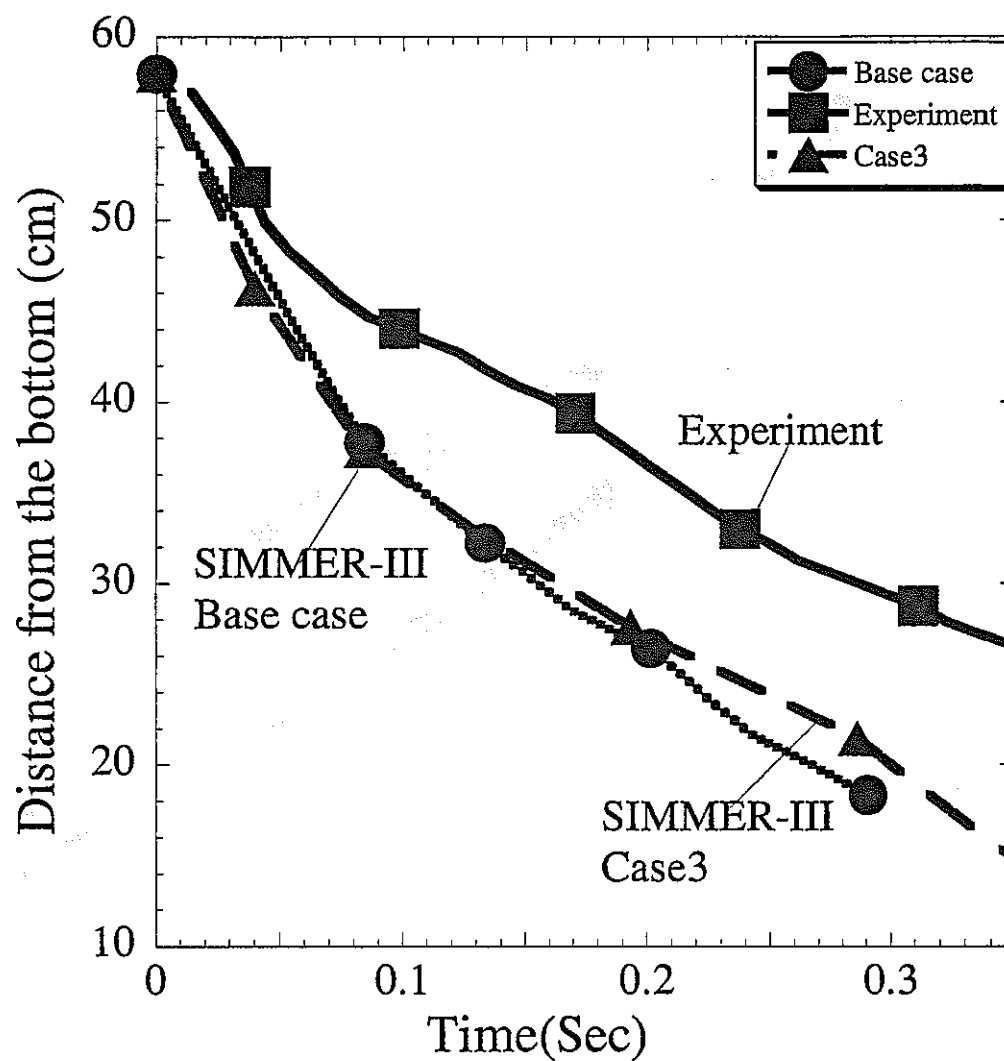


Fig. 4- 13 Front advancement of the droplet stream in the simulation of MIXA-06 with different fragmentation time interval in Taylor correlation.
Case3: fragmentation time is divided by 1000.

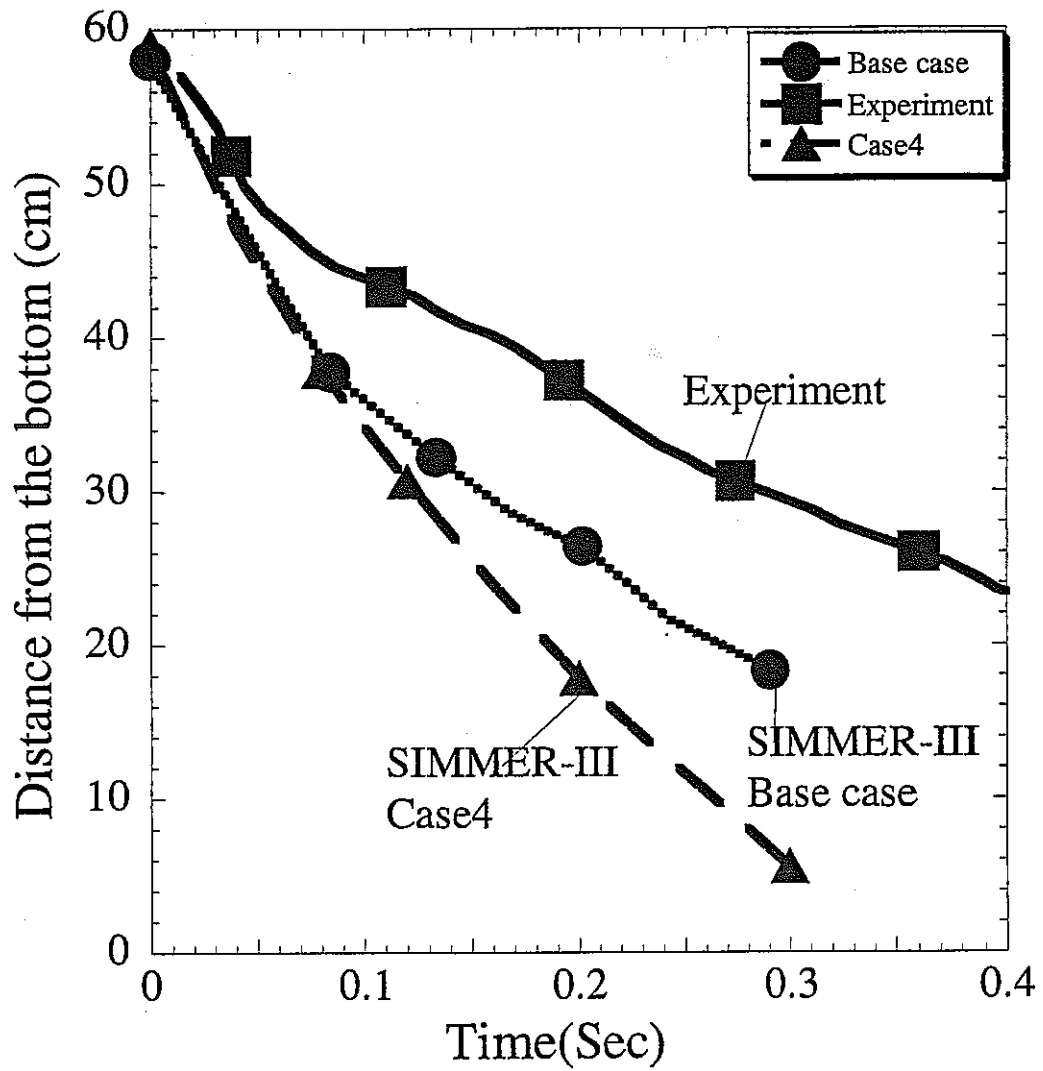


Fig. 4- 14 Front advancement of the droplet stream in the simulation of MIXA-06 with different fragmentation models (1). Base case: Taylor correlation. Case4: no fragmentation.

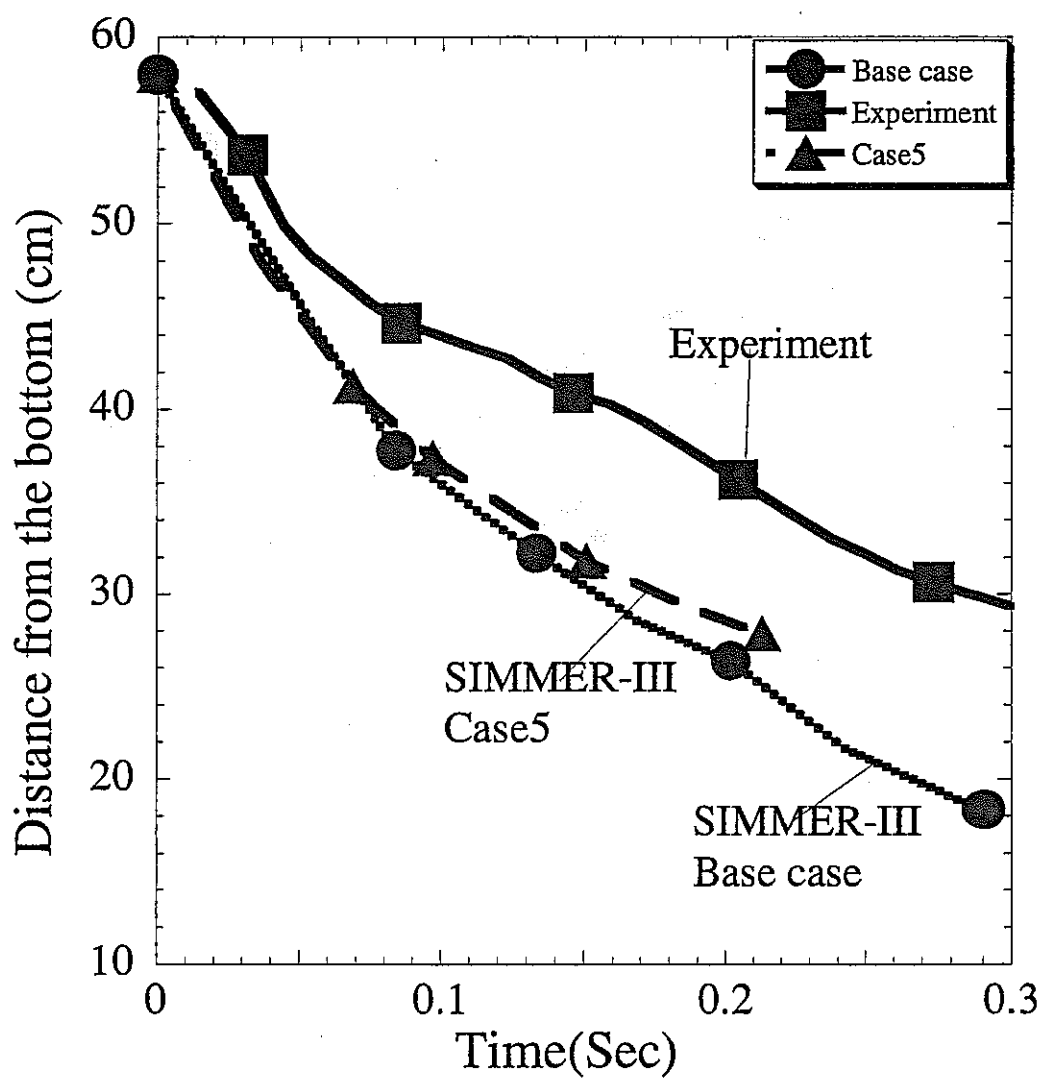


Fig. 4- 15 Front advancement of the droplet stream in the simulation of MIXA-06 with different fragmentation models (2). Base case: Taylor correlation. Case5: Pilch_Erdman correlation.

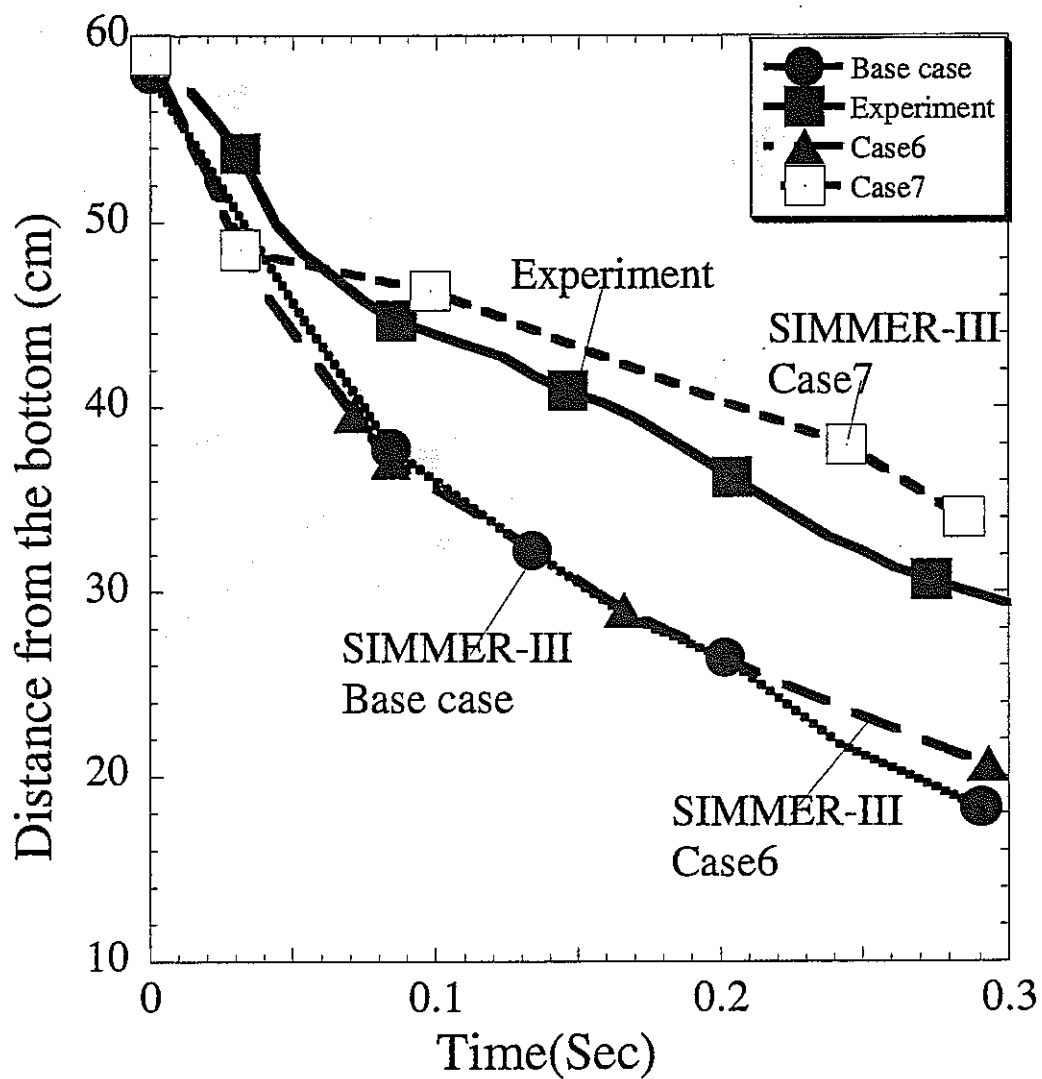


Fig. 4- 16 Front advancement of the droplet stream in the simulation MIXA-06 with different fragmentation rate. Base case: CFSB, CFSD=1.0, $We_{cr}=12$. Base6: CFSB, CFSD=1.0, $We_{cr}=0.12$. Case7: CFSB, CFSD=0.001, $We_{cr}=0.12$.

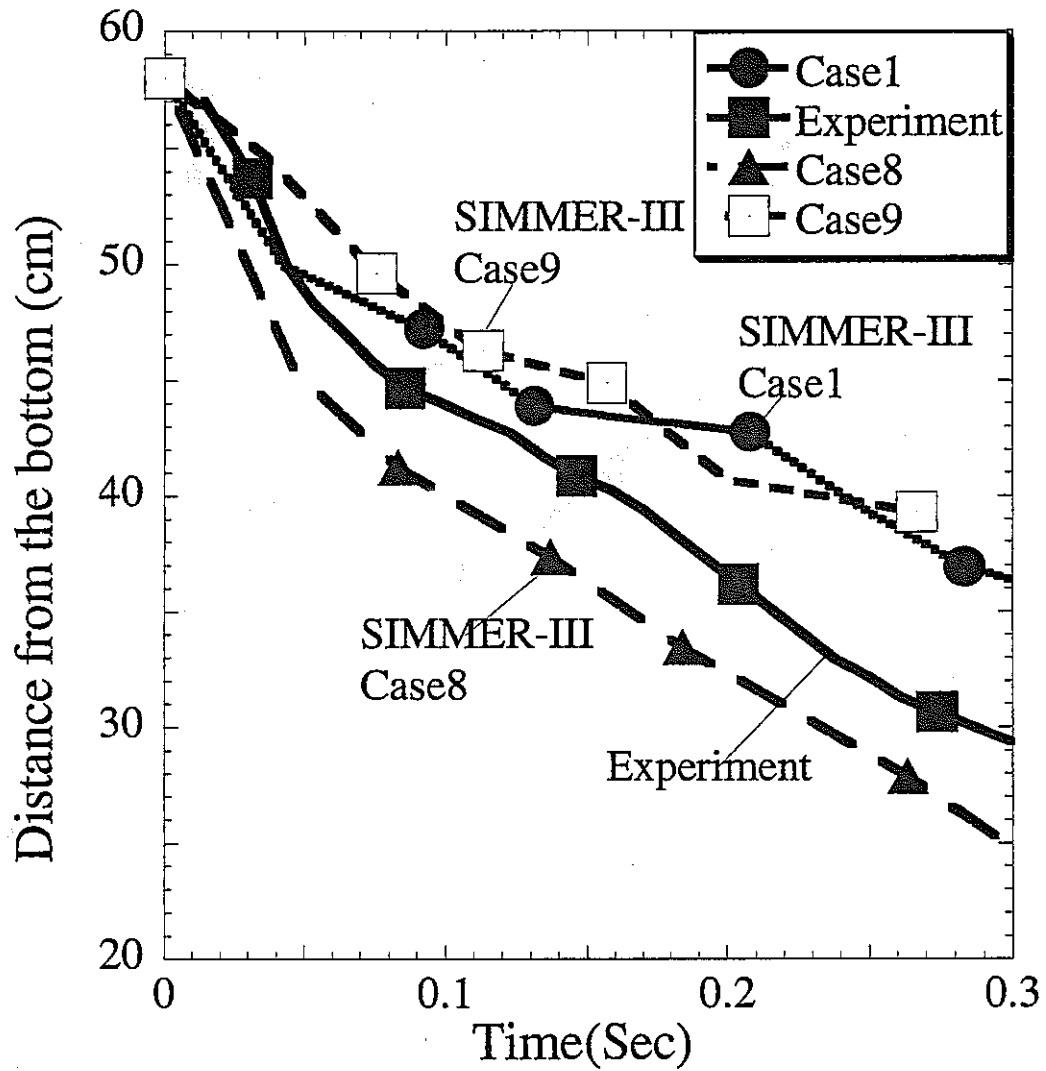


Fig. 4- 17 Front advancement in the simulation of MIXA-06 with different fragment size. Case1: the radius of fragmented droplets is set to 0.001. Case8: the radius of fragmented droplets is set to 0.0015. Case9: the radius of fragmented droplets is set to 0.0007.

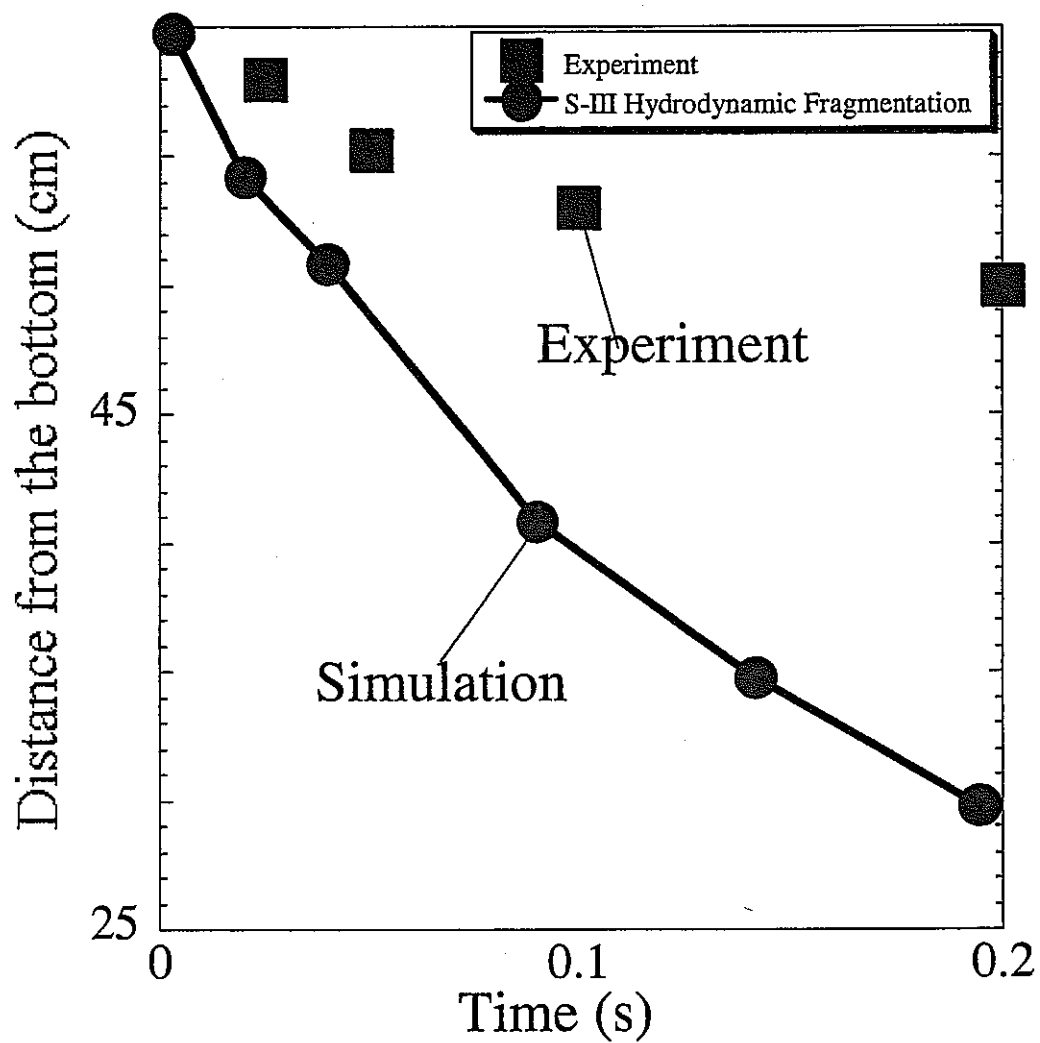


Fig. 4- 18 Front advancement of the droplet stream in water in the experiment and the simulation (base case) of MIXA-01.

5. Proposal of Thermal Fragmentation Models for Numerical Study of Fuel-Coolant Interaction

5.1 Introduction

The fragmentation model of melt droplets is essential to numerically study the FCI process. In the current multi-phase multi-component mathematical model, SIMMER-III, which was applied to simulate the propagation phase of a FCI experiment [1], only a hydrodynamic fragmentation model has been employed [2]. The code was also applied to simulate the premixing phase of another FCI experiment, the MIXA06 experiment [3], in which melt droplets (81% uranium dioxide and 19% molybdenum) with a diameter of 6 mm at a temperature of 3600K were released as a stream of the droplets into the water pool at a rate of 3 kg/s in 1 second. The simulated results showed that there was a certain difference between the simulated and experimental results on the front advancement of the droplet stream moving in coolant liquid. This was caused by underestimation of the droplet surface area. The analysis also suggests that the freezing-provoked droplet fragmentation mechanism may be the dominant fragmentation mechanism in this experiment. Since, in the case with low Weber number, the fragmentation of the droplet may not be triggered by hydrodynamic effect and may be triggered by thermal effect, including the boiling effect, film collapse induced by external pressure pulse or surface solidification, the fragmentation model based on a thermal mechanism is required to simulate the experiment properly.

The fragmentation model in SIMMER-III code [1,2] was verified by comparing the front advancement of the droplet stream moving in coolant liquid between the simulated and experimental results [3]. The front advancement in the simulated results is governed by the momentum equation, which can be written as

$$\begin{aligned} \frac{\partial(\bar{\rho}_q V_q)}{\partial t} + \sum_{m \in q} \nabla \cdot (\bar{\rho}_m V_q V_q) = & -\alpha_q \nabla \cdot p + \bar{\rho}_q g - K_{qs} V_q + \sum_q K_{qq} (V_q - V_q) + VM_q \\ & - \sum_q \Gamma_{qq} [H(\Gamma_{qq}) V_q + H(-\Gamma_{qq}) V_q] \end{aligned} \quad (5-1)$$

where the momentum exchange coefficient in the 4th term of the right hand side is

$$K_{qq} = A_{qq} + B_{qq} (V_q - V_q). \quad (5-2)$$

For the case of the melt droplets immersed in coolant liquid, the term $V_q - V_q$ is the relative velocity between the droplets and the coolant liquid, and the coefficients are written as

$$A_{qq} = \frac{3}{2} A_d \frac{\mu_c}{r_d} \quad (5-3)$$

and

$$B_{qq} = \frac{1}{8} A_d \rho_c C_D. \quad (5-4)$$

The interfacial area (A_d per unit volume) between the droplets and the coolant can be described by

$$\frac{\partial A_d}{\partial t} + \nabla \cdot (V A_d) = \sum_k S_d. \quad (5-5)$$

The source term (S_d) of the interfacial area of the droplets is modeled by

$$S_d = \frac{A_d^e - A_d}{\tau_d}, \quad (5-6)$$

where the equilibrium interfacial area A_d^e is calculated by the equilibrium radius r_d^e and the volume fraction α_d of the droplets:

$$A_d^e = \frac{3\alpha}{r_d^e}. \quad (5-7)$$

In current hydrodynamic model, the fragmentation time interval and interfacial area increase are related to the relative velocity between the droplets and the coolant. In this model the equilibrium radius is calculated as:

$$r_d^e = \frac{We_{cr} \sigma}{2\rho_c \Delta v^2}, \quad (5-8)$$

where Δv is the relative velocity difference between continuous and dispersed phases, σ is the surface tension, ρ_c is the continuous phase density and the critical Weber number We_{cr} is 12. The fragmentation time interval is calculated by

$$t_b^* = \frac{\Delta v \varepsilon^{0.5}}{2r_d} \tau_d, \quad (5-9)$$

where ε is the density ratio of the continuous dispersed phases and for liquid-liquid system t_b^* is given as

$$t_b^* = 13.7 Bo^{-0.25}, \quad (5-10)$$

where Bo is the Bond number, which is

$$Bo = \frac{3}{8} C_d \frac{\rho r_d \Delta v}{\sigma}. \quad (5-11)$$

Besides the SIMMER-III code, in other developing multi-phase multi-component simulation codes for studying FCI, for example, PM-ALPHA [4], CHYMES [5] and MC3D [6] codes, the correlation (hydrodynamic model) deduced by Young [7] for IFCI from the work of Pilch (1981) is employed, in which the melt droplets are fragmented by hydrodynamic forces related to relative motion in the coolant.

One fragmentation model considering thermal fragmentation mechanism is included in TEXAS code [8]. This model is developed by Kim [9], based on the mechanism that the vapor film collapse is triggered by external force (pressure pulse) and coolant jets impinge on the melt droplet surface.

$$\frac{dm_f}{dt} = C_f \rho_f \pi D_f^2 N_f [(P - P_\infty) / \rho_c]^{1/2} F(t_f). \quad (5-12)$$

As many studies showed, during the fuel coolant interaction process, the melt droplets may be broken up (or fragmented) by hydrodynamic mechanism, induced by relative motion, or by thermal mechanism, triggered by external pressure pulse, nucleate boiling or surface solidification. Currently the hydrodynamic model has been widely studied, but under some conditions of FCIs, especially in the premixing stage of FCIs, the thermal mechanism is dominant. Since the fragmentation model affects the mixing region in the premixing stage of FCIs, further affects the estimation of energy conversion, a fragmentation model based on thermal mechanism should be required to the simulation codes to study the molten material interaction with coolant. The thermal mechanism is related to the thermal condition of the melt droplets and the coolant, such as the properties and temperatures of melt droplets and coolant, as shown in Swift's

experiments [10]. Although many researches have been made on the thermal fragmentation mechanisms, a thermal fragmentation model based on the triggering event, such as nucleate boiling or surface solidification has not been proposed for simulation codes. Since the thermal fragmentation is triggered by different events, the fragmentation model should be developed based on different triggering events.

The objective of this study is to develop a fragmentation model induced by the thermal fragmentation mechanism, which can be employed in the numerical studies of FCIs. First the mechanism of the thermal fragmentation will be reviewed. Then a fragmentation model considering the thermal condition will be developed. Finally the proposed fragmentation model will be implemented into the SIMMER-III code and applied to simulate MIXA experiment again and KROTOS experiment to verify the proposed fragmentation models.

5.2 Thermal Fragmentation Mechanism

5.2.1 Review of Fragmentation Mechanism

The fragmentation mechanisms of melt droplets under different conditions have been studied for many years. Corradini [11] reviewed the mechanisms and models and categorized the fragmentation mechanisms into two classes; hydrodynamic and thermal effects. The hydrodynamic fragmentation occurs when the melt droplets are subjected to external surface forces sufficient to overcome the droplet surface tension. Several kinds of fragmentation mechanisms have been proposed for the hydrodynamic effects; Rayleigh-Taylor instability, Kelvin-Helmholtz instability and boundary layer stripping. The thermal fragmentation mechanisms include boiling effects, internal pressurization and surface solidification effects. In thermal mechanism, the internal forces break the droplet into parts (fragments). When the melt droplets are released into coolant, due to the evaporation of the coolant, a vapor film is formed to surround the droplet, as shown in Nelson's experiment [12]. The behavior of the vapor film is related to the temperatures

of the droplet and the coolant, ambient pressure and properties of the coolant and the droplet. During the interaction process, the triggering event for the fragmentation can be surface solidification, boiling effect or external pressure. In some cases several triggering events maybe induce the fragmentation at the same time, but for simplicity only one triggering event is considered at one time in this study.

When melt droplets are released into coolant, the triggering event (inducing the fragmentation) can be clarified by the boiling curve, as shown in Fig. 5-1. The thermal fragmentation mechanism of a melt droplet is related with the droplet's and coolant's temperature and properties. The triggering events are mapped out in Fig. 5-2 according to the thermal conditions. During the period of the stable film boiling, if an external triggering event is not applied to the system, the vapor film does not collapse itself. When the surface temperature of the droplet is reduced to the solidus temperature, if the solidus temperature is higher than the minimum film boiling temperature (MFBT) of the coolant, the solid surface shell is formed, as shown in the region I of Fig. 5-2. Several mechanisms are proposed for this kind of thermal fragmentation. One of them is solidification and fracture on the droplet surface. As the droplet cools in the coolant it solidifies. Such rapid quenching and solidification of the droplet may lead to the development of thermal stresses in the droplet. When the resultant thermal stress is greater than the yielding stress of the material, fissures may develop in the outer frozen shell, inducing the breakup of the molten droplet [13]. Cronenberg [14, 15] studied the fragmentation of Molten UO₂ upon contact with sodium coolant and concluded that the thermal stresses induced in the thin outer shell and the pressurization of the inner molten core are responsible for the fragmentation. Hsiao [16] and Witte [17] analyzed the heat-transfer process and calculate the thermal stress using elastic theory for the case of aluminum quenched in water and indicated that the tangential stress mainly induced by solidifying shell is the dominant factor in the rupture of the shell. But none of them gave the model of the fragmentation rate, which can be used in the simulation tools.

Brauer et al [18] made an experiment of one droplet fuel coolant interaction, in which the aluminum and lead droplets were released into water. The pictures of the droplet after the interactions are shown in Fig. 5-3 and 5-4. The figure 5-3 shows that the

molten aluminum appears to have been forced through a porous solid exterior shell. The figure 5-4 shows that lead formed a spongy mass, which shows the portion of the metal was violently ejected from the original droplet. Their explanation is that the molten metal droplet, upon contact with the quench liquid or shortly thereafter, forms a solid shell due to rapid heat transfer from the metal surface. Somehow, some of the quench liquid is trapped inside this shell. The trapped liquid is rapidly vaporized and produces a large internal pressure in trying to escape. The interior molten metal, due to this internal pressure, breaks through the weakest part of the metal shell and is dispersed. Since it is believed that when a droplet is released into coolant liquid, a vapor film is formed to surround the droplet, it is difficult to explain the water droplet trapped into the droplet. But the experimental results show the existence of the internal pressure.

When the surface temperature is reduced to the value under the MFBT, if the temperature is higher than its melting point, the boiling effect is dominant to the fragmentation of the droplet, as shown in the region II of Fig. 5-2. As the temperature of the droplet decreases to point D, shown in Fig. 5-1, the vapor film becomes unstable and collapses toward the surface of the droplet. In this transition region, coolant periodically contacts the droplet surface. The transition can be very violent and continue until the nucleate boiling regime is attained at point C. The liquid-liquid contact induces the high pressure in the vapor film and then induces the breakup of the droplet. Although many researchers have studied the boiling effect on fragmentation [11, 17], the fragmentation rate model has not been proposed.

When the temperature is very high and the film boiling is stable, the collapse of the vapor film also can be caused by strong triggering event (external force), which causes liquid-liquid contact and generates local high pressure and dominates the fragmentation of the droplet, in the region III of Fig. 5-2. Kim [9] proposed a mechanism for this kind of fragmentation that the collapse of the vapor film may cause the coolant jets entrapment into the droplet and evaporation of the coolant jets break the droplet into small parts. Based on this four-phase fragmentation mechanism, Kim [9] proposed a thermal fragmentation model, which was implemented in TEXAS code [8]. But this fragmentation model is only for the case that the external pressure is a triggering event

and the proposed mechanism contradicted with phenomena observed in Ciccarelli's experiments [19], the single drop experiment using flash X-ray radiography.

Several fragmentation mechanisms have been proposed based on the three triggering events. From the review of the fragmentation mechanisms, it can be found that a pressure generation is a common factor in all these mechanisms. The fragmentation model will be proposed based on the pressure generation, which will be discussed in detail in the following section.

5.2.2 Acceleration Mechanisms

5.2.2.1 External Pressure Pulse

When an external pressure pulse is applied to a droplet with a vapor film, the vapor film around the droplet will collapse and generate a pressure pulse inside the vapor film. The generated pressure pulse is thought to be exerted on the droplet surface and may induce the instability on the surface of the droplet, as described in [20, 21]. The generation of the pressure during the vapor film collapse is related to the duration and amplitude of the initial pressure pulse, the temperatures and the properties of the droplet and the coolant, and the ambient pressure. A detailed vapor film collapse model due to the external pressure pulse, described in Appendix D, is developed to study the vapor film collapse and the pressure generation in the vapor film.

5.2.2.2 Boiling Effect

When a droplet is immersed into coolant liquid, a vapor film is formed to surround the droplet. At the beginning of the immersion, because the temperature of the droplet is over the minimum film boiling temperature (MFBT), the vapor film is stable. When the surface temperature becomes lower than MFBT, the nucleate boiling heat transfer is featured at this stage. Due to the change of heat transfer from film boiling to nucleate boiling, the vapor film may be collapsed and a pressure pulse is generated at the vapor film. Like the above case, the generated pressure pulse is exerted on the droplet surface

and may induce the instability on the surface of the droplet. The generation of the pressure during the vapor film collapse is related to the heat transfer change, the temperatures and the properties of the droplet and the coolant, and the system pressure. A detailed vapor film collapse model due to heat transfer change, described in Appendix D, is developed to study the vapor film collapse and the pressure generation in the vapor film. In this model the heat transfer mode change is simulated by adding a heat transfer flux term in the boundary condition of energy.

5.2.2.3 Surface Solidification

When a droplet is exposed to a coolant liquid, solidification begins on its surface and a vapor film is formed around the droplet, which is stable. The hot molten material is encased in a thin shell. Due to the temperature distribution in the solid shell, the deformation induced in the solid shell tends to compress the inner liquid region. The pressurization on the interface between the solid shell and the inner molten liquid may be induced during the solidification process on the surface. A detailed surface solidification model, described in Appendix E, is developed to study the solidification process and the pressure generation in the droplet. Since, during the solidification process, the solid shell squeezes the liquid part inside the shell, if the solid shell is taken as a membrane with ductility and no thickness, it can be thought that the generated pressure pulse (by squeezing) is exerted on the surface of the liquid droplet. Then the initial perturbation on the surface of the droplet may be grown under the action of the generated pressure pulse. The grown molten metal spikes are broken by turbulent flow and mix with coolant liquid. This is thought to be the fragmentation mechanism of a droplet induced by the surface solidification in this study. Even if the fracture on the surface is considered, the instability analysis method still can be used to model the fragmentation. In the ejection mechanism, which is observed in experiments, the liquid metal inside the droplet is ejected from the fracture out of the droplet under the action of the pressure. If it is assumed that the ejection of the liquid melt can be considered as the spikes on the surface, although the fragmentation mechanism is different from the proposed one, the proposed instability method can be used to model the fragmentation. The detailed fragmentation

mechanism induced by the surface solidification is described in Appendix E.

In all the three cases, the pressure generation is clarified and exerts on the surface of the liquid droplet. The analysis shows that since the droplet surface is accelerated by the generated pressure-pulse, the Taylor instability can be induced. Therefore, in order to develop the thermal fragmentation model, in this study, the instability is proposed to be the mechanism of the thermal fragmentation triggered by all the three triggering events, including external triggering (film collapse) and self-triggering fragmentation (solidification and film collapse). Due to the instability, the spikes grow quickly from the surface of the droplet. Then the spikes are broken into fragments due to the turbulent flow of the coolant vapor and liquid around the droplet. A detailed instability analysis model is developed and appended in Appendix C. In the next section, the thermal fragmentation model will be developed based on this proposed mechanism.

5.3 Development of Thermal Fragmentation Models

5.3.1 Growth Rate of the Spikes on the Surface of a Melt Droplet

Considering a configuration that a spherical droplet (liquid) with density of ρ and a radius of R is immersed into coolant, according to the Taylor instability analysis (the detailed instability analysis is described in Appendix C), the amplitude of the perturbations (spikes) on the surface of a droplet under the action of an acceleration can be written as

$$a = a_0 e^{kt} \quad (5-13)$$

where a is the amplitude of the perturbations (spikes), a_0 is the amplitude of the initial perturbations and the k is the growth index of the perturbations (spikes). Here the fastest growth mode is considered as the growth rate of the perturbations, then one can obtain

$$k_m = \sqrt{-(n_m + 2) \frac{\ddot{R}}{R} - (n_m - 1)(n_m + 2) n_m \frac{\sigma_f}{R^3 \rho}} \quad (5-14)$$

and

$$n_m = \frac{1}{3} \sqrt{1 - 3 \left(\frac{\ddot{R} R^2 \rho}{\sigma_i} - 2 \right)} \quad (5-15)$$

where \ddot{R} is the acceleration exerted on the droplet surface, for the three triggering events mentioned in previous section, it is negative (described in Appendices D and E) and n_m is the wave number on the surface, at which the perturbations growth is the fastest.

The growth rate of the perturbations (spikes) on the surface of the droplet can be written as

$$\frac{dm}{dt} = \rho n_m s v \quad (5-16)$$

where s is the area of the cross section of the spikes and v is the growth velocity of the spikes,

$$v = \frac{da}{dt} \quad (5-17)$$

5.3.2 Fragmentation Rate of a Melt Droplet

If it is assumed that the spikes on the surface of the droplet are all broken into the fragments, then one can write the fragmentation rate as

$$\frac{dm}{dt} = 2 \rho \pi R^2 a_0 k_m e^{k_m t} \quad (5-18)$$

If it is further assumed that the amplitude of the initial perturbations is the $\beta\%$ of the radius of the droplet, the normalized fragmentation rate can be written as

$$\frac{1}{m_0} \frac{dm}{dt} = 0.015 \beta K_m e^{K_m t} \quad (5-19)$$

Since the acceleration exerted on the droplet, triggered by surface solidification, external pressure pulse and boiling effect, can be obtained, the fragmentation rate can be written as the unified and normalized formulation,

$$\frac{1}{m_0} \frac{dm}{dt} = C_A C_B e^{C_B t} \quad (5-20)$$

where C_A is constant and C_B is the parameter related to the droplet condition and the

acceleration exerted on the droplet surface. For the cases that the fragmentation is triggered by surface solidification, external pressure pulse or boiling effect, respectively, the acceleration is calculated in Appendices D and E. The fragmented mass can be written as

$$m_{frag} = \int_0^t \frac{1}{m_0} \frac{dm}{dt} dt \quad (5-21)$$

Since in this study the spikes on the surface is considered as the fragments, the diameter of the cross section of the spikes due to the instability is considered as the size of the fragments, which can be written as

$$d_{frag} = \frac{d}{\left(\frac{\Delta P d}{2\sigma_t} \right)^{0.25}} \quad (5-22)$$

where d_{frag} is the fragment size, d is the diameter of the original droplet, σ_t is the surface tension of the droplet including the effect of shell stiffness in the case of solidification and ΔP is pressure exerted on the droplet surface.

5.3.3 Proposal of Thermal Fragmentation Models

5.3.3.1 Thermal Fragmentation Model Induced by Surface Solidification

The fragmentation triggered by the surface solidification, is calculated by using the model developed above as an example. The initial conditions of the calculation system are based on the conditions of MIXA06's experiment [22], in which the melt droplets with a radius of 3 mm and a melting temperature of 3120 K were released into water with a temperature of 370 K. The relative velocity between the droplets and water is about 5 m/s, estimated from the experiment. Since the melting point of UO₂ is larger than the MFBT (Minimum Film Boiling Temperature) of the water, the fragmentation of the droplet will be provoked by surface solidification. Because the pressure generation is

related to the temperature distribution in the droplet, coolant temperature and properties of the materials involved, a heat conduction model, described in Appendix E, is constructed to calculate the pressure exerted on the liquid part of the droplet. This model is based on the assumption that the solidified shell acts in an elastic manner, like a membrane with elasticity on the droplet surface.

The calculated thickness of the solid shell, total surface tension and pressure on the interface are plotted in Figs. 5-5 to 5-7. Due to the fast contact between the droplet and coolant, the generated pressure is very large and the instability index $G(t)$ is positive, shown in Fig. 5-8, which means that the instability on the surface of the droplet can be induced by the solidification. The fragmented mass from the droplet calculated by equation (5-21) is shown in Fig. 5-9. The parameter C_B in Eq. (5-20) in this case, as shown in Fig. 5-10, is calculated by the model of surface solidification according to the physical configuration of the system. It is shown that the fragmentation rate predicted by the proposed thermal model is much larger than that given by hydrodynamic model.

The equation (5-20) is difficult to be introduced in simulation tools. For the case that the fragmentation is induced by the solidification on the droplet surface, as investigated in Appendix E, the pressure generation is related to Young's module, radius of the droplet, fusion temperature, thermal expansion and heat transfer coefficient, and the fragmentation time is inversely proportional to the pressure generation. By using the developed models as the numerical experiment, the average fragmentation rate, Γ_{ss} (1/sec), triggered by surface solidification, can be fitted as the following formulation,

$$\Gamma_{ss} = 2.1 \times 10^{-2} Bi^{0.1} \left(\frac{\alpha_t (T_{mp} - T_c) E}{R^2 \rho_m} \right)^{0.5} \quad (5-23)$$

where Bi is Biot number (hR/k), k is thermal conductivity, h is unit surface thermal conductance, T_{mp} is the fusion temperature of the droplet, T_c is the temperature of the coolant, α_t is the coefficient of thermal expansion, E is Young's modulus, R is the radius of the droplet and ρ_m is the density of the droplet. This correlation is fitted within the range of Bi , from 100 to 10000, $T_{mp} - T_c$, from 1000 to 3000 K, and R , from 0.001 to 0.01 m. Since the triggering time is very short comparing with the fragmentation time, the time delay (fragmentation starts after the triggering condition is reached) can be

neglected. The proposed fragmentation rate increases with the increase of the pressure generation, which is proportional to Bi number, fusion temperature, thermal expansion and Young's module, which agrees with the investigation in Appendix E. The triggering condition is that the surface temperature reaches the solidus temperature.

In order to estimate the fragments' size by Eq. (5-22), the average pressure inside the droplet and the thickness of the solid shell are required. They can be fitted as the following formulations,

$$\Delta P = 1.54 \times 10^{-2} Bi^{0.12} \alpha_i E (T_m - T_c) \quad (5-24)$$

and

$$\delta = \frac{k_m (T_m - T_c)}{LR \rho_m} \frac{1}{\Gamma_{ss}} \quad (5-25)$$

respectively, where L is the latent heat of fusion and δ is the thickness of the solid shell. The total surface tension of the droplet including the term of shell stiffness is calculated by (described in Appendix E)

$$\sigma_t = \sigma + \frac{D_s}{2R^2} \quad (5-26)$$

5.3.3.2 Thermal Fragmentation Model Induced by External Pressure Pulse

An example, in which the fragmentation is triggered by the external pressure pulse, is calculated by using the proposed model. The initial conditions are based on the conditions of Nelson's experiments, in which the amplitude of the pressure pulse 0.7 MPa is assumed to apply on the droplet with a radius of 2 mm. Since the pressure in the vapor film during the film collapse is related to the droplet temperature, ambient pressure, coolant temperature and properties of the materials involved, a vapor film collapse model, described in Appendix D, is constructed to solve the pressure generation in the vapor film during the collapse. In this model, the dynamic film boiling process is modeled by writing a momentum equation for film dynamics, an energy equation for each region of the droplet, coolant vapor and liquid and linking each region by the appropriate boundary

conditions. The integral approach is used in each region for the energy equations where the differential equation is integrated over the region and a temperature profile is assumed. The Runge-Kutta-Gill method is employed to solve the nonlinear differential equations.

By using these developed models, the fragmented mass of the droplet triggered by external pressure, can be calculated by Eq. (5-20), which is plotted in Fig. 5-11. Since the relative velocity of the melt droplet to coolant is estimated from the experiment as about 4 m/s, the calculated results shows that hydrodynamic fragmentation rate is much less than that given by the proposed thermal fragmentation model. The pressure generation in the vapor film is plotted in Fig. 5-12, showing that the fragmentation process is finished in several bubble collapse and growth processes. The parameter C_b in Eq. (5-20), in the case that the fragmentation is triggered by external pressure pulse, is calculated by this model according to the physical configuration of the system, as plotted in Fig. 5-13, showing that it is a function of pressure in the vapor film.

As investigated in Appendix D, the acceleration exerted on the droplet surface is related to the amplitude of the external pressure pulse, ambient pressure, the temperature of the droplet and coolant, and radius of the droplet, and the fragmentation time is inversely proportional to the acceleration. To use the developed formula Eq. (5-20) as a tool for numerical experiments, the averaged fragmentation rate, Γ_{pp} (1/sec), of a melt droplet triggered by external pressure pulse, is fitted as the following formula, described by thermal parameters,

$$\Gamma_{pp} = 1.66 \times 10^1 Th^{0.22} \left(\frac{\Delta P_p}{R^2 \rho_c} \right)^{0.5} \quad (5-27)$$

where Γ_{pp} is the fragmentation rate, defined as normalized fragmented mass of a droplet

(fragmented mass is divided by initial droplet's mass) per second, $Th = \left(\frac{k_m k_c \Delta T_{mc}^2}{h_{fg}^2 R^2 \rho_c P_a} \right)$,

which is a dimensionless number to describe the thermal conditions of the system (including melt droplet and coolant), $\Delta T_{mc} = T_m - T_c$ is the temperature difference between droplet and coolant, k_c is the heat conductivity of coolant liquid, k_m is the heat

conductivity of melt droplet, P_a is the ambient pressure, ΔP_p is the amplitude of the external pressure pulse (Pa), h_{fg} is the latent heat, R is the radius of the droplet and ρ_c is the density of coolant liquid. This correlation is fitted within the range of: ΔP_p , from 5 to 30 bar; T_m , from 1000 to 3500 K; R , from 0.001 to 0.01 m; P_a , from 1 to 10 bar; and ΔT_c , from 10 to 80 K. In the fitness of this correlation, it is assumed that the external pressure pulse is exerted on droplet in the whole fragmentation process. When the external pressure is over 30 bar, the pressure in the vapor film is over 220 bar (the critical pressure), which can not be calculated by the EOS employed in this study. Although this correlation is fitted with the pressure limitation, it can be applied to the cases out of this range, because the generated pressure is proportional to the input pressure. Due to the very short triggering time, comparing with the fragmentation time, the time delay after the external pressure arrive the droplet can be neglected. The proposed fragmentation rate decreases with the increase of the droplet temperature and the ambient pressure, which is in agreement with the investigation in Appendix D.

The averaged fragments' size can be also estimated by Eq. (5-22) with an averaged pressure buildup in vapor film during vapor film collapse. By using the vapor film collapse model, developed in Appendix C, as a tool for numerical experiments, the averaged pressure buildup due to external pressure pulse is fitted as follows,

$$\Delta P = 1.9 \times 10^2 Th^{0.15} \Delta P_p \quad (5-28)$$

where the meaning of the parameters in the correlation is the same as above.

5.3.3.3 Fragmentation Model Induced by Boiling Effect

For the case that the fragmentation is triggered by the boiling effect, an example is calculated by using the proposed model. The initial condition is that a melt droplet with a radius of 1 cm and a melting temperature of 400K is immersed into water with a temperature of 300 K. Since the melting point is less than MFBT of water, as shown in Fig. 5-1, the boiling effect dominates the fragmentation of the droplet. When the melting point is less than the MFBT, in order to estimate the pressure generation in the vapor

film due to the change of the heat transfer mode from film boiling to nucleate boiling, it is assumed that the heat fluxes at the MFBT and at nucleate boiling are $2 \times 10^5 \frac{W}{m^2}$ and $10^6 \frac{W}{m^2}$ respectively (shown in Fig. 5-1).

By using the developed film collapse model, described in Appendix D, the fragmented mass induced by the boiling effect is calculated by equation (5-21), as shown in Fig. 5-14. After the relative velocity of the melt droplet to coolant is assumed to be 5 m/s, usual velocity in the single droplet experiment, the calculated results show that the thermal fragmentation model given by the proposed model is much larger than that given by hydrodynamic model. The results show that the process of the fragmentation of the droplet is finished in several bubble growth and collapse circle, which is determined by the pressure in the vapor film, as shown in Fig. 5-15. The parameter C_B in Eq. (5-20), in the case that the fragmentation is triggered by boiling effect, is calculated by this model according to the physical configuration of the system, as plotted in Fig. 5-16, showing that it is a function of pressure in the vapor film.

For the case that the fragmentation is triggered by the boiling effect, since the pressure pulse in the vapor film is related to the evaporation rate difference between the stable vapor film boiling (MFBT) and nucleate boiling, which is related to the difference of the heat transfer to the interface of the vapor/coolant liquid, the temperature of droplet and coolant, radius of the droplet, and the properties of the materials involved. To use the developed formula Eq. (5-20) as a tool for numerical experiments, the averaged fragmentation rate, Γ_{BE} (1/sec), of a melt droplet triggered by boiling effect, is fitted as the following formula, described by thermal parameters,

$$\Gamma_{BE} = 5.6 \times 10^1 Th^{-0.25} \left(\frac{q}{Rh_{fb} \rho_c} \right) \quad (5-29)$$

where Γ_{BE} is the fragmentation rate, defined as normalized fragmented mass of a droplet (fragmented mass is divided by initial droplet's mass) per second, Th is a dimensionless number as defined above and q is the heat transfer flux change due to the mode change from film boiling to nucleate boiling. This correlation is fitted within the range of: q ,

from 5×10^5 to 1×10^6 w/m^2 ; T_m , from 400 to 800 K; R , from 0.001 to 0.01 m; P_a , from 1 to 10 bar; and ΔT_c , from 10 to 80 K. The time delay term is not considered in this correlation due to the very short triggering time. The proposed fragmentation rate increases with the increase of the ambient pressure, but it does not mean that high ambient pressure induces high probability of the occurrence of the fragmentation, which conflict with the fact observed in experiments. Since the probability of the occurrence of the triggering event is not studied, in the fitness of the proposed correlation, the triggering condition is assumed that the surface temperature of the droplet is reached to the MFBT of coolant. Then the unstable heat transfer mode causes the high pressure pulse in the vapor film. When the ambient pressure is increased, the vapor film becomes more stable, which reduces the probability of triggering, which will be considered in the simulation tool.

The averaged fragments' size can be also estimated by Eq. (5-22) with an averaged pressure buildup in vapor film during vapor film collapse. By using the vapor film collapse model, developed in Appendix C, as a tool for numerical experiments, the averaged pressure buildup due to boiling effect is fitted as follows,

$$\Delta P = 3.7 \times 10^3 T h^{-0.61} \left(\frac{q}{h_{fg} \rho_c} \right)^2 \rho_c \quad (5-30)$$

where the meaning of the parameters in the correlation is the same as above.

5.4 Verification of the Proposed Thermal Fragmentation Models

In order to introduce the proposed thermal fragmentation models into SIMMER-III, the source term for the interfacial area of the droplets in Eq. (5-5) can be modeled by

$$S_d = \Gamma_i (A_d' - A_d) \quad (5-31)$$

where Γ_i is the fragmentation rate, given by Eqs. (5-23), (5-27) and (5-29) for the

triggering events of surface solidification, external pressure pulse and boiling effect, respectively, A_d' is the surface area of the fragmented droplet A_{fraged} and fragments A_{frag} , which can be calculated by fragments' size and fragmentation rate,

$$A_d' = A_{fraged} + A_{frag} \quad (5-32)$$

and A_d is the surface area of the original droplets. Then the proposed thermal fragmentation models triggered by surface solidification, external pressure pulse and boiling effect can be used in the simulation tool and will be verified by the simulation of selected experiments, respectively.

5.4.1 Thermal Fragmentation Model Induced by Surface Solidification

Due to the lack of the experimental data (fragmentation process triggered by surface solidification), the proposed fragmentation model (Eq. (5-23)) can not be directly verified by the fragmentation process. The sizes of debris in MIXA06 [22], PNC (Mizuta) [25] and Armstrong's [14] experiments are selected to verify the proposed model. The predictions of fragment sizes by Eq. (5-22), plotted in Fig. 5-17, are compared with the experimental data collected after these experiments, indirectly verifying the proposed thermal model.

The proposed thermal model (Eq. (5-23), triggered by surface solidification, is introduced into the SIMMER-III code and applied to simulate the experiment of MIXA Nos. 01 and 06 to verify the proposed thermal fragmentation model. Due to the high solidus temperature of the droplet (3120K, the initial temperature of the droplet is 3600K) and the initial liquid-liquid contact, the triggering event can be the surface solidification. The simulation is carried out by using Eq. (5-31) as the fragmentation model. The front advancement of the stream of the melt droplets in water, plotted in Figs. 5-18 and 5-19, is used to verify the proposed fragmentation model. The results show that in the low Weber number case the proposed thermal fragmentation model much improves the prediction of the front advancement of the stream of the melt droplets in water comparing with hydrodynamic fragmentation model.

5.4.2 Thermal Fragmentation Model Induced by External Pressure Pulse

Due to the same reason as described in the previous section, the proposed fragmentation model (Eq. (5-27)), triggered by external pressure pulse, is indirectly verified by the comparison of the fragment size. The sizes of debris in KROTOS-28 [23], Nelson's [12] and SIGMA-2000 [26] experiments are selected to verify this model. The predictions of fragment sizes by Eq. (5-22) and their experimental data collected after these experiments are plotted in Fig. 5-20 for these three experiments, indirectly verifying the proposed thermal model.

The proposed thermal model (Eq. (5-27)), triggered by external pressure pulse, is also introduced into the SIMMER-III code and applied to simulate the experiment of KROTOS Nos. 28 and 44, performed at JRC Ispra [23]. The objective of the experiment is to investigate the propagation phase of a steam explosion in an alumina melt/water mixture, triggered by pressured gas. This experiment already has been simulated by SIMMER-III code with hydrodynamic fragmentation model [2]. It is simulated again in this study to verify the proposed thermal fragmentation model. As shown in Fig. 5-21, the mixture is established by releasing 1.45 kg of melt at 2673 K into a vertical tube initially filled with 7.2 kg of water at 360 K. The test tube is modeled by a one-dimensional geometry, filled with the mixture of molten alumina droplet, water and vapor with volume fractions of 0.08, 0.88 and 0.04, respectively. The calculation starts from the triggering of the explosion in the pre-mixture using a release of argon gas pressurized to 8.5 and 15 MPa from the bottom of the tube, respectively. The simulation is carried out by using Eq. (5-31) as the fragmentation model. The advancements of the shock wave in the test tube in both experiments are plotted in Figs. 5-22 and 5-23. The results show that in the large Weber number case the proposed thermal fragmentation model can also predict the front advancement of the shock wave in the test tube like the hydrodynamic fragmentation model used in ref. [2].

5.4.3 Thermal Fragmentation Model Induced by Boiling Effect

The size of debris in the experiment of ref [27] is selected to verify the proposed fragmentation model (Eq. (5-29)), triggered by boiling effect. The prediction of fragment sizes by Eq. (5-22) is 0.54 mm, which is near to the experimental data of 0.1 to 0.5 mm estimated from the photos of the debris, indirectly verifying the proposed thermal model.

Although the proposed fragmentation model (Eq. (5-29)), triggered by boiling effect, is introduced into SIMMER-III, due to lack of the multi-droplet experiment, in which the fragmentation is triggered by the boiling effect, the proposed thermal fragmentation model is not verified by the simulation of multi-droplet experiment. And, under the condition of the reactor cases, the thermal fragmentation triggered by the boiling effect may not be the dominant fragmentation mechanism.

5.4 Conclusions

The thermal fragmentation mechanisms have been studied for many years, but the fragmentation models based on the thermal fragmentation mechanisms, triggered by boiling effect and surface solidification effect, are not available for numerical simulation tools. In this study, based on the understanding of the thermal fragmentation mechanisms, in which a pressure pulse is generated and exerted on the melt droplet, for developing the fragmentation model, Taylor instability is proposed to be the mechanisms for thermal fragmentation of the droplet triggered by external pressure pulse, boiling effect and surface solidification effect. The vapor film collapse model and the surface solidification model are developed to estimate the generated pressure. It is assumed that the spikes growing from the droplet surface are broken by the coolant flow around the droplet and are considered to be the fragmented part of the droplet. The fastest growth mode of the instability and the diameter of the spikes are considered to be the fragmentation rate and fragment size, respectively. A unified and normalized thermal fragmentation model is proposed for all the three triggering events. The proposed model is indirectly verified by

comparing the prediction of the fragment size with the experimental data collected after these experiments.

For the convenient application of the model to the simulation tools, simplified correlations of the thermal fragmentation model are proposed for each triggering event, based on the fragmentation mechanism.

The proposed thermal fragmentation correlations are introduced into the SIMMER-III code. The experiments of MIXA 01 and 06 and the KROTOS 28 and 44 are simulated to verify the proposed thermal models for the cases with low and large Weber number, respectively.

For the case that the fragmentation is provoked by surface solidification, the proposed fragmentation mechanism is that when a melt droplet contacts with coolant, due to the rapid heat transfer, the solid shell on the surface of a droplet is formed, it contracts, squeezes the liquid part into the shell and generates high pressure on the interface between the liquid and solid parts. The generated pressure causes the instability of the interface, which induces the growth of the spikes. In this model the solid shell is taken as a membrane with ductility. The stiffness of the shell is considered in the instability analysis by using a total surface tension concept.

The influence of the fracture on the surface is not considered in this model. Even if the fracture on the surface is considered, the proposed instability model can also be used to model the fragmentation by assuming that the velocity of the ejected liquid metal from the inside of the droplet and the fracture area on the surface are equivalent to the velocity and cross section of the spikes, respectively.

The thermal fragmentation mechanisms are related to the triggering events. Under experimental or reactor conditions, the triggering event is determined by the thermal conditions and other mechanical conditions in the system. Those conditions are not all considered in this study, in which the instability is proposed to be the thermal fragmentation mechanism. In the future the more triggering events should be studied. The proposed thermal fragmentation models should be verified by simulating more experiments with different thermal conditions.

References

- (1) K.Morita, Sa.Kondo, Y.Tobita and D.J.Brear, SIMMER-III Application to Fuel-Coolant Interactions, Proceedings of the OECD/CSNI Specialists Meeting on Fuel- Coolant Interactions May 19-21, 1997, Tokai-mura, Japan.
- (2) Sa. Kondo, D.J.Brear, Y.Tobita, K.Morita, W.Maschek, P.Coste and D.Wilhelm, Status and Achievement of Assessment Program for SIMMER-III, a Multiphase, Multicomponent Code for LMFR Safety Analysis, Proceedings of Eighth International Topical Meeting on Nuclear Reactor Thermal-Hydraulics, Vol. 3, Kyoto, Japan, Sept. 30-Oct. 4 1997.
- (3) X. Cao and Y. Tobita, Simulation of the MIXA-06 Experiment by SIMMER-III, JNC report, JNC TN9401 2001-122.
- (4) T.Theofanous, W.Yuen and S.Angelini, The Verification Basis of The PM-ALPHA Code, Proceedings of the OECD/CSNI Specialists Meeting on Fuel-Coolant Interactions May 19-21, 1997, Tokai-mura, Japan.
- (5) D. F. Fletcher and A. Thyagaraja, The CHYMES Coarse Mixing Model, Progress in Nuclear Energy, Vol. No. 1, pp. 31-61, 1991.
- (6) G. Berthoud, F.Crecy, R.Meignen and M.Valette, Description of Premixing with The MC3D Code Including Molten Jet Behavior Modeling Comparison with FARO Experimental Results, Proceedings of the OECD/CSNI Specialists Meeting on Fuel-Coolant Interactions May 19-21, 1997, Tokai-mura, Japan.
- (7) M. F. Young, IFCI: An Integrated Code for Calculation of All Phases of Fuel-Coolant Interactions, NUREG/CR-5084, SAND87-1048, 1987.
- (8) M.L. Corradini, M. El-Beshbeeshy, S. Nilsuwankowsit, J. Tang, Fuel Fragmentation Model Advances using TEXAS-V, Proceedings of the OECD/CSNI Specialists Meeting on Fuel- Coolant Interactions May 19-21, 1997, Tokai-mura, Japan.
- (9) B. Kim and M.L. Corradini, Modeling of Small-Scale Single Droplet Fuel/Coolant Interactions, Nucl. Sci. Eng., Vol. 98, pp. 16-28, 1988.
- (10) D. Swift, J. Pavlik, Fuel coolant and cladding coolant interaction studies,

ANL-7125, pp. 187-193, 1966.

- (11) M. L. Corradini, B. J. Kim and M. D. OH, Vapor Explosion in Light Water Reactors: A Review of Theory and Modeling, Progress in Nuclear Energy, Vol. 22, No. 1. pp. 1-117, 1988.
- (12) L.S.Nelson, P.M.Duda, Steam Explosion Experiments with Single Drops of Iron Oxide Melted with a CO₂ Laser Part II. Parametric Studies, NUREG/CR-2718, SAND82-1105, 1985.
- (13) W. Zyszkowski, Thermal interaction of molten copper with water, Int. J. Heat Mass Transfer, Vol. 18, No. 2, pp. 271-287, 1975.
- (14) A.W. Cronenberg and M. A. Grolmest, Fragmentation Modeling Relative to the Breakup of Molten UO₂ in Sodium, Nuclear Safety, Vol. 16, No. 6, November-December 1975.
- (15) A.W.Cronenberg, T.C.Chawla and H.K. Fauske, A thermal stress mechanism for the fragmentation of Molten UO₂ upon contact with sodium coolant, Nuclear Eng. Des. Vol. 30 (1974) , pp. 434-443.
- (16) K.H. Hsiao, J. E. Cox, P. G. Hedgcoxe and L. C.Witte, Pressurization of a Solidifying Sphere, Transactions of the ASME, Journal of Applied Mechanics, Vol. 94, pp.71-77, March 1972.
- (17) L.C. Witte, T. J. Vyas and A. A. Gelabert, Heat transfer and fragmentation during Molten-Metal/Water Interactions, Transactions of the ASME, Journal of Heat Transfer, pp.521-527, Nov. 1973.
- (18) F. E. Brauer, N. W. Green and R. B. Mesler, Metal/Water Explosions, Nuclear Science and Engineering, Vol. 31, 1968, pp. 551-554.
- (19) G. Ciccarelli and D. L. Frost, Fragmentation mechanisms based on single drop steam explosion experiments using flash X-ray radiography, Nucl. Eng. Des. Vol. 146 pp.109-132, 1994.
- (20) X. Cao, R. Hajima, K. Furuta, S. Kondo, "A Numerical Analysis of Molten Metal Drop and Coolant Interaction", Journal of Nuclear Science and Technology, Vol. 37, No. 12 pp.1047-1053.
- (21) A. Inoue, M. Aritomi, M. Takahashi and Y. Tobita, An analytical model on vapor

- explosion of a high temperature molten metal drop in water induced by a pressure pulse, Chem. Eng. Comm. 1992, Vol. 118, pp. 189-206.
- (22) M.K.Denham, A.P.Tyler and D.F.Fletcher, Experiments of The Mixing of Molten Uranium Dioxide with Water and Initial Comparison with CHYMES code Calculations, NURETH-5, Salt Lake City, UT, 1992, pp. 1667-1675.
- (23) M. L. Corradini, Phenomenological Modeling of the Triggering Phase of Small-Scale Steam Explosion Experiments, Nucl. Sci. & Eng. Vol. 78, pp. 154-170 (1981)
- (24) H. Hohmann, D. Magallon, H. Schins and A. Yerkess, FCI experiments in the aluminum oxide/water system, Nuclear Engineering and Design, Vol. 155 (1995), pp. 391-403.
- (25) H. Mizuta, Fragmentation of Uranium Dioxide after Molten Uranium Dioxide-Sodium Interaction, J. of Nuclear Science and Technology, Vol. 11, pp. 480-487 (1974)
- (26) X.Chen, W.W.Yuen and T.G.Theofanous, On the constitutive description of the microinteractions concept in system explosions, Proceedings of A Multidisciplinary International Seminar on Intense Multiphase Interactions, Santa Barbara, June 9-13, 1995.
- (27) K. Mishima, T.Hibiki, Y.Saito and Yamamoto, Visualization study of Molten Metal-Water Interaction by Using Neutron Radiography, Dynamics of Vapor Explosions, Edited by Mamoru Akiyama, March, 1998.

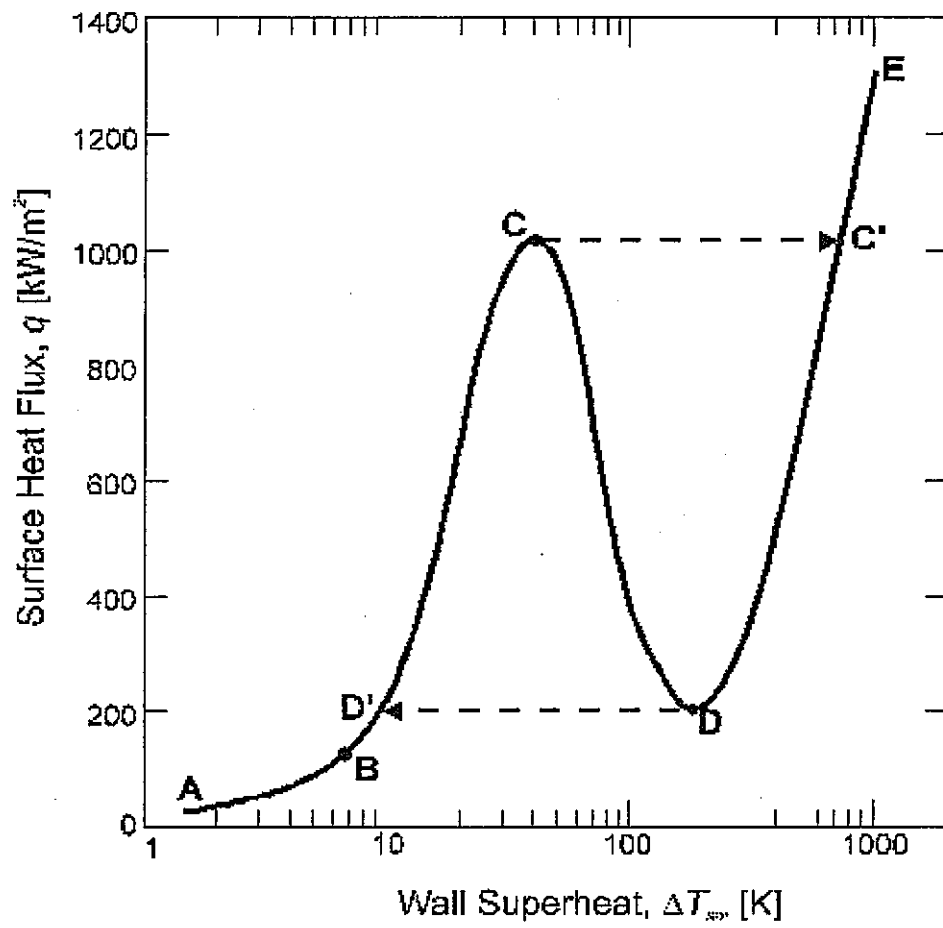


Fig. 5- 1 Typical boiling curve for saturated pool boiling of water at atmospheric pressure

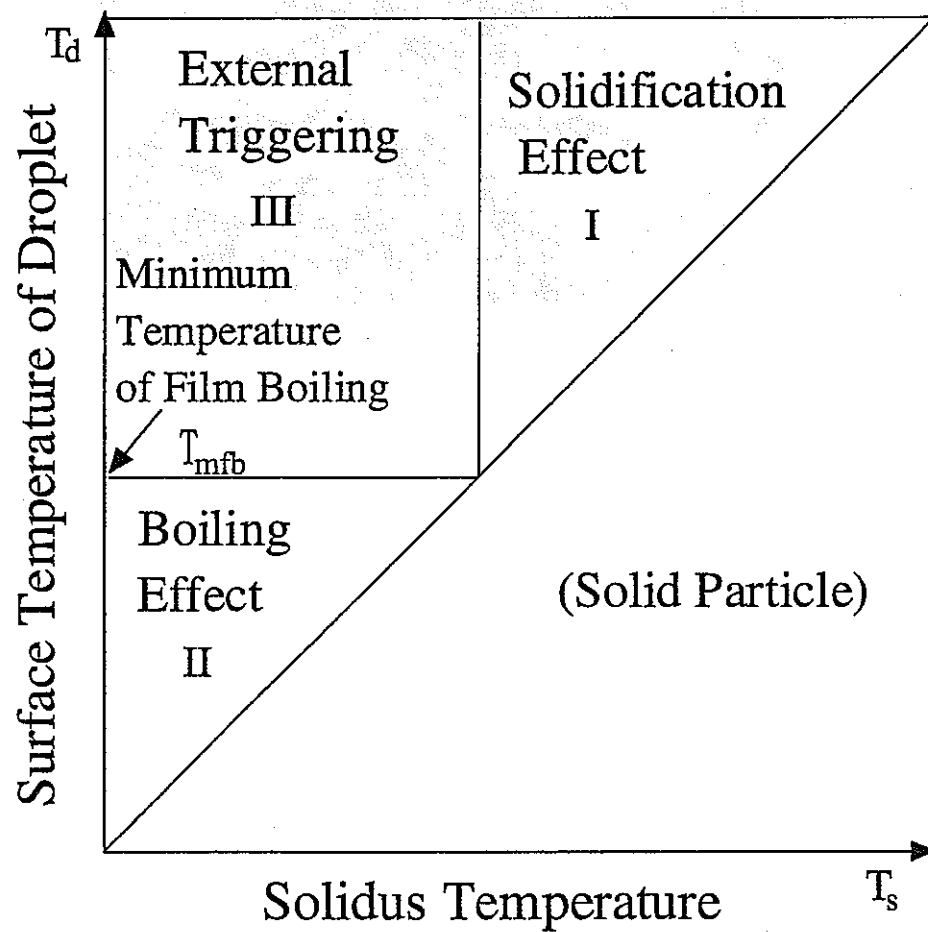


Fig. 5- 2 The Fragmentation mechanism map considering the thermal condition of the melt droplet and coolant



Fig. 5- 3 Aluminum bubble showing what appears to be interior aluminum that was forced through the outer shell.

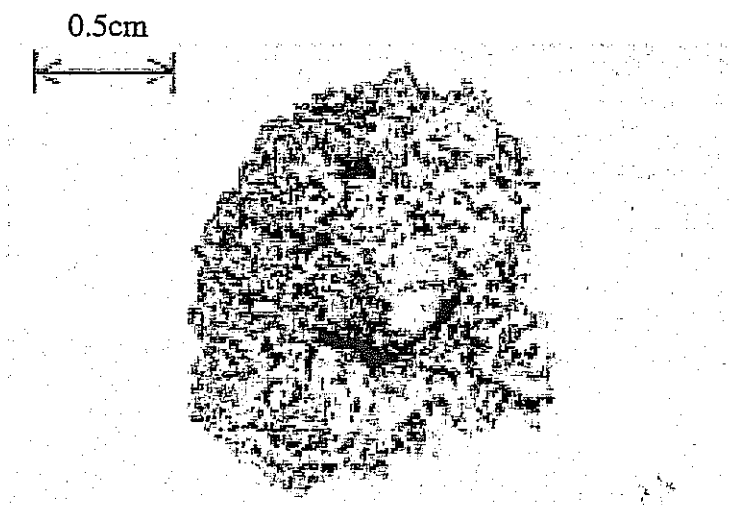


Fig. 5- 4 Interior of completely mossy lead after fragmentation.

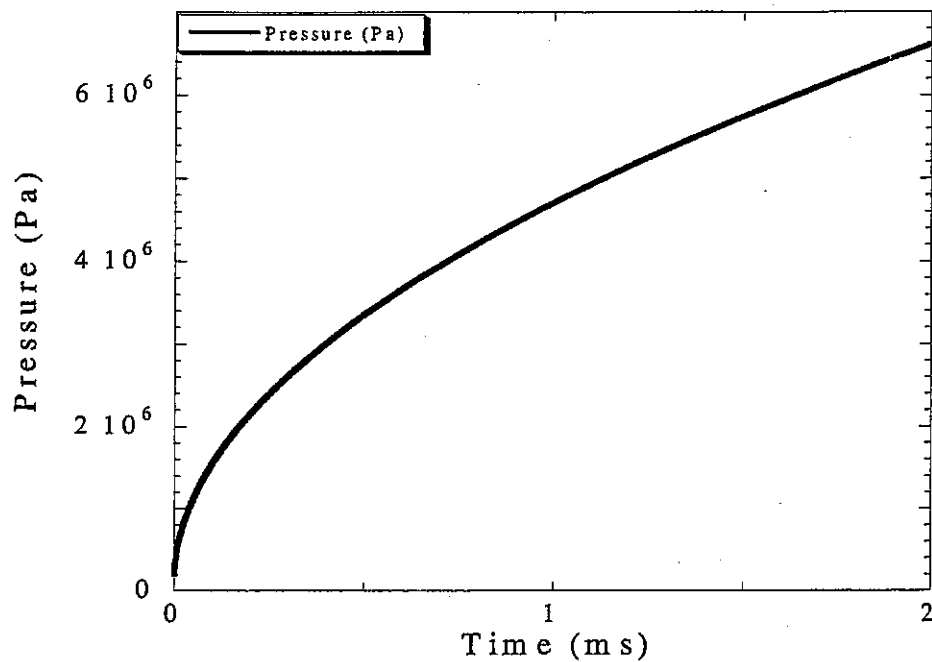


Fig. 5- 5 Pressurization on the solid-liquid interface induced by the surface solidification of the melt droplet

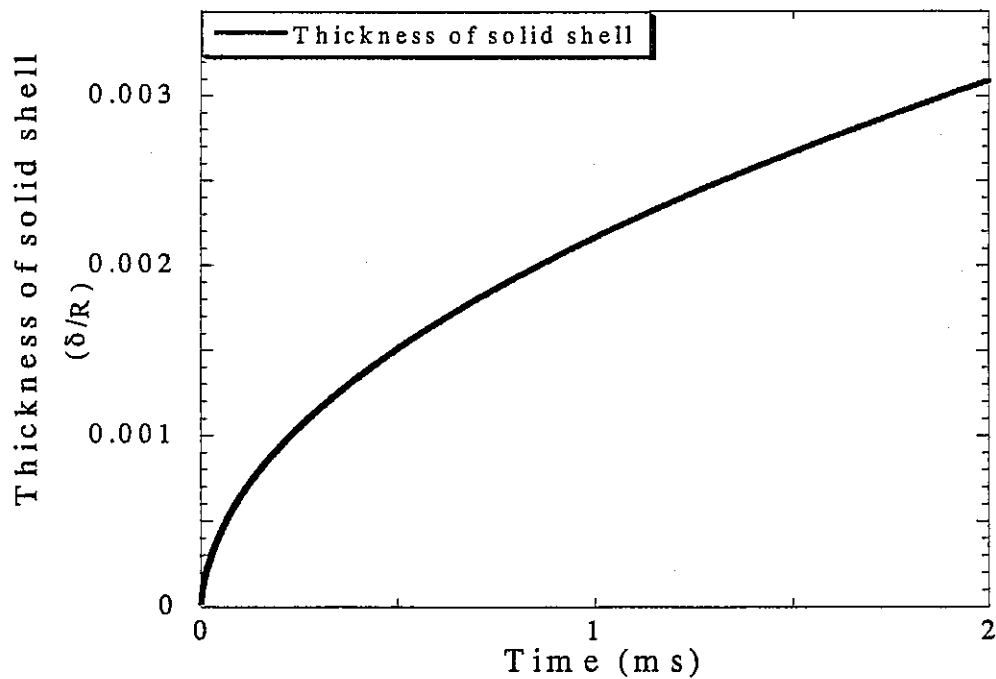


Fig. 5- 6 Thickness of the shell during the solidification process

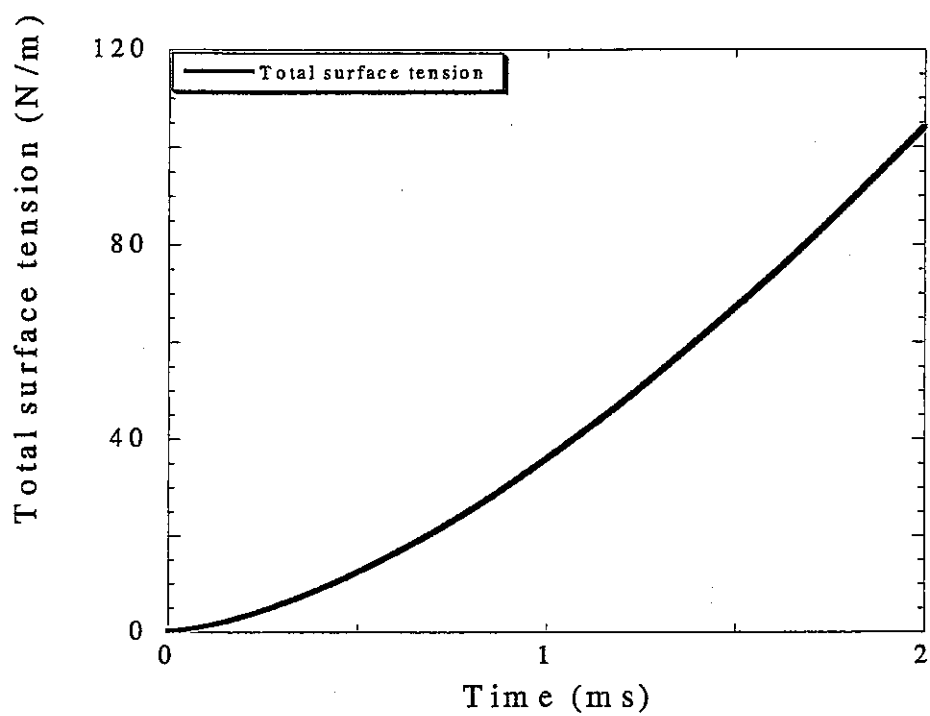


Fig. 5- 7 Total surface tension including the effect of the solid shell

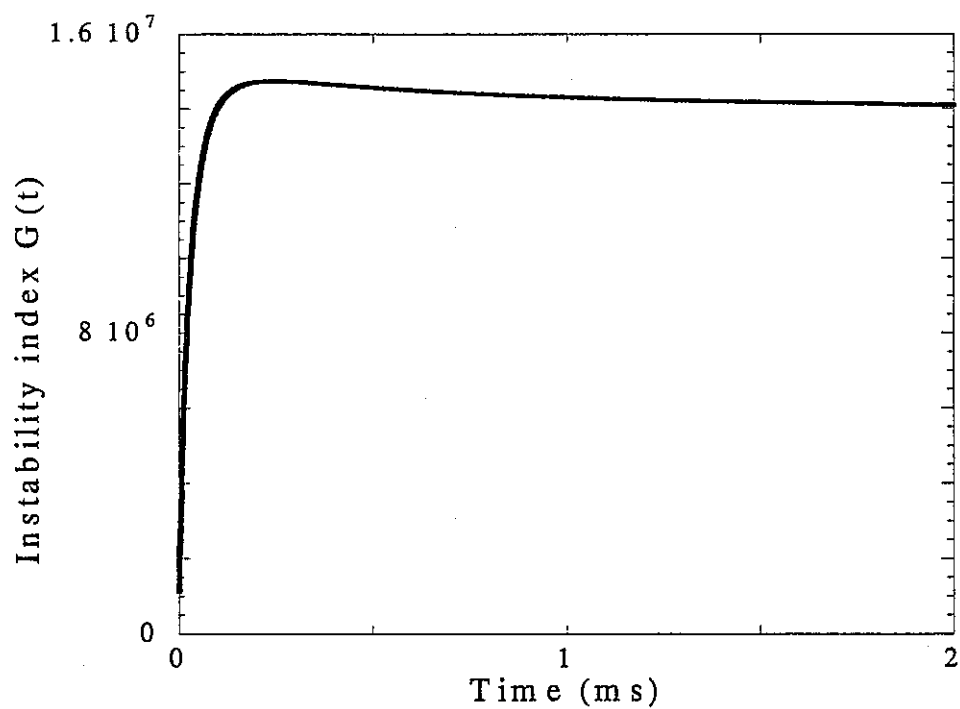


Fig. 5- 8 The instability index during the solidification process

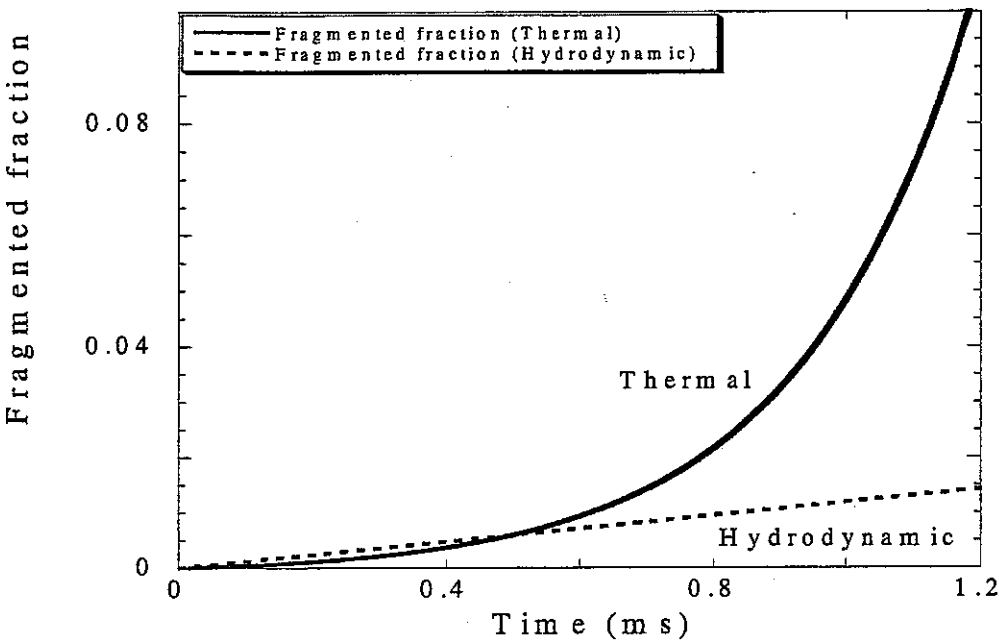


Fig. 5- 9 Fragmented mass induced by the surface solidification of the melt droplet

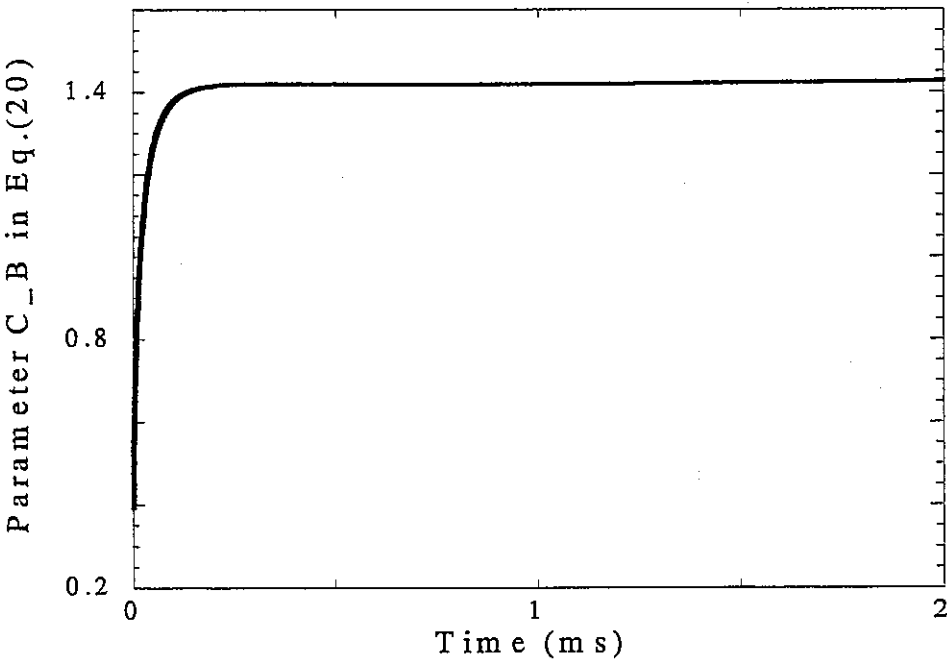


Fig. 5- 10 The parameter C_B in equation (20) for the case that the fragmentation is induced by surface solidification

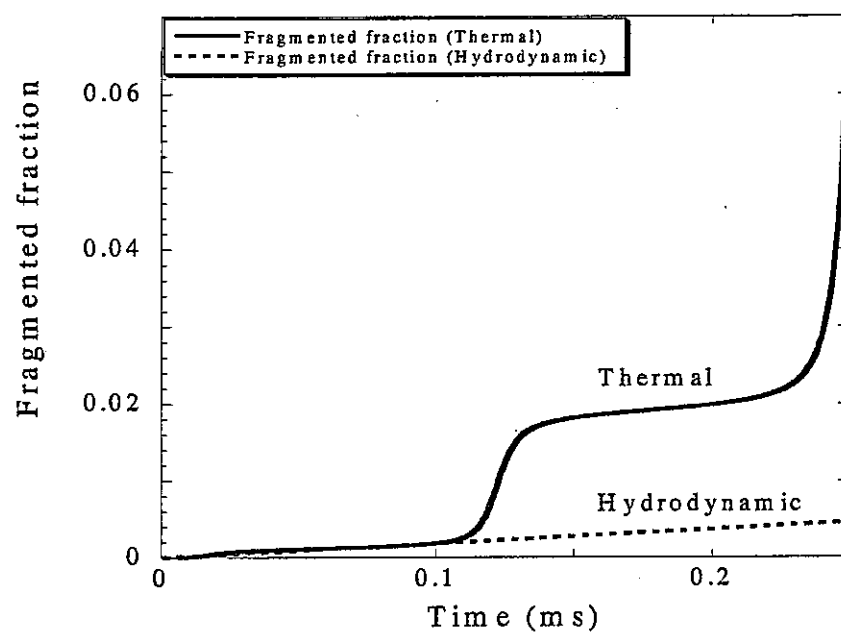


Fig. 5- 11 Fragmented mass induced by external pressure pulse applying on the melt droplet

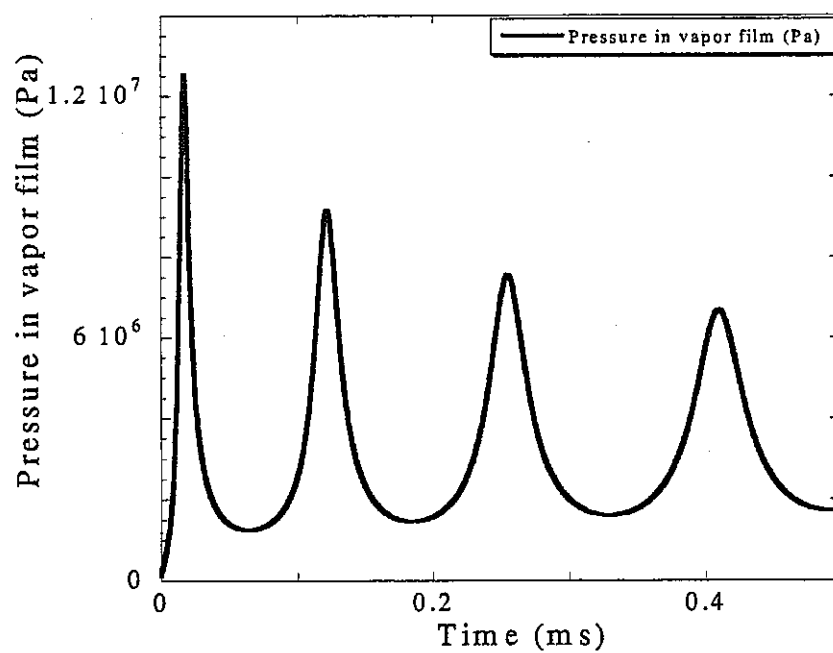


Fig. 5- 12 Pressure in vapor film induced by external pressure pulse applying on the melt droplet

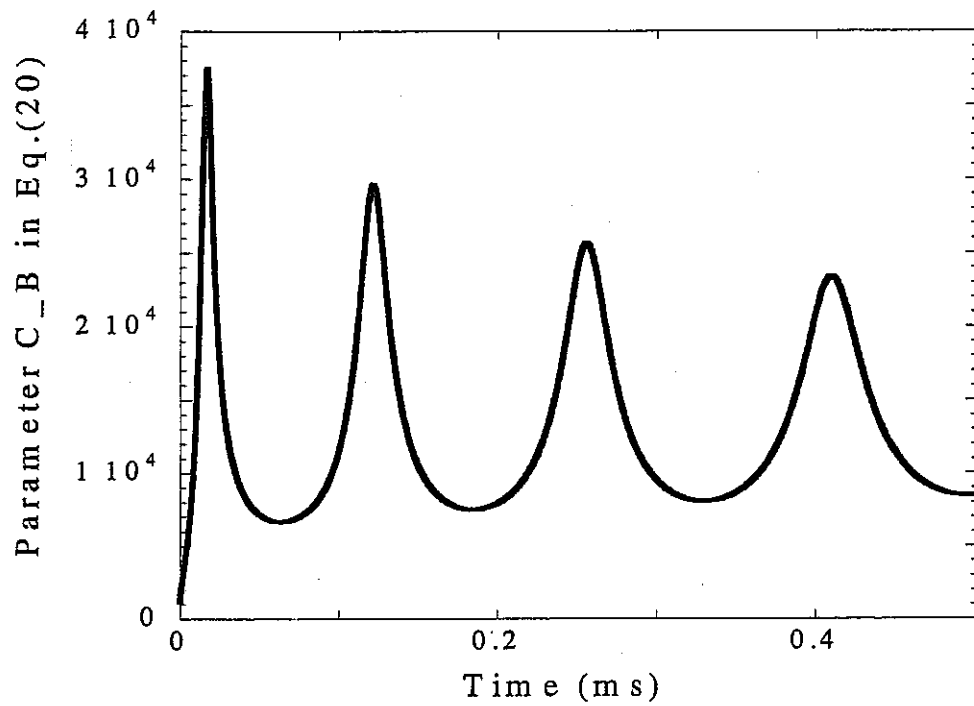


Fig. 5- 13 The parameter C_B in equation (20) for the case that the triggering event is external pressure pulse

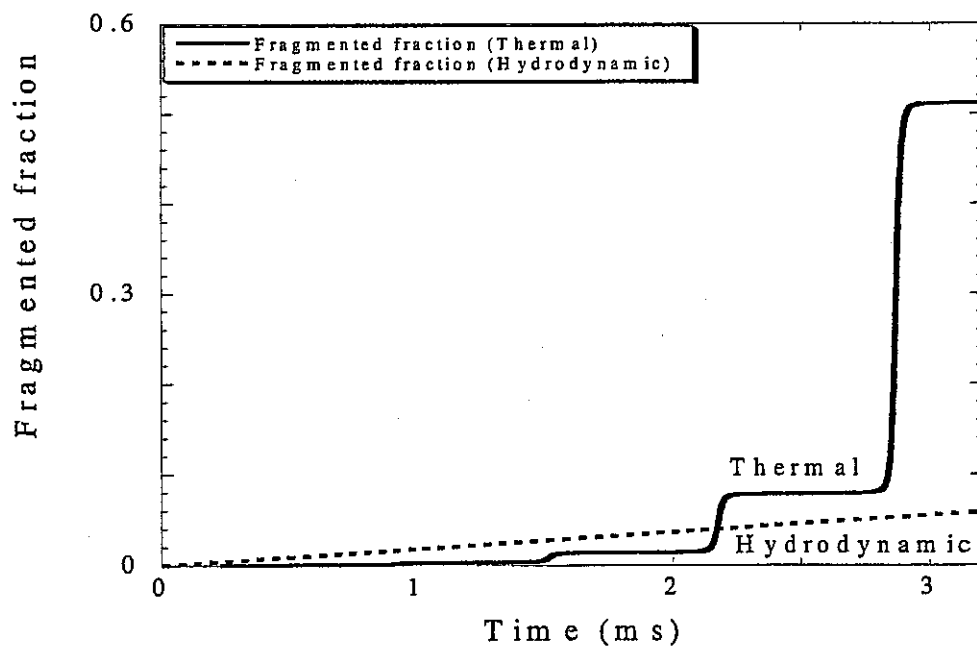


Fig. 5- 14 Fragmented mass induced by external pressure pulse applying on the melt droplet

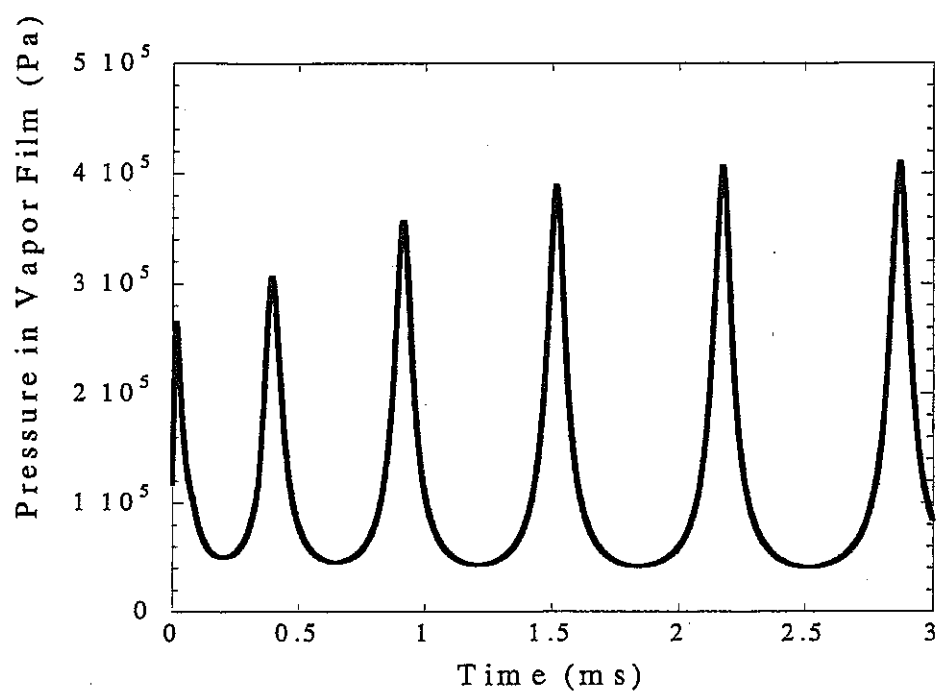


Fig. 5- 15 Pressure in vapor film induced by boiling effect

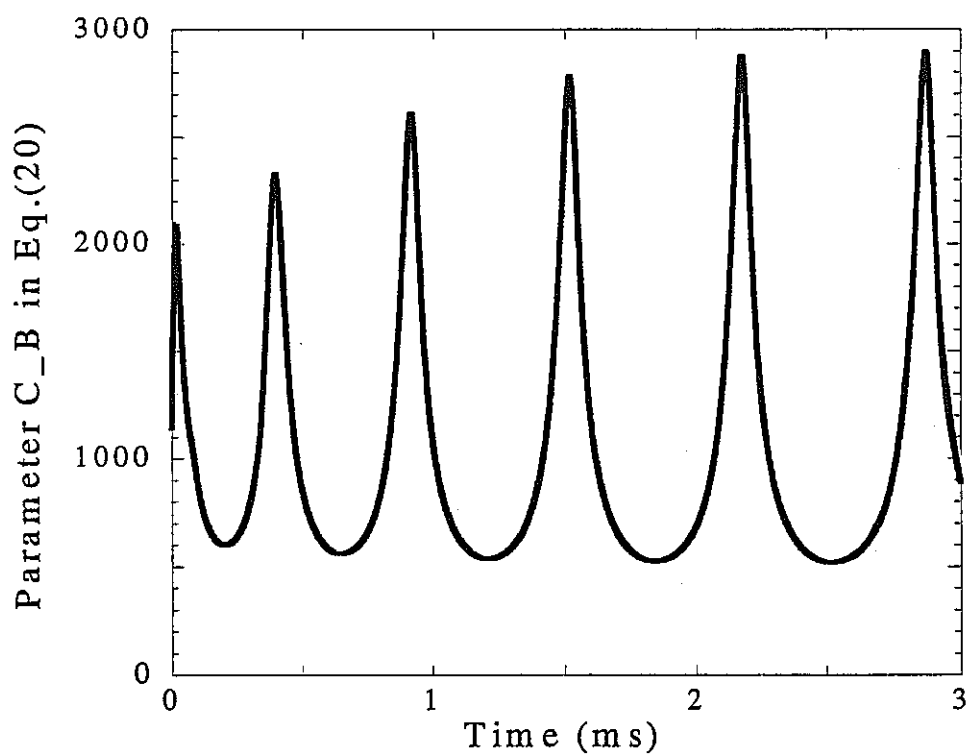


Fig. 5- 16 The parameter C_B in equation (20) for the case that the fragmentation is triggered by boiling effect

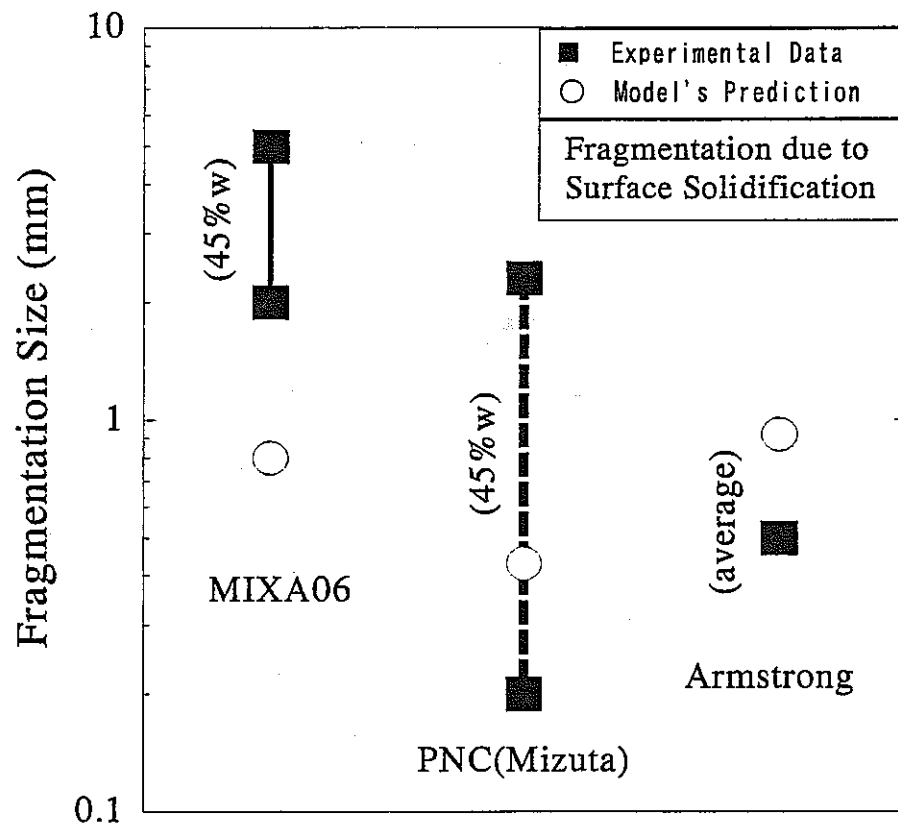


Fig. 5- 17 The comparison of fragment size with experimental data

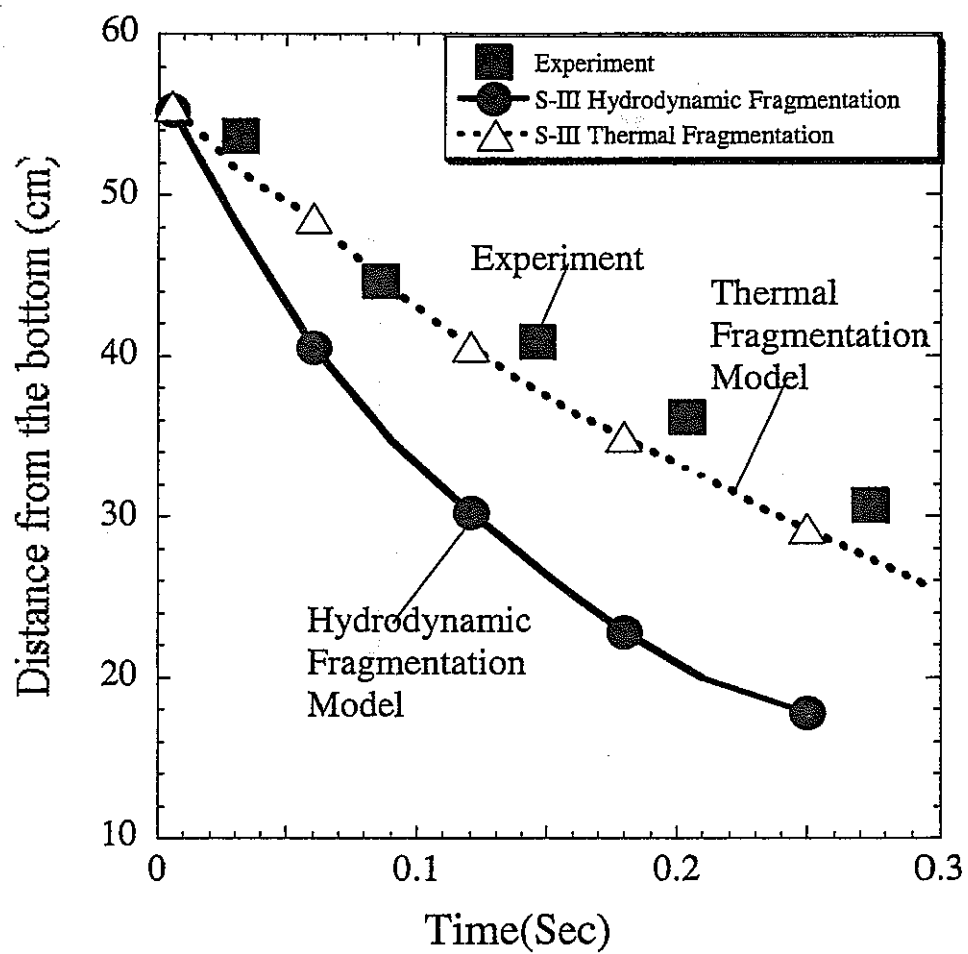


Fig. 5- 18 Front Advancement of the melt droplets in water in MIXA-06

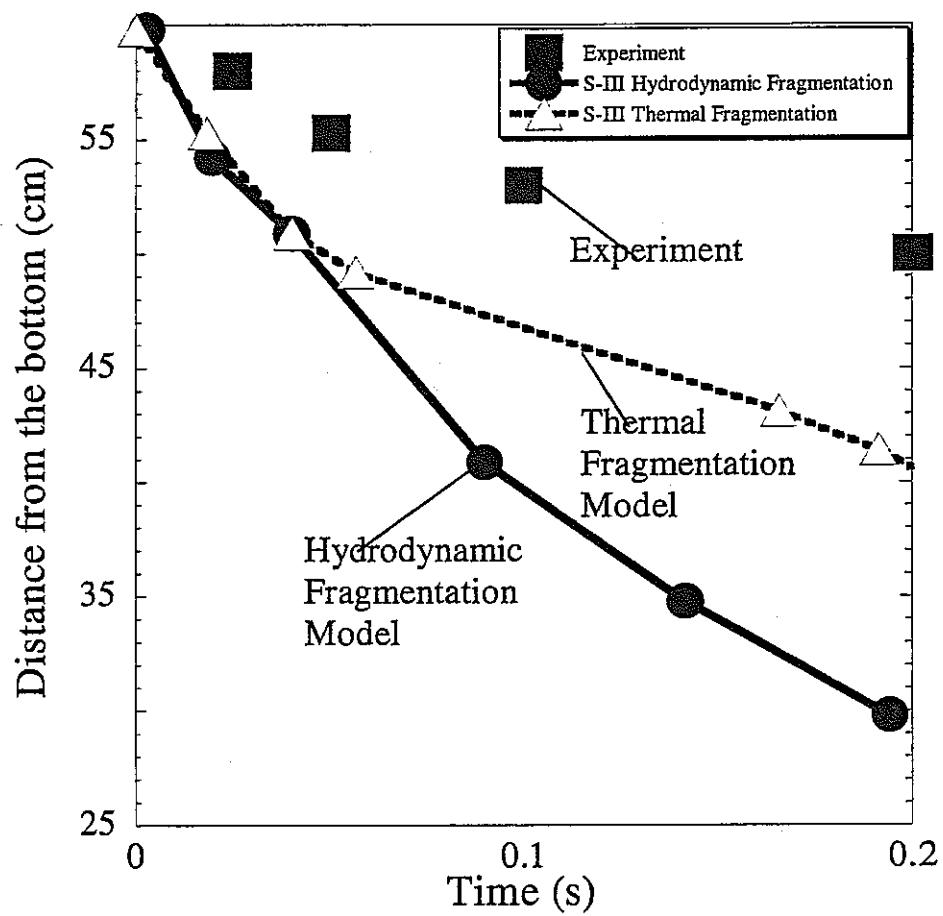


Fig. 5- 19 Front Advancement of the melt droplets in water in MIXA-01

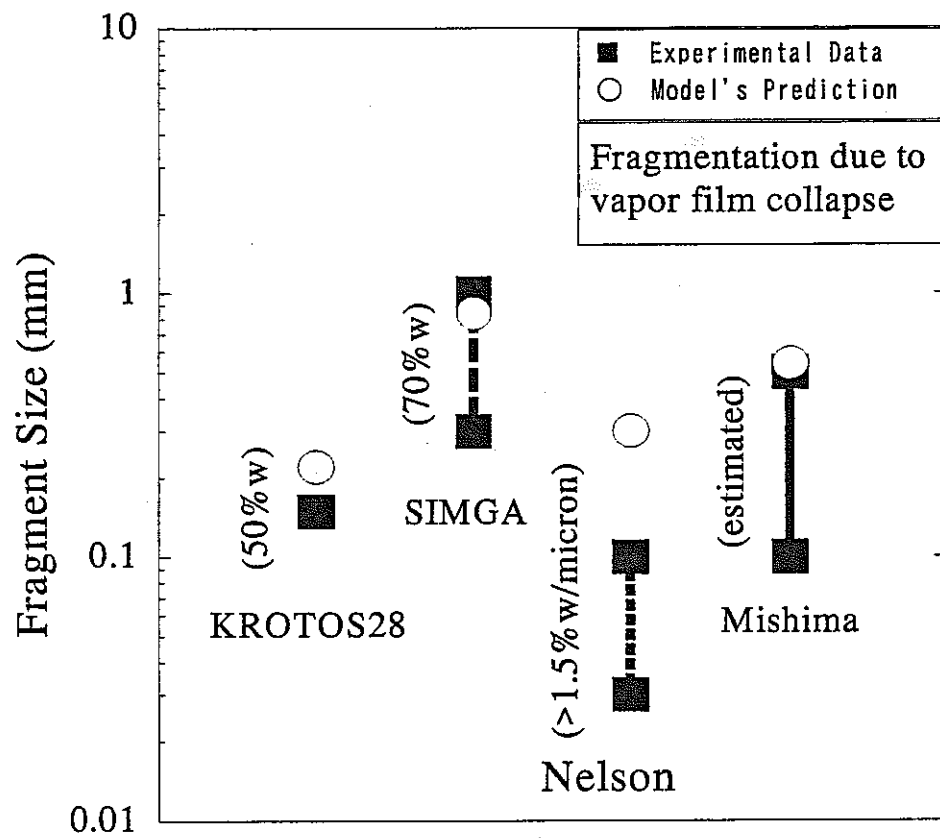


Fig. 5- 20 The comparison of fragment size with experimental data

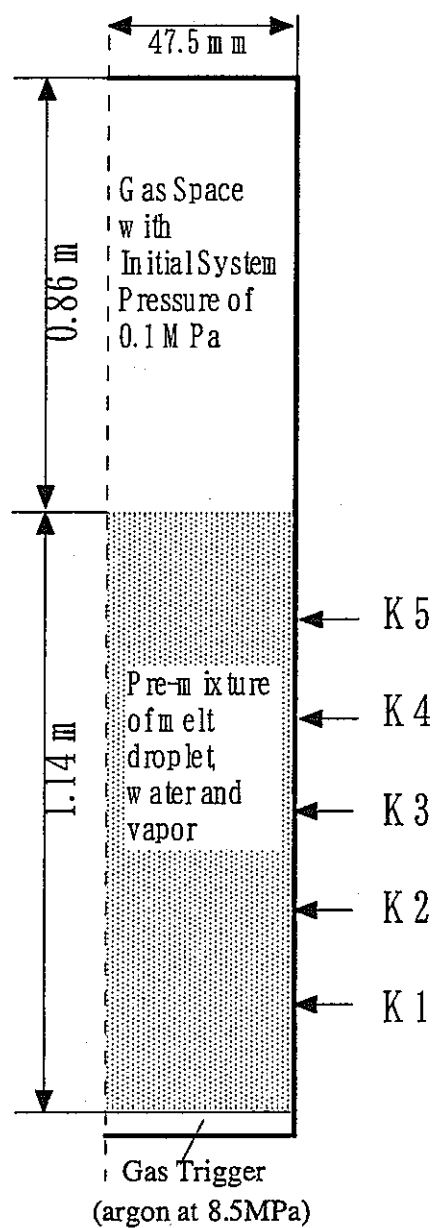
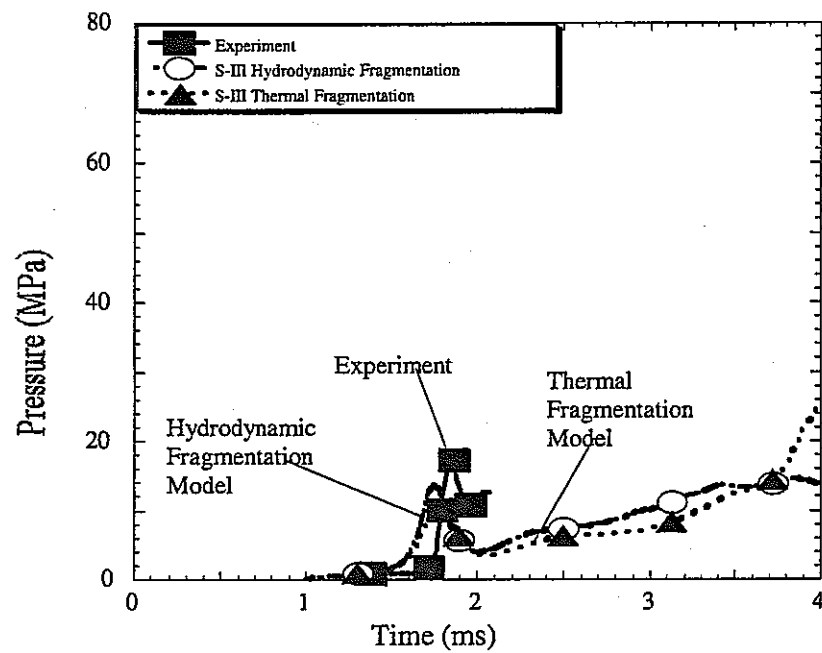
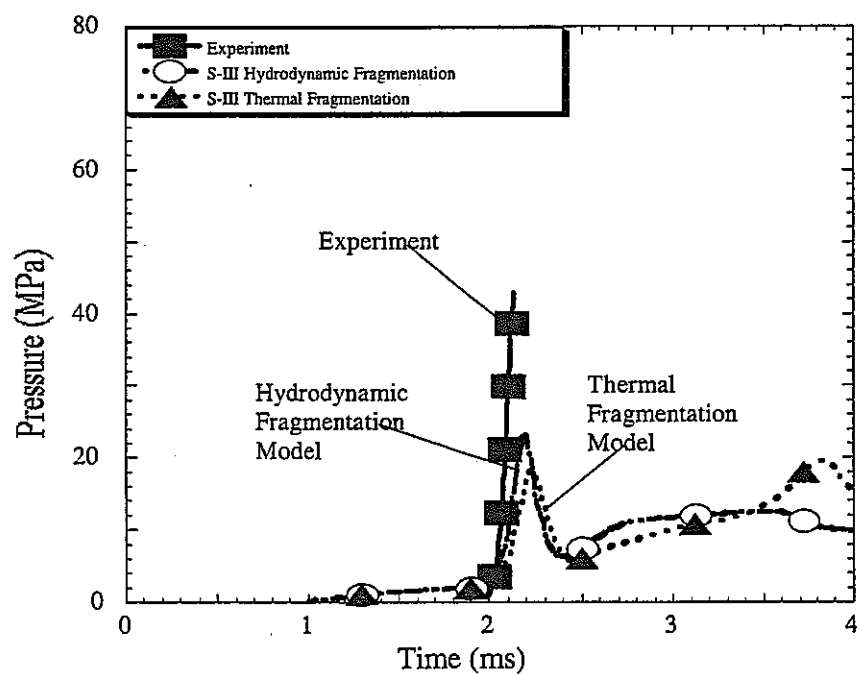


Fig. 5- 21 KROTOS test facility simulation model

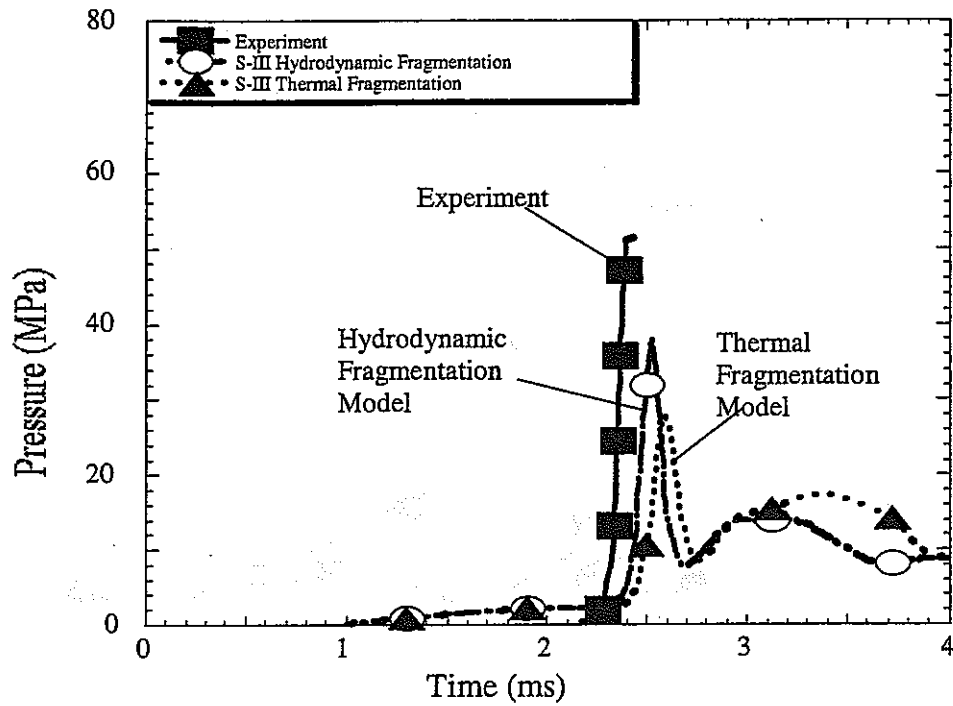


Pressure profile at K1 position in test tube

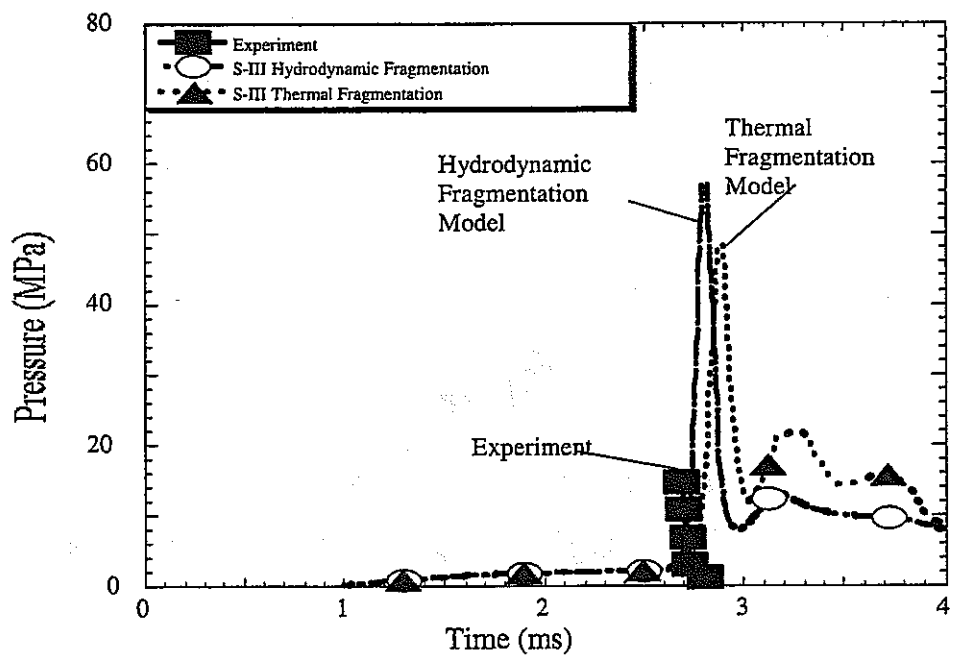


Pressure profile at K2 position in test tube

Fig. 5- 22 Advancement of shock wave in the test tube in KROTOS 28

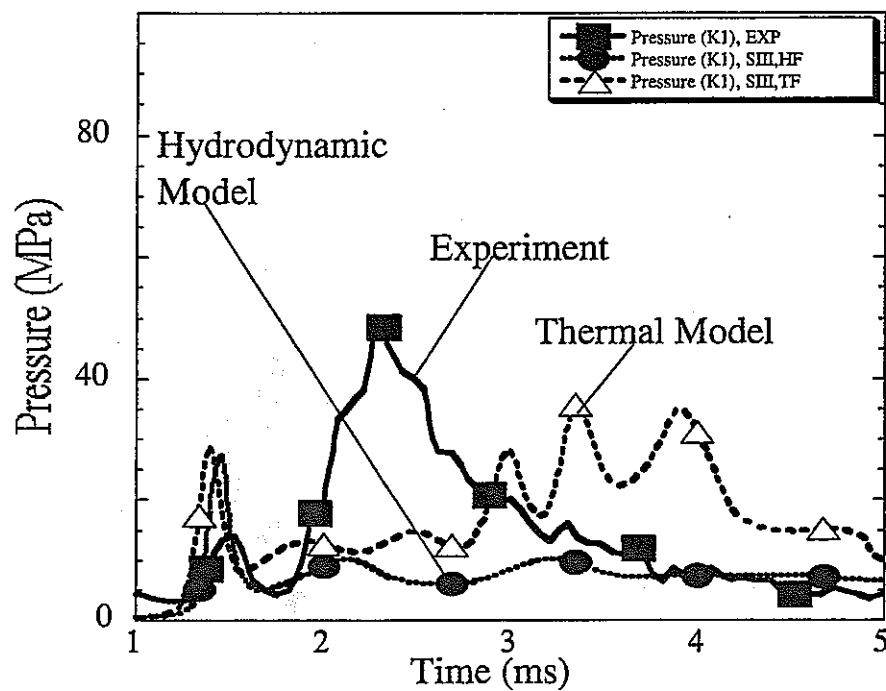


Pressure profile at K3 position in test tube

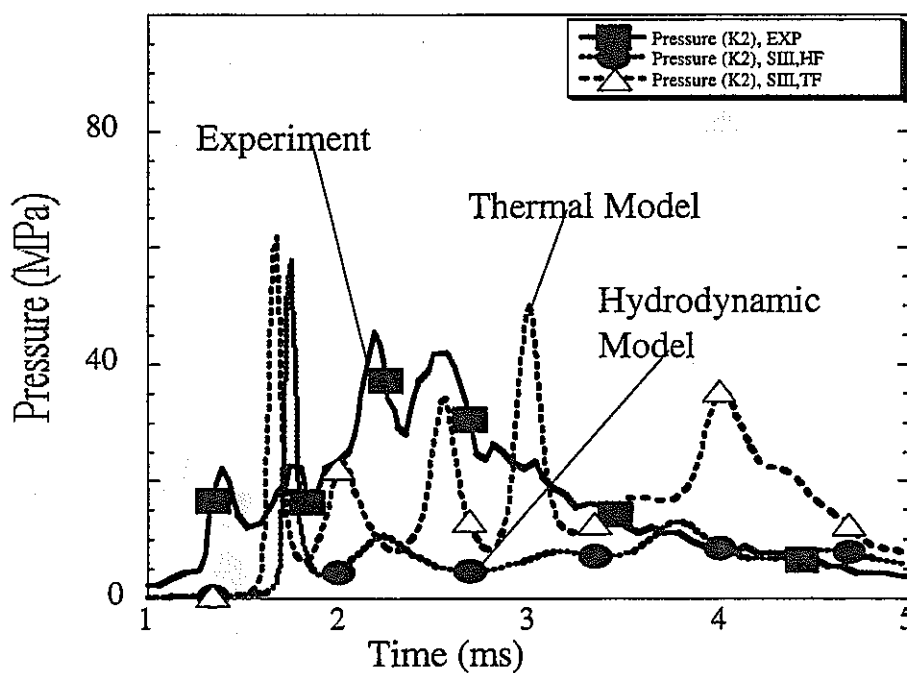


Pressure profile at K4 position in test tube

Fig. 5-22 Advancement of shock wave in the test tube in KROTOS 28 (Continue)

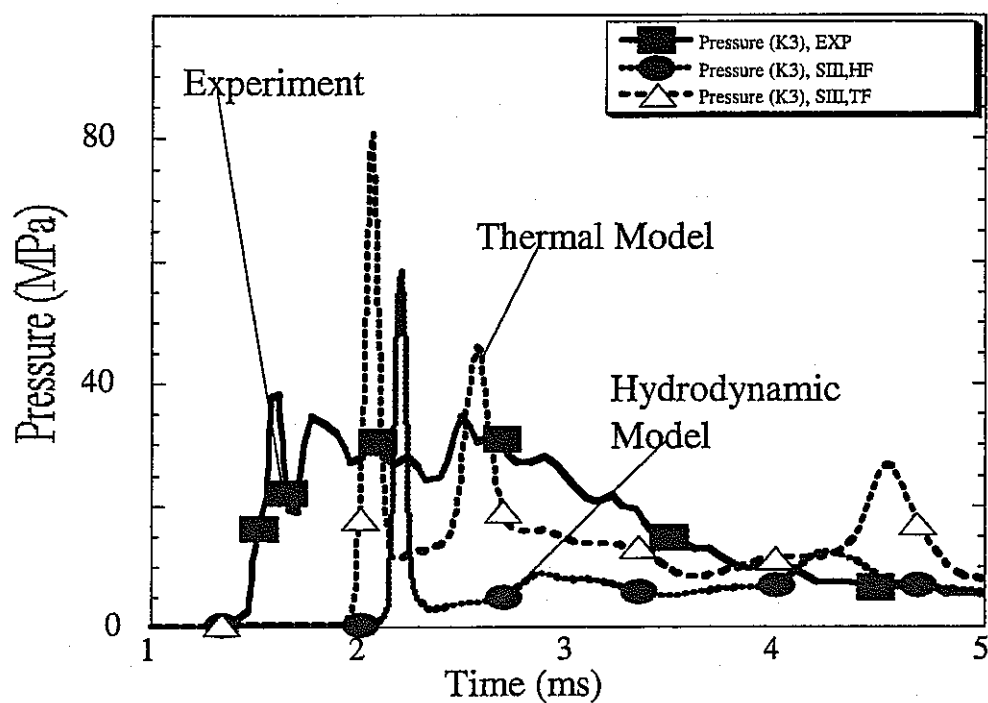


Pressure profile at K1 position in test tube

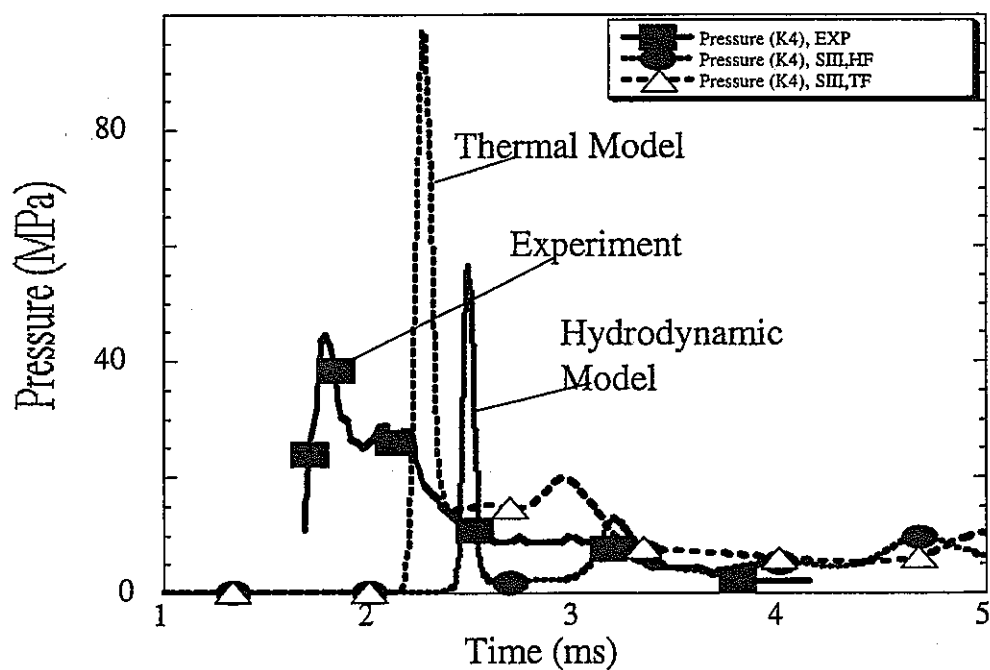


Pressure profile at K2 position in test tube

Fig. 5- 23 Pressure profile in test tube in KROTOS 44



Pressure profile at K3 position in test tube



Pressure profile at K4 position in test tube

Fig. 5-23 Pressure profile in test tube in KROTOS 44 (continue)

6. Conclusions

6.1 Concluded Remarks

In this study the simulation of QUEOS experiments shows that the development of the drag coefficient of melt droplets is required based on the specific configuration. The drag coefficients for a single particle surrounded by vapor film moving in coolant liquid under laminar and turbulent flow conditions are studied, based on the conservative equations and assumptions. The drag correlations can be described by the Reynolds number, vapor/liquid viscosity and density ratios and the two dimensionless numbers, newly introduced in this study to suitably describe the effect of the vapor film on the drag coefficient. In the turbulent flow regime, the drag coefficient correlation is fitted by experimental data and is smaller than that of the particle without vapor film.

Based on the single particle model and the mixture viscosity concept, the drag correlations of the particle with vapor film in multi-particle system are proposed for the laminar and turbulent flow cases, respectively. The proposed drag correlations are employed to simulate the QUEOS experiment and the results show that the proposed correlations improve the agreement of the simulated results with the experimental data.

The results of the simulation of MIXA experiments show that the fragmentation model is required for the simulation code in the case of that the thermal fragmentation mechanism is dominant. A thermal fragmentation mechanism induced by surface solidification is proposed to develop a new fragmentation model. That is, when a melt droplet contacts with coolant, due to the rapid heat transfer, the solid shell on the surface of a droplet is formed, it contracts, squeezes the internal liquid part and generates high pressure on the interface between the liquid and solid parts. The generated pressure causes the instability of the interface, which induces the growth of the spikes on the droplet surface. The spikes, which are considered as the fragments, are broken by the coolant flow around the droplet.

Based on the proposed mechanism, a fragmentation model is developed. The fastest growth mode of the instability and the diameter of the spikes are considered to be the fragmentation rate and fragment size, respectively. The solid shell is taken as a

membrane with ductility. The stiffness of the shell is considered in the instability analysis by using a total surface tension concept.

For the convenient application of the model to simulation tools, a simplified correlation is proposed, based on the numerical investigation of the theoretical model. The proposed fragmentation model is indirectly verified by comparing the prediction of the fragment size with the experimental data collected after these experiments.

The proposed thermal fragmentation model is introduced into the SIMMER-III code. The experiments MIXA 01 and 06 are simulated to verify the proposed thermal fragmentation model for the case with low and large Weber number.

The influence of the fracture on the surface is not considered in this model, but the model still can be applied to model the fragmentation by assuming that the velocity of the ejected liquid metal from the inside of the droplet and the fracture area on the surface are equivalent to the velocity and cross section of the spikes, respectively.

Another fragmentation model is also developed for numerical codes, based on a mechanism, in which the fragmentation is induced by vapor film collapse. That is, the vapor film collapses make a pressure buildup in vapor film during vapor film collapse, which cause the instability on the droplet surface, inducing the growth of spikes on the droplet surface. The simplified correlations of fragmentation model described by the thermal condition of a system are proposed for cases that the vapor film collapse is induced by external pressure pulse or boiling effect respectively. The proposed model is indirectly verified by comparing the predictions of fragments' size with experimental data.

The proposed correlations are introduced into the SIMMER-III code. Although the experiments are simulated to verify the correlation that the fragmentation is induced by external pressure pulse, due to many parameters affecting the fragmentation model, the proposed correlation should be further verified by simulating more experiments under different thermal conditions.

6.2 Future Study

In the jet breakup and bubble expansion stages of the FCIs during CDAs in

LMFBRs or CMAs in LWRs , a global interface, a interface between fluids, exists in a much larger scale than fluid particle sizes determined from local flow conditions. Such a global interface can extend over multiple mesh cells or restricted within a single cell. In order to enlarge the application of current multi-phase and multi-component fluid dynamic code to analyze these phenomena, the modeling of the treatment of the global interface and the breakup of the global interface should be studied in the future, which includes:

- (1) Development of an algorithm for trucking the global interfaces in a computational domain, in which bubble/jet size is larger than mesh size;
- (2) Modeling of the phenomena that cause instabilities and breakup of the global interfaces;
- (3) Modeling of the phenomena that may result from breakup of the global interfaces and
- (4) Application of the multi-phase and multi-component fluid dynamic code to analyze the FCIs as a whole process under reactor conditions.

Nomenclature

English Symbols

- A surface area of droplets (m^2)
- Bi Biot number ($Bi=hR/k$)
- Bo instantaneous Bond number ($Bo = \frac{3}{8} C_d \frac{\rho r_d \Delta v^2}{\sigma}$)
- C_d drag coefficient
- C_{d-fb}^I drag coefficient of a hot particle/droplet with vapor film under laminar condition
- C_{d-fb}^T drag coefficient of a hot particle/droplet with vapor film under turbulent condition
- D diameter (m)
- E Young's module
- Ev evaporation flow number, which is defined to describe the vapor flow inside the vapor film induced by the evaporation of coolant liquid on the coolant liquid/vapor interface $Ev = \frac{\text{dynamic_force}}{\text{viscous_force}}$, written as ($Ev = \frac{\Gamma D_p}{\mu}$)
- F force (N)
- g gravity (m/s^2)
- g_0 dimensionless number which is defined to describe the particle in coolant system with gravity g, $g_0 = \frac{\text{gravity_force}}{\text{viscous_force}}$, written as ($g_0 = \frac{D_p^3 \rho_c^2 g}{\mu_c^2}$)
- h heat transfer coefficient
- h_{fg} latent heat
- m mass
- P pressure (Pa)
- Ps Poisson's ratio
- r radius (m)

Re	Reynolds number $(Re = \frac{v_{cp} \rho_c D_p}{\mu_c})$
S	interfacial area source term
t	time
T	temperature
Th	A dimensionless number $(Th = \left(\frac{k_m k_c \Delta T_{mc}^2}{h_{fg}^2 R^2 \rho_c P_a} \right))$
u	vapor velocity in x direction (m/s).
\bar{u}	average vapor velocity along vapor film (m/s).
v	velocity (m/s)
V_{cp}	velocity (m/s)
We	Weber number $(We = \frac{\rho_c D \Delta v^2}{\sigma})$

Greece Symbols

α	volume fraction of the droplet
α_t	thermal expansion
Γ	evaporation rate $(kg/(m^2 \cdot s))$
ε	density ratio
θ	angle
δ	thickness of vapor film (m)
μ	viscosity $(Pa \cdot s)$.
μ_0	dimensionless number which is the ratio of the viscosity of the vapor to coolant liquid $(\mu_0 = \frac{\mu}{\mu_c})$
ρ	density (kg/m^3) .
ρ_0	dimensionless number which is the ratio of the densities of the vapor to coolant

liquid ($\rho_0 = \frac{\rho}{\rho_c}$)

σ surface tension of the droplet

τ time interval

Subscripts and superscripts:

c coolant, continuous phase

cr criticality

d droplet

e equilibrium quantity

p particle/droplet

s surface, separation point

y y direction

θ x direction

List of Publications

- (1) Xuewu Cao, Yoshiharu Tobita, Werner Mascheck and P Teyssier, Analysis of QUEOS Experiments Q08 and Q12, Summary Report on a SIMMER-III Application in the Phase 2 Assessment Program, JNC TN9400 2000-105.
- (2) Xuewu Cao and Yoshiharu Tobita, Simulation of Premixing Experiment QUEOS by SIMMER-III, JNC TN9400 2001-100.
- (3) Xuewu Cao and Yoshiharu Tobita, Study on Drag Coefficient For the Particle/Drop Under FCI Condition, JNC TN9400 2001-055.
- (4) Xuewu Cao and Yoshiharu Tobita, Verification of SIMMER-III Modeling on FCI Through Simulation of QUEOS experiments, 日本原子力学会「2000年春の年会」N41. 愛媛大学、松山、2000年3月28日～30日。
- (5) Xuewu Cao and Yoshiharu Tobita, Drag Correlations For Hot Particle/Droplet with Vapor Film, Journal of Nuclear Science and Technology, Vol. 38, No. 9, pp.721-728, (2001).
- (6) Xuewu Cao and Yoshiharu Tobita, "Analysis of QUEOS Experiments", 9th International Meeting on SIMMER, September 4-8, 2000, Oarai, Japan.
- (7) Xuewu Cao and Yoshiharu Tobita, Simulation of MIXA-06 Experiment by SIMMER-III, JNC report, JNC TN9400 2001-122.
- (8) Xuewu Cao and Yoshiharu Tobita, A Drag Correlation For A Hot Particle/Drop With A Vapor Film, 日本原子力学会「2000年秋の大会」G7.青森大学、青森、2000年9月14日～16日。
- (9) Xuewu Cao and Yoshiharu Tobita, Verification of SIMMER-III Modeling on FCI Through the Simulation of MIXA Experiment, 日本原子力学会「2001年春の年会」J24.武蔵工業大学、東京、2001年3月27日～29日。
- (10) Xuewu Cao and Yoshiharu Tobita, Verification of Drag Coefficient Model on Premixing Phase of Fuel Coolant Interaction, ICMF 2001, 4th International Conference on Multiphase Flow, May 27-June 1, 2001, New Orleans, USA.
- (11) Xuewu Cao and Yoshiharu Tobita, "Verification of Drag Coefficient Model in Multi-Particle System Through Simulation of FCI's Premixing Experiment", 14th AFMC, Dec. 10-14, 2001, Adelaide, Australia.

- (12) X. Cao, Y. Tobita, "Momentum coupling for droplets under film boiling", 10th International Meeting on SIMMER, Oct. 22-25, 2001, Karlsruhe, Germany.
- (13) Xuewu Cao and Yoshiharu Tobita, A Proposal of the Thermal Fragmentation Model for Numerical Study of FCI, 日本原子力学会「2001 年秋の大会」J70. 北海道大学、札幌、2001 年 9 月 19 日～21 日。
- (14) Xuewu Cao and Yoshiharu Tobita, "Proposal of the Thermal Fragmentation Models for Numerical Study of FCI, JNC report", JNC TN9400 2001-123.
- (15) Xuewu Cao and Yoshiharu Tobita, "A Thermal Fragmentation Model Induced by Surface Solidification", Journal of Nuclear Science and Technology (submitted).
- (16) Xuewu Cao and Yoshiharu Tobita, "Proposal of The Thermal Fragmentation Model For A Droplet Induced by vapor Film Collapse", Journal of Nuclear Science and Technology (submitted).
- (17) X. Cao, Y. Tobita, "Analysis of MIXA experiment and proposal of thermal fragmentation model", 10th International Meeting on SIMMER, Oct. 22-25, 2001, Karlsruhe, Germany.
- (18) Xuewu Cao and Yoshiharu Tobita, A Thermal Fragmentation Model of Melt Droplets Induced by Vapor Film Collapse, 日本原子力学会「2002 年春の年会」.神戸商船大学、神戸、2002 年 3 月 27 日～29 日。

Acknowledgments

I would like to express my sincere gratitude to Japan Nuclear Cycle Development Institute (JNC) for giving me a chance to do research on this field. I wish to express my sincere gratitude to Mr. Satoru Kondo, Deputy Director of Advanced Technology Division, JNC, for his guidance and encouragement. I would like to express my sincere gratitude to Dr. Ikken Sato, leader of Nuclear System Safety Research Group, JNC, for his guidance and support. I would like to express my special gratitude to Mr. Yoshiharu Tobita, Sub-leader of Nuclear System Safety Research Group, JNC, for his constant guidance, support, encouragement and discussions. I also would like to express my sincere gratitude to Dr. Hajime Niwa, former leader of Nuclear System Safety Research Group, JNC, (now leader of Nuclear Safety Design Group, JNC) for his constant guidance, support, encouragement and discussions.

I would like to express my sincere appreciation to Dr. W. Maschek, FZK, Germany, for giving me the data of QUEOS experiment. I would like to express my sincere appreciation to Mr. S. Fujita, Mr. S. Hosono and Mr. T. Kondo for the help of computer system. I am thankful to other persons in Nuclear System Safety Research Group, JNC, for their kindly help on my research and stay.

Finally I would like to borrow this page to express my deepest appreciation to Mr. Satoru Kondo, Dr. Hajime Niwa, Dr. Ikken Sato, Mr. Yoshiharu Tobita, Dr. Tohru Suzuki, Ms. T. Fujita, Mr. S. Fujita, S. Hosono and other persons in JNC for their encouraging and helping me to study Japanese language.

Appendix A: Drag coefficient for a single particle under laminar flow condition

The governing equations for the vapor in the film are

$$\frac{\partial \rho u}{\partial x} = 0, \quad (\text{A-1})$$

$$\frac{\partial \rho u^2}{\partial x} = -\frac{\partial P}{\partial x} - \rho g \sin \theta + \mu \frac{\partial^2 u}{\partial y^2}. \quad (\text{A-2})$$

The boundary conditions are

$$\begin{aligned} y=0; \quad u=0, \\ y=\delta; \quad u=u_i. \end{aligned}$$

The interfacial velocity is

$$u_i = \frac{3}{2} V_{cp} \sin \theta \quad (\text{A-3})$$

From equations (A-1) and (A-2) we can obtain

$$\frac{\partial P}{\partial x} = -\rho_c g \sin \theta + \mu \frac{\partial^2 u}{\partial y^2} \quad (\text{A-4})$$

The pressure distribution can be written as

$$P(\theta) = P_0 + \rho_c g r_p \cos \theta + \rho_c \frac{V_{cp}^2}{2} - \frac{\rho_c}{2} \left(\frac{3}{2} V_{cp} \sin \theta \right)^2 \quad (\text{A-5})$$

Then

$$\frac{\partial P}{\partial x} = -\rho_c g \sin \theta - \frac{1}{2r_p} \rho_c V_{cp}^2 \sin 2\theta \quad (\text{A-6})$$

By combining the equations (A-4) and (A-6), we can get

$$\mu \frac{\partial^2 u}{\partial y^2} = -(\rho_c - \rho) g \sin \theta - \frac{1}{2r_p} \rho_c V_{cp}^2 \sin 2\theta \quad (\text{A-7})$$

Then the velocity distribution can be obtained

$$u = \frac{3y}{2\delta} V_{cp} \sin \theta - \left(\frac{(\rho_c - \rho)g}{2\mu} \sin \theta + \frac{9\rho_c V_{cp}^2}{16\mu r_{cp}} \sin 2\theta \right) (y^2 - y\delta) \quad (\text{A-8})$$

The viscous force on the particle surface can be written as

$$\begin{aligned}
\tau_{s_1} &= \mu \frac{\partial u}{\partial y} \Big|_{y=0} \\
&= \frac{3\mu}{2\delta} V_{cp} \sin \theta + \left(\frac{(\rho_c - \rho)g}{2} \sin \theta + \frac{9\rho_c V_{cp}^2}{16r_{cp}} \sin 2\theta \right) \delta
\end{aligned} \tag{A-9}$$

The forces exerted on the part I include pressure and viscous force

$$\begin{aligned}
F_y^I &= \int_0^{\theta_s} (P \cos \theta + \tau_{s_1} \sin \theta) 2\pi r_p^2 \sin \theta d\theta \\
&= 2\pi r_p^2 \left[\left(P_0 + \rho_c \frac{V_{cp}^2}{2} \right) \frac{\sin^2 \theta_s}{2} - \frac{\rho_c g r_p}{3} (\cos^3 \theta_s - 1) - \frac{9\rho_c V_{cp}^2}{32} \sin^4 \theta_s \right] \\
&\quad + 2\pi r_p^2 \left[\left(\frac{3\mu V_{cp}}{2\delta} + \frac{\rho_c g \delta}{2} \right) \left(\frac{1}{3} \cos^3 \theta_s - \cos \theta_s + \frac{2}{3} \right) + \frac{9\rho_c \delta V_{cp}^2}{32r_p} \sin^4 \theta_s \right]
\end{aligned} \tag{A-10}$$

The force exerted on the part II can be calculated as

$$\begin{aligned}
F_y^{II} &= \int_{\theta_s}^{\pi} P_{\theta_s} 2\pi r_p^2 \sin \theta \cos \theta d\theta \\
&= 2\pi r_p^2 \left[- \left(P_0 + \rho_c \frac{V_{cp}^2}{2} \right) \frac{\sin^2 \theta_s}{2} - \frac{\rho_c g r_p}{2} \cos \theta_s \sin^2 \theta_s + \frac{9\rho_c V_{cp}^2}{16} \sin^4 \theta_s \right]
\end{aligned} \tag{A-11}$$

The total force is

$$F_y = F_y^I + F_y^{II} . \tag{A-12}$$

The drag coefficient can be written as

$$\begin{aligned}
C_{D-fb} &= \frac{F_y}{\pi r_p^2 \frac{1}{2} \rho_c V_{cp}^2} \\
&= \frac{9}{8} \left(1 + \left(\frac{2\delta}{D_p} \right) \right) (1 - \cos^2 \theta_s)^2 \\
&\quad + \frac{12\mu}{V_{cp} D_p \rho_c} \left(\frac{2\delta}{D_p} \right)^{-1} \left(\frac{1}{3} \cos^3 \theta_s - \cos \theta_s + \frac{2}{3} \right) \\
&\quad - \frac{2D_p g}{V_{cp}^2} \left(\frac{1}{2} \cos \theta_s - \frac{1}{6} \cos^3 \theta_s + \frac{1}{3} \right) \\
&\quad + \frac{D_p g}{V_{cp}^2} \left(\frac{2\delta}{D_p} \right) \left(\frac{1}{3} \cos^3 \theta_s - \cos \theta_s + \frac{2}{3} \right)
\end{aligned} \tag{A-13}$$

with

$$\left(\frac{\delta}{D_p}\right)^3 + \frac{3\mu V_{cp}}{2D_p^2 \rho_c g} \left(\frac{\delta}{D_p}\right) = \frac{\Gamma \mu_0}{D_p^2 \rho_c^2 g \rho}. \quad (\text{A-14})$$

and

$$\cos \theta_s = -\frac{8\mu}{3D_p V_{cp} \rho c} \left(\frac{\delta}{D_p}\right)^{-2} - \frac{2D_p g}{9V_{cp}^2}. \quad (\text{A-15})$$

Appendix B: Drag coefficient for a single particle under turbulent flow condition

The governing equations for the vapor in the film are

$$\frac{\partial \rho u}{\partial x} = 0, \quad (\text{B-1})$$

$$\frac{\partial \rho u^2}{\partial x} = -\frac{\partial P}{\partial x} - \rho g \sin \theta + \mu \frac{\partial^2 u}{\partial y^2}. \quad (\text{B-2})$$

The boundary conditions are

$$y=0; \quad u=0,$$

$$y=\delta; \quad u=u_i.$$

The interfacial velocity is

$$u_i = AV_{cp} \sin \theta. \quad (\text{B-3})$$

From equations (B-1) and (B-2) we can obtain

$$\frac{\partial P}{\partial x} = -\rho_c g \sin \theta + \mu \frac{\partial^2 u}{\partial y^2}. \quad (\text{B-4})$$

The pressure distribution is

$$P(\theta) = P_0 + \rho_c g r_p \cos \theta + \rho_c \frac{V_{cp}^2}{2} - B \rho_c \frac{(1 - A \sin \theta)^2}{2} V_{cp}^2 - \frac{\rho_c}{2} (AV_{cp} \sin \theta)^2. \quad (\text{B-5})$$

Then

$$\frac{\partial P}{\partial x} = -\rho_c g \sin \theta - \frac{1}{2r_p} A^2 \rho_c V_{cp}^2 \sin 2\theta + \frac{1}{r_p} AB \rho_c (1 - A \sin \theta) \cos \theta V_{cp}^2. \quad (\text{B-6})$$

By combining the equations (B-3) and (B-5), we can get

$$\mu \frac{\partial^2 u}{\partial y^2} = -(\rho_c - \rho)g \sin \theta - \frac{1}{2r_p} \rho_c V_{cp}^2 \sin 2\theta + \frac{1}{r_p} AB \rho_c (1 - A \sin \theta) \cos \theta V_{cp}^2. \quad (\text{B-7})$$

Then the velocity distribution can be obtained

$$\begin{aligned} u = & \frac{y}{\delta} AV_{cp} \sin \theta - \left(\frac{(\rho_c - \rho)g}{2\mu} \sin \theta + \frac{\rho_c V_{cp}^2}{4\mu r_p} A^2 \sin 2\theta \right) (y^2 - y\delta) \\ & + \frac{1}{2\mu r_p} B \rho_c (1 - A \sin \theta) A \cos \theta V_{cp}^2 (y^2 - y\delta) \end{aligned} \quad (\text{B-8})$$

The viscous force on the particle surface can be written as

$$\begin{aligned}
\tau_{s_1} &= \mu \frac{\partial u}{\partial y} \Big|_{y=0} \\
&= \frac{\mu}{\delta} A V_{cp} \sin \theta + \left(\frac{(\rho_c - \rho)g}{2} \sin \theta + \frac{\rho_c V_{cp}^2}{4 r_{cp}} A^2 \sin 2\theta \right) \delta \\
&\quad - \frac{1}{2r_p} B \rho_c (1 - A \sin \theta) A \cos \theta V_{cp}^2 \delta.
\end{aligned} \tag{B-9}$$

The forces exerted on the part I include pressure and viscous force

$$\begin{aligned}
F_y^I &= \int_0^{\theta_s} (P \cos \theta + \tau_{s_1} \sin \theta) 2\pi r_p^2 \sin \theta d\theta \\
&= 2\pi r_p^2 \left[\left(P_0 + \rho_c \frac{V_{cp}^2}{2} \right) \frac{\sin^2 \theta_s}{2} - \frac{\rho_c g r_p}{3} (\cos^3 \theta_s - 1) - \frac{A^2 \rho_c V_{cp}^2}{8} \sin^4 \theta_s \right] \\
&\quad - 2\pi r_p^2 \left[\frac{B \rho_c V_{cp}^2}{2} \left(\frac{1}{2} \sin^2 \theta_s - \frac{2A}{3} \sin^3 \theta_s + \frac{A^2}{4} \sin^4 \theta_s \right) \right] \\
&\quad + 2\pi r_p^2 \left[\left(\frac{\mu V_{cp}}{\delta} + \frac{\rho_c g \delta}{2} \right) \left(\frac{1}{3} \cos^3 \theta_s - \cos \theta_s + \frac{2}{3} \right) + \frac{\rho_c \delta V_{cp}^2}{8 r_p} A^2 \sin^4 \theta_s \right] \\
&\quad - 2\pi r_p^2 \left[\frac{B \rho_c V_{cp}^2 \delta A}{2 r_{cp}} \left(\frac{1}{3} \sin^3 \theta_s - \frac{A}{4} \sin^4 \theta_s \right) \right].
\end{aligned} \tag{B-10}$$

The force exerted on the part II can be calculated as

$$\begin{aligned}
F_y^{II} &= \int_{\theta_s}^{\pi} P_{\theta_s} 2\pi r_p^2 \sin \theta \cos \theta d\theta \\
&= 2\pi r_p^2 \left[- \left(P_0 + \rho_c \frac{V_{cp}^2}{2} \right) \frac{\sin^2 \theta_s}{2} - \frac{\rho_c g r_p}{2} \cos \theta_s \sin^2 \theta_s + \frac{\rho_c V_{cp}^2}{4} \sin^4 \theta_s \right] \\
&\quad + 2\pi r_p^2 \left[\frac{B \rho_c V_{cp}^2}{4} (1 - A \sin \theta_s)^2 \sin^2 \theta_s \right]
\end{aligned} \tag{B-11}$$

The total force is

$$F_y = F_y^I + F_y^{II}. \tag{B-12}$$

The drag coefficient can be written as

$$C_{D-fb} = \frac{F_y}{\pi r_p^2 \frac{1}{2} \rho_c V_{cp}^2}$$

$$\begin{aligned}
&= \frac{A^2}{2} \left(1 + \left(\frac{2\delta}{D_p} \right) \right) \left(1 - \cos^2 \theta_s \right) + \frac{4A\mu}{V_{cp} D_p \rho_c} \left(\frac{2\delta}{D_p} \right)^{-1} \left(\frac{1}{3} \cos^3 \theta_s - \cos \theta_s + \frac{2}{3} \right) \\
&- \frac{2D_p g}{V_{cp}^2} \left(\frac{1}{2} \cos \theta_s - \frac{1}{6} \cos^3 \theta_s + \frac{1}{3} \right) + \frac{D_p g}{V_{cp}^2} \left(\frac{2\delta}{D_p} \right) \left(\frac{1}{3} \cos^3 \theta_s - \cos \theta_s + \frac{2}{3} \right) \\
&- \left[2B \left(\frac{1}{3} A \sin^3 \theta_s - \frac{1}{4} A^2 \sin^4 \theta_s \right) + \frac{2AB\delta}{r_p} \left(\frac{1}{3} \sin^3 \theta_s - \frac{1}{4} A \sin^4 \theta_s \right) \right] \quad (B-13)
\end{aligned}$$

where θ_s satisfies

$$\left(\frac{A^2 V_{cp}}{2} + \frac{BA^2 V_{cp}}{2} \right) \cos \theta_s - \frac{AB V_{cp}}{2} \frac{\cos \theta_s}{\sin \theta_s} + \left(\frac{AD_p \mu}{2\delta^2 \rho_c} + \frac{gD_p}{4V_{cp}} \right) = 0 \quad (B-14)$$

and

$$6\delta (AV_{cp}\mu + \rho_c g \delta^2) = \frac{6\Gamma \mu D_p^2}{\rho} \quad (B-15)$$

Appendix C: Instability Analysis on the Surface of a Droplet

The Taylor instability is one of the mechanisms proposed to study the fragmentation in fuel coolant interactions (FCIs). Based on the Taylor instability, Inoue [1] developed an analytical model on vapor explosion of a high temperature molten metal droplet in water induced by a pressure pulse to study the vapor film collapse. Epstein [2] studied the stability of a submerged frozen crust. Cooper [3] studied the Taylor instabilities in fuel coolant interactions, which show that the instability of a droplet with a solid shell under acceleration is possible under a given condition. In this study the instability of a melt droplet immersed into coolant is studied based on the method developed by Plesset [4], in order to calculate the growth rate of the spikes on the droplet surface, which is taken as the fragments.

The configuration for instability analysis is that a spherical droplet (liquid) with density of ρ and a radius of R is immersed into a fluid (coolant) with density ρ_c , occupies the region exterior to this droplet and $\rho \gg \rho_c$, as shown in Fig. C-1. The fluids are assumed to be immiscible, incompressible and non-viscous. The initial and boundary conditions have symmetry, then the motion for the unperturbed surface of the droplet can be written as [4]

$$\ddot{R} + \frac{3}{2} \frac{\dot{R}^2}{R} = \frac{P - P_c - 2\sigma_t / R}{\rho R}, \quad (\text{C-1})$$

where P is the pressure in the droplet, P_c is the ambient pressure, ρ is the density of the droplet, σ_t is the surface tension, R is the radius of the droplet, \dot{R} is the velocity of the surface and \ddot{R} is the acceleration exerted on the surface. The differential equation for the disturbance a on the surface of the droplet can be written as

$$\ddot{a} + 3\frac{\dot{R}}{R}\dot{a} - Aa = 0, \quad (\text{C-2})$$

where

$$A = \frac{[\rho_v n(n-1) - \rho (n+1)(n+2)]\ddot{R} - \frac{\sigma_l}{R^2} n(n^2-1)(n+2)}{(n\rho_v + (n+1)\rho)R}, \quad (C-3)$$

n is the wave number on the surface of the droplet. By using transformation of

$$a = \left(\frac{R_0}{R}\right)^{\frac{3}{2}} \alpha, \quad (C-4)$$

the disturbance equation for α becomes

$$\ddot{\alpha} - G(t)\alpha = 0, \quad (C-5)$$

where

$$G(t) = \frac{3}{4} \frac{\dot{R}^2}{R^2} - \frac{\ddot{R}}{R} \left(n + \frac{1}{2}\right) - \frac{n(n-1)(n+2)\sigma_l}{R^3 \rho}. \quad (C-6)$$

If the instability index $G(t)$ is positive, from Eq. (C-5), the α increases with time, meaning that the perturbation grows. Conversely, that the α decreases with time means that the perturbation decreases.

For the case of vapor film collapse around the droplet, which is induced by the external pressure pulse or by the boiling effect, a pressure pulse is generated in the vapor film surrounding the droplet (see Appendix D), resulting $\ddot{R} < 0$. Comparing with the first and second terms in the right side of Eq. (C-6), the third term, surface tension term, can be neglected. From Eq. (C-6), it is shown that the $G(t) > 0$ and it is an unstable factor, resulting in an instability on the surface of the droplet.

For the case that the fragmentation is triggered by the solidification on the surface of a droplet, the velocity term can be neglected (it is smaller than other terms), then Eq. (C-6) can be written as

$$G(t) = -\frac{\ddot{R}}{R} \left(n + \frac{1}{2}\right) - \frac{n(n-1)(n+2)\sigma_l}{R^3 \rho}. \quad (C-7)$$

From Eq. (C-7) it is shown that when

$$\ddot{R} < -\frac{n(n-1)(n+2)\sigma_l}{R^2 \rho \left(n + \frac{1}{2}\right)}, \quad (C-8)$$

the $G(t) > 0$ and it is an unstable factor, which means that the perturbation on the surface

of the droplet grows. Conversely it is a stable factor.

During the freezing process of the surface, a solid shell is formed. The shell shrinks, squeezes the liquid part of the droplet and generates a pressure pulse on the interface between the solid shell and liquid inside the droplet. It can be thought that the generated pressure is exerted on the surface of the liquid part. Then this instability analysis method can be applied to the liquid droplet.

Due to the existence of the solid shell, its effect on the instability should be considered. In this study a total surface tension concept is introduced to study the effect. The total surface tension, which includes surface tension and the stiffness of the shell, is defined as (see Appendix E)

$$\sigma_t = \sigma + \frac{D_s}{2R^2}, \quad (\text{C-9})$$

where σ_t is the total surface tension of the droplet including shell stiffness, which is very large and can not be neglected, and D_s is the shell stiffness.

During the first several milliseconds of the freezing of the droplet surface, the left side of the Eq. (C-8) (minus) is much less than the right side, from Eq. (C-7), it is shown that the $G(t) > 0$ and it is an unstable factor, resulting in an instability of the droplet surface. This analysis means during the freezing process of the surface shell, the instability of the droplet can be induced. The detailed calculation is shown in Appendix E.

The analysis shows that in all three cases that the fragmentation is triggered by the boiling effect, the external pressure pulse or the solidification on the droplet surface, $\ddot{R} < 0$, and $G(t) > 0$, resulting in an instability on the surface of the droplet. The instability can be proposed as the mechanism of the thermal fragmentation, which will be used to develop the fragmentation rate model.

In order to obtain the grow rate of the perturbation on the surface of the droplet, an exponential solution of $a = a_0 e^{kt}$ is considered for Eq. (C-2), then one has the following equation

$$k^2 + \frac{3\dot{R}}{R}k - A = 0, \quad (\text{C-10})$$

and roots are

$$k_{1,2} = \frac{-\frac{3\dot{R}}{R} \pm \sqrt{\left(\frac{3\dot{R}}{R}\right)^2 + 4A}}{2}. \quad (\text{C-11})$$

Comparing with the acceleration term, the velocity term can be neglected, then one can obtain

$$k = \sqrt{-(n+2)\frac{\ddot{R}}{R} - (n-1)(n+2)n\frac{\sigma_t}{R^3\rho}}. \quad (\text{C-12})$$

The larger the positive roots, the greater the growth of a is. The maximum k (the fastest growth mode) can be found from $\frac{dk}{dn} = 0$, one has

$$n_m = \frac{1}{3} \sqrt{1 - 3\left(\frac{\ddot{R}R^2\rho}{\sigma_t} - 2\right)} \quad (\text{C-13})$$

where n_m is the wave number on the surface, at which the perturbations growth is the fastest.

Substituting Eq. (C-13) into Eq. (C-12), finally the growth rate of the perturbations (spikes) on the surface of the droplet can be obtained by

$$\dot{a} = a_0 k_m e^{k_m t}. \quad (\text{C-14})$$

In order to calculate the growth rate of the spikes on the surface, the acceleration exerted on the surface of the droplet is required, which is calculated by

$$\ddot{R} = \frac{P - P_c}{R\rho}. \quad (\text{C-15})$$

The pressure $P - P_c$ is calculated by the vapor film collapse model or by surface solidification model, developed in Appendices D and E, respectively. Then the growth rate of the spikes on the surface of the droplet can be obtained by Eq. (C-14). In this study this growth rate is assumed to be the fragmentation rate of the droplet. Several examples are calculated by this developed model. The results are described in the main body of this report.

References

- (1) A. Inoue, M. Aritomi, M. Takahashi and Y. Tobita, An analytical model on vapor explosion of a high temperature molten metal drop in water induced by a pressure pulse, Chem. Eng. Comm. 1992, Vol. 118, pp. 189-206.
- (2) M. Epstein, Stability of a submerged frozen curst, Transactions of the ASME, Journal of Heat Transfer, Vol. 99, pp.527-532, Nov. 1977.
- (3) F. Cooper and J. dienes, The role of Rayleigh-Taylor instabilities in Fuel Coolant Interactions, Nucl. Sci. Eng., Vol. 68, pp. 308-321, 1978.
- (4) M.S. Plesset, On the stability of fluid flows with spherical symmetry, Journal of Applied Physics, Vol. 25, No. 1, 1954.

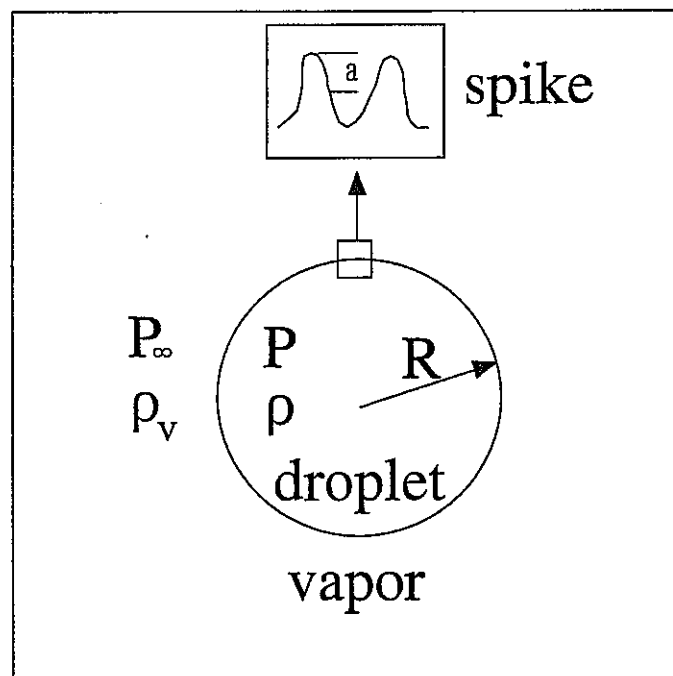


Fig. C- 1 The instability analysis model

Appendix D: Vapor Film Collapse Model

The pressure pulse generation in a vapor film during its collapse is required to calculate the spikes growth on the surface of a melt droplet. The spikes are assumed to be the fragments. In this study, the vapor film collapse is modeled, which is similar to the method developed by Corradini [1][2]. The analytical model is shown in Fig. D-1. The dynamic vapor film collapse process is modeled by writing a momentum equation for vapor film dynamics and an energy equation for each region, as shown in Fig. D-1, droplet, coolant vapor and coolant liquid, and linking each region by the appropriate boundary conditions. The equilibrium is assumed on the interface between the vapor and coolant liquid. The integral approach is used in each region for the energy equations where the differential equation is integrated over the region and a temperature profile is assumed. The model will be described in detail in the following.

The momentum equation for vapor film growth is modeled by the Rayleigh equation that neglects the effects of viscosity in a spherically symmetric system.

$$\frac{dU}{dt} + \frac{3}{2} \frac{U^2}{R_\delta} = \frac{P_v - P_\infty}{\rho_c R_\delta}, \quad (D-1)$$

where P_v is the pressure in the vapor film, P_∞ is the ambient pressure, ρ_c is the density of the coolant liquid, U is the velocity of the liquid on the interface of the coolant liquid/vapor and R_δ is the sum of the radius of the droplet and the thickness of the vapor film,

$$R_\delta = R + \delta. \quad (D-2)$$

The ambient pressure during the growth of the vapor film is held constant. To initiate the film collapse, the ambient pressure is raised to a value of pressure pulse P_p for a specified time τ_p .

Considering the evaporation of the coolant liquid on the interface, the velocity of the interface is given by

$$\frac{dR_\delta}{dt} = U + \frac{dm_v/dt}{4\pi R_\delta^2 \rho_c}, \quad (D-3)$$

where $\frac{dm_v}{dt}$ is the evaporation (or condensation) rate on the interface, which can be calculated by the energy equation of the vapor,

$$\frac{dm_v e_v}{dt} = \dot{Q} - P_v \frac{dV}{dt} + \dot{m}_v h_v, \quad (D-4)$$

where the internal energy of the vapor is

$$e_v = h_v - \frac{P_v}{\rho_v}, \quad (D-5)$$

the volume of the vapor film is

$$V = \frac{4}{3} \pi (R_\delta^3 - R^3), \quad (D-6)$$

the enthalpy of vapor is

$$h_v = c_p T_v, \quad (D-7)$$

and

$$\dot{Q} = \frac{2k_v}{\delta} (T_i - T_v) + \frac{2k_v}{\delta} (T_s - T_v), \quad (D-8)$$

where T_i is the temperature on the interface between the coolant vapor and liquid, T_s is the temperature on the surface of the droplet. The boundary conditions on the surface of the droplet and the interface of the coolant liquid/vapor can be written as

$$k_h \left. \frac{\partial T_h}{\partial r} \right|_{r=R} = k_v \left. \frac{\partial T_v}{\partial r} \right|_{r=R} + \varepsilon_r \sigma_r (T_s^4 - T_i^4) \quad (D-9)$$

and

$$k_c \left. \frac{\partial T_c}{\partial r} \right|_{r=R+\delta} + \frac{dm_v}{dt} h_{fg} = k_v \left. \frac{\partial T_v}{\partial r} \right|_{r=R+\delta} + \varepsilon_r \sigma_r (T_s^4 - T_i^4) + q \quad (D-10)$$

respectively. The last term in the right hand side of Eq. (D-10) is added to consider the boiling effect (local liquid-liquid contact). When the heat transfer mode changes from film boiling to nucleate boiling, the heat transfer flux is increased. From the boiling curve for saturated pool boiling of water at atmospheric pressure, the heat transfer flux change is about $8 \times 10^5 \text{ W/m}^2$, as shown in Fig. 5-1.

The temperature changes with time inside the droplet and coolant liquid near the

vapor film can be written as

$$\frac{\partial T_h}{\partial t} = \frac{\alpha_h}{r^2} \frac{\partial}{\partial r} \left(r^2 \frac{\partial T_h}{\partial r} \right), \quad (\text{D-11})$$

and

$$\frac{\partial T_c}{\partial t} + \frac{\partial r}{\partial t} \frac{\partial T_c}{\partial r} = \frac{\alpha_c}{r^2} \frac{\partial}{\partial r} \left(r^2 \frac{\partial T_c}{\partial r} \right), \quad (\text{D-12})$$

where $\alpha_h = \frac{k_h}{\rho_h c_{ph}}$ and $\alpha_c = \frac{k_c}{\rho_c c_{pc}}$.

The pressure in the vapor film and the temperature on the interface are calculated by the equation of state of the coolant

$$P_v = P_v(T_v, \rho_v) \quad (\text{D-13})$$

and

$$T_i = T_{sat}(P_v) \quad (\text{D-14})$$

The temperature distributions in the r direction in the droplet and the coolant liquid are required to solve these equations. Here a quadratic temperature distribution in the droplet is assumed

$$T_h = T_{hc} + (T_s - T_{hc}) \left(1 - \frac{x}{\lambda_h} \right)^2 \quad (\text{D-15})$$

where $x = R - r$. The temperature distribution in the coolant liquid is assumed as

$$T_c = T_{c0} + (T_i - T_{c0}) \left(1 - \frac{x}{\lambda_c} \right)^2 \quad (\text{D-16})$$

where $x = r - R + \delta$.

The six differential equations with six unknown variables can be solved by the Runge-Kutta-Gill method. An example is calculated, in which the vapor film collapse is induced by an external pressure pulse. The initial conditions are based on the conditions of Nelson's experiments. The pressure generation in the vapor film during the collapse is plotted in Fig. D-2, showing that the amplitude of the generated pressure is the several times as that of the input pressure pulse, the triggering pressure pulse. The generated pressure pulse can induce the instability of the droplet surface according to the instability analysis in Appendix C. The instability causes the fragmentation of the droplet, which

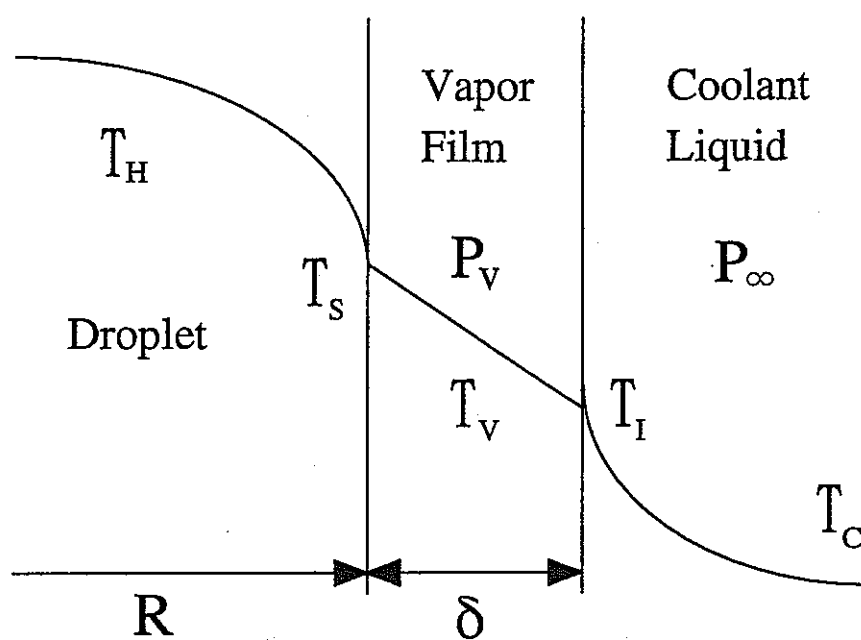


Fig. D- 1 The analytical model for vapor film collapse

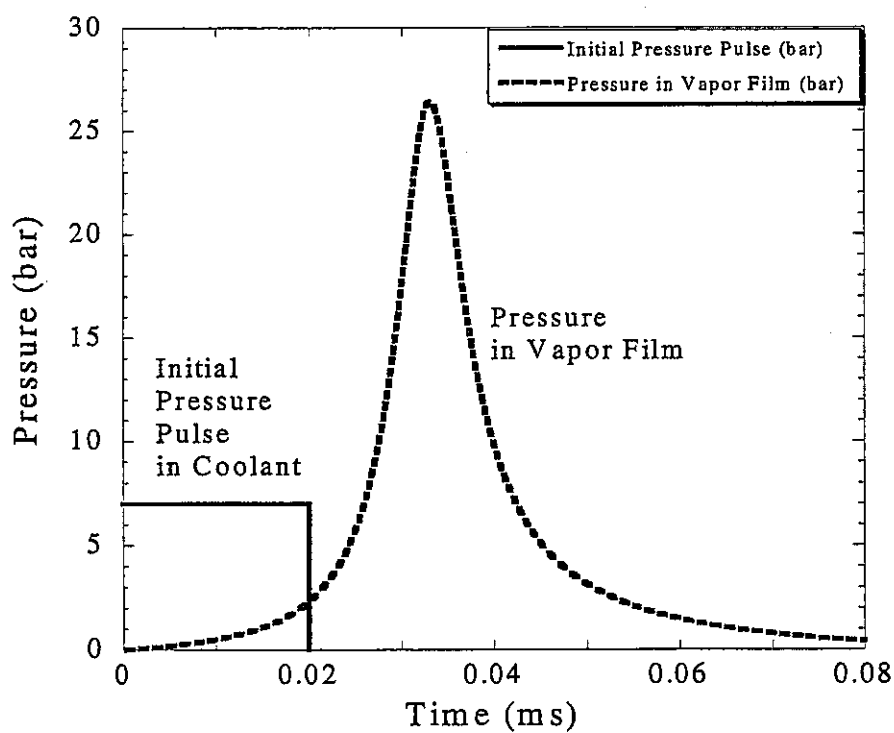


Fig. D- 2 The generated pressure in the vapor film during the collapse induced by external pressure pulse

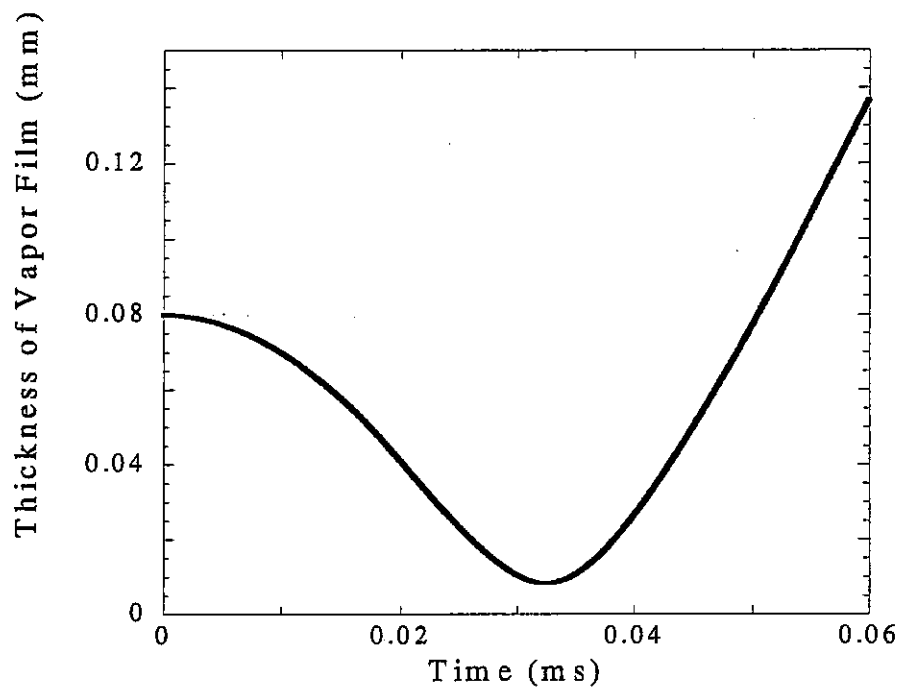


Fig. D- 3 The thickness of the vapor film during the collapse induced by external pressure pulse

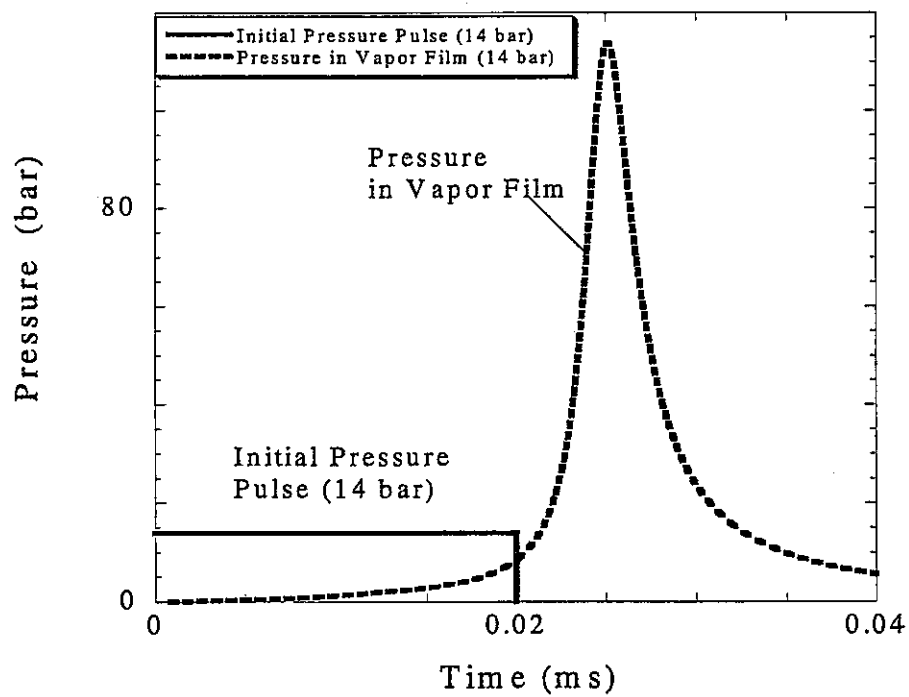


Fig. D- 4 The initial pressure pulse effect on the generated pressure in the vapor film during the collapse induced by external pressure pulse

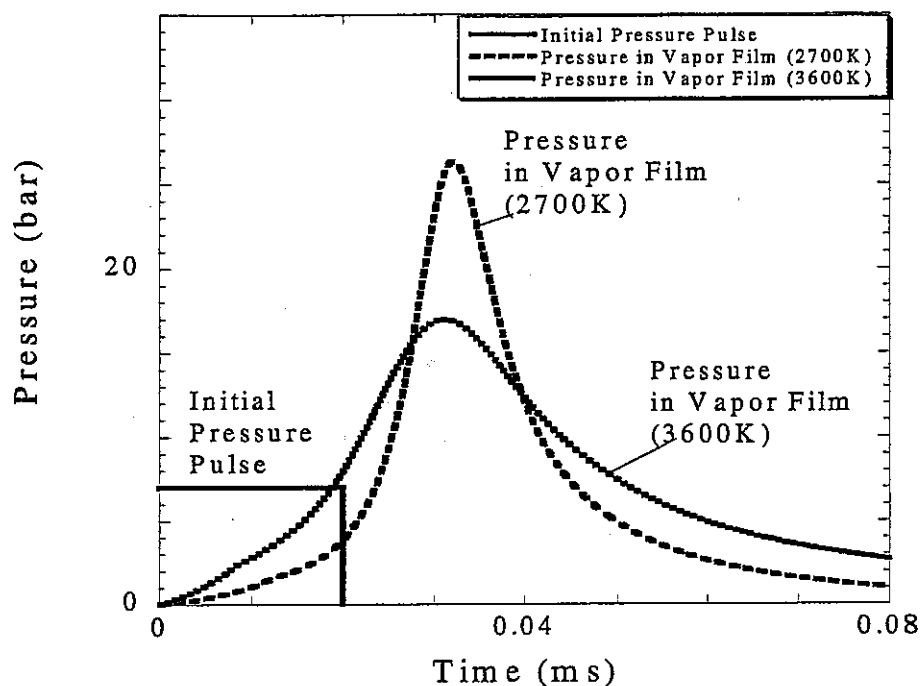


Fig. D- 5 The droplet temperature effect on the generated pressure in the vapor film during the collapse induced by external pressure pulse

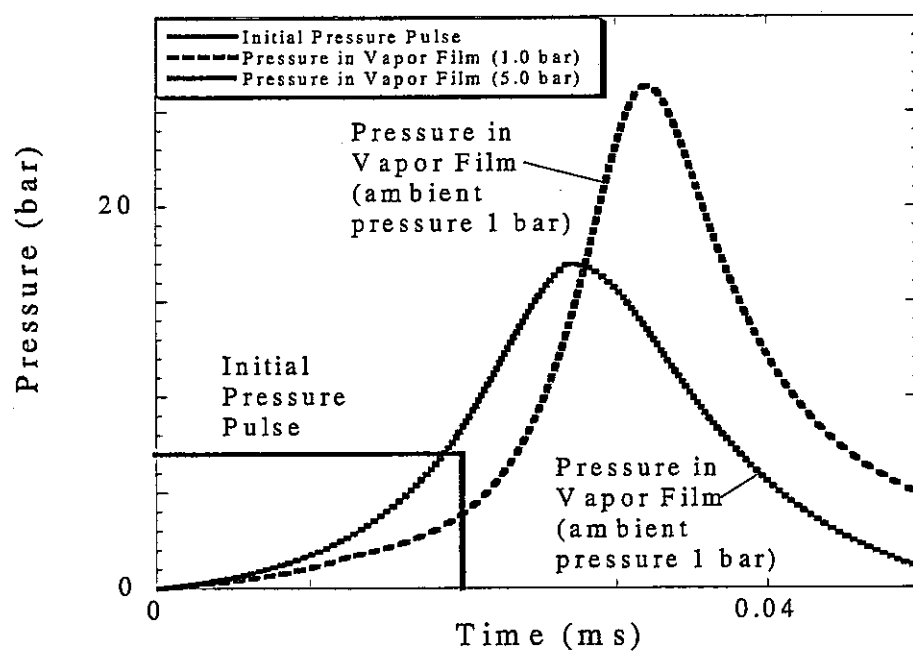


Fig. D- 6 The ambient pressure effect on the generated pressure in the vapor film during the collapse induced by external pressure pulse

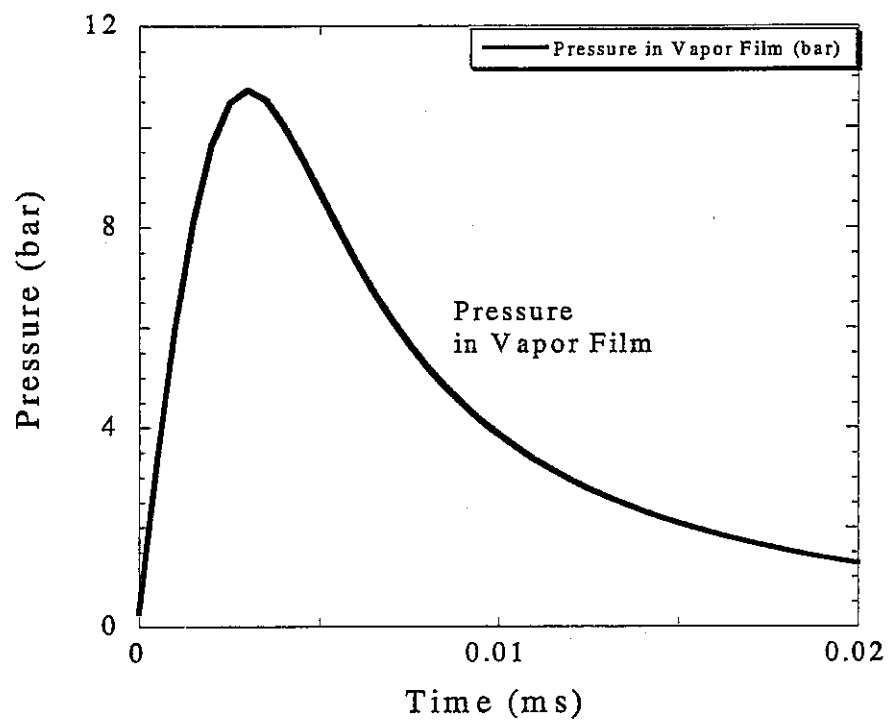


Fig. D- 7 The generated pressure in the vapor film due to heat transfer model change

Appendix E: Estimation of the pressurization in a melt droplet immersed into coolant

When a melt droplet is exposed to a coolant liquid, solidification begins on its surface and the hot molten material is encased in a thin solid shell. The shell shrinks, squeezes the liquid part of the droplet and generates a pressure on the interface between the solid shell and liquid inside the droplet. Cronenberg [1,2,3] analyzed UO₂ solidification in sodium and indicated that the heat transfer controlled solidification velocity is dominant comparing crystal growth rate. Hsiao [4] developed a heat conduction model to calculate the stress in the solid shell during the solidification process. In this section the model of the surface solidification due to heat conduction will be derived to calculate the pressure generation inside the droplet with a solid shell, which is similar to the model used by Cronenberg and Hsiao.

The analytical model of the solidification on the surface of a droplet is shown in Fig. E-1. The heat transfer between the droplet and coolant can be written as convection heat transfer. The solidification progresses inward with an spherically moving interface. At the interface between the solid shell and the molten metal inside, the temperature is always equal to the melting temperature with constant. Due to the temperature distribution in the solid shell, the deformation induced in the solid shell tends to compress the inner liquid region and the pressurization on the interface may be induced during the solidification process. The thermal stresses [5] for the hollow spherical shell with inside radius η and outside radius R due to the temperature are:

for $\eta \leq r \leq R$,

$$\sigma_r = \frac{2\alpha_i E}{1 - \nu} \left[\frac{r^3 - \eta^3}{(R^3 - \eta^3)^3} \int_{\eta}^R T(r) r^2 dr - \frac{1}{r^3} \int_{\eta}^r T(r) r^2 dr \right] \quad (\text{E-1})$$

and

$$\sigma_{\theta} = \frac{2\alpha_i E}{1 - \nu} \left[\frac{2r^3 + \eta^3}{2(R^3 - \eta^3)^3} \int_{\eta}^R T(r) r^2 dr + \frac{1}{2r^3} \int_{\eta}^r T(r) r^2 dr - T(r) \right] \quad (\text{E-2})$$

where σ_r and σ_{θ} are the stresses in radial and tangential direction due to the temperature distribution, α_i is the coefficient of thermal expansion, E is Young's

modulus and P_s is the Poisson's ratio for the shell. The corresponding radial displacement relation is

$$\Delta r_i = \frac{\eta}{E} [\sigma_u - P_s(\sigma_{ri} + \sigma_u)] + \alpha_i T(r) \eta. \quad (\text{E-3})$$

The stresses due to the pressurization [6] can be described by the following:

for $\eta \leq r \leq R$, the stresses

$$\sigma_{rp} = \frac{p_m \eta^3 (R^3 - r^3)}{r^3 (\eta^3 - R^3)} \quad (\text{E-4})$$

and

$$\sigma_{\theta p} = \frac{-p_m \eta^3 (2r^3 + R^3)}{2r^3 (\eta^3 - R^3)}, \quad (\text{E-5})$$

where σ_{rp} and $\sigma_{\theta p}$ are the stresses in radial and tangential direction due to pressurization inside the droplet and p_m is the pressure. The corresponding radial displacement relation is

$$\Delta r_p = \frac{\eta}{E} [\sigma_{\theta p} - P_s(\sigma_{rp} + \sigma_{\theta p})] \quad (\text{E-6})$$

Here it is assumed that the radial displacement would be zero at the interface. Then the pressure induced inside the droplet can be evaluated as

$$P_m = \frac{6\alpha_i E}{R^3 + 2\eta^3 - P_s(4\eta^3 - R^3)} \int_{\eta}^R T(r) r^2 dr. \quad (\text{E-7})$$

For the simplicity to solve the temperature distribution in the shell, the heat conduction equation at steady-state is considered as

$$\frac{d^2[rT(r)]}{dr} = 0 \quad (\text{E-8})$$

with boundary conditions

$$-k \frac{dT(r)}{dr} \Big|_{r=R} = hT(R), \quad (\text{E-9})$$

$$k \frac{dT(r)}{dr} \Big|_{r=\eta} = \rho L \frac{d\eta}{dt} \quad (\text{E-10})$$

and

$$T(\eta) = T_m - T_c \quad (\text{E-11})$$

Then the temperature distribution can be obtained

$$T(r) = T(\eta) \frac{\left(\frac{\eta}{R}\right) \left[1 + \left(\frac{r}{R}\right) \left(\frac{1}{Bi} - 1\right)\right]}{\left(\frac{r}{R}\right) \left[1 + \left(\frac{\eta}{R}\right) \left(\frac{1}{Bi} - 1\right)\right]} \quad (\text{E-12})$$

By solving the heat conduction equations, the pressure in the shell is obtained as

$$P_m = \alpha_t E (T_m - T_c) \frac{3 \left[\left(\frac{\eta}{R}\right) - \left(\frac{\eta}{R}\right)^3 \right] + 2 \left[\left(\frac{\eta}{R}\right) - \left(\frac{\eta}{R}\right)^4 \right] \left(\frac{1}{Bi} - 1\right)}{\left[1 + 2 \left(\frac{\eta}{R}\right)^3 + P_s - 4 P_s \left(\frac{\eta}{R}\right)^3 \right] \left[1 + \left(\frac{\eta}{R}\right) \left(\frac{1}{Bi} - 1\right) \right]}, \quad (\text{E-13})$$

where Bi is the Biot number (hR/k), k is thermal conductivity, h is unit surface thermal conductance, R is the radius of the droplet, η is the radius of the interface of the solid and melt liquid, α_t is the coefficient of thermal expansion, E is Young's modulus, T_m is the fusion temperature and T_c is the coolant temperature.

The thickness of the solid shell δ can be calculated by equation (E-10) as

$$\frac{d\delta}{dt} = \frac{k(T_m - T_c)}{\rho L (R - \delta) \left[1 + \left(1 - \frac{\delta}{R}\right) \left(\frac{1}{Bi} - 1\right) \right]}, \quad (\text{E-14})$$

where L is the latent heat of fusion and k is the heat conductivity. The generated pressure in the droplet and the thickness of the shell can be obtained from Eq. (E-13) and Eq. (E-14). In the following the instability on the surface of the droplet induced by the generated pressure will be discussed.

Epstein [7] studied the stability of a submerged frozen crust under the gravitation by considering the elastic crust stiffness and concluded that the stability depends on a race between the fuel crust growth process and the rate of the development of the perturbation. Yang [8] studied the solidification effects on the fragmentation of a molten metal droplet behind a pressure shock wave. Cooper [9] examined the effect of freezing on instability growth and concluded that instability growth is possible under a given condition. These studies show that the instability of the droplet with a solid shell under a given acceleration is possible, but, in this study, the instability of a melt droplet induced by the freezing process on its surface will be discussed.

During the freezing process on the surface, a solid shell is formed. The shell shrinks, squeezes the liquid part of the droplet and generates a high pressure on the interface between the solid shell and liquid inside the droplet. It can be thought that the generated pressure is exerted on the surface of the liquid part. At the early stage of the solidification, the pressure increases sharply. If the squeezing situation is considered, the pressure inside the liquid is lower than that exerted on the interface, which can be considered as $\Delta P < 0$, then $\ddot{R} < 0$. If only the surface tension on the liquid surface is considered, one has $G(t) > 0$, resulting in an instability. The detailed instability analysis is described in Appendix C.

Due to the existence of the solid shell, its effect on the instability should be considered. The schematic model of the solid shell stability is plotted in Fig. E-2. Considering the solid shell with elasticity, the force balance across the interfacial shell of a plate between two fluids with a perturbation under pressure action across the interface is given

$$D_s \frac{\partial^4 a}{\partial x^4} + 2\sigma \frac{\partial^2 a}{\partial x^2} = P_2 - P_1, \quad (\text{E-15})$$

where $P_2 - P_1$ is the pressure difference across the solid shell and D_s is the shell stiffness, which can be written as [5,10]

$$D_s = \frac{E\delta^3}{12(1 - P_s^2)}, \quad (\text{E-16})$$

where δ is the thickness of the shell, P_s is the Poisson's ratio for the shell and E is the Young's modulus. The force balance across the interfacial solid shell, considering the curvature, can be written as

$$P_2 - P_1 = \frac{D_s}{R^3} + \frac{2\sigma}{R} \quad (\text{E-17})$$

where R is the curvature of the shell.

If the surface tension of the liquid region and the solid shell elasticity are considered as a stabilization tension, named as total surface tension, it can be written as

$$\sigma_t = \sigma + \frac{D_s}{2R^2} \quad (\text{E-18})$$

where σ is the surface tension on the interface and σ_i is the surface tension of the droplet including the term of shell stiffness. The second term in above equation represents the shell elasticity, which acts to stabilize the shell.

After the total surface tension is introduced in this study, for the case that the fragmentation is induced by the solidification of the droplet surface, the instability analysis method (described in Appendix C) can be applied to the liquid droplet including a solid shell. The instability index on the surface can be written as

$$G(t) = -\frac{\ddot{R}}{R} \left(n + \frac{1}{2} \right) - \frac{n(n-1)(n+2)\sigma_i}{R^3 \rho}. \quad (\text{E-19})$$

If the instability index satisfies

$$\ddot{R} < -\frac{n(n-1)(n+2)\sigma_i}{R^2 \rho \left(n + \frac{1}{2} \right)}, \quad (\text{E-20})$$

one has instability.

An example is calculated to discuss the instability of a droplet during the freezing process. The initial conditions are based on the MIXA-06 experiment. A UO₂ droplet with a radius of 3mm and a fusion temperature of 3120K is immersed into water with a temperature of 370K. The thickness of the solid shell, the total surface tension and the generated pressure are plotted in Figs. E-5 to E-7 in the main body of this report. In the range of the time scale of the fragmentation (several milliseconds), the total surface tension is not increased very large. During this period, the generated pressure increases to several dozens bars. That means the instability can be induced by the solidification on the droplet surface, as shown in Fig. E-8 (showing positive instability index) in the main body of this report.

In order to investigate the influence of the parameters on the pressure generation, based on this example, several cases are calculated. The effects of the radius of the droplet, Young's module of the material and the fusion temperature of the droplet on the growth rate of the instability are investigated as shown in Fig. E-3 to E-5. The growth rates of the instability increase with the decrease of the radius of the droplet and with the increase of the Young's module, thermal expansion and fusion temperature of the

material.

In the above discussion, the fracture on the solid shell is not considered. If the ultimate tensile stress is exceeded, the fracture can be expected. The maximum tangential stress in the solid shell of this example is plotted in Fig. E-6, which shows that, at the beginning of the freezing, the stress in the solid shell is very large due to the thin thickness of the shell and the stress decreases with the increase of the solid shell. According to this analysis, since the stress is always less than the ultimate tensile stress of the material, the fracture on the surface is not induced. It is conflicted with the phenomena observed from the experiment [11]. This result is caused by not considering the effect of the perturbation growth on the surface in this model. Due to the instability growth the shape of the solid shell will be changed. On the top peak of the spikes, the stress becomes very large, due to the small local curvature, exceeding the tensile stress, and fractures may be induced.

Even if the ejection mechanism, which is observed in experiments, is considered, that is, the liquid metal inside the droplet is ejected from the fracture out of the droplet under the action of the pressurization, the instability analysis still can be used to model the fragmentation induced by solidification. Here the ejected liquid metal from the droplet is considered as the fragments. If it is assumed that the velocity of the ejected liquid metal from the inside of the droplet and the fracture area on the surface are equivalent to the velocity and cross section of the spikes, respectively, although the fragmentation mechanism is different from the one we proposed, the proposed instability model can be used to model the fragmentation induced by solidification. Therefore, in this study, the instability is proposed to be the mechanism of the fragmentation provoked by the freezing on the surface of a droplet.

References

- (1) A.W. Cronenberg, T.C.Chawla and H.K. Fauske, A thermal stress mechanism for the fragmentation of Molten UO₂ upon contact with sodium coolant, Nuclear Eng. Des.

- 30 (1974) 434-443.
- (2) A.W. Cronenberg and M. A. Grolmest, Fragmentation Modeling Relative to the Breakup of Molten UO₂ in Sodium, Nuclear Safety, Vol. 16, No. 6, November-December 1975.
 - (3) A.W. Cronenberg and H.K. Fauske, UO₂ Solidification Phenomena Associated with Rapid Cooling in Liquid Sodium, Journal of Nuclear Materials 52 (1974) 24-32.
 - (4) K.H. Hsiao, J. E. Cox, P. G. Hedgcoxe and L. C. Witte, Pressurization of a Solidifying Sphere, Transactions of the ASME, Journal of Applied Mechanics, Vol. 94, pp.71-77, March 1972.
 - (5) S. Timoshenko and J. N. Goodier, Theory of Elasticity, McGraw-Hill, New York, 1951, pp. 399-437.
 - (6) R. J. Roark, W. C. Young, Formulas for Stress and Strain, McGraw-Hill, Singapore, 1976, Fifth Edition, pp. 503-508.
 - (7) M. Epstein, Stability of a submerged frozen curst, Transactions of the ASME, Journal of Heat Transfer, Vol. 99, pp.527-532, Nov. 1977.
 - (8) J. W. Yang, S. G. Bankoff, Solidification Effects on the Fragmentation of Molten Metal Drops Behind a Pressure Shock Wave, Transactions of the ASME, Journal of Heat Transfer, Vol. 109 Feb. 1987, 226-231.
 - (9) F. Cooper and J. Dienes, The Role of Rayleigh-Taylor Instabilities in Fuel Coolant Interactions, Nucl. Sci. and Eng. Vol. 68, pp. 308-321, 1978.
 - (10) J. W. Miles, On the Aerodynamic Instability of Thin Panels, Journal of The Aeronautical Sciences, Vol. 23, Aug. 1956, pp.771-780.
 - (11) F. E. Brauer, N. W. Green and R. B. Mesler, Metal/Water Explosions, Nucl. Sci. Eng. Vol. 31, 1968, pp.551-554.
 - (12) L.C. Witte, T. J. Vyas and A. A. Gelabert, Heat transfer and fragmentation during Molten-Metal/Water Interactions, Transactions of the ASME, Journal of Heat Transfer, pp.521-527, Nov. 1973.

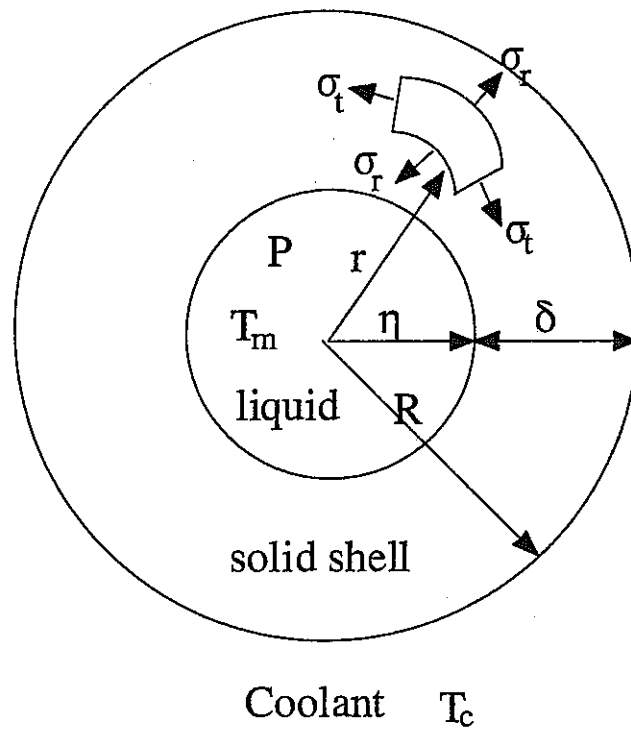


Fig. E- 1 Analytical model of solidification

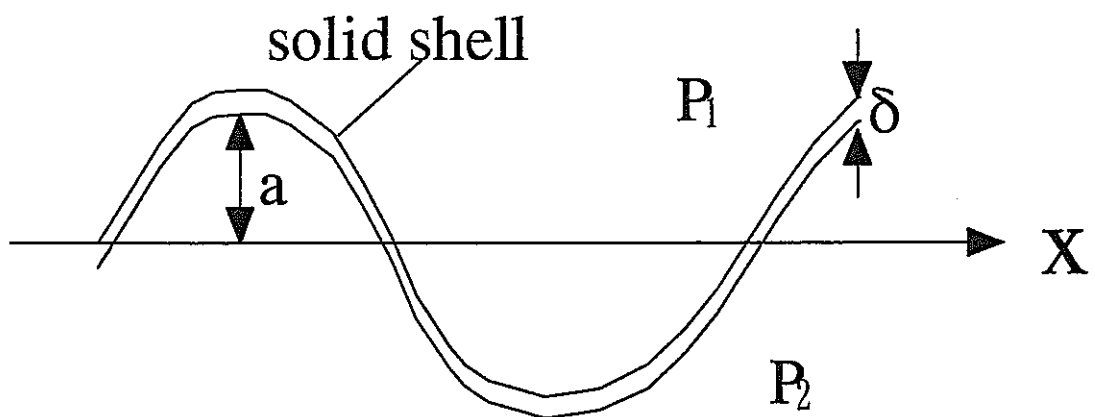


Fig. E- 2 Schematic of solid layer stability model

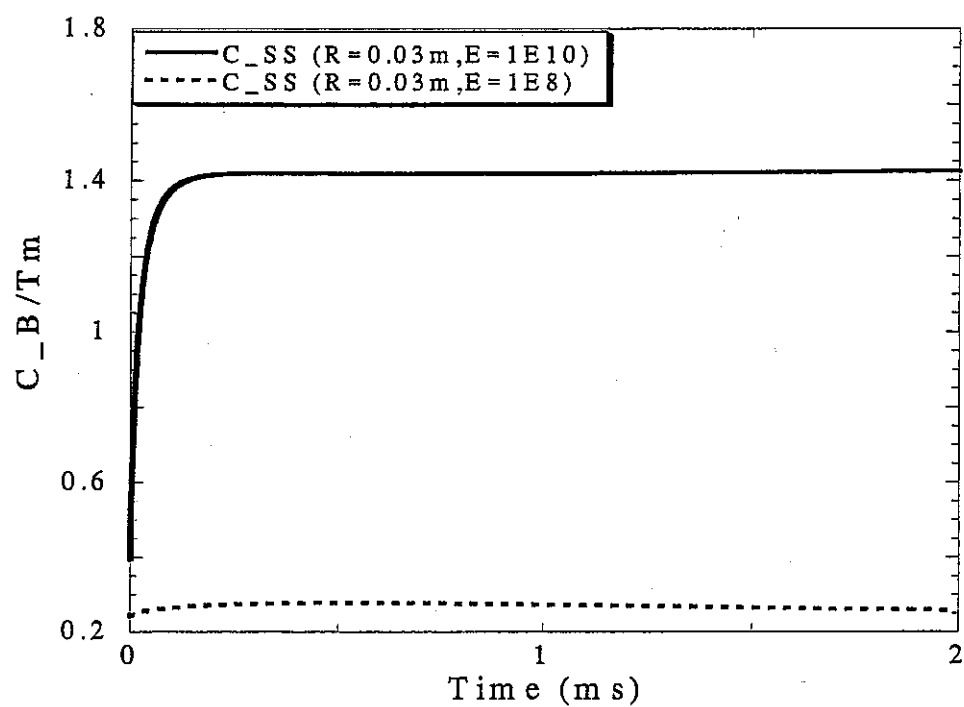


Fig. E- 3 The variation of the C_B in equation (20) with the Young's module

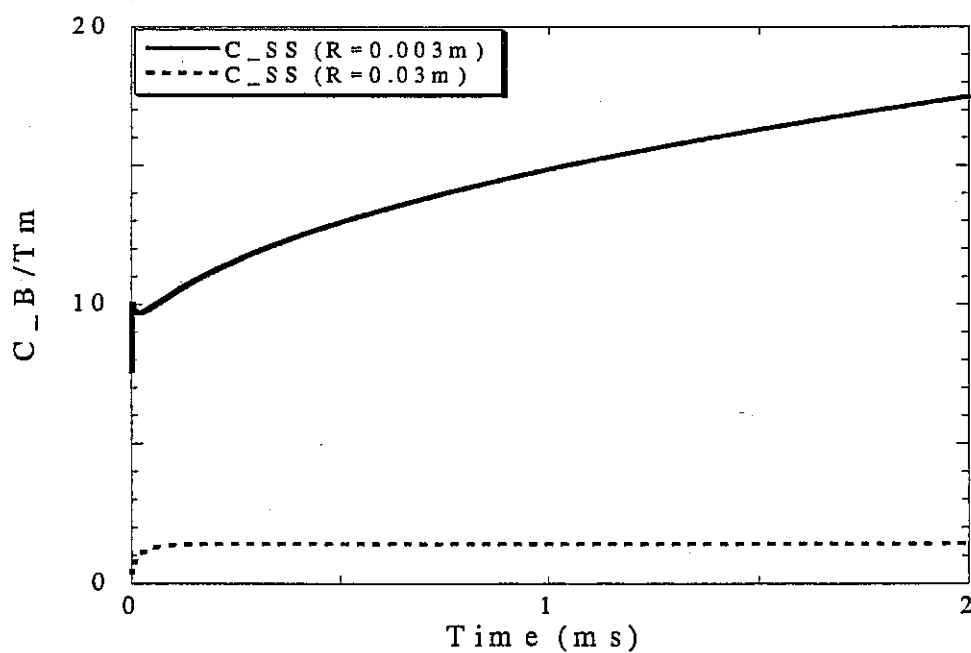


Fig. E- 4 The variation of the C_B in equation (20) with the radius of the droplet

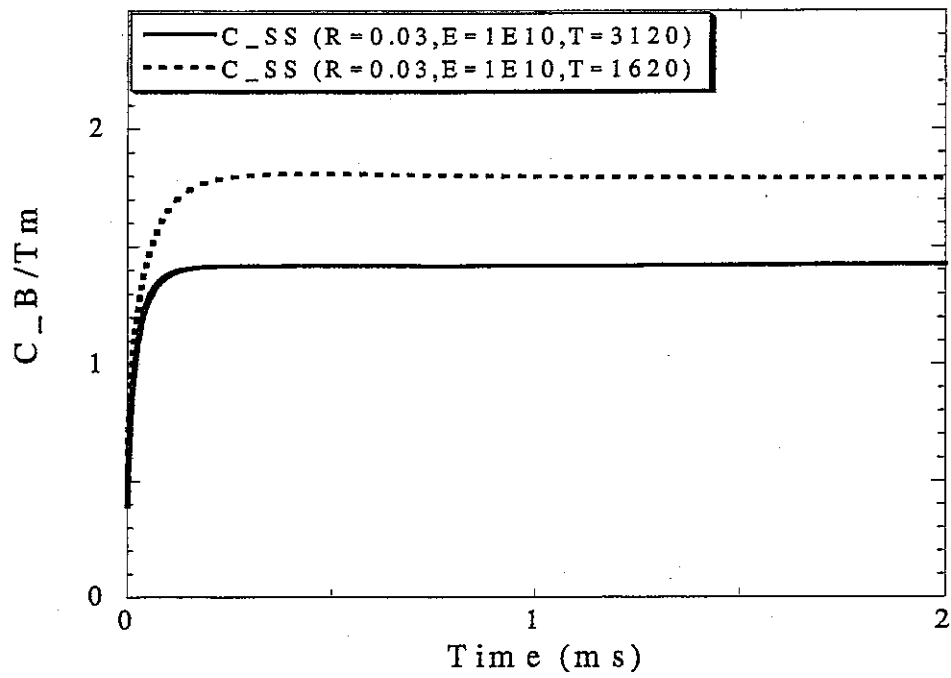


Fig. E- 5 The variation of the C_B in equation (20) with the melting temperature of the droplet

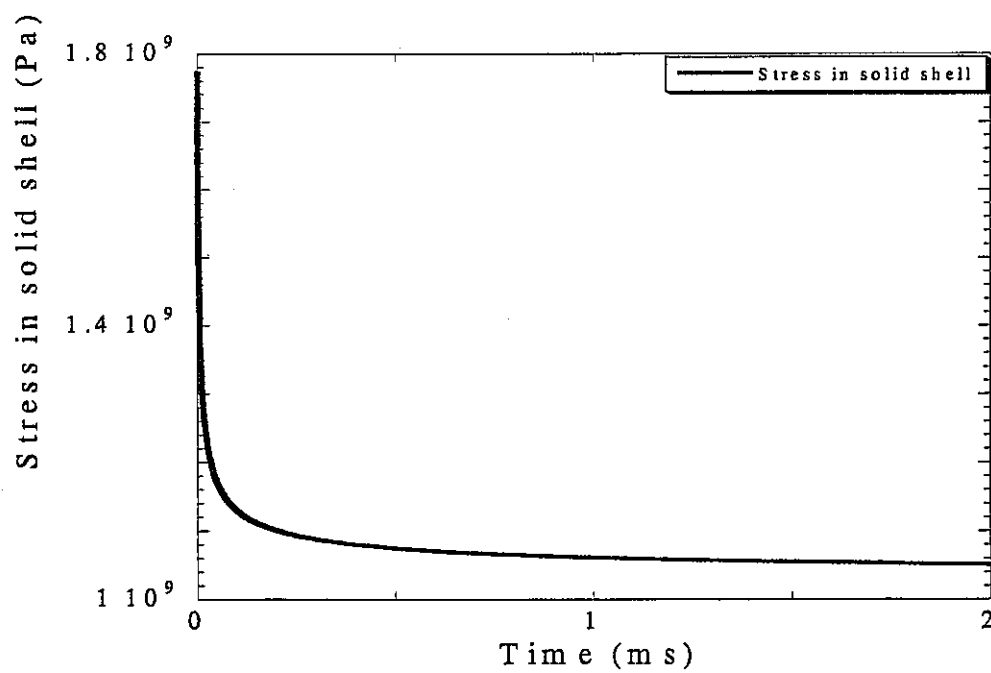


Fig. E- 6 Stress in the solid shell induced by the surface solidification of the melt droplet